

A MODEL FOR THE DIG-IN INSTABILITY IN SERIAL SECTIONING AND ITERATIVE  
ORTHOGONAL CUTTING

by

Aaron E. Ramirez

S.M. Mechanical Engineering  
Massachusetts Institute of Technology, 2012

S.B. Mechanical Engineering  
Massachusetts Institute of Technology, 2010

Submitted to the Department of Mechanical Engineering  
in Partial Fulfillment of the Requirements for the Degree of  
Doctor of Philosophy in Mechanical Engineering  
at the

Massachusetts Institute of Technology

February 2021

© 2021 Massachusetts Institute of Technology  
All rights reserved.

Signature of Author.....  
Department of Mechanical Engineering  
January 15, 2021

Certified by.....  
Martin L. Culpepper  
Professor of Mechanical Engineering  
Thesis Supervisor

Accepted by.....  
Nicolas Hadjiconstantinou  
Professor of Mechanical Engineering  
Graduate Officer

*(this page intentionally left blank)*

# A MODEL FOR THE DIG-IN INSTABILITY IN SERIAL SECTIONING AND ITERATIVE ORTHOGONAL CUTTING

by

Aaron E. Ramirez

Submitted to the Department of Mechanical Engineering  
on January 15, 2021 in Partial Fulfillment of the  
Requirements for the Degree of Doctor of Philosophy in  
Mechanical Engineering

## ABSTRACT

---

Microtome serial sectioning is a key part of building brain maps of neurological tissue, which are made by serially cutting resin-embedded brain tissue into thin sections, followed by imaging on an electron microscope; features of interest are traced through a stack of images. However, lateral dimensions of the sections typically do not exceed 1 *mm* due to instabilities encountered when attempting to cut wider sections. One such instability is the dig-in instability, which occurs in any cutting process with a cutting force component pulling the tool deeper into the workpiece; it is a niche phenomenon in industrially important processes such as machining, where it is easily avoided, and thus is not studied in-depth in the literature; however, microtome cutting is especially susceptible to the dig-in instability due to the combination of high rake angles, small cutting tool wedge angles, and highly lubricated cutting. There are currently no models for the dig-in instability nor engineering guidelines available linking mechanical characteristics of the cutting system, such as stiffness requirements, to dig-in instability regimes, despite system stiffness being acknowledged in the microtome cutting literature as important to successful cutting.

The goal of this research is to generate a model for the dig-in stability which ties together cutting system mechanical characteristics to the maximum allowable width of cut to avoid digging in. A second model was generated to model how variations in cutting parameters result in variations on the resulting cut surface, and how this variation would change with each cutting pass. An instrumented cutting setup was designed and built to measure cutting forces and record cutting videos. A compliant knife was designed to control the stiffness characteristics of the cut. Delrin polymer specimens were designed as stepped “pyramids” which would increase in width as the cut progressed, to identify the cutting width for which the cutting is unstable. Achieving this link between cutting system characteristics and successful sectioning outcome will enable designing machines capable of cutting at larger widths, and be a stepping stone towards mapping larger brain volumes. This in turn would enable greater understanding of neural function and pathology.

Thesis supervisor: Martin Luther Culpepper  
Title: Professor of Mechanical Engineering

# ACKNOWLEDGEMENTS

---

A PhD comes together as the summation of many different inputs, and I here dedicate space to give special thanks to those who were essential bringing all of this together. I would first of all like to thank my mother for all that she did in raising me, and making sure I had everything I needed as a budding geek sprout; buying me used science textbooks at the school bookfair, taking me to the thrift stores to buy electrojunk to disassemble, and taking me on frequent trips to our wonderful Chicago museums. *Mamá* wanted me to be a dentist or an architect, but engineering called out to me like a flame does to a moth; not too long into the PhD program in mechanical engineering, a career in dentistry was suddenly looking a *whole* lot more appealing.

I would next like to thank my wife Rachel, who has been *very* patiently waiting for me to wrap up the PhD project so that we can move on to the next stage in our lives together. We somehow managed to live in a cramped Central Square studio for 4 years, and are finally moving to a larger place.

I cannot thank my advisor enough; Prof. Martin Culpepper, a.k.a Marty, who brought me on board the Precision Compliant Systems Lab many years ago as a UROP, and has over many years patiently advised and mentored me in precision engineering methodology. He has been essential to this project, and I'm not just saying nice things about him here so that he'll sign off on this dissertation. I'll be dropping off care packages of spicy Mexican *chorizo* at *Casa Culpepper* for years to come.

I would of course like to give effusive thanks to my thesis committee Profs. Peter So and Rohan Abeyaratne, for their support in this project; you all have provided thoughtful feedback, and have been patient, flexible, and reassuring throughout a difficult and sinuous project, and this means the world to this frazzled PhD candidate.

I'd like to thank the technical staff at the LMP machine shop, past and present, for being a big part of my hands-on education at MIT. I would like to especially thank Pat of the Edgerton center in the N51 machine shop, for helping me machine several of the more challenging experimental setup components and keeping my nerves steady when I hit that "Cycle Start" button.

I would like to thank the MIT Libraries, which has been an essential and ever-helpful "behind-the-scenes" resource in finding information. I very much appreciated the inter-library borrowing services and the digitized document delivery services.

I'd like to thank my good pals Jonny and Tyler, who've made getting through the PhD program more bearable by way of late-night inane online chats, video game nights, and all the coffee breaks with quasi-philosophical arguments about whether there can be an objectively best pizza.

I'd like to thank my PCSL labmates past and present – there were many, but I'd specifically like to thank Marcel and Charlie, who I've been with for so long in the PCSL trenches. I would also like to thank all of the PCSL lab admins past and present - you all had to juggle so much, and the lab couldn't function without you. Saana in particular was always a boundless source of energy.

I would like to give special thanks to Leslie Regan, our outgoing departmental administrator, for everything she does for the department and in particular for us grad students – she’s the interface between us and the department, and has done a wonderful job all of these years making sure we’re all submitting the forms we need to and keeping us apprised of important deadlines while being a warm, welcoming, and reassuring presence.

I’d like to thank my UROP of many semesters, Rebecca – she put in many hours during the early period of this project where I was still figuring out what exactly this PhD project was going to shape up to be.

I’d like to thank Richard Schalek of the Lichtman Lab at Harvard University, for taking the time to discuss with me some of the difficulties encountered in ultramicrotome cutting, and for showing me the ATUM and ATLUM hardware.

Lastly, none of this would have been possible without financial support. This work was supported in part by the McGovern Institute Neurotechnology Program, by UChicago Argonne LLC, by MIT’s project Manus, and by several teaching assistantships.

*(this page intentionally left blank)*

# CONTENTS

---

<b>Abstract</b> .....	<b>3</b>
<b>Acknowledgements</b> .....	<b>4</b>
<b>Contents</b> .....	<b>7</b>
<b>Figures</b> .....	<b>13</b>
<b>Tables</b> .....	<b>25</b>
<b>1 INTRODUCTION</b> .....	<b>29</b>
1.1 Synopsis .....	29
1.2 Volumetric tissue imaging and cutting difficulties .....	31
1.2.1 The serial sectioning process.....	31
1.2.2 Brain mapping via serial sectioning and 3D slice reconstruction .....	33
1.2.3 Motivation for understanding the dig-in instability .....	34
1.2.4 Contributions summary .....	35
1.3 Thesis scope and organization .....	36
<b>2 BACKGROUND</b> .....	<b>37</b>
2.1 Serial sectioning, microtomy, and 3D volumetric tissue imaging .....	37
2.1.1 Manual serial sectioning and EM imaging - ssTEM.....	38
2.1.2 Tape collection approach (ATUM).....	38
2.1.3 Serial block-face approach – 3VIEW.....	40
2.1.4 FIB serial sectioning.....	42
2.1.5 Large-area serial sectioning .....	43
2.2 Cutting difficulties in serial sectioning .....	44
2.2.1 Chatter .....	45
2.2.2 Thick/thin sectioning and skip-sectioning.....	47
2.2.3 Dig-in .....	48
2.2.4 Tool wear and breakage .....	48
2.3 State of the art in microtome cutting force measurement .....	49
2.3.1 Lack of understanding the role of compliance in successful microtomy .....	52
2.4 Key differences between metal cutting and microtome cutting.....	54
2.4.1 Cutting speeds in microtomy are much slower .....	54
2.4.2 Work materials in metal cutting are stronger and stiffer.....	54

2.4.3	Tool geometry and rake angles .....	55
2.4.4	Thermal properties of the workpiece in microtomy vs machining .....	55
2.5	The orthogonal cutting model .....	56
2.6	The mechanistic model of cutting .....	59
2.7	Chatter stability in machining versus microtomy .....	60
2.7.1	Summary of the state of the art in chatter stability in metal cutting .....	61
2.7.2	Regenerative chatter: comparing machining and microtomy .....	62
2.8	The dig-in phenomenon in cutting .....	62
2.8.1	Dig-in in machining: a regime to be avoided .....	63
2.8.2	Wood veneering, a high-rake cutting process .....	63
2.9	Motivation for a dig-in stability relationship derivation .....	64
<b>3</b>	<b>DIG-IN STABILITY MODELING .....</b>	<b>67</b>
3.1	Single-pass dig-in stability criteria .....	67
3.1.1	Static offset from nominal feed .....	74
3.1.2	Numerical simulations of single-pass dig-in instability .....	75
3.1.3	Comparing instability behavior of positive versus negative specific feed pressure <b><math>Kf</math></b> 76	
3.2	Series dig-in cutting stability .....	77
3.2.1	Modeling stability of a series of cuts using the geometric series .....	77
3.2.2	Series cutting with positive <b><math>Kf</math></b> .....	81
3.2.3	Series cutting with negative <b><math>Kf</math></b> : Thick-thin sectioning .....	83
3.3	Depth of cut variance propagation model .....	89
3.3.1	Derivation via equilibrium position and propagation of uncertainty .....	89
3.3.2	Stability limit and relation to dig-in stability limit .....	90
3.3.3	Discussion and model implications .....	91
3.3.4	Numerical implementation .....	92
3.4	Regenerative chatter in microtome serial sectioning .....	95
3.4.1	Comparison to machining regenerative chatter stability theory .....	95
3.4.2	Regenerative steady-state amplitude growth: two-pass model .....	96
3.4.3	Regenerative chatter model predictions .....	101
3.4.4	Numerical implementation .....	102
3.5	Cantilevered knife tip compliance modeling .....	106
3.5.1	Knife tip deflection analytical model definitions .....	107



3.5.2	Finite element analysis validation .....	110
3.5.3	Knife tip deflection model discussion .....	113
3.6	Modeling workpiece deformation and compliance.....	113
3.6.1	Localized workpiece deformations via Hertzian model.....	114
3.6.2	Bulk deformation modeling .....	118
3.7	Cutting zone thermal modeling.....	121
3.7.1	First-order section temperature modeling .....	121
3.7.2	Including heat transfer to cutting tool and bulk workpiece.....	122
3.7.3	The thermal (Peclet) number .....	125
3.7.4	Workzone thermal modeling discussion .....	126
<b>4</b>	<b>CUTTING INSTRUMENT DESIGN AND CHARACTERIZATION .....</b>	<b>127</b>
4.1	Instrumented sectioning visualizer design summary .....	127
4.2	Motivation for combined force and video recording .....	130
4.3	First-order instrument analysis and design .....	131
4.3.1	Cutting forces estimation .....	132
4.3.2	Functional requirements .....	133
4.3.3	Loads and thermal structural loop analysis .....	135
4.4	Module design and analytical load-induced error model.....	141
4.4.1	Force sensor.....	143
4.4.2	Feed stage .....	151
4.4.3	Slice stage.....	154
4.4.4	Camera and optics module .....	157
4.4.5	Knifeholder.....	160
4.4.6	Workholding.....	161
4.4.7	Goniometer and knife edge adjustment.....	163
4.4.8	Chassis.....	168
4.5	Instrumentation and data acquisition hardware .....	175
4.6	Fabrication and assembly.....	176
4.6.1	Invar machining.....	177
4.6.2	Instrument assembly.....	177
4.7	Instrument control software .....	179
4.8	Data acquisition, analysis, and post-processing.....	181
4.8.1	Data acquisition.....	181

4.8.2	Data post-processing .....	182
4.8.3	Data organization and review .....	183
4.9	Commissioning and characterization .....	184
4.9.1	Force sensor calibration and commissioning .....	184
4.9.2	Force sensor noise floor .....	193
4.9.3	Minimum motion increment.....	194
4.9.4	Microscope objective calibration .....	195
4.9.5	Instrument stiffness .....	195
<b>5</b>	<b>DIG-IN STABILITY EXPERIMENTS.....</b>	<b>201</b>
5.1	Series dig-in stability test via stepped-width specimen cutting and compliant knives.....	201
5.1.1	Changing the width of cut using a stepped specimen .....	203
5.1.2	Introducing a known feed compliance using a compliant knife carrier .....	209
5.2	Stepped-width specimen cutting experiment data processing .....	223
5.2.1	Specific feed pressure $Kf$ measurement .....	223
5.2.2	Cutting variance increase with cutting width .....	224
5.2.3	Uncertainty estimates and measurements .....	225
5.3	Series cutting instability onset indicators .....	229
5.3.1	Skip sections.....	229
5.3.2	Increasing magnitude of mean force difference between successive sections .....	230
5.3.3	Feed position standard deviation increases each cut.....	231
5.4	Dig-in stability test without additional compliance .....	234
5.5	Cutting with positive $Kf$ , in the push-out regime .....	234
5.6	Regenerative chatter cutting tests .....	234
5.6.1	Measuring damping ratio with acetal and compliant knife .....	235
<b>6</b>	<b>DIG-IN STABILITY RESULTS AND DISCUSSION .....</b>	<b>239</b>
6.1	Cutting force data from dig-in stepped width cutting experiments .....	239
6.1.1	Dig-in regime cutting with feed compliance .....	240
6.1.2	Dig-in control cutting; cutting with a knife with no added compliance.....	245
6.2	Series dig-in instability assessment .....	250
6.2.1	Detecting instability via skip-sections.....	250
6.2.2	Detecting instability via divergent steady-state offset per pass .....	253
6.2.3	Feed position variance increase per pass.....	254
6.2.4	Measured vs predicted maximum series-stable cutting widths .....	256

6.3	Feed force and position variance propagation with cutting width .....	256
6.3.1	Feed force standard deviation vs cutting width.....	257
6.3.2	Position standard deviation vs cutting width.....	259
6.4	Resolving the discrepancy between modeled and observed dig-in instability behavior 261	
6.4.1	Troubleshooting stiffness via microscope video .....	261
6.4.2	Knife tip 3D FEA reveals additional compliance .....	263
6.4.3	Stability limits with additional compliance.....	270
6.5	Comparison of cutting behavior for positive and negative $K_f$ .....	272
<b>7</b>	<b>CONCLUSIONS AND FUTURE WORK .....</b>	<b>275</b>
7.1	Conclusions.....	275
7.2	Contributions.....	276
7.3	Future work.....	276
7.3.1	An improved understanding of the specific feed pressure .....	277
7.3.2	An improved model for localized knife tip compliance.....	278
7.3.3	Expanding dig-in stability criteria to cross-coupled MDOF stiffness.....	279
7.3.4	Understanding excitation source for chatter regeneration.....	282
7.3.5	Roll/twist dig-in.....	282
	<b>References .....</b>	<b>285</b>
<b>A</b>	<b>CUTTING WITH POSITIVE <math>K_f</math> .....</b>	<b>291</b>
A.1	Specific feed pressure calculation.....	295
A.2	Mean feed force vs cutting pass – positive $K_f$ .....	296
A.3	Feed force standard deviation vs cutting pass - positive $K_f$ .....	297
A.4	Positive- $K_f$ cutting dataset discussion .....	299
A.5	Material tear-out and “sawtooth” forces .....	299
<b>B</b>	<b>REGENERATIVE CHATTER.....</b>	<b>303</b>
B.1	Compliant knife and Delrin, negative $K_f$ .....	303
B.2	Compliant knife and Acrylic, positive $K_f$ .....	309
B.3	Regenerative chatter discussion.....	315
<b>C</b>	<b>COMPLIANCE ERROR MODELING AND GEOMETRY DEFINITIONS .....</b>	<b>317</b>
C.1	Knife and knifeholder – CS1 .....	318
C.2	Goniometer and knife edge adjustment – CS2 .....	321
C.3	Force sensor – CS3 .....	323

C.3.1	Force sensor coordinate system geometry definitions.....	323
C.3.2	Force sensor stiffness model and compliance matrix.....	324
C.3.3	Bend and shear force shunting membrane design .....	326
C.4	Feed stage – CS4.....	329
C.5	Machine basebeam – CS5.....	332
C.6	Machine column – CS6.....	334
C.7	Slice stage – CS7 .....	337
C.8	Workholder contact stiffness – CS8 .....	339
C.9	Specimen stub cantilever deflections – CS9.....	341
<b>D</b>	<b>COMPLIANCE MODELING FORMULAE .....</b>	<b>347</b>
D.1	Description of compliance matrix transformation technique.....	347
D.2	Miscellaneous stiffness and compliance formulas.....	347
D.3	Ballscrew decoupler design .....	348
D.3.1	Concept description .....	349
D.3.2	Decoupler analysis and modeling.....	350
D.3.3	Decoupler design process .....	350
D.3.4	Ballscrew decoupler design concept .....	351
D.4	Cantilever beam compliance matrices .....	352
D.4.1	Cantilever beam loaded at its tip, at its neutral axis.....	352
D.4.2	Cantilever beam loaded at its tip, offset from its neutral axis.....	354

# FIGURES

Figure 1.1: Instrumented cutter developed in this work to study cutting stability. The cutter measures cutting forces in three degrees of freedom while recording cutting videos via an optical microscope. ....	30
Figure 1.2: The serial sectioning process. (a) A cartoon schematic of the serial sectioning process: sections from an embedded tissue specimen are cut and floated onto a liquid trough. The sections are imaged on an SEM, then the images are stacked digitally, and features of interest are traced through the image stack. The tissue structures of interest are then reconstructed and presented in 3D. (b) An embedded specimen loaded in an ultramicrotome chuck, with a diamond knife, trough, and a silicon chip “platter” to collect the ribbons as they are cut and floated into the trough (here shown empty). (c) The silicon chip with a collected ribbon of sections (d) Two zoom magnifications of the imaged sections. Images (b-d) are from [1] .....	32
Figure 2.1: ATUM-tome tape collection system (a) complete system, with tape collector mounted in front of the ultramicrotome and ready to take up sections (b) close-up of tape collector taking up sections as they are being sectioned. From [13] .....	39
Figure 2.2: The block-face scanning electron microscopy process, (SBF-SEM, now usually referred to as SBEM) (a) Freshly exposed embedded tissue is imaged with the scanning electron beam, then the in-SEM knife slices off material to expose new fresh material (b) SEM image of cutting zone (c) CAD model of in-SEM custom designed microtome (d) close-up of cutting zone in CAD model. Figure from [14] .....	41
Figure 2.3: Schematic of the FIB serial sectioning process. From [19] .....	43
Figure 2.4: Chatter artifact, from [30], showing chatter marks in a liver specimen .....	46
Figure 2.5: Helander's two-direction cutting force sensor, figure from [34] .....	50
Figure 2.6: An isometric view of the orthogonal cutting model. Figure from [46], with modifications.....	56
Figure 2.7: Merchant's circle for calculating forces in the orthogonal cutting model. Figure from [46].....	57
Figure 3.1: Lumped-parameter model of a single-degree of system to model dig-in stability. A feed force, $F_x$ , is applied to a cutting system with mass, $m$ , stiffness, $kx$ , and damping coefficient, $b$ . The feed force is determined by the width of cut $a$ , the depth of cut, $t$ , and the material-tool combination’s specific feed pressure, $Kf$ .....	68
Figure 3.2: Feed force cutting data in acetal (left) and nylon (right) resins vs depth of cut, at a cutting speed of $317 \text{ ft/min}$ [ $97 \text{ m/min}$ ]. Figure from [51].....	69
Figure 3.3: Cutting and feed force data in acetal resin versus cutting speed, at multiple rake angles, at a depth of cut of $0.123 \text{ mm}$ . Figure and data from [44] .....	70
Figure 3.4: Steady-state feed offset from nominal resulting from finite feed stiffness $kf$ . The cut is set to a nominal feed of $t_o$ (dotted line), but due to the finite stiffness of the system the steady-state position of the cut will be a (typically fractional) multiple of the nominal feed $Gt_o$ (dashed line). .....	75

Figure 3.5: Time-domain simulation, normalized feed offset from nominal vs time, at increasing normalized cutting widths. The feed offset  $x$  is normalized to the nominal feed  $to$ , and the cutting widths  $a$  are normalized to the single-pass stability limit  $adig1p$ . The final cutting pass is unstable and decreases without bound ..... 76

Figure 3.6: Schematic of series cutting; the same specimen is cut five times by a knife with a feed stiffness  $kf$  at a constant cutting velocity  $Vcut$ . The cut is set at a nominal feed of  $to$  (dashed lines); due to the system's feed stiffness, the knife will be pulled into the material (assuming negative specific feed pressure  $Kf$ ) and the knife's steady state position will be some distance from the nominal feed (dotted line). For stable series cutting, the steady state offset should reach a constant value. .... 78

Figure 3.7: Plot of steady-state offset feed from nominal feed, versus cut number in a cutting sequence. Each line represents a series of cuts taken at a different normalized width of cut, normalized to the series stability limit. Such a limit doesn't exist for positive  $Kf$  but is still a useful normalization factor. .... 82

Figure 3.8: Schematic of thick/thin cutting, occurring when cutting with negative  $Kf$ . For each cut, the knife is fed in a constant feed  $to$ ; when the knife engages the material, it will be pulled in proportional to the feed. During the first cut, the knife is pulled in and removes additional material, resulting in a thick section. The next cut, cut #2, engages less material, and is pulled in less; a smaller section results. For a stable system, the thickness would eventually reach steady state. .... 84

Figure 3.9: Series cutting at different widths, negative  $Kf$  case ..... 85

Figure 3.10: Schematic of skip-section cutting at the stability limit. The black dashed lines represent the nominal cutting depths, and the dotted red lines represent the knife's trajectory as it is pulled into the material. The first cut is pulled in one nominal feed's worth of feed ( $to$ ), for a total depth of cut of  $2to$ ; for the 2<sup>nd</sup> cut the knife is fed in  $to$ , however there is no material to cut; no material is removed during the second cut. The cycle repeats itself with the third cut, as the feed is once again  $to$ . .... 86

Figure 3.11: Cutting sequence with negative  $Kf$ , when the width is the series stable cutting limit. The cutting alternates between diving in an additional feed's worth of material, leaving no material for the next cut ..... 87

Figure 3.12: Numerical simulation of steady-state offset behavior for a sequence of cuts. The cutting width in microns of each cut is indicated in the inset numbers. The negative normalized offset indicates that this is a dig-in offset, meaning that the cut will be thicker than the nominal feed..... 88

Figure 3.13: Plots of equilibrium uncertainty propagation numerical simulation, with ten cutting passes at each cut width (a) Normalized position uncertainty against the  $Nth$  cutting pass, with cutting width shown overlaid on each series of cuts (b) Normalized position uncertainty against the normalized cut width..... 94

Figure 3.14: Block diagram representing the cutting equation of motion for the two-pass system ..... 97

Figure 3.15: Stable versus unstable regeneration in serial sectioning. A sequence of cuts is visually represented, from top to bottom; each wavy surface represents a freshly cut surface. A

surface profile has been imprinted on surface on the first cut. (a) For a regeneratively stable system, the amplitude of the surface will attenuate each cutting pass. (b) For a regeneratively unstable system, the surface profile will be amplified each cutting pass. .... 102

Figure 3.16: A sequence of 5 cuts overlaid on one another for a stable cut. The width of cut is 10% of the maximum allowable width of cut. (a) Entire simulated trace (b) a close-up showing attenuation of the different cuts (c) the FFT magnitude of each cut (d) Parameters used for simulation..... 104

Figure 3.17: A sequence of cuts overlaid on one another for an unstable cut. The width of cut is 110% of the maximum allowable width of cut. (a) Entire simulated trace (b) a close-up showing attenuation of the different cuts (c) the FFT magnitude of each cut (d) Parameters used for simulation..... 106

Figure 3.18: Schematic of disposable knife glue assembly used in cutting experiments in this work. A disposable microtome blade (disposable knife) is glued on to an aluminum substrate (the knife mount) and withstands cutting forces in the cutting velocity direction ( $F_c$ ) and in the feed direction ( $F_f$ )..... 108

Figure 3.19: Narrow wedge truncated cantilever beam stiffness model and parameters ..... 109

Figure 3.20: 2D plane strain knife tip deflection analysis setup. (a) a schematic of the high-density control mesh zone spanning a  $50 \mu m$  radius from the apex of the truncated wedge; the shaded region contains smaller elements (b) table of mesh element parameters (c) screenshot of the complete mesh..... 111

Figure 3.21: Truncated cantilevered wedge knife tip FEA results (a) Y deflection (b) von Mises stresses (c) equivalent strain ..... 112

Figure 3.22: Hertzian contact model of knife tip indenting elastic workmaterial, used to get a first order estimate of how much deflection to expect in the workmaterial surface due to indentation forces (a) Side view showing the knife tip indenting the workmaterial (b) Top view, omitting the knife tip but showing the contact zone as an ellipse with high aspect ratio ..... 116

Figure 3.23: (a) Bulk workpiece tension/compression model, (b) bulk workpiece shear model 119

Figure 3.24: Two-source model for calculating chip (section) temperature in machining. Plastic deformation at the shear zone and the resulting power dissipated ( $P_s$ ) increases the temperature of the chip, and the power input from the power dissipated at the tool face due to friction ( $P_f$ ) further contributes to temperature rise. Figure from [58]..... 123

Figure 4.1: Analytical model load-induced feed error at the point of interest (the relative displacement between the specimen tip and the knife tip) broken down into contributions from the instrument modules. Each module's error contribution is further broken down into the direct translation error, and the error induced by each module's rotations and the subsequent lever effect (the sine errors) ..... 129

Figure 4.2: Schematic of the machine structural loop for a simple planar two-axis machine. (a) The structural loop (dashed red line) is longest at one extreme of the  $X$  range of motion and (b) is a minimum at the opposite end of the  $X$  range ..... 136

Figure 4.3: Estimating the structural loop length: if the machine can provide the required motion without adding any bulk, then the worst-case structural loop length would be the perimeter of the

square formed by the two ranges of motion  $\Delta x$  and  $\Delta y$ ; however, the machine will need “overhead” space to include motion and structural components, and sensors. This overhead length is added to each range of motion  $l_x$  and  $l_y$ . For a first order estimate, the overhead lengths are estimated to be a multiple of the range of motion..... 137

Figure 4.4: First-order estimation of the required stiffness. (a) Schematic of a general two-dimensional machine, with two axes of motion (dashed arrows). A process force is generated at the interaction point between the two axes, and this load must be carried by the machine’s structural loop (dashed red loop). (b) The elements in the structural loop can be modeled as a single continuous structure. (c) For a rough, conservative estimate of the required stiffness, the structure can be “unfurled” into a cantilever beam of equivalent length, and the deflections calculated. An alternate approach is to model the structural loop as an open ring, with forces attempting to spread the hoop open (d) or shear the hoop in-plane (e). ..... 138

Figure 4.5: Errors in the sensitive direction introduced with thermal loading; for estimation it was assumed that in the worst case, only a part of the structure expands so that symmetry would not cancel out the thermal error. .... 140

Figure 4.6: Schematic of machine structure with error modeling coordinate systems labeled. Detailed geometry is given in Appendix C..... 142

Figure 4.7: Schematic of 3-axis force sensor built up from three single-axis piezo force sensors – the tops of the cylinders are rigidly mounted to a sensing platform, and also to a sheet that shunts shear loads to ground (not shown). Each sensor can measure in the Y direction only.  $F_x, F_y$  and  $F_z$  are the applied loads at  $P$ , which in use will correspond to the knife edge..... 145

Figure 4.8: Schematic of force platform (a) with and (b) without a force shunting membrane. Each force sensor senses force along its longitudinal axis only, bending and shearing forces can damage the sensors and contribute to cross-talk noise. With the addition of a membrane which is compliant in its out-of-plane direction, but rigid in its in-plane direction, the shear and bending loads are shunted to ground with minimal decrease in sensitivity..... 147

Figure 4.9: Coordinate system and variables used for force sensor assembly modeling ..... 148

Figure 4.10: The feed stage subassembly, highlighted within the full assembly ..... 152

Figure 4.11: Feed stage subassembly with components labeled..... 153

Figure 4.12: The slice stage subassembly, highlighted in the context of the full assembly ..... 155

Figure 4.13: Annotated slice stage component diagram..... 156

Figure 4.14: Optics subassembly. A long working distance objective lens mounted on a zoom lens and recorded at 170 frames per second. The entire optical column is mounted on a hexapod allowing fine positioning of the optical column. .... 158

Figure 4.15: Annotated optical column components ..... 159

Figure 4.16: Quasi-kinematic knifeholder (a) full subassembly CAD model (b) quasi-kinematic contacts shown from side view ..... 161

Figure 4.17: (a) Specimen workholding module CAD model. An 8 mm cylindrical specimen sits in a V-slot and is clamped with a setscrew from above. (b) Workholder clamping mechanism



detail. A swivel-tip setscrew applies clamping pressure on the back side of a leaf spring and clamping pad.....	162
Figure 4.18: Schematic front and side views of workholding module with mounted specimen (a) Front view shows specimen nested in V-groove and three lines of contact (b) Side view, showing undercut on the top clamping pad. Clamping on the front and back of the specimen improves pitching resistance.....	163
Figure 4.19: Goniometer and knife edge adjustment module, shown in full assembly.....	164
Figure 4.20: Kinematic goniometer concept, shown in 2D. The instant center of rotation of the rigid body lies at the intersection of the instantaneous surface normals; a third movable contact rotates the rigid body. Valid for small displacements. Friction is the main performance limiter for such a mechanism. ....	165
Figure 4.21: Detail of kinematic goniometer and knife edge adjustment module. A magnetically preloaded screw allows for edge translation to use different parts of the cutting edge. The other contacts are preloaded with extension springs. This design is good for a range of approximately 10 deg and is primarily limited by friction. ....	166
Figure 4.22: (a) Polished tungsten carbide contacts in plastic tray; a reflection off of a nearby container is visible in the reflection of one of the contacts (b) the polished tungsten carbide contacts (red arrows) mounted in the goniometer stage .....	168
Figure 4.23: Instrumented cutter chassis subassembly, consisting of the basebeam and column subassemblies. Diagonal braces are shown, but were not used in the final assembly.....	169
Figure 4.24: Error modeling coordinate systems used for the machine base – CS4 is taken as the point-of-interest for CS5 .....	170
Figure 4.25: Chassis column subassembly .....	173
Figure 4.26: Error modeling coordinate systems between CS6 (Column) and CS5 (Basebeam) .....	174
Figure 4.27: Instrumentation block diagram with arrows indicating signal flows .....	175
Figure 4.28: Assembled cutting instrument column and basebeam. <i>Inset</i> : torque screwdriver and torque wrenches used for assembly. Starrett square visible in foreground.....	178
Figure 4.29: Instrument control VI (visible in lower left) running on control laptop. The control VI centralizes communications between the different modules, displays instrument status to the operator, and allows the operator to jog the machine and set experiment parameters (such as video recording length and feed) .....	180
Figure 4.30: Calibration module assembly overlaid on full cutting instrument assembly. The module consists of a frame holding three pulleys (shown simplified as red discs), each of which can be loaded with a dead weight in one of two positions to allow for bidirectional loading. A wire (not shown) couples the pulley output to the force sensor. The frame locates against the machine such that the module can be placed without requiring any instrument disassembly....	185
Figure 4.31: Force application loading mechanism schematic (a) Schematic of force sensor bidirectional bell crank loading arrangement for applying loads in the X and Z directions (b) Lever mechanism used for applying bidirectional loads in the Y direction (parallel and	

antiparallel to gravity vector). For both concepts the load can be applied on either arm of the loading crank pulley to apply loads bi-directionally.....	186
Figure 4.32: (a) Schematic of Y-direction (parallel and anti-parallel to gravity) loader, overlaid on CAD model of implementation via flexure pivot. This implementation has a gain of $(r_2/r_1)$ , currently 1.5 and (b) Bell-crank converts a gravity dead-weight load ( $F_1$ or $F_2$ ) into a load at the output rotated 90 degrees. This implementation has unity gain and is used to apply X and Z direction loads.....	187
Figure 4.33: CAD model of load-transferring dummy knife for force sensor calibration. The clamping force is applied via an M2 screw which threads into an M2 nut inserted into a pocket. INSET: side view showing the clamping pad guided by a simple flexure bearing. This dummy knife allows for bidirectional load application in any of the three directions without requiring the knife to be removed from the force sensor knifeholder.....	188
Figure 4.34: Loading frame module CAD model (a) and assembly (b).....	189
Figure 4.35: Force sensor calibration module in place over the cutting instrument, configured to apply Z loads. Inset zoom: focus on XZ loading pulley. Arrows show monofilament loops for hooking weights on. Also shown is a wire clamping module mounted in the vise in place of a specimen, but this was not used for calibration.....	191
Figure 4.36: Results of quiescent force sensor noise floor measurement with 95% noise confidence interval ( $4\sigma$ value).....	194
Figure 4.37: Results of force sensor noise floor measurement with slice stage in motion, with 95% noise confidence interval ( $4\sigma$ value).....	194
Figure 4.38: Schematic of structural loop stiffness measurement, shown with X direction load and resulting X deflection. (a) During cutting, $F_x$ is generated and acts on each end of the structural loop, causing X deflections (b) In the simplified approach, loads are applied on one “half-loop” of the structural loop at a time, and are reacted by the table; deflections are measured with respect to the table (the ‘ground’ frame). The two stiffnesses are then added in series. ....	196
Figure 4.39: Detail schematic of load-transferring to the slice and feed arms. (a) Slice arm loading, X direction (b) Feed arm loading, X direction (c) Slice arm loading, Y direction (d) Feed arm loading, Y direction .....	197
Figure 4.40: Physical implementation of two of the loading configurations (a) Y-direction loading on the specimen to characterize slice arm stiffness and (b) Y direction loading on the knife feed arms of the structural loop to characterize feed arm stiffness .....	198
Figure 5.1: Schematic of dig-in stability experiment cutting. ....	202
Figure 5.2: Front view of dig-in stability experiment concept. Cutting is attempted at increasing widths of cut until instability is evident.....	202
Figure 5.3: Stepped specimen design machined from rod (cylinder) stock, (a) isometric view (b) front view .....	203
Figure 5.4: Delrin stepped specimen machining in custom pallet fixture in a Microolution 363-S micromachining center. (a) The stepped specimen just after machining and (b) close up of the specimen .....	206

Figure 5.5: Microscope images of machined thinwall specimen (a) Specimen profile with ImageJ measurements of wall thicknesses (b) side profile image taken at a lower zoom level, to inspect for gross imperfections. Some parts of the sidewall are rounded off, this appeared to be due to a toolpath error and was consistent among specimens. .... 208

Figure 5.6: Machined thin-wall specimens (a) acetal (b) Acrylic ..... 209

Figure 5.7: Compliant knife used for dig-in stability testing. The body contains a set of flexures providing single-degree-of-freedom motion in the feed direction, and the cutting edge is a glued-in insert cut from a commercially available microtome blade..... 210

Figure 5.8: Compliant knife concept – introduce a single degree-of-freedom compliance while maintaining the profile of a 45°-45°-90° wedge knife. This avoids modification to the knifeholder hardware or force sensor recalibration..... 213

Figure 5.9: Microtome cutting blades on sacrificial waterjet cutting fixture (a) before being cut (b) after being cut. Knives remain stored on the fixture until they are needed..... 215

Figure 5.10: Schematic of compliant knife and knife insert assembly process ..... 217

Figure 5.11: Schematic of compliant knife characterization setup. A small electromagnetic coil wrapped around a capacitive displacement probe provides excitation and measurement to characterize the cKnife’s resonant frequency ..... 218

Figure 5.12: Compliant knife stiffness characterization setup signal block diagram ..... 219

Figure 5.13: Photograph of compliant knife characterization setup: the exciter is clamped in the vise where a specimen would be during cutting, and the compliant knife with magnet adapter instead of a knife insert is clamped in the knifeholder. The gap has been exaggerated to show the forcer and capacitance probe more clearly. .... 220

Figure 5.14: Compliant knife dynamic response magnitude. The resonant peak occurs at 1022 Hz..... 221

Figure 5.15: Knife carrier without added compliance (a) freestanding, shown with some Acrylic cutting debris (b) shown mounted in cutting machine while cutting an acetal resin sample..... 222

Figure 5.16: Calculating the specific feed pressure from measured cutting forces. (a) Side view of the calibration cut, showing the nominal feed  $t_o$  (b) Front view of the cut, showing the width of cut  $a$  (c) Resulting force trace. The entry and exit portions of the trace are trimmed. The average of the remaining data points,  $Ff, avg$  is used to calculate  $Kf$  together with  $a$  and  $t_o$  223

Figure 5.17: Schematic of force traces with increasing feed force variation as cut width increases (a) force trace of cutting on the  $Nth$  section, at a cut width of  $a$ ; (b) force trace of cutting on the  $N + 1th$  section, with a larger cut width  $a + \Delta a$ . In the latter force trace, the force swings are larger, and the average force magnitude has increased..... 224

Figure 5.18: Schematic of the expected cutting variance progression with cutting width. The vertical axis plots the ratio of the standard deviation of the cut, to the nominal feed. At lower widths of cut, the cutting width may be small enough that the resulting forces aren’t significantly higher than the noise floor. At larger widths of cut, the amount of variations exceeds the nominal feed, which means the tool will be disengaging from the material, which is not a modeled effect. .... 225

Figure 5.19: Schematic of force traces expected for a skip-section event, which would only occur after the series has gone unstable. (a) A typical feed force vs time plot (b) The subsequent section, which has zero or near-zero force, due to the previous section removing more than a nominal feed's worth of material..... 230

Figure 5.20: Numerical implementation of the normalized offset from nominal feed for incrementing width of cut, versus cutting pass. Cutting width (in  $\mu m$ , shown inset) is held constant for 10 cuts, and is then incremented by  $100 \mu m$ . As the system approaches stability, the steady state offset takes more cuts to settle down (green dashed line). ..... 231

Figure 5.21: Numerical implementation of the normalized feed position standard deviation vs cutting pass. The standard deviation is normalized against the nominal feed  $t_0$ . Cutting width (in  $\mu m$ , shown inset) is held constant for ten cuts, then incremented by  $100 \mu m$ . Note that values of the standard deviation approaching 1.0 are troublesome, as this would imply that the tool is potentially exiting the cut, and deviations from modeled behavior would be expected here. When the system is unstable, the standard deviation will monotonically increase, pass-over-pass, and this growth is faster depending on how far over the stability limit the cutting width is..... 232

Figure 5.22: Schematic of buried-tool damping characterization; a cutting test with a compliant knife cutting a Delrin specimen was stopped approximately halfway through the cut, leaving the tool engaged in the material. A small Allen wrench is used as a mini-mallet to tap on the backside of the compliant knife; the resulting vibrations are recorded and used to measure the damping ratio for the vibrations during cutting. .... 236

Figure 5.23: Impulse response of compliant knife, with knife buried in a Delrin specimen (a) an extracted impulse response from a series of mallet taps. (b) The same impulse response with a best-fit decay curve overlaid and peaks identified..... 237

Figure 6.1: Cutting force sign convention for  $F_x$ , the feed force, and  $F_y$ , the cutting force. .... 240

Figure 6.2: Feed force cutting data for two sequential cuts at  $600 \mu m$  cutting width. Cutting force vs time plots (a) and (c), and corresponding video stills (b) and (d). The feed force in (c) drops to near zero, with occasional rubbing. It is evident from the video (d) that the knife is not engaged in the material, and only removes wisps of material. This skip section is indicating that the system is already unstable..... 252

Figure 6.3: Measured average feed force per cutting pass, at different cutting widths. Each data point is presented in the sequence the cut was performed. At  $400 \mu m$  the cutting behavior changes, but is still consistent with stable behavior (the average feed force appears to be settling to a final steady-state value). At  $500 \mu m$ , the cut appears to have become unstable (the average feed force does not look like it's converging to a final steady-state value), and by  $600 \mu m$  the cut is certainly series-unstable – the average force drops below zero, indicating skip sectioning as discussed in 6.2.2. .... 254

Figure 6.4: Plot of measured feed force standard deviation, vs cutting width. Each data point represents a measured standard deviation for a cutting pass. Cuts at widths smaller than  $500 \mu m$  had feed force standard deviations below the force sensor's noise floor (95% confidence interval). At  $500 \mu m$  width, the feed force variance increases every cutting pass. .... 255

Figure 6.5: Measured feed force standard deviation vs cutting width (a) plotted with cutting width on the horizontal axis (b) plotted with normalized cutting width, normalized against the nominal series stability limit.....	258
Figure 6.6: Feed position variance progression plotted in terms of the derived feed position. (a) Normalized position standard deviation vs cutting width (b) Normalized position standard deviation vs normalized cutting width, normalized to series stability limit .....	260
Figure 6.7: Cutting system stiffness measurement using video frames (a) frame 1, t1487 f226 (b) frame 2, t1487 f213, reference frame.....	262
Figure 6.8: Survey microscope image of knife geometry; the knife appears to have a second bevel, although the very tip cannot be resolved.....	263
Figure 6.9: Close-up of knife tip and workpiece interaction zone used to obtain knife tip geometry for FEA simulation. (a) (b) with measurements overlaid .....	264
Figure 6.10: Knife tip mesh zones detail. Control meshes are applied in two zones: Zone 1 for high-density meshing at the load application area, Zone 2 for an edge general mesh, and Zone 3 is the knife body general mesh. The load acts uniformly over the load area within Zone 1 (inset, highlighted). Mesh parameters are given in Table 6-10. ....	265
Figure 6.11: Mesh and close-up of contact zone (Zone 1). ....	266
Figure 6.12: 3D Knife tip deflection FEA results screenshots at 100 $\mu\text{m}$ width (a) section view showing deflection in the loaded area with little deflection away from the loaded zone (b) 3D view of deflections; the loads on the edge cause local deformations .....	267
Figure 6.13: FEA-derived compliance matrices for localized tip bending, averaged over estimated chip contact area .....	268
Figure 6.14: Measured feed force standard deviation at each cutting width, with lower bound of apparent tip stiffness, $k_f$ . <i>app.</i> 100, (a) plotted against cutting width (b) with cut width normalized against the stability limit at this apparent stiffness. The observed stability limit is indicated on the plots; experimental data points are not expected to correspond with the variance propagation model. ....	271
Figure 6.15: Comparison between positive and negative $K_f$ dataset – Feed force mean increase with cut width (a) positive $K_f$ dataset (b) negative $K_f$ dataset .....	272
Figure 6.16: Comparison between positive and negative $K_f$ dataset – $F_f$ stddev increase with cut width .....	273
Figure 7.1: Roll/twist dig-in. (a) 3D view – the knife tip rotates about the dashed line (b) 2D side view. Rotations about this line would cause one end to dig deeper into the workpiece, and the other end to lift out of the material. ....	283
Figure 7.2: Knife rolling motions caused by force variations across the width of the knife edge; the knife as drawn here is seen looking down towards the knife edge, as if the knife was moving towards the viewer. In the worst case, the max variation $\delta F$ acts on each side of the knife edge, in opposite directions, which causes displacements at each edge in opposite rotations. ....	284
Figure A.3: Mean forces vs cutting pass for the 100 $\mu\text{m}$ width $K_f$ calibration cuts in the positive- $K_f$ dataset with stepped width specimen and compliant knife.....	296

Figure A.4: Mean feed force per cutting pass, positive $K_f$ dataset, Acrylic specimen and compliant knife .....	297
Figure A.5: Feed force standard deviation vs cutting width, positive- $K_f$ dataset (Acrylic and compliant knife) .....	298
Figure A.6: Tear-out cutting observed in an Acrylic stepped-width specimen cutting experiment, test ID #868, frame 732, 1.1 mm width of cut (a) original video still (b) annotated video still highlighting the jagged tear-outs on the incoming material left over from the previous cutting pass and on the newly-created surface. The direction of material flow is shown with filled red arrows.....	300
Figure A.7: Force plots for test #868, frame 732, Acrylic stepped-width specimen at 1.1 mm width of cut (a) entire force trace (b) zoomed in on time around 4.306 s, corresponding to frame 732. In each plot, the top trace corresponds to the out-of-plane force, the intermediate trace corresponds to the feed force, and the bottom trace corresponds to the cutting force. This cut was slowed down to 0.75 mm/s compared to 1.5 mm/s for the rest of the dataset to capture higher-quality images less affected by motion blur. ....	301
Figure C.1: Stick figure model of the cutting instrument, with coordinate systems labeled. Each coordinate system was used to capture a specific source of compliance. CS9 is fixed and used as a reference frame, and the cutting loads are applied at the labeled POI. The gap between CS9 and the POI is exaggerated for clarity. ....	318
Figure C.9: Knifeholder CAD model (a) cross section (b) with contacts replaced by springs to be modeled with Hertzian contacts.....	319
Figure C.10: Ring contact stiffness modeling (a) the ring clamping pad is (b) subdivided into four quadrants. (c) Each quadrant is modeled as a uniaxial tension/compression stiffness (d) planar model.....	320
Figure C.11: Geometry of contact layout for kinematic goniometer (a) isometric (b) top view and side view .....	322
Figure C.12: CS2 and CS3 geometric definitions.....	324
Figure C.13: (a) Individual force sensor local coordinate system used to define the stiffness matrix at each node. The $y$ direction is the sense direction. (b) Geometry used to derive the compliance matrix between CS2 and CS3. The goal is to compute the equivalent compliance of this system for loads applied at the CS2 origin, with respect to CS3. ....	325
Figure C.14: Force sensor triad with shear shunting membrane (a) basic implementation and (b) slightly more refined version used for a basic stiffness model, with the supports closer to $F_3$ . The shaded areas are the “strips” of material which will take the brunt of the $XZ$ loads and are used to model the $XZ$ stiffnesses.....	327
Figure C.15: (a) Schematic of force sensor and membrane assembly and spring model, focusing on a single force sensor/membrane attachment node. (b) Each attachment node will have a stiffness contribution from the force sensor and the membrane; if the membrane is too stiff, no force will be sensed by the sensor.....	327
Figure C.16: Feed stage stiffness model schematic .....	330
Figure C.17: Feed stage load path for determining X stiffness. (a) top view (b) oblique view..	331

Figure C.18: CS5 geometry definitions capturing compliance of the basebeam with respect to the top of the X feed bearing table.....	332
Figure C.19: Basebeam box beam member dimensions. Units are in <i>mm</i> .....	333
Figure C.20: CS5 and CS6 locations, used to model column deflections .....	335
Figure C.21: Column with attached faceplate dimensioned cross section (units in <i>mm</i> ) .....	336
Figure C.22: Slice stage stiffness model. Loads are applied at the CS6 origin and deflections are calculated with respect to CS7.....	338
Figure C.23: CS8 geometry definitions – modeling compliance contributions due to the workholder contact stiffnesses, with the CS7 origin as the load input .....	339
Figure C.24: Contact definitions for workholder stiffness modeling; four line contact regions are modeled.....	340
Figure C.25: Local contact stiffness coordinate system for contacts modeled in the workholder stiffness model. ....	341
Figure C.26: CS9 error modeling geometry definitions, layout of coordinate system geometry between CS8 and CS9.....	342
Figure C.27: Modeled geometry for specimen deflection analysis – it is modeled that the cylindrical shank of the specimen is firmly held in the vise, and a portion of the specimen is machined to a controlled geometry to be cut during testing. The machine portion of the specimen protrudes from the vise and is unsupported, and will deflect in response to cutting loads. ....	343
Figure C.28: Stub cantilever FEA validation modeled in SolidWorks Simulation. (a) Mesh setup and (b) Y-direction deflections .....	345
Figure D.29: Two-stage ballscrew decoupler concept (a) isometric view (b) front view. The thin lines represent wire constraints, and the thicker gray bodies are ideal blade constraints. Achieving the desired constraint will require two stages in series. ....	349
Figure D.30: Decoupler design parametrization.....	350
Figure D.31: CAD model of finalized decoupler design (a) the decoupler body and faceplate (b) assembled and mounted in the drivetrain.....	352
Figure D.32: Loads and coordinate system for cantilever beam compliance matrix.....	353
Figure D.33: Loads and coordinate system for off-axis cantilever beam compliance matrix ....	354

*(this page intentionally left blank)*



# TABLES

---

Table 3-1: Parameters used to generate plot of normalized offset from nominal feed for a sequence of cuts (Figure 3.12) .....	88
Table 3-2: Model inputs for variance propagation vs cutting width model; the resulting $\sigma_{xeq}$ progression vs cutting width is shown in Figure 3.13 .....	93
Table 3-3: Parameters and outputs for truncated tapered beam deflection calculations.....	110
Table 3-4: Comparison between analytical model and FEA deflections for 2D truncated cantilever beam .....	113
Table 3-5: Parameters used for Hertzian line contact model .....	118
Table 3-6: Parameters used to calculate bulk specimen compression and shear deflections .....	120
Table 3-7: Parameters used in first-order chip temperature modeling, and calculation results..	122
Table 3-8: Two-source model implementation parameters and results. ....	124
Table 3-9: Calculating a Peclet number for microtome cutting.....	125
Table 4-1: Instrumented cutting visualizer capabilities summary table .....	128
Table 4-2: Estimating cutting forces for modeling. Measured data from [39] .....	132
Table 4-3: Estimating cutting forces used for first-order modeling .....	132
Table 4-4: Functional requirements for $\mu m$ -scale cutting visualizer; discussion of the numbers selected in the body text can be found in the following paragraphs .....	133
Table 4-5: First order sizing of structural components in aluminum and steel, with the equivalent cantilever beam model and open/closed C frames.....	139
Table 4-6: First order thermal error analysis results with aluminum, steel, and Invar as candidate structural materials .....	140
Table 4-7: List of coordinate systems used for load-induced error modeling, and the primary compliance modeled .....	142
Table 4-8: Functional requirements for force sensor .....	143
Table 4-9: Force sensor (CS3) load-induced error contributions .....	151
Table 4-10: Feed stage component summary .....	153
Table 4-11: Feed stage (CS4) load-induced error contributions to the POI .....	154
Table 4-12: Slice stage component summary .....	156
Table 4-13: Slice stage (CS7) load-induced error contributions .....	157
Table 4-14 Configuration summary for optics.....	159
Table 4-15: Optics subassembly system configuration .....	160
Table 4-16: Knifeholder (CS1) load-induced error contributions .....	161
Table 4-17: Workholder (CS8) load-induced error contributions .....	163

Table 4-18: Goniometer (CS2) load-induced error contributions.....	167
Table 4-19: Chassis basebeam (CS5) load-induced error contributions.....	172
Table 4-20: Chassis column (CS6) load-induced error contributions .....	174
Table 4-21: Instrumentation summary.....	175
Table 4-22: Feeds and speeds used for Invar 36 machining operations .....	177
Table 4-23: Bolted joint bolt torque table.....	179
Table 4-24: Summary of LabVIEW instrument control VI parallel loop responsibilities .....	180
Table 4-25: Metadata collected for each recorded cutting experiment.....	181
Table 4-26: Force sensor calibration matrix converts sensor loads $F_n$ to applied loads $F_{xyz}$ units are $N$ .....	192
Table 4-27: Maximum allowable cutting load ( $F_y$ ) at a given level of feed force ( $F_x$ ) to avoid saturating any force sensors and causing a measurement error. Assumes that $F_z$ is zero (no out-of-plane load).....	193
Table 4-28: Compliance measurements and stiffness calculations, for the feed and slice arms of the structural loop (measured separately) .....	199
Table 4-29: Analytical error model stiffness predictions .....	199
Table 4-30: Measured vs analytical error model predictions, with percent error relative to analytical model predictions .....	199
Table 5-1: Stepped specimen step widths.....	204
Table 5-2: Feeds and speeds used for machining stepped specimen .....	207
Table 5-3: Compliant knife design parameters.....	214
Table 5-4: Contributors to compliant knife moving mass, to be used in stiffness calculation ...	222
Table 5-5: Summary of uncertainty estimates for modeling feed variance propagation.....	226
Table 5-6: Specific feed pressure variance calculation, rigid knife dataset.....	228
Table 5-7: Parameters used to generate Figure 5.20 and Figure 5.21.....	233
Table 5-8: Measured experimental damping ratio for buried-tool vibrations measurement .....	237
Table 6-1: Cutting force plot at each cutting width with compliant knife and negative $K_f$ . $F_x$ blue, $F_y$ red, $F_z$ yellow. The feed force is nominally positive, indicating a dig-in force with the coordinate system in Figure 6.1. Units on the horizontal axis are seconds, units on the vertical axis are Newtons. ....	241
Table 6-2: Statistics from cutting forces – means and standard deviations of cutting forces. Units are in Newtons. ....	244
Table 6-3: Cutting data used to calculate specific feed pressure ( $K_f$ ) for the stepped-width cutting experiment. ....	245

Table 6-4: Control knife cutting dataset force plots. $F_x$ blue, $F_y$ red, $F_z$ yellow. The feed force is nominally positive, indicating a dig-in force with the coordinate system in Figure 6.1. Units on the horizontal axis are seconds, units on the vertical axis are Newtons. ....	246
Table 6-5: Cutting force mean and standard deviation in each direction for the flexure-less knife. Units are in Newtons. ....	249
Table 6-6: Cutting data used to calculate specific feed pressure ( $K_f$ ) for the stepped-width cutting experiment, flexureless knife. ....	250
Table 6-7: Calculated vs measured maximum stable cutting width .....	256
Table 6-8: Parameters used for feed force and position propagation model used in Sections 6.3.1 and 6.3.2. ....	259
Table 6-9: Optical stiffness measurements .....	262
Table 6-10: FEA meshing parameters for knife tip localized deflection simulations, at $100 \mu m$ cut width. The wider cut widths used the same parameters for the control mesh, with a resulting larger number of mesh elements. ....	266
Table 6-11: FEA input loads and calculated displacements, at different cutting widths. Input loads were based on measured values in the compliant knife and acetal resin cutting dataset. Loads were applied one at a time, and the resulting $\delta x, \delta y$ displacements were measured as the average value of the elements in the Load Area shown in Figure 6.10. ....	267
Table A-1: Force plots from stepped-width Acrylic specimen and compliant knife cutting (a positive $K_f$ combination). Cutting forces are plotted at each cutting width. $F_x$ blue, $F_y$ red, $F_z$ yellow. The feed force is nominally negative, according to the coordinate system in Figure 6.1. This indicates a push-out force. Units on the horizontal axis are seconds, units on the vertical axis are Newtons. ....	292
Table A-2: Cutting force mean and standard deviation in each force direction for the positive- $K_f$ stepped-width cutting dataset. Units for statistics are Newtons. ....	295
Table A-3: Parameters used for feed force and position propagation model used in Figures ....	298
Table B-4: FFT X data, compliant knife and Delrin (negative $K_f$ dataset) .....	304
Table B-5: Feed direction FFT progression plots, compliant knife and Acrylic (positive $K_f$ dataset) .....	310
Table C-1: POI location with respect to CS1 .....	318
Table C-7: Knifeholder compliance matrix modeling the deflections at the POI w.r.t. CS1 origin, capturing deflections due to the knifeholder contacts (units are $mm/N$ for translations, $rad/N-mm$ for rotations) .....	321
Table C-8: Geometry definitions: location of CS1 origin w.r.t CS2 .....	321
Table C-9: Parameters used to define kinematic goniometer geometry .....	322
Table C-10: Summary of modeled contact stiffnesses .....	323
Table C-11: Kinematic goniometer module compliance matrix used for load-induced error modeling (units are $mm/N$ for translations, $rad/N-mm$ for rotations) .....	323

Table C-12: Geometry definitions: location of CS2 origin w.r.t CS3 .....	324
Table C-13: Force sensor stiffness model parameters .....	325
Table C-14: Force sensor compliance matrix used for load-induced error modeling for deflections seen at CS2 origin, due to loads at CS2 origin, with respect to CS3 orientation (units are $mm/N$ for translations, $rad/N-mm$ for rotations) .....	326
Table C-15: Relative stiffness vs percentage of input load sensed.....	328
Table C-16: Parameters used to compare membrane stiffness to force sensors bending stiffness .....	329
Table C-17: Geometry definitions: location of CS3 origin w.r.t CS4 .....	330
Table C-18: Geometry definitions: location of CS4 origin w.r.t CS5 .....	333
Table C-19: Compliance matrix of box beam, with box beam fixed at CS5 origin and loaded at CS4 origin (units are $mm/N$ for translations, $rad/N-mm$ for rotations).....	334
Table C-20: Geometry definitions: location of CS5 origin with respect to CS6 .....	335
Table C-21: Compliance matrix of displacements at CS5 origin w.r.t. CS6, modeling deflections of the column tube with faceplate subassembly (units are $mm/N$ for translations, $rad/N-mm$ for rotations).....	336
Table C-22: Geometry definitions, locating CS6 origin in CS7 .....	338
Table C-23: Geometry definitions, locating CS7 origin in CS8 .....	339
Table C-24: Compliance matrix modeling deflections at CS7 origin with respect to CS8, capturing the compliance of the workpiece vise contact stiffnesses (units are $mm/N$ for translations, $rad/N-mm$ for rotations) .....	341
Table C-25: Geometric relationship for CS8 w.r.t CS9 origin and orientation .....	342
Table C-26: Comparison of results of different stub-beam deflection models.....	345
Table C-27: CS9 specimen deflections compliance matrix used for modeling load-induced errors (units are $mm/N$ for translations, $rad/N-mm$ for rotations) .....	346
Table D-1: Formulae for calculating the effective stiffness of the stiffnesses of a planar ring, subject to prying and shearing forces.....	348

# INTRODUCTION

---

## 1.1 Synopsis

Understanding the structure of the mammalian brain down to the synaptic interfaces between constituent neurons is a major effort in neuroscience today, with the goal of building a wiring diagram, or “connectome”, of the human brain. Such understanding of human brain structure could ultimately lead to understanding neurological function and pathology, and major advances in treating brain-related maladies such as degenerative neurological diseases (Parkinson’s and Alzheimer’s) and combat injuries. Synaptic-resolution and large-volume three-dimensional volumetric imaging of neural tissues is performed via a serial sectioning process, whereby plasticized tissue is cut into thin layers, each layer is imaged with high resolution, and the features within the volume are reconstructed by tracing features through each image. Imaging larger volumes requires cutting larger volumes, which in turn requires cutting wider sections. However, increasing the section width of cut eventually causes cutting instabilities, and the underlying mechanics for these instabilities remain unknown. It is not currently possible to specify engineering parameters, such as cutting machine stiffnesses, to design a machine capable of cutting at a specified width of cut.

This work investigates the deterioration of cutting performance with increasing cut width and identifies a relevant cutting phenomenon, termed here the dig-in instability. The dig-in instability also exists in other industrially important cutting processes such as industrial

machining, but the particular mix of process parameters required for dig-in to be present are unlikely to be used and are easily avoided in industrial machining. Dig-in remains a niche, unstudied phenomenon. However, the requirements of serial sectioning make the dig-in instability much more likely.

In this work an instrumented cutter (Figure 1.1) measuring cutting forces and recording videos with a light microscope was designed to study the cutting process.

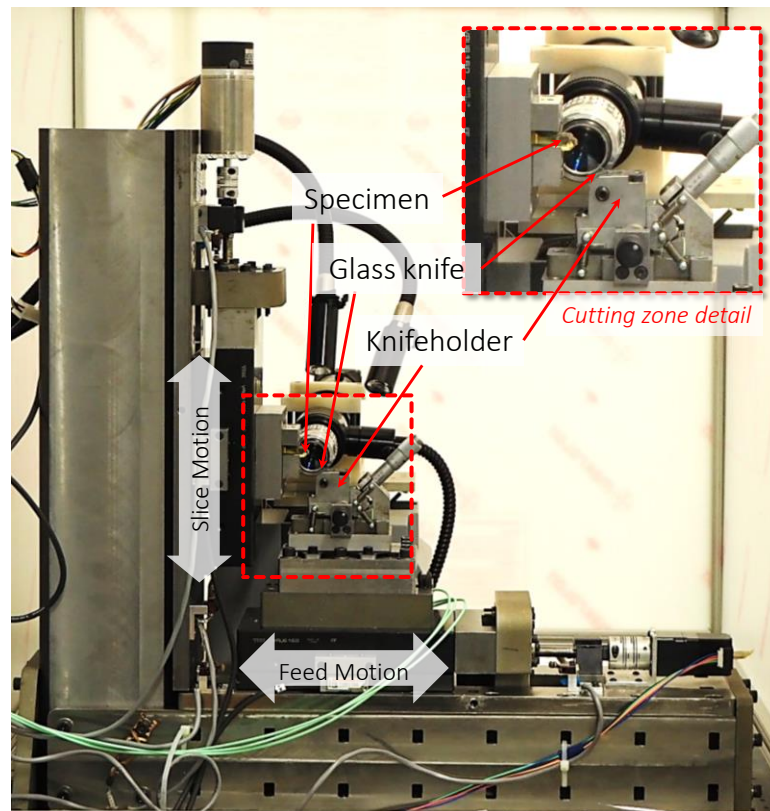


Figure 1.1: Instrumented cutter developed in this work to study cutting stability. The cutter measures cutting forces in three degrees of freedom while recording cutting videos via an optical microscope.

After observations made during exploratory cutting using this instrument, two models describing the dig-in stability were developed. The first model establishes a maximum stable width of cut for a series of cuts, for a given system stiffness and system specific feed pressure. The second model, the variance propagation model, was developed after examining the series

cutting experiment data and observing a transition zone between stable and unstable behavior. This model describes the general increase of sensitivity of the system to perturbations in the system's cutting parameters. Importantly, it describes how existing surface variation will grow with each cutting pass.

An experiment was designed to validate the dig-in stability models. The instrumented cutter was equipped with a knife carrier of known stiffness and used to cut a polymer specimen at increasing widths of cut. The width of cut for which the system became dig-in unstable was compared to model predictions. The system was observed to be dig-in unstable at a cutting width between 400– 500  $\mu\text{m}$ , corresponding to stability widths 71% – 63% smaller than predicted by the series dig-in stability model. Additional unmodeled compliance in the system was tracked down to local deflections of the knife tip and cross-compliance effects due to its geometry. With the stiffness adjustments made from this additional compliance, the discrepancy was resolved to between 2% – 21%. Thick-thin cutting is identified and explained by the dig-in model. Avenues for future exploration of dig-in stability and sensitivity are identified and discussed.

## **1.2 Volumetric tissue imaging and cutting difficulties**

This section provides a brief overview of the brain mapping 3D reconstruction workflow and the cutting issues encountered therein to motivate the need for understanding underlying cutting behavior and relating this behavior back to system and process parameters. Further background on the processes mentioned in this section are provided in Chapter 2.

### **1.2.1 The serial sectioning process**

Three-dimensional volumetric imaging of neural tissue is currently accomplished via a serial sectioning process in conjunction with electron microscopy. The electron microscope is used to study each tissue slice for volumes of less than 1  $\text{mm}^3$ , with voxel resolution ranging

between 10 – 100 nm (Figure 1.2). The tissue of interest is fixed and embedded in resin, and is subsequently sliced into a series of thin slices (‘sections’) whose thickness may range between 10-1000 nm. Each slice’s surface is imaged via electron microscopy to generate a high-resolution, two-dimensional image of each slice.

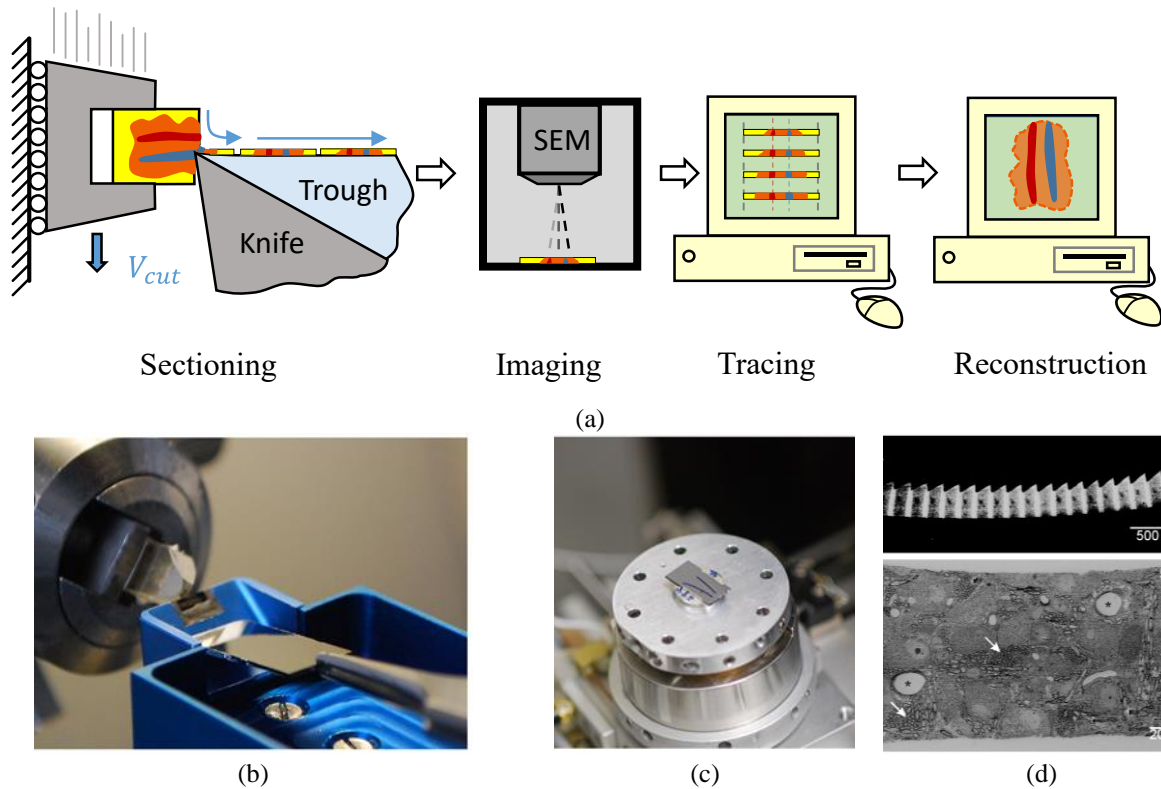


Figure 1.2: The serial sectioning process. (a) A cartoon schematic of the serial sectioning process: sections from an embedded tissue specimen are cut and floated onto a liquid trough. The sections are imaged on an SEM, then the images are stacked digitally, and features of interest are traced through the image stack. The tissue structures of interest are then reconstructed and presented in 3D. (b) An embedded specimen loaded in an ultramicrotome chuck, with a diamond knife, trough, and a silicon chip “platter” to collect the ribbons as they are cut and floated into the trough (here shown empty). (c) The silicon chip with a collected ribbon of sections (d) Two zoom magnifications of the imaged sections. Images (b-d) are from [1]

Automated software (in some cases with human expert assistance) is then used to trace features through the volume, and reconstruct the tissue in 3D for visualization, interpretation, and study.



## 1.2.2 Brain mapping via serial sectioning and 3D slice reconstruction

A major milestone towards building a complete connectome of the human brain is to first build a connectome of a smaller mammalian brain, such as that of a mouse. This would require imaging a tissue volume of approximately  $1000 \text{ mm}^3$ , or  $1 \text{ cm}^3$ . Currently, small regions of interest as large as  $1 \text{ mm}^3$  must be excised from the brain in order to be studied with serial sectioning-based volumetric imaging. Several technical challenges remain to building a whole-brain connectome of a mouse brain. These include:

- Difficulties in reliably cutting section areas larger than about  $1 \text{ mm}^2$  at slice thicknesses required for the resolution to allow tracing [2]
- Difficulties in storing the tremendous amount of data generated (estimated on the order of 10-100 petabytes) [3]
- Slow image acquisition time – a single cubic millimeter of volume is estimated to require 18 years of acquisition time with a scanning electron microscope [4]
- The lack of robust methods for tracing the neurons [5]

The focus of this research is to make inroads towards solving the first problem in the above list. Progress has been made in the other areas, for example The technology to preserve an entire mouse brain is an active research area and is at the point where it is now possible to preserve an entire mouse brain [6], and the parallelization of image acquisition using an SEM with 61 electron beams working in parallel [7]. However, no advancements in understanding the relationship between cutting system characteristics such as stiffness have been published. Mikula notes in his review of progress towards whole-brain connectomics that for block-face imaging methods such as SBEM, the technical challenge in scaling up to larger areas lies in designing in-chamber microtomes “with sufficient precision and stiffness”, and with ATUM “the reliable collection of thin, intact, wrinkle- and chatter-free sections” [2]. A major difficulty encountered here by a cutting instrument designer is understanding what it means for a sectioning system to

have “sufficient” stiffness. No research has been published establishing a link between mechanical characteristics of a system and the resulting quality of sectioning.

### **1.2.3 Motivation for understanding the dig-in instability**

The microtome cutting process is highly susceptible to the dig-in stability, as will be discussed further in Section 2.9, and has not been studied in other cutting contexts (such as machining) because the process parameters used in other cutting are such that dig-in is easily avoided. One of the outcomes of this work has been that the dig-in phenomenon has been observed generating wavy surfaces via a quasi-static physical mechanism (e.g., it does not depend on system dynamics). In the microtome cutting literature, there has been an observed tendency to describe undesired variations on a section surface introduced during cutting as the chatter artifact, where these variations have been left on the surface due to some vibration. Part of the difficulty in understanding chatter is that these vibrations could be caused by different physical origins, and the simple “chatter” nomenclature does not give insight into the physical origins of the vibration. This is a difficult problem, since a microtome user encountering the chatter artifact may not be able to troubleshoot their cutting system to fully understand the source of the artifact. However, this understanding must be in place if machines are to be designed that can cut at wider widths without introducing the variations. Different physical origins for the vibrations require different countermeasures – for example, eliminating a dig-in vibration would require tuning the process to leave the dig-in regime, making the system stiffer, or reducing the width of cut, as compared to a forced vibration, which would require finding and eliminating the input excitation or modifying the system dynamics. There is also the possibility of multiple vibration-inducing phenomenon happening simultaneously; for example, if the cutting parameters are in the dig-in regime, and the cut is also being excited due to high speeds and the initial impact of

the tool against the sample, then the resulting vibrations would be even more complex due to interaction between the two phenomena.

Cutting equipment designers must first understand the potential failure modes, and the regime of process and machine parameters accompanying the failure modes in order to design sectioning instruments capable of reliably cutting large-width sections to *cm*-scale and beyond. Equipment operators would find the information useful for understanding their machines' limits of performance, and the consequences for pushing acceptable process bounds, and for when to expect cutting performance to deteriorate. Understanding the failure regimes would enable cutting machines capable of cutting high-fidelity sections at larger widths of cuts, and more effective process automation via recognizing the symptoms of early-onset cutting failure. Understanding the consequences of operating in the near-failure regime would allow for the reduction of process variation and thus higher process precision and robustness.

#### **1.2.4 Contributions summary**

In this work, an instrument designed to record force and video for micron-scale orthogonal cutting was designed and fabricated to characterize cutting and stability. During exploratory cutting, the dig-in instability was identified as a major cause of serial sectioning failure. Core knowledge for understanding and mitigating dig-in was generated, including the maximum cutting width before the onset of series cutting dig-in instability, and understanding the system sensitivity leading up to series instability. Key process characteristics, and how to measure them, were defined in the course of designing and running experiments. Cutting stability was linked to instrument and cutting parameters. Requirements were set on machine stiffness and cutting specific feed pressure to successfully cut at a specified cutting width. Thick-thin sectioning and skip-sectioning, two effects influenced by the same parameters that influence

dig-in stability are described. The effect on section accuracy via the steady-state offset is described.

### **1.3 Thesis scope and organization**

The scope of this thesis was to generate and validate a model for the dig-in instability in serial sectioning, and provide engineering guidelines to avoid this instability. The thesis is organized as follows: Chapter 1 establishes the motivation and scope of the thesis. Chapter 2 provides additional background on serial sectioning and related cutting processes. Chapter 3 presents the dig-in stability model derivations. Chapter 4 describes the design, development, fabrication, and characterization of the cutting instrument used in this work. Chapter 5 describes the experiments designed to validate the dig-in stability model. Chapter 6 discusses the results of the experiments. Chapter 7 concludes the work and provides future directions for this area of research.

**BACKGROUND**

---

This background chapter begins with an overview of the motivation behind embedded tissue serial sectioning, 3D high-resolution nervous tissue reconstructions, and brain mapping. This is followed by an overview of the state of the art in understanding how cutting difficulties arise in serial sectioning, followed by a review of the state of the art in understanding how cutting forces are generated as a function of process parameters and the role of system compliance in cutting. Comparison is made to the state of the art in metal cutting. The digging-in phenomenon in multiple fields of cutting is explored.

**2.1 Serial sectioning, microtomy, and 3D volumetric tissue imaging**

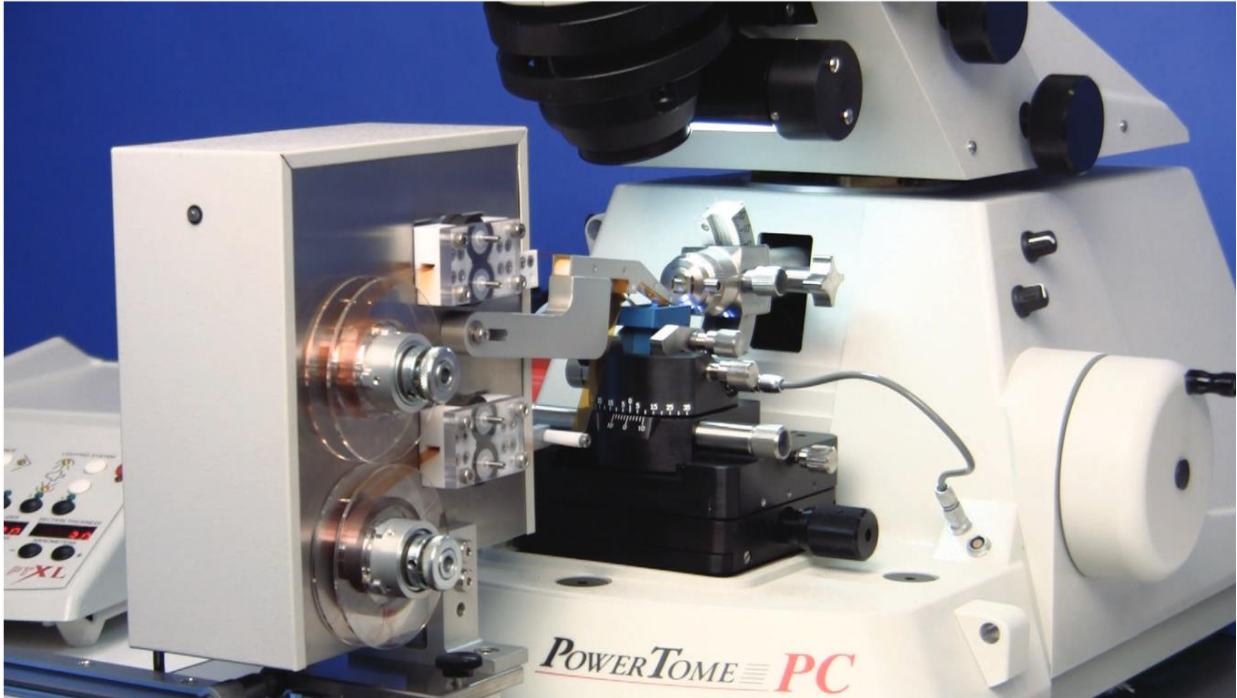
Understanding mammalian neural circuit functionality requires the necessary (but insufficient) precursor step of obtaining wiring maps, or “connectomes”, of mammalian neural tissue [8]. Volume electron microscopy (VEM) makes it possible to resolve the connections between all neurons contained within a given tissue volume down to synaptic levels [8]. There exist several approaches for gathering VEM datasets with synaptic resolution, each with advantages and disadvantages. These are discussed in depth in [9] and are summarized in the following subsections.

### **2.1.1 Manual serial sectioning and EM imaging - ssTEM**

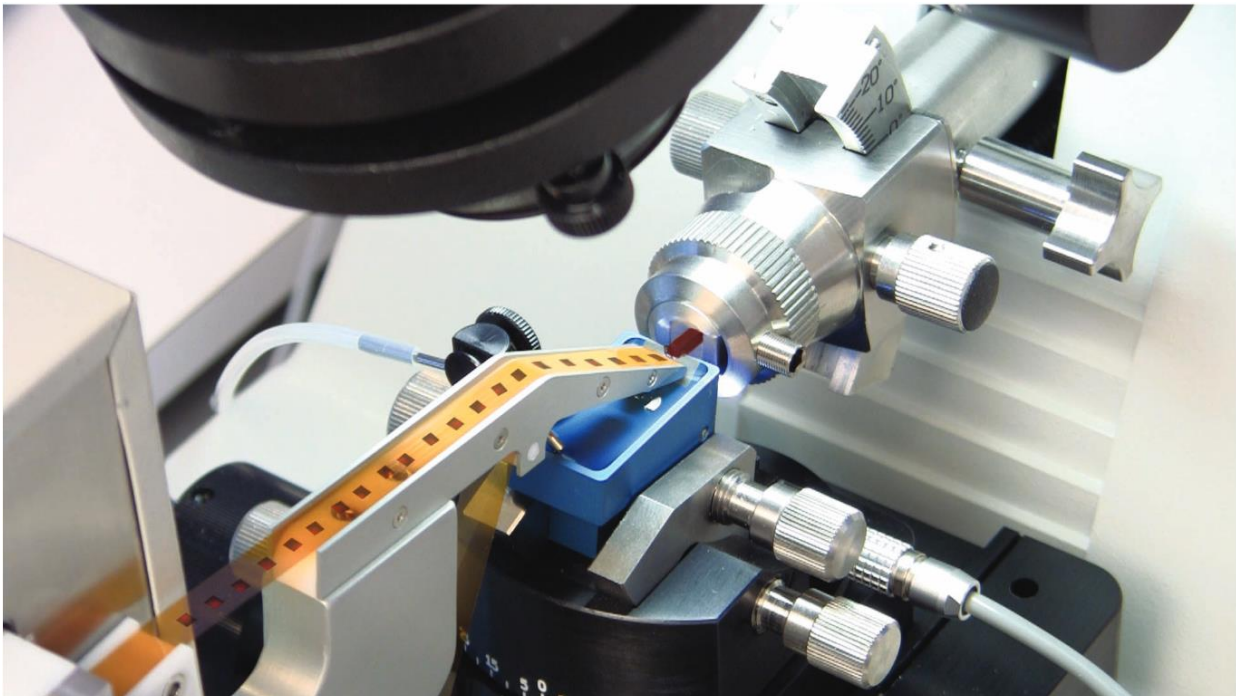
The original method for volumetric EM reconstruction was performed by cutting a series of ultra-thin sections on an ultramicrotome, collecting and arranging (by hand) these sections on a suitable substrate, imaging them on an electron microscope, then tracing features through the image stack. This technique was used to generate the first connectome of an entire organism, the roundworm *C. Elegans*, with its 302 neurons [10]. Cutting the sections, generating the images, and tracing features through the image stack was done without any automation and took 15 years [11].

### **2.1.2 Tape collection approach (ATUM)**

A natural evolution to the manual serial sectioning method was to minimize section handling as much as possible – handling the sections introduced the possibility of damaging or destroying sections during transfer, and risks introducing temperature fluctuations to the machine which would alter cutting characteristics. The automated tape collection method (ATUM) was introduced in [12]. Sections were collected on a tape reel as they are cut. Segments of the tape were then cut and arranged on a suitable substrate (typically silicon wafers) and then scanned in an SEM. Image alignment is automated with software. This approach is scalable and could be used to store tissue volumes in tape reels. Downsides of this method are the need to manipulate the sections with the specialized tape collection system, and requiring the specialized tape collection system.



(a)



(b)

Figure 2.1: ATUM-tome tape collection system (a) complete system, with tape collector mounted in front of the ultramicrotome and ready to take up sections (b) close-up of tape collector taking up sections as they are being sectioned. From [13]

### **2.1.3 Serial block-face approach – 3VIEW**

The serial block face approach, or serial blockface electron microscopy (SBEM), was first used for imaging nervous tissue in [14]. With this approach, cutting and imaging are done in the SEM chamber with a specialized in-chamber ultramicrotome. The blockface scanning approach does not require any section manipulation, eliminating a major potential error source and allowing for greater automation. Image-to-image registration along the stack of images is simplified since the images are being imaged in the same



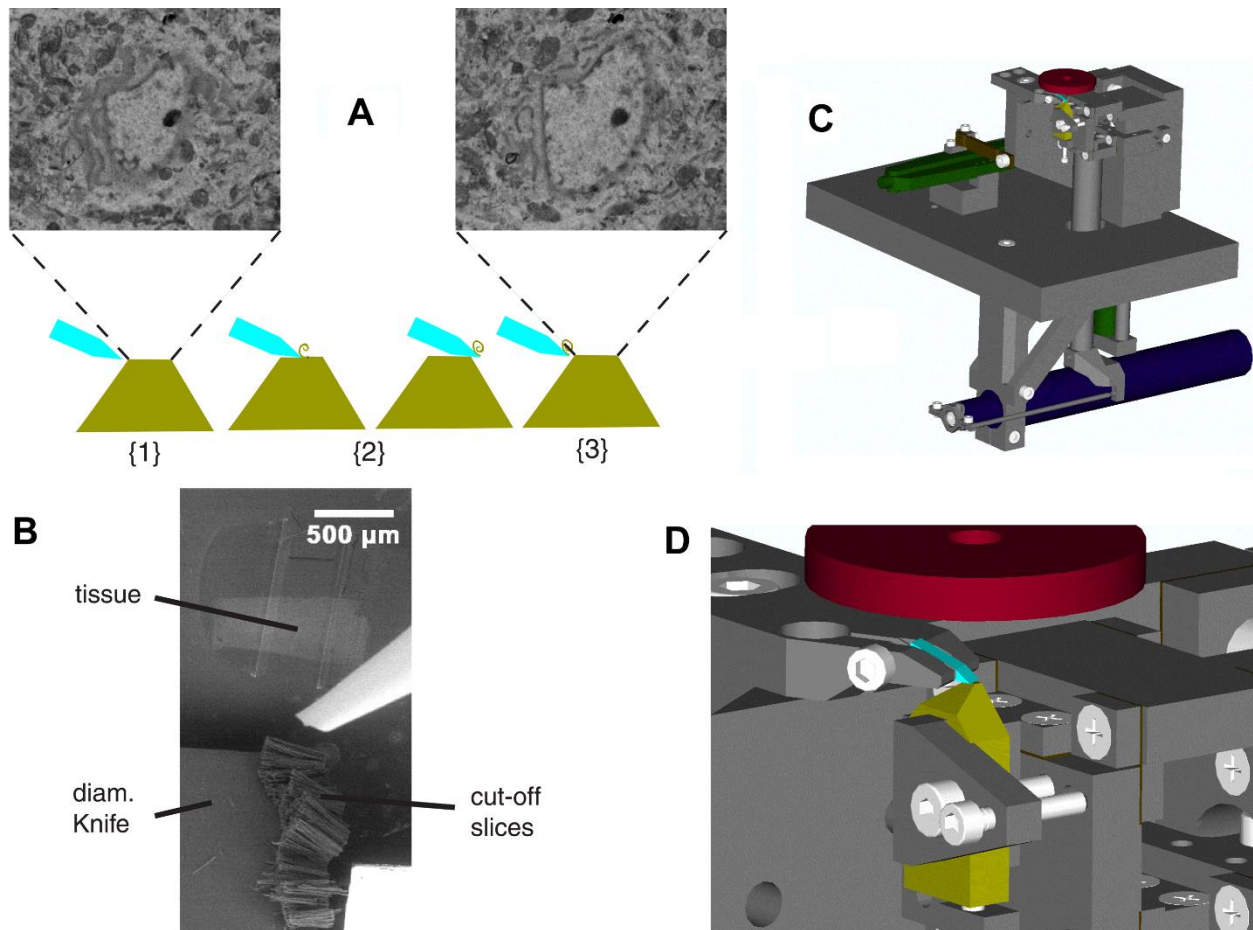


Figure 2.2: The block-face scanning electron microscopy process, (SBF-SEM, now usually referred to as SBEM) (a) Freshly exposed embedded tissue is imaged with the scanning electron beam, then the in-SEM knife slices off material to expose new fresh material (b) SEM image of cutting zone (c) CAD model of in-SEM custom designed microtome (d) close-up of cutting zone in CAD model. Figure from [14]

Downsides to this approach are that the process is limited to what can fit in an SEM – the entire cutting mechanism must fit within the SEM chamber, which places limits on the volume that can be imaged. The SBEM process is limited by the SEM’s imaging speed, which can be a serious bottleneck, although recent advances in parallelization with multibeam SEMs are improving throughput [15]. The sections are discarded after they are cut from the blockface, so the imaging must work on the first try (sections discarded after image), and there is no option of “going back” to the section to look at any features at higher resolution as for the tape-collected

systems. This technology has been commercialized and can be purchased as an add-on for SEMs [16].

#### **2.1.4 FIB serial sectioning**

The serial sectioning processes mentioned thus far all require mechanical cutting; e.g., using a knife to slice off a section from the block face. Focused-Ion Beam serial sectioning, introduced in [17], is an alternative process which uses a focused beam of ions to “mill” away material, exposing fresh material for imaging. Sectioning with a FIB does not require the use of a cutting tool to remove material. This avoids the issues introduced by mechanical cutting, however the process does not scale well due to the slow throughput. Scaling is also hampered by the beam’s diminishing ability to cut through larger samples, and the problem of material redeposition after milling. FIB sectioning is excellent for high-resolution, small-volume sectioning processes, but faces many difficult challenges for large-volume sectioning. Despite its advantages, FIB serial sectioning is uncommon in connectomics research due to the severe volume limitation – the volume that can be studied is typically smaller than that spanned by a neuron, though some improvements have been made to improve upon this [18].

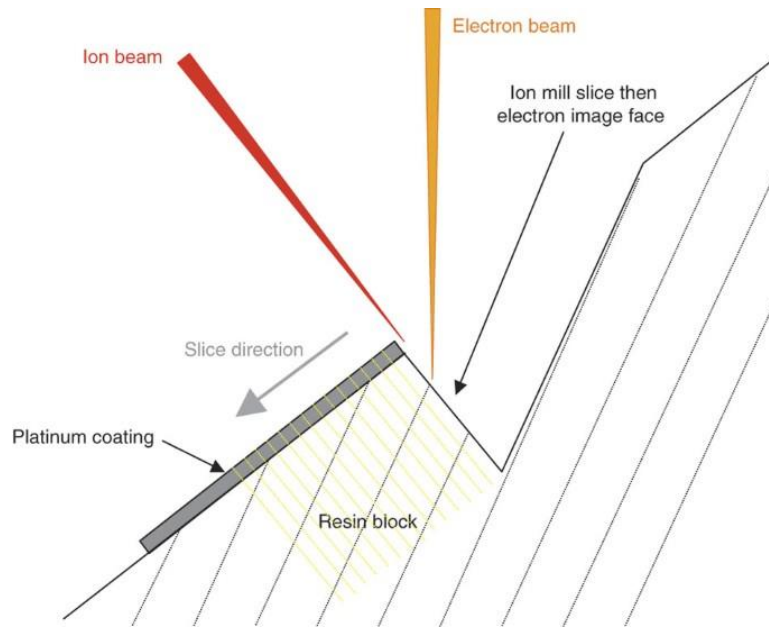


Figure 2.3: Schematic of the FIB serial sectioning process. From [19]

### 2.1.5 Large-area serial sectioning

The discussion here will be restricted to obtaining large-volume datasets and imaging with synaptic resolution (voxel resolution of between 20-50 nm), which eliminates some technologies (such as MRI and CAT scan imaging). A requirement of large-scale connectomics to obtain datasets with synaptic resolution over an overall tissue volume spanning several tens of mm's.

The BigBrain instrument was capable of cutting a paraffin-embedded human brain with 20  $\mu\text{m}$  thick sections [20]; researchers reported that the cutting introduced many defects which had to be manually repaired when possible, and no mention was made in the work of any of the mechanical details of the cutting instrument. Other instruments, such as the 3View instrument [16] can cut sections thin enough for neuron tracing, but with correspondingly small block faces and volumes. The built-in microtome in knife-edge scanning microscopy (KESM) [21] is capable of cutting whole embedded rodent organs at thicknesses down to 0.5  $\mu\text{m}$  using a custom

wide diamond blade 12.5 mm wide, but no mention is made of a maximum viable cutting thickness, and much chatter is evident in the images. The built-in vibrating steel knife microtome in two-photon tomography [22] is capable of sectioning whole organs fixed in agar with section thicknesses as large as 50  $\mu\text{m}$ .

An alternative hybrid approach which has promise to achieve the goal of simultaneous high-resolution and high volume EM datasets [9], is a combined FIB and knife-cutting strategy: the block of embedded tissue is initially partitioned into smaller blocks with a heated diamond knife, and the partitioned blocks are serially sectioned with a FIB at high resolution [23, 24]. Further improvements to the process are reported in [18]; improvements were made to allow for larger volumes, speed up imaging, improve reliability for months-long operation, and speed up proof-reading (less reliance on human proofreading). Attempting to cut thick sections of embedded tissue generally causes sections to crumble and be rendered unusable. The hot-knife microtome technique, where the knife is pre-heated before cutting, was introduced in [25] with steel knives and was demonstrated as capable of cutting embedded tissue areas on the order of 100  $\text{mm}^2$  and larger, but with unknown quality. The technique was then applied to diamond knives in [23] to achieve excellent quality sections in 20  $\mu\text{m}$  thick embedded tissue. Vibratory cutting was added to the technique in [24] to further enhance section quality with a block face area of approximately 4.5  $\text{mm}^2$ . The authors of these papers provide cutting parameters that worked for their application but do not provide a physical model for why the techniques work; understanding the underlying cutting phenomenon is still an active area of research.

## 2.2 Cutting difficulties in serial sectioning

Several problems can arise during ultramicrotome cutting of embedded tissue specimens. [26] provides a summary of these:

- Section skipping
- Holes or tears in sections
- Fine scratches, or knife marks
- Chatter and vibration

The dig-in phenomenon can manifest as section skipping and/or a form of chatter vibration; a problem with the “chatter” nomenclature as used in the microtomy literature is that it does not distinguish the source or nature of the vibration – the chatter in question could be a forced vibration, a regenerative vibration (as in machining), a stick-slip vibration, or vibration due to periodic digging-in (and quite possibly some combination of all of these). Understanding the physical origins of the vibration allows one to design machines and processes to avoid the different forms of chatter. Sectioning technique handbooks advise that increasing the block-face area will cause the knife edge and section quality to degrade sooner; block faces over  $0.5 \text{ mm}^2$  tend to have more chatter artifacts and compression [27]. A  $3 \text{ mm} \times 3 \text{ mm}$  square was considered “fairly large” [28]. In this section the major issues will be reviewed.

### **2.2.1 Chatter**

Chatter, sometimes also referred to as “flutter”, is a variation in the section thickness caused by tool vibration; the tool edge deviates from the nominal depth of cut, causing a variation of the section thickness which can show up as bands of dark and light lines when imaged on a microscope; in extreme cases the bands will obscure features of interest. In even more extreme cases, the tool vibration amplitude will be high enough that the tool disengages from the material (“jumps out” of the cut) and the section becomes a set of discontinuous “shreds”. Chatter marks are typically spaced  $1 \text{ }\mu\text{m}$  or finer [26]. In knife-edge scanning microscopy, a sectioning thickness of  $50 \text{ nm}$  was desired but chatter and the associated large

thickness variations (on the order of hundreds of nanometers) made this impossible [29]. Sectioning handbooks recommend decreasing sectioning speed to suppress this [26].

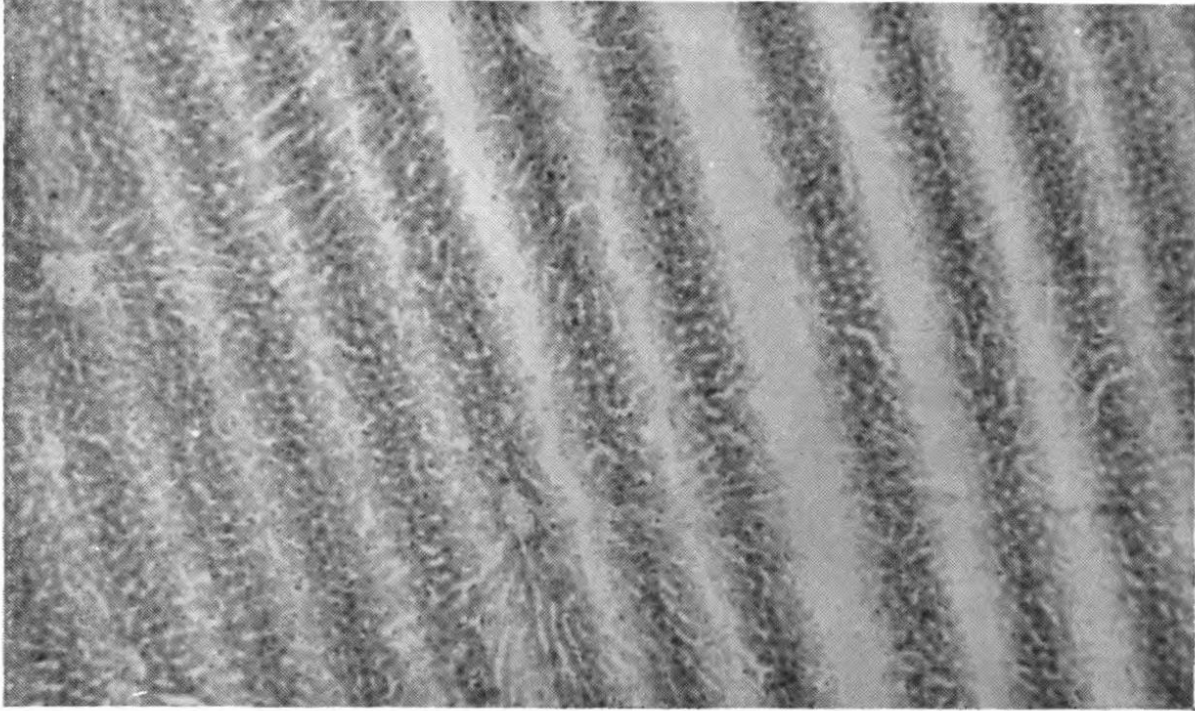


Figure 2.4: Chatter artifact, from [30], showing chatter marks in a liver specimen

Part of the difficulty in understanding and modeling chatter is that chatter can have several underlying physical causes; “chatter” is widely used as a catch-all term for periodic variations in the section thickness. The chatter vibration could be a forced vibration caused by excitation elsewhere in the system, it could be due to a regenerative effect, or it could be due to the tool periodically digging into the material, or some combination of all of these. The underlying physical causes of chatter are still unknown and an active area of research. In a study on microtomy of metals, [31] points out that earlier researchers had called some artifacts they were seeing ‘chatter’, but the surface structures observed were actually caused by cutting stresses. Researchers in [32] noted that a poor contact interface in the mounting of the

knifeholder caused by ill-fitting mechanical contact between the parts – e.g., a low-stiffness interface – can cause chatter.

### **2.2.2 Thick/thin sectioning and skip-sectioning**

One of the problems that can occur is that the microtome will remove sections in a thick/thin alternating sequence – first a thick section is removed, followed by a thin section, then the sequence is repeated [26]. This is known as thick-thin sectioning. In extreme cases, a thick section will be removed, followed by one or more cutting passes with no sections being removed – one or more sections are skipped after the initial thick section is cut, and after a few empty cutting passes, a thick section is removed and the pattern repeats. There are several proposed explanations for this phenomenon and it appears that each can be the underlying cause. One explanation for the physical cause of thick/thin sectioning is that the tool edge has blunted, so it takes multiple sections' worth of feed before there is enough material for the rounded edge to remove. In this case, it would be expected that the cut section would be severely distorted due to the effective negative rake angle from the blunt tool, making this physical cause of thick/thin sectioning easily distinguishable. Another possibility is that the tool is set such that the clearance face is interfering with the workpiece and compressing it down as a cut is taken; this material then springs out for the next pass. In this case it would be expected that there would be some surface damage caused by the rubbing between the knife clearance face and the workpiece. The series dig-in stability model presented in this thesis proposes yet another explanation for this phenomenon, based on a knife's tendency to pull into the material in situations where the resultant force has a negative thrust component.

### **2.2.3 Dig-in**

The phenomenon explored in this work is briefly mentioned in general guide to microtome usage [30] – the cutting forces involved in microtome usage can push the knife out of the block entirely and produce an incomplete section, or the knife can bend back towards (e.g., into) the block. “This back and forth movement may be repeated many times before the complete section is cut, and the section therefore has a series of thick and thin regions.” This is inherently caused by a cutting stiffness that is too low, but this relationship between stiffness and digging-in or pushing-out is not described in the literature.

### **2.2.4 Tool wear and breakage**

All cutting tools eventually wear to the point where they cannot be used to remove sections at the desired section thickness. It is possible to damage the edge on even a diamond knife – these are not recommended for cutting sections greater than 1 micron [26]. While there is no single comprehensive study of microtome knife longevity, several works in the context of serial sectioning and VEM share information about diamond knife failure and longevity. A new diamond knife began missing sections when cutting 29 nm sections, sometime after 5,000 sections, and that this number decreased with finer (i.e., smaller) section thickness. At 25 nm thick sections, the knife could cut around 1,000 sections before beginning to miss cuts, and would subsequently miss cuts at a rate of about 5% [12]. The authors hypothesize that the dulling is caused by the metal stains used – tissues that had been stained more strongly tended to dull knives quicker. A diamond knife required shifting to a fresh portion of the knife edge after approximately 7,000 sections when cutting larval zebrafish embedded in resin cutting at 60 nm section thickness [33].



## 2.3 State of the art in microtome cutting force measurement

As ultramicrotome technique evolved in the latter half of the 20<sup>th</sup> century it became evident that quantitative evaluation of microtome cutting forces would be needed to advance microtome capabilities. Efforts to measure the cutting forces increased in complexity as technology improved (e.g., with the introduction of piezo-based high-stiffness force sensors), as researchers recognized that the force sensing subsystem could itself influence the cutting process, and as researchers recognized the utility in measuring the feed-direction cutting force in addition to the cut-direction force.

Qualitative measurements of the cutting force were made in [30] by measuring containers of water on the opposite end of a microtome rocker arm to obtain a relative evaluation of the cutting forces required for sharp versus blunt knives, and for hand-sharpened microtome knives versus machine-sharpened razor blades.

A custom knifeholder instrumented with piezoresistive transducers to measure cutting forces in two directions (the slice and feed directions) based on a design adapted from the metal cutting literature was built in [34]. Compliance of the transducers, which relied on a change in resistance in response to applied loads as being smaller than  $0.14 \mu\text{m}/\text{N}$ , corresponding to a stiffness of  $0.007 \text{ N}/\mu\text{m}$ , or  $7 \text{ N}/\text{mm}$ .

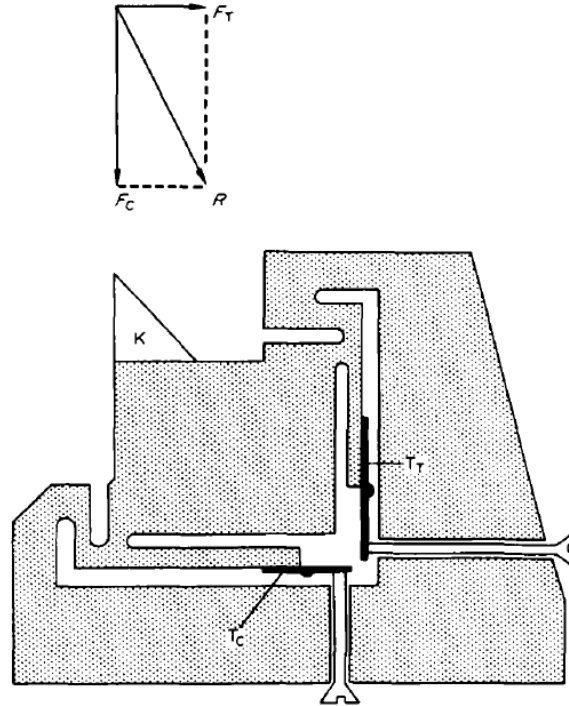


**Fig. 3.** Knife (K) mounted in knife holder adapted for measurements of cutting forces. The cutting force  $R$  can be divided into two components: a horizontal (thrust) force  $F_T$ , and a vertical (tangential) force  $F_C$ . These forces are transmitted to the transducers via thin bridges in the knife holder. The vertically mounted transducer ( $T_T$ ) is influenced mainly by the horizontal force component, and the horizontally mounted transducer ( $T_C$ ) is influenced mainly by the vertical force component.

Figure 2.5: Helander's two-direction cutting force sensor, figure from [34]

Cutting forces in the cut direction during cryo-ultramicrotomy, a variation of microtome cutting performed at very low temperature, were measured using a strain-gauge load cell in the drive arm of an ultramicrotome [35]. There was no comment on any compliance issues.

An instrumented microtome with single axis force measurement based on strain gauges mounted in a modified knifeholder was used to study the effects of sectioning variables on section quality and forces [36]. In follow up work, a second sense direction with a two-axis strain-gauge force sensor is added, with compliance measured to be  $0.7 \mu\text{m}/\text{N}$  corresponding to a stiffness of  $1.43 \text{ N}/\mu\text{m}$  in the slice direction (feed direction stiffness is unreported) [37]. The author notes that previous studies [34, 35] suffered from insufficient stiffness, without further

qualification, for example, how much stiffness is required for a given cut, and what the consequences of insufficient stiffness are. They note that the conventional wisdom is that the specimen and knife must be as rigid as possible, but there is no published information as to what these stiffnesses should be. It is of interest to note that it is implied that the cutting machine itself, e.g. the microtome, also must be of sufficient stiffness, but this isn't explicitly mentioned, and they acknowledge the need for high stiffness in the feed direction. The authors note that the instrumented microtome used in [34] was likely deflecting an amount equal to the section cutting. The authors acknowledge that their own design is likely not adequately stiff – they mention encountering problems when attempting to cut good sections without further qualification.

Motivated by a lack of understanding of the mechanics underlying microtome cutting, Allison & Vincent measured sectioning cutting force in wax-embedded tissue samples [38]. The authors argue that an improved understanding of microtome cutting mechanics was a necessary step to automating the cutting process and optimizing cutting parameters. Force measurement could be used to troubleshoot the cutting process, for example, by noting changes in cutting forces that could correspond to section thickness changes. This machine measured cutting loads in one direction only, the cutting direction. The authors mention that the design in [35] introduced excessive compliance, though a lack of rigidity is not mentioned at all in the cited work.

A high-stiffness (in comparison to previous literature designs) two-axis force sensor was designed in [39] to measure cutting forces in microtoming amorphous polymers and to measure the energy dissipation and fracture energy involved in the process. This was an improvement upon their earlier work in [40], and included several usability enhancements in addition to the

second sense direction. This sensor appears to suffer from signal decay in the piezoelectric sensor. They report a stiffness of 350 N/um based on the load cell stiffness values. This reference is of special interest in this work, as they give the most details on the cutting forces generated in both the cutting and feed direction, for an embedding resin (DGEBA epoxy) and these forces are used as representative values to design the instrumented cutter used in this work.

$$\frac{F_c}{b} = 60 \frac{N}{m}, \quad \frac{F_t}{b} = -10 \frac{N}{m} \quad \text{at } h = 0.225 \mu m \quad (2.1)$$

where  $F_c$  and  $F_t$  are the forces in the cut velocity and thrust (feed) directions respectively,  $b$  is the width of cut, and  $h$  is the feed, or uncut chip thickness. The negative sign on the thrust force indicates that the tool is being pulled in to the workpiece (i.e., this is a dig-in force). At a width of cut of 1 mm, the cutting forces would be 0.06 N and -0.01 N for the cut and thrust forces respectively. For sizing, it is useful to estimate cutting forces at feeds of 1 μm and 10 μm; if, as an approximation, a linear scaling with the feed is assumed, the estimated cutting forces ( $F_c, F_t$ ) are (0.27 N, -0.044 N) at 1 μm feed and (2.7 N, -0.44 N) at 10 μm feed; these forces can be scaled with cutting width to approximate cutting forces at other widths of cuts.

### **2.3.1 Lack of understanding the role of compliance in successful microtomy**

The experiments in microtome force measurement in conjunction with common experience in microtome cutting have made clear that cutting system compliance is an important characteristic in ensuring successful sectioning, and that there is currently insufficient research linking successful sectioning outcomes with cutting system compliance characteristics.

Compliance must be low enough (equivalently, stiffness must be high enough) for a given set of cutting parameters, but it is as yet unclear when a system has adequate stiffness, and what exactly are the penalties if the minimum stiffness is not achieved for a given cut. There have

been no studies to date explicitly making this important link between cutting parameters, system stiffness/compliance characteristics and the degree of quality of the output.

General guidelines on microtome usage are given in [30]. The author notes that the cutting forces can be of a large enough magnitude and in the correct orientation to force the knife out of the block, and that the cutting forces involved when cutting large blocks can cause knife or instrument vibration. He refers to a lack of “strength” in the knife, which can be interpreted as an issue of compliance rather than that of knife breakage.

A thick/thin cycle of cutting is described when cutting with an instrumented microtome at large rake angles [37]. The authors hypothesize that this is caused by blade edge deflection away from the sample being cut caused by interference between the tool flank and the sample, although this combination of parameters would likely cause the cutting to be in the dig-in regime and also exhibit thick/thin cutting at large sample widths.

The design of an automated lathe ultramicrotome designed to be capable of collecting tens of thousands of sections at thickness on the order of 10 nm is discussed in [41]. The author mentions that the mechanical system focused on maximizing stiffness to avoid sectioning issues, though with no further details on what stiffness was required and what the machine’s stiffness characteristics ultimately were. Their system was able to measure forces in five degrees of freedom (three forces and two moments), though this cutting data was not published.

The role of compliance in cutting has been generally recognized; in his treatise on cutting [42] Atkins recognized that introducing a force-measurement system into a cutting system introduces compliance and can introduce chatter and ringing where there would otherwise be none without the force sensor. In particular, an industrially important area of cutting since the late 19<sup>th</sup> century is machining, which has long dealt with the issue of sufficient cutting

machine stiffness to obtain acceptable surface quality. The metal cutting and machining literatures provide inspiration and insight into understanding the rigidity issue. Examined next are some key differences between metal cutting and microtomy.

## **2.4 Key differences between metal cutting and microtome cutting**

The kinematics of the orthogonal cutting process (the “baseline” metal cutting model) bear strong similarity to microtome cutting. The following sections describe the differences between microtomy and metal cutting.

### **2.4.1 Cutting speeds in microtomy are much slower**

Typical cutting speeds used in ultramicrotomy are around 1 mm/s. In contrast, machining using a carbide cutting tool typically takes place at speeds of 500 – 10,000 mm/s [100 – 2000 sfpm] depending on the material being machined [43]. Machining of polymers is closer material-wise to the resins used in microtomy; these typically cannot be machined at too high of a speed because they will melt and gum up the tool, preventing proper chip clearance while also negatively affecting the surface quality and accuracy. Typical cutting speeds for polymers such as polymethyl methacrylate (PMMA) are around 1000 - 10000 mm/s [44]

### **2.4.2 Work materials in metal cutting are stronger and stiffer**

The material being cut in machining will be stiffer and stronger than the materials being cut in microtomy (the exception to this being in materials science research – sometimes harder materials are sectioned on ultramicrotomes). Workpiece stiffness will be proportional to the Young’s modulus; a typical metal will have a Young’s modulus of between 70 GPa and 200 GPa, for aluminum and steel, respectively, compared to a Young’s modulus of between 1-3 GPa for a hard resin that would typically be the embedding matrix in ultramicrotomy. The strength of

the material will be proportional to the material yield stress; metals can vary greatly depending on their composition and heat treatment. A mild steel may have a yield strength of approximately 250 MPa, whereas a hardened steel can have a yield strength of above 1,000 MPa. The Young's modulus in polymers, in contrast, will be a fraction of that of the mild steels'; Acrylic has a yield strength of approximately 72 MPa.

### **2.4.3 Tool geometry and rake angles**

Cutting tool shapes in metal cutting are generally of a higher wedge angle compared to microtome knives, and rake angles are shallower and mostly negative for harder materials, in order to withstand the higher stresses and forces involved in metal cutting. The offcut is severely deformed in the machining process, especially with negative rake angles; this is in contrast to microtome cutting, where the offcut (in this case, the section) is of interest and whose structure must be preserved as much as possible – this is accomplished only with knife-like tools of high rake. Microtome cutting tools typically have an included angle of between 35-45°, and the tool is typically set up with a clearance of about 5°. This yields a rake angle of between 50 – 40°, respectively.

When machining aluminum with a high-speed steel tool, a rake angle of between 15-35° with a relief angle of about 15°. When machining the same material with a carbide tool are rake of 8 – 30° with a relief angle of about 13° [45].

### **2.4.4 Thermal properties of the workpiece in microtomy vs machining**

Generally speaking, the materials being cut in machining are better thermal conductors than the polymers and resins used in microtome cutting, which are thermal insulators. This is explored in the thermal modeling done in Section 3.7.

## 2.5 The orthogonal cutting model

The orthogonal cutting model, also known as the thin-shear-zone model or Merchant model, is an idealized two-dimensional model of the cutting process used to relate cutting parameters to resulting cutting forces. It is briefly discussed here, as it is an important foundational model in metal cutting, however it is not used in this work as will be explained later in the section.

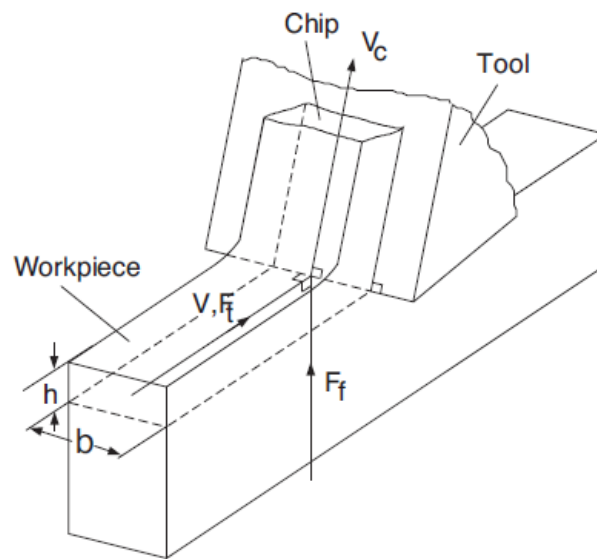


Figure 2.6: An isometric view of the orthogonal cutting model. Figure from [46], with modifications

The assumptions made in the orthogonal cutting model include [45]:

- The tool is perfectly sharp, and has no contact on the clearance face
- The shear surface is a plane extending from the tip of the tool up to the surface
- The cutting edge is perpendicular to cutting direction of motion (e.g., the tool is not skewed)
- Cutting is plane-strain; there is no material flow out of the plane
- The depth of cut, or feed, does not change during the cut
- The tool is wider than the workpiece



- The cutting speed is constant
- The chip is continuous, and there is no built-up edge at the tip of the tool
- The shear and normal stress on the shear plane are uniformly distributed
- The friction coefficient is independent of shear angle

Cutting forces are computed using Merchant's circle, Figure 2.7, once enough information is known about this system (in particular  $\phi$ ,  $\beta$  and  $\tau_s$ )

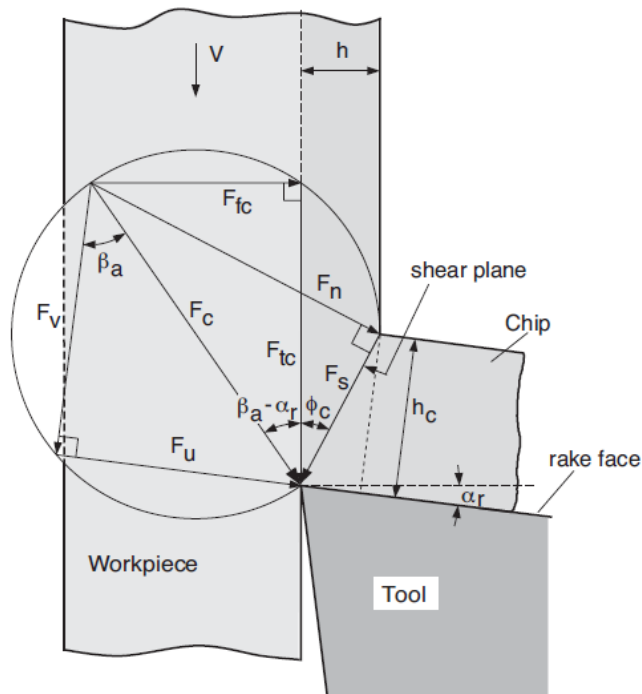


Figure 2.7: Merchant's circle for calculating forces in the orthogonal cutting model. Figure from [46]

There are three sets of cutting vectors that are all related to the resultant cutting force vector

- $F_f$  and  $F_c$ , the measured cutting forces in the feed and cut direction respectively
- $F_v$  and  $F_u$ , the cutting forces normal to the tool rake face and parallel to the tool rake face respectively
- $F_s$  and  $F_n$ , the cutting forces parallel to and normal to the thin shear plane

Predicting the magnitude and direction of the resultant cutting forces using the orthogonal cutting model requires *a priori* knowledge of the shear angle, the friction coefficient between the tool and workpiece, and the maximum shear stress the material can withstand in the shear zone. Accurate analytical shear angle prediction remains a subject of research (there exist at least 50 shear angle relationships [47]), and the general consensus in the metal cutting literature is that shear angles cannot be accurately predicted *a priori* and must be experimentally determined [46]. It is well known in metal cutting that simple Coulomb friction does not apply in machining – the nature of the contact between tool and workpiece involves multiple zones of contact on the tool rake face, which includes a “sticking” zone where the material does not actually slide along the tool face, but rather shears within the material; followed by a transition zone, which is characterized by some sticking and some sliding, and finally a sliding zone before the chip loses contact [45]. One cannot look up tabulated sliding friction coefficients for a pair of materials; the friction coefficient during machining must also be experimentally determined [45]. Lastly, the maximum shear stress in machining is distinct from the maximum shear stress determined from materials testing due to the high strains, strain rates, and temperatures encountered in machining; this too must be experimentally determined [45].

The orthogonal cutting model has in the past been applied to microtome cutting of embedding resins, with questionable results [34]. The rake angle was back-solved using the measured cutting forces and cut chip thickness; the back-solved rake angle was in error by about 40° compared to the set value. At least three of the important parameters in the orthogonal cutting model must be derived from experimental measurements;  $\phi$  can be measured by comparing the chip thickness ratio of the cut vs uncut chip thickness and the rake angle, Eq.

(2.2). The friction angle  $\beta$  must be calculated from cutting force measurements and the rake angle, Eq (2.3). The friction coefficient can then be obtained from the friction angle via Eq (2.4).

$$\phi = \text{atan} \frac{r_c \cos \alpha}{1 - r_c \sin \alpha}, \quad r_c = \frac{h}{h_c} \quad (2.2)$$

$$\beta = \alpha + \text{atan} \frac{F_f}{F_c} \quad (2.3)$$

$$\mu = \tan \beta \quad (2.4)$$

In this work, an alternative modeling strategy was used, the empirical mechanistic cutting model, which is a simpler modeling technique requiring fewer assumptions and intermediate calculations.

## 2.6 The mechanistic model of cutting

In many cutting situations the orthogonal cutting model cannot be used directly due to some of the assumptions being violated, for example when cutting with a tool with a rounded nose or a rounded edge. An alternative convenient approach used in metal cutting to predict cutting forces is the *mechanistic approach*, and this is the approach used in this work due to its simplicity and fewer required assumptions that must be made. The tradeoff is that this is a “black-box” approach, and the cutting force constants must only be used under the exact same cutting conditions under which they were measured (though this would also be true if using the orthogonal model – the parameters  $\phi$ ,  $\beta$ , and  $\mu$  could change with cutting parameters and would have to be shown to remain constant under varying cutting conditions). The concept of a specific cutting pressure and specific feed pressure is introduced – these are forces generated per unit width, per unit depth of cut for a given set of cutting conditions. These conditions include the

cutting tool and workpiece material combination, the tool edge condition, the cutting speed, the depth of cut.

$$F_f = K_f a t_o \quad (2.5)$$

$$F_c = K_c a t_o \quad (2.6)$$

Cutting parameters which can affect  $K_f$ ,  $K_c$  include

- Tool edge condition
- Tool rake angle
- Cutting speed
- Cutting zone temperature
- Depth of cut (uncut chip thickness, or feed)
- Lubrication condition

For a given set of cutting conditions,  $K_f$  and  $K_c$  can be derived from measured cutting forces by dividing the feed force  $F_f$  or cut force  $F_c$  by the width of cut and depth of cut.

If needed, the mechanistic specific feed pressures can be written in terms of orthogonal cutting parameters, via

$$K_f = \tau_s \frac{\sin(\beta - \alpha)}{\sin(\phi)\cos(\phi + \beta - \alpha)} \quad (2.7)$$

$$K_c = \tau_s \frac{\cos(\beta - \alpha)}{\sin(\phi)\cos(\phi + \beta - \alpha)} \quad (2.8)$$

## 2.7 Chatter stability in machining versus microtomy

Chatter in microtomy has been an open problem for as long as the technique has existed and remains an unsolved problem; general techniques to avoid chatter are presented in handbooks of microtomy technique such as in [26] but there is still no link between cutting

parameters, system parameters, and the conditions for the onset of chatter. Chatter is similarly an issue in metal cutting, and because of its economic significance much effort has been made to understand the physical origins of chatter and the conditions under which chatter occurs. Since microtomy shares much in common with the basic metal cutting process of orthogonal cutting, there exists a great opportunity to apply some of the vast metal cutting literature towards understanding the limitations in microtomy.

### **2.7.1 Summary of the state of the art in chatter stability in metal cutting**

Chatter stability in metal cutting has been an active area of research in the latter half of the 20<sup>th</sup> century and continues today. Review articles such as [48] and [49] summarize the state of the art and current difficulties; salient points are summarized here.

Chatter can have many physical origins; [48] describes four:

- Frictional chatter exists due to excitation caused by friction on the tool's clearance face and possibly also rake face exciting system modes.
- Thermomechanical chatter occurs due to temperature and strain rate effects in the cutting zone
- Mode-coupling chatter is caused by interaction between the different modes of vibration in the system, e.g., if cut-direction vibrations excite feed-direction vibrations (which would show up as variations in the thickness section).
- Regenerative chatter is caused by interaction between the previous cut surface, the current cut surface, and the dynamics of the cutting system.

Of these, regenerative chatter is recognized as being the most important physical basis of chatter, and in the metal-cutting literature by convention the term 'chatter' when used singularly refers specifically to regenerative chatter [48].

### **2.7.2 Regenerative chatter: comparing machining and microtomy**

Regenerative chatter stability as developed for metal cutting such as in [46] has a key difference when compared to the serial sectioning process: the lack of control of the phase relationship between the current and previous cutting pass. In machining, such as a turning operation, the tool position and velocity at the end of the previous pass becomes the initial conditions of the current pass; this tool position combined with the phase delay introduced by the dynamics of the cutting system itself forms the complete phase relationship between the two cutting passes which under the right phase will become unstable. Changing the cutting speed changes the phase between the two passes, and is the basis of the chatter stability lobe diagrams used in metal cutting to avoid and minimize chatter.

However, in microtome cutting, there is no such direct relationship between the end of the last section and the beginning of the current section – the cut effectively “resets” every pass.

At lower speeds (although the definition of “lower” is ambiguous), chatter stability is observed to improve; this is known as the ‘process damping’ regime [46]. Additional damping at low speed is great for improving system stability, however slowing down the cutting reduces productivity, so in metal cutting it is generally unacceptable except as a last resort to improve cutting stability by slowing the cut into the process damping regime.

## **2.8 The dig-in phenomenon in cutting**

The tendency for a cutting tool to “dig-in” to a material can occur in any cutting process where a cutting force component is directed into the material. In this section two industrially important cutting processes where dig-in occurs are discussed, machining and wood veneering. In either of the two processes, dig-in appears to be a niche phenomenon and is not studied or quantified.

### **2.8.1 Dig-in in machining: a regime to be avoided**

In his treatise on metal cutting based on research spanning the latter half of the 20<sup>th</sup> century, Shaw [45] notes that cutting with high rake angles is inherently unstable, as the tool digs into the workpiece resulting in larger cutting forces, which drive the tool in further - a positive feedback loop. “Rake angles for which the resultant force vector is directed below the direction of cut are generally to be avoided, particularly when the machine and tool are not very rigid,” though no guidelines or recommendations are given as to the appropriate amount of stiffness the system must have. Shaw recommends arriving at optimal cutting conditions using general guidelines followed by trial and error, and to avoid regimes which include a cutting force component which pulls the tool into the work – i.e., he recommends avoiding the dig-in regime entirely. He provides a table of recommended rake angles for common metals for a turning process; the rake angles generally decrease as the strength of the materials increase. An exception to this trend is noted to be brass – the rake angles recommended for brass are lower than similar strength materials due to its tendency to “dig into” and gouge the workpiece.

### **2.8.2 Wood veneering, a high-rake cutting process**

Veneering is a cutting technique used to obtain high-quality thin sheets of wood of around a millimeter in thickness by “peeling” it off a log with a long, sharp knife while the wood is rotated, similar to a turning process. The process resembles microtomy in two important regards:

- The quality of the offcut is important
- High rake angles are used
- Both materials are anisotropic depending on local tissue structures

However, there are also some important differences

- The material being cut is wood, which is highly moisture-sensitive
- The cutting is continuous, as in lathe turning; regenerative instabilities can be controlled with spindle speed and knowledge of system dynamics
- A pressure bar is used to apply a large amount of compressive stress ahead of the tool, to prevent the wood from cracking during cutting.

In a handbook on wood science and technology, [50] notes that too high a rake angle will lead to “short-wave vibrations”, too low a rake angle leads to “long-wave” thickness variations. It is very possible that dig-in is a contributing factor to these undulations, but there is not enough published information with controlled experiments to know this for certain.

## **2.9 Motivation for a dig-in stability relationship derivation**

It has been shown that the microtome cutting literature acknowledges the importance of cutting system stiffness, but does not provide a functional relationship between system stiffness, cutting parameters, and the maximum allowable cutting width for stable cutting. The stiffness-stability relationship is vaguely known, and cannot be used to set engineering requirements to achieve specific goals: for example, a cutting system which can successfully cut a given material at a given width of cut.

Similarly, the metal cutting literature identifies the dig-in regime as an unstable/quasi-stable cutting regime, and recommends avoiding the regime entirely; no attempt is made at modeling or explaining cutting behavior in this regime. In metal cutting it is trivial to avoid the dig-in zone by reducing the rake angle; this typically severely deforms the offcut and increases cutting forces, but this is of little consequence in metal cutting as the machines are large, heavy, and rigid, and the offcut is discarded. In microtomy, however, damage to the offcut must be minimized, and minimized cutting forces are desirable to minimize damage to the section; the dig-in regime cannot be so simply avoided as in metal cutting.



In the next chapter, functional relationships are derived linking the system's feed-direction stiffness, material cutting properties, and the width of cut resulting in unstable or marginally stable behavior.

*(this page intentionally left blank)*

## DIG-IN STABILITY MODELING

---

This chapter discusses stability modeling for discontinuous and iterative orthogonal cutting, e.g., microtome-style cutting, as opposed to a continuous rotating-spindle type cutting process such as turning. The focus is primarily on dig-in stability, but consideration is also made for regenerative chatter stability.

### 3.1 Single-pass dig-in stability criteria

A dig-in stability model is developed by examining the equation of motion of a single degree-of-freedom (DOF) cutting system and the conditions under which the knife position would increase or decrease without bound – i.e., conditions for which the knife position would go unstable, after being set up for a cut with a nominal depth of cut,  $t_o$ . This is the simplest model that captures all of the system parameters necessary to assess dig-in stability; because so little is currently known about the cutting system, the strategy employed in this work is to develop experiments based on this SDOF model, and suggest model improvements based on observed behavior (this is discussed in Chapter 7).

A schematic of the modeled system is shown below in Figure 3.1. All of the moving mass in the system is lumped into a single mass  $m$ , and the feed-direction (here used synonymously with the  $x$  direction) stiffness is lumped into a single feed stiffness  $k_x$ , with a cutting feed force applied in the feed direction  $F_x$ .

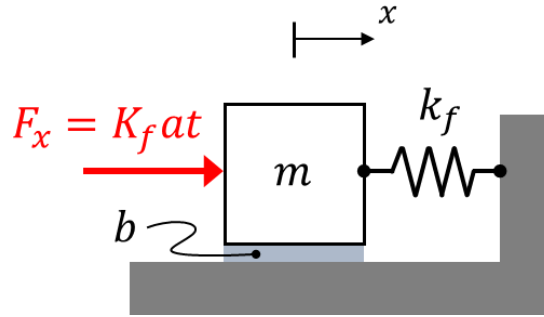


Figure 3.1: Lumped-parameter model of a single-degree of system to model dig-in stability. A feed force,  $F_x$ , is applied to a cutting system with mass,  $m$ , stiffness,  $k_x$ , and damping coefficient,  $b$ . The feed force is determined by the width of cut  $a$ , the depth of cut,  $t$ , and the material-tool combination's specific feed pressure,  $K_f$

In developing this model, the following assumptions are made:

1. The total stiffness of the system in the feed direction is represented as a single constant feed stiffness  $k_x$
2. The feed cutting force is proportional to the depth of cut,  $t$ , and width of cut,  $a$ , with a proportionality constant of  $K_f$  (the specific feed pressure); that is,  $F_x = K_f a t$
3. The cutting forces are independent of cutting speed

The first assumption relies on the stiffness components which sum to the net lumped stiffness all remaining constant. Generally, machine elements will stiffen with increased load and displacement (such as the deflections of a cantilevered beam, or of a Hertzian contact), but it is undesirable for the system to deflect in the first place as this would indicate that the system is already approaching instability. The approach used here is to use the nominal values to provide a conservative estimate of when the system will begin to exhibit instability without relying on any system stiffening characteristics. The real risk here as experienced in this work is in ensuring that **all** contributions to the system stiffness are accounted for, as it only takes one compliant element in a series of springs to drop the net stiffness of the entire chain.

Some confidence is built in the second assumption from cutting data in polymers [51].

Figure 3.2 shows plots of feed forces in an acetal and nylon resin vs depth of cut. A linear relationship between force vs feed with a zero value at the origin would indicate a constant specific feed pressure. It can be seen from the figure that the force vs feed relationship can vary depending on the exact material used, and linear behavior is exhibited over feed ranges of approximately  $100 \mu\text{m}$  [ $0.004 \text{ in}$ ], which is ten times larger than the feed used in the experiments in this work, and feed displacements from nominal that large would indicate that the tool is already unstable.

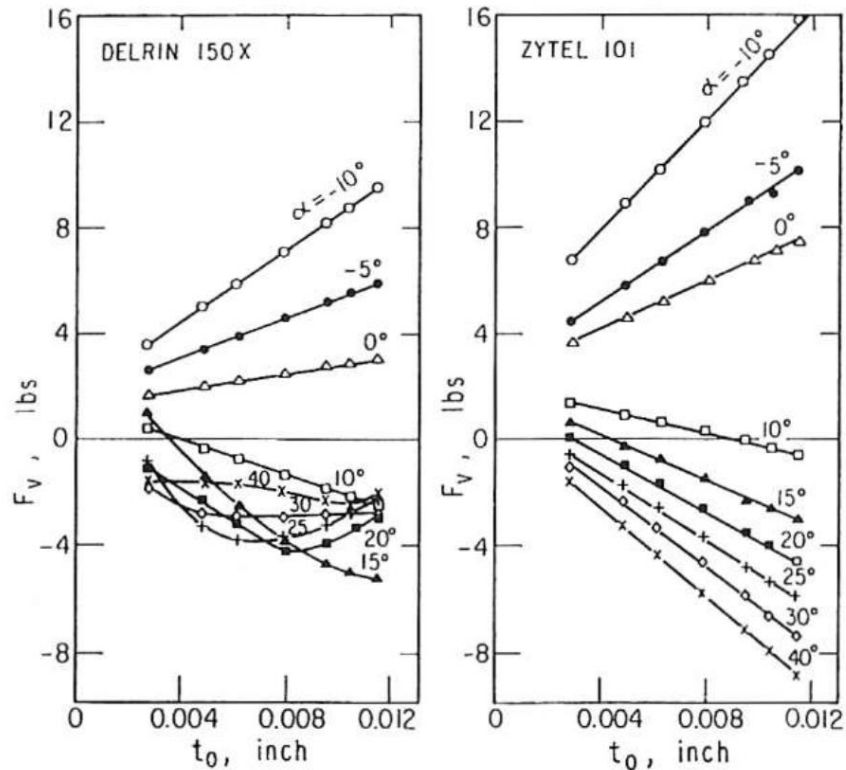


Figure 3.2: Feed force cutting data in acetal (left) and nylon (right) resins vs depth of cut, at a cutting speed of  $317 \text{ ft/min}$  [ $97 \text{ m/min}$ ]. Figure from [51].

Confidence is built in the third assumption again from Kobayashi's cutting data. Figure 3.3 shows cutting forces in acetal resin versus cut speed at multiple rake angles; for dig-in

stability, we are mainly interested in the positive rake angles, as this is where a negative feed force is likely to be encountered. The feed force is nearly constant over a range between 30 – 400  $m/min$  for positive rake angles. Furthermore, microtome cutting speeds are typically between 0.1 – 10  $mm/s$ ; compare this to the plot’s sweep range of 30 – 400  $m/min$  corresponding to 500  $mm/s$  – 6667  $mm/s$ .

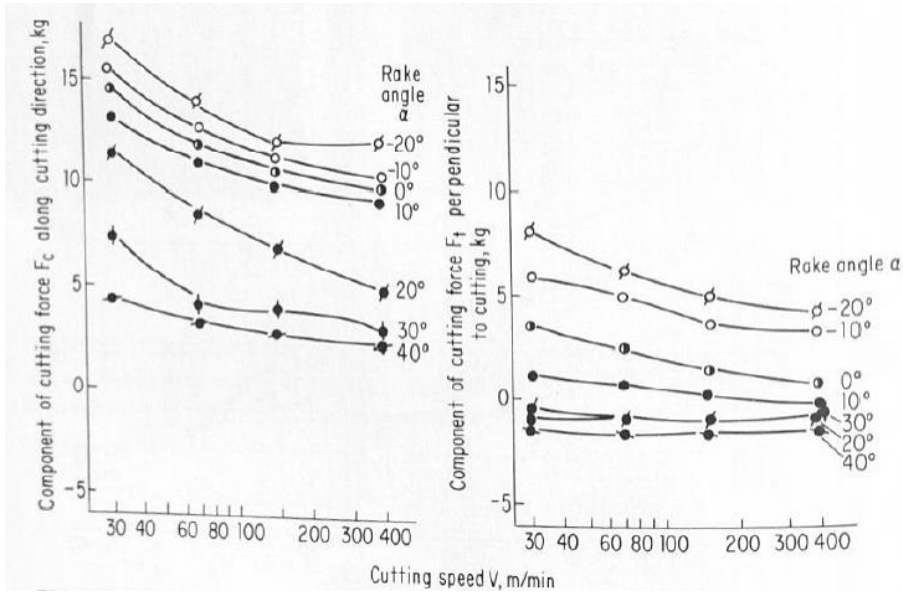


Figure 3.3: Cutting and feed force data in acetal resin versus cutting speed, at multiple rake angles, at a depth of cut of 0.123  $mm$ . Figure and data from [44]

The equation of motion for the lumped parameter system is written as

$$m\ddot{x} + b\dot{x} + k_x x = F_x = K_f a(t_o - x) \tag{3.1}$$

Stability is assessed via the system’s Laplace transform. When the characteristic polynomial of the system has a root with a positive real part, the knife’s position will grow without bound; the conditions under which this is true are the dig-in instability regime. The goal of this analysis is to relate the instability regime conditions back to the physical parameters of the modeled system, and assess under what conditions the system would go unstable. These represent the conditions under which a cut would be “dig-in unstable” in a single cutting pass –

i.e., attempting to cut with these parameters would be immediately unsuccessful as the knife would dig in continuously or be pushed out of the cut (depending on the sign of  $K_f$ ).

The Laplace transform of the EOM is taken assuming that the initial feed and position are zero (zero initial conditions).

$$s^2mX + sbX + k_xX = \frac{1}{s}K_fat_o - K_faX \quad (3.2)$$

There are two terms proportional to  $X$ ; these are combined together into a single effective feed stiffness term:

$$s^2mX + sbX + (k_x + K_fa)X = \frac{1}{s}K_fat_o \quad (3.3)$$

$$s^2mX + sbX + k_{eff}X = \frac{1}{s}K_fat_o \quad (3.4)$$

$X$  is solved for and written out as

$$X = \frac{K_fat_o}{s(ms^2 + bs + (k_x + K_fa))} \quad (3.5)$$

The stability of this system is determined by the roots of the characteristic polynomial, i.e. the roots of the denominator. The denominator can be factored and written as

$$X = \frac{K_fat_o}{sm(s - p_1)(s - p_2)} \quad (3.6)$$

where

$$p_{1,2} = \frac{-b \pm \sqrt{b^2 - 4mk_{eff}}}{2m} \quad (3.7)$$

The system will be unstable if any pole has positive real part. This behavior will depend on whether  $k_{eff}$  is greater than or less than zero; each case is examined here.

Case 1:  $k_{eff} > 0$

In this case, the two poles are

$$p_1 = \frac{-b + \sqrt{b^2 - 4mk_{eff}}}{2m} \quad (3.8)$$

$$p_2 = \frac{-b - \sqrt{b^2 - 4mk_{eff}}}{2m} \quad (3.9)$$

For both poles, when  $k_{eff} > 0$  the sign of the quantity under the radical will be less than zero under the condition that the discriminant  $b^2 - 4mk_{eff} < 0$ , which means that the system response must be underdamped. The real part of the poles will be  $-\frac{b}{2m}$ , a negative quantity – therefore in the case where  $k_{eff}$  is positive, and the system is underdamped, the system will always be stable. In the overdamped case, the system poles will still be real-negative, and will tend towards zero on the real axis with increasing damping, a condition of marginal stability (the response will take longer to die out).

Case 2:  $k_{eff} < 0$

The poles are still (3.8) and (3.9), however with  $k_{eff} < 0$ , the value under the radical can now evaluate to a real positive value; when combined with the existing real part of the pole, the two can combine to form an overall positive real value, resulting in an unstable system. Written out as an inequality, this condition for the positive pole  $p_1$  is

$$-b + \sqrt{b^2 - 4mk_{eff}} > 0 \quad (3.10)$$



This simplifies to

$$\sqrt{b^2 - 4mk_{eff}} > b \quad (3.11)$$

which can ultimately be simplified to

$$k_{eff} < 0, \quad m \neq 0 \quad (3.12)$$

Writing this in terms of the original system parameters, with the added condition that  $K_f$  must be negative in order for  $k_{eff}$  to be negative, since  $k$  and  $a$  are always positive:

$$k + K_f a < 0, \quad K_f < 0 \quad (3.13)$$

$$K_f a < -k, \quad K_f < 0 \quad (3.14)$$

Keeping in mind that  $K_f$  is in this case a negative quantity, the direction of the inequality flips when solving for  $a$ , resulting in the instability criteria:

$$a > -\frac{k}{K_f}, \quad K_f < 0 \quad (3.15)$$

For the negative pole  $p_2$ , the real part can never be positive if  $k_{eff} < 0$

$$-b - \sqrt{b^2 - 4mk_{eff}} > 0, \quad k_{eff} < 0 \quad (3.16)$$

The value under the radical will evaluate to a real number, and will be subtracted from  $-b$  which will result in a further negative real part; therefore this pole does not place any restrictions on the stability criteria.

### 3.1.1 Static offset from nominal feed

If the system is stable, it is expected to reach a steady-state value since the forcing input to the system is constant. The final value of  $x$  can be obtained via the Final Value Theorem and the Laplace transform of the equation of motion (3.5). The final value theorem states that

$$x(\infty) = \lim_{s \rightarrow 0} sX(s) \quad (3.17)$$

Applying this criterion to (3.5):

$$x(\infty) = \lim_{s \rightarrow 0} sX(s) = s \cdot \frac{K_f a t_o}{s(ms^2 + bs + (k_x + K_f a))} \quad (3.18)$$

$$x(\infty) = \frac{K_f a t_o}{k_x + K_f a} \quad (3.19)$$

This quantity represents the steady-state deviation from the nominal depth of cut  $t_o$  for each cutting pass, shown schematically in Figure 3.4, with the offset from nominal as a constant  $G$  proportional to  $t_o$ .

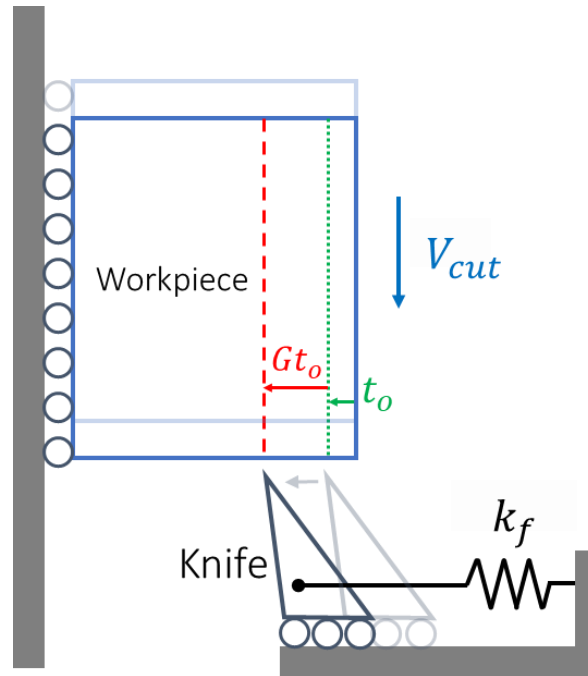


Figure 3.4: Steady-state feed offset from nominal resulting from finite feed stiffness  $k_f$ . The cut is set to a nominal feed of  $t_o$  (dotted line), but due to the finite stiffness of the system the steady-state position of the cut will be a (typically fractional) multiple of the nominal feed  $Gt_o$  (dashed line).

### 3.1.2 Numerical simulations of single-pass dig-in instability

The equations of motion are implemented in a MATLAB script to simulate the stable/unstable behavior and the steady state offset, normalized to the nominal feed,  $t_o$ . Shown below in Figure 3.5 are simulations of the cutting equation of motion simulated at multiple widths of cut. With increasing width of cut, the steady-state position of the knife grows larger. Once the width of cut is larger than the maximum stable value, the position of the knife decreases without bound.

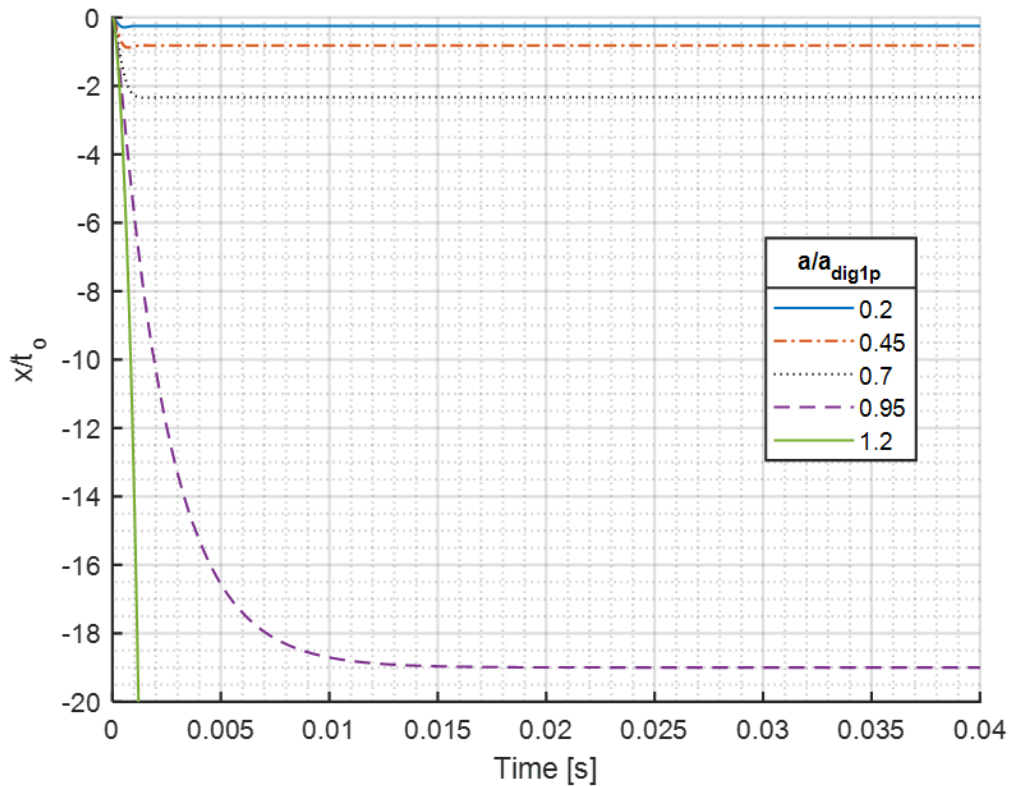


Figure 3.5: Time-domain simulation, normalized feed offset from nominal vs time, at increasing normalized cutting widths. The feed offset  $x$  is normalized to the nominal feed  $t_o$ , and the cutting widths  $a$  are normalized to the single-pass stability limit  $a_{dig1p}$ . The final cutting pass is unstable and decreases without bound

### 3.1.3 Comparing instability behavior of positive versus negative specific feed pressure $K_f$

When  $K_f$  is positive, meaning that the feed-direction forces are in the direction that would reduce the depth of cut, i.e. a “push-out” force, the instability behavior would manifest as the knife being pushed out of the cut; physically, the knife would then skim across the top surface of the workpiece without removing any material.

When  $K_f$  is negative, meaning that the feed-direction forces are in the direction that would increase the depth of cut, i.e. a “pull-in” force, the knife will get pulled deeper into the material during a cut; the restoring force of the spring will be insufficient to bring the knife back to the nominal depth of cut. Physically, this would result in increasing forces and an overload

failure somewhere in the cutting system – either the tool would break, the cutting machine would break, or the workpiece would fail.

## 3.2 Series dig-in cutting stability

It will be shown in this section that the stability criteria for a *series* of cuts is more restrictive than the stability criteria for a single cut; series stability places more stringent criteria on the allowable width of cut for a given  $K_f$  to ensure stable cutting. For series stability to exist, the steady-state depth of cut (that is, the nominal feed plus the offset from nominal due to digging-in or pushing-out) must converge to a final value; for an unstable series of cuts, the depth of cut (and thus the resulting thickness of the section) will change with each cutting pass and ultimately grow without bound.

### 3.2.1 Modeling stability of a series of cuts using the geometric series

A preliminary assumption is made here that the series is already single-pass stable – that is, the depth of cut for each pass will converge to some value before the cut finishes. It was shown previously in Eq. (3.19) that each cut would always be accompanied by an offset from the nominal depth of cut, i.e., the tool will always be pushed or pulled away slightly from the nominal depth of cut, with the result that the steady-state depth of cut will be slightly lower or higher than nominal. Inspection of Eq. (3.19) shows that each steady-state depth of cut will be a fraction of the previous steady-state depth of cut; each cut will have an offset that is proportional to the nominal depth of cut  $t_o$ , which we represent as a gain  $G$  in (3.20).

$$x_\infty = \frac{K_f a}{k_f + K_f a} t_o = G t_o \quad (3.20)$$

A model for series cutting can be developed based on the geometric series and this steady-state offset. The analysis begins by recognizing that for each cut, there will be a deviation from nominal  $\Delta t$  that depends on  $G$ , and the total amount of material engaged, which would nominally be  $t_o$  but may be different if more or less material was removed during the previous cut. A schematic of this behavior is shown in Figure 3.6.

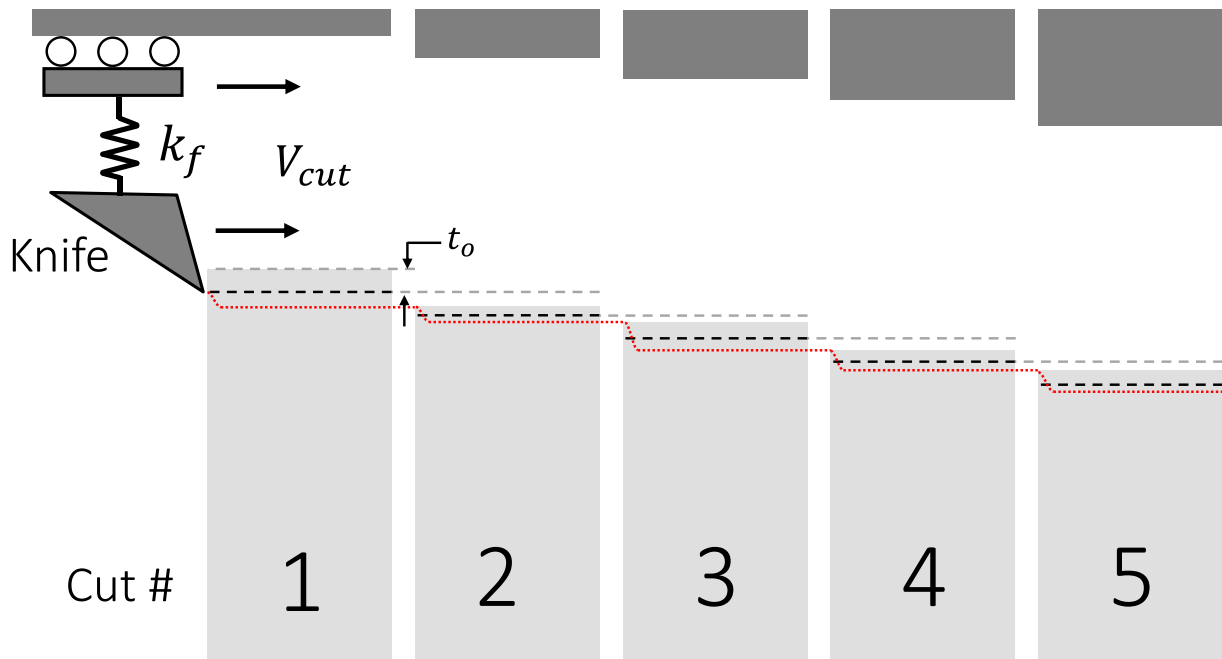


Figure 3.6: Schematic of series cutting; the same specimen is cut five times by a knife with a feed stiffness  $k_f$  at a constant cutting velocity  $V_{cut}$ . The cut is set at a nominal feed of  $t_o$  (dashed lines); due to the system's feed stiffness, the knife will be pulled into the material (assuming negative specific feed pressure  $K_f$ ) and the knife's steady state position will be some distance from the nominal feed (dotted line). For stable series cutting, the steady state offset should reach a constant value.

The first offset  $\Delta t_1$  will be proportional to the nominal depth of cut  $t_o$ ; the amount of material left for the next cut (e.g., the next cut's true depth of cut) will be  $t_o + \Delta t_1$ , therefore the offset of the next cut will be proportional to  $(t_o + \Delta t_1)$ . This relationship for how the depth of cut changes each pass can be written out as a series as in (3.21)

$$\begin{aligned}
\Delta t_1 &= Gt_o \\
\Delta t_2 &= G(t_o + \Delta t_1) = Gt_o + G^2t_o \\
\Delta t_3 &= G(t_o + \Delta t_2) = G(t_o + G(t_o + \Delta t_1)) = Gt_o + G^2t_o + G^3t_o \\
&\vdots \\
\Delta t_N &= Gt_{N-1} = Gt_o + G^2t_o + G^3t_o + \dots + G^Nt_o
\end{aligned} \tag{3.21}$$

The steady state offset of the  $N^{th}$  cut has the same form as a geometric series, and a geometric series with a common ratio  $r$  can be written in closed-form as:

$$a + ar + ar^2 + \dots + ar^{N-1} = \sum_{k=0}^{N-1} ar^k = a \left( \frac{1 - r^N}{1 - r} \right) \tag{3.22}$$

For this series to converge, the magnitude of the ratio  $r$  must be less than unity. As  $N$  goes to infinity, the series would converge to

$$\sum_{k=0}^{\infty} ar^k = a \left( \frac{1}{1 - r} \right) \tag{3.23}$$

The offset of the  $N$ th cut can be written similarly as

$$\Delta t_N = Gt_{N-1} = Gt_o(G^0t_o + G^1t_o + G^2t_o + \dots + G^{N-1}t_o) = Gt_o \left( \frac{1 - G^N}{1 - G} \right) \tag{3.24}$$

With a final steady state offset converging to

$$\Delta t_{\infty} = Gt_o \left( \frac{1}{1 - G} \right) \tag{3.25}$$

The stability criteria for the series to converge is that  $|G| < 1$ . The ratio  $G$  is written in terms of system parameters

$$-1 < \frac{K_f a}{k_f + K_f a} < 1 \quad (3.26)$$

For this analysis, it is already assumed that the system is single-pass stable – e.g., that  $k_f + K_f a$  is a positive quantity. The expression (3.26) is rewritten to express the stability criteria in terms of the width of cut  $a$ :

$$-(k_f + K_f a) < K_f a < k_f + K_f a \quad (3.27)$$

$$0 < k_f + 2K_f a < 2k_f + 2K_f a \quad (3.28)$$

$$0 < k_f + 2K_f a \text{ AND } k_f + 2K_f a < 2k_f + 2K_f a \quad (3.29)$$

$$2K_f a > -k_f \text{ AND } 1 < 2 \quad (3.30)$$

The statement on the right is always true. To simplify the expression on the left will require considering two cases – whether or not  $K_f$  is positive or negative

Case 1:  $K_f$  positive

$$a > -\frac{k_f}{2K_f} \quad (3.31)$$

The width of cut,  $a$ , is a positive real number, therefore this statement will always be true.

When the cutting system has a positive  $K_f$ , the series stability of the system is unconditional.

Case 2:  $K_f$  negative

The expression now simplifies to:

$$a < -\frac{k_f}{2K_f} \quad (3.32)$$



The system is series-stable if this condition is fulfilled; this stability restriction on the width of cut is half of the single-pass maximum stable width of cut. This is an important consequence: if a cutting machine operator is attempting to set up a cut empirically, and assesses the stability of a cut via a single-pass stability check – e.g., if a machine operator tunes settings, attempts to take a cut, and the cut satisfactorily completes – this may be inadequate for stability in the *series* sense. A cut that is stable in the single-pass sense but not in the series sense will eventually diverge, eventually resulting in cuts where the knife digs in deeply (resulting in a thick section), leaving no material for the next cut, so that the next cut produces no section.

The sign of  $K_f$  ultimately determines series behavior; in either case, too large a width of cut results in undesirable cutting behavior, however in the negative- $K_f$  case the increased cutting forces could lead to damage.

### **3.2.2 Series cutting with positive $K_f$**

With positive  $K_f$ , the series never diverges; instead, the steady-state offset becomes a larger multiple of the nominal feed. As cutting width increases, this offset becomes a larger fraction of nominal; ultimately, as the width of cut continues to increase, each cutting pass the tool will be pushed almost entirely out of the cut, and the true depth of cut will be a very small fraction of the nominal depth of cut.

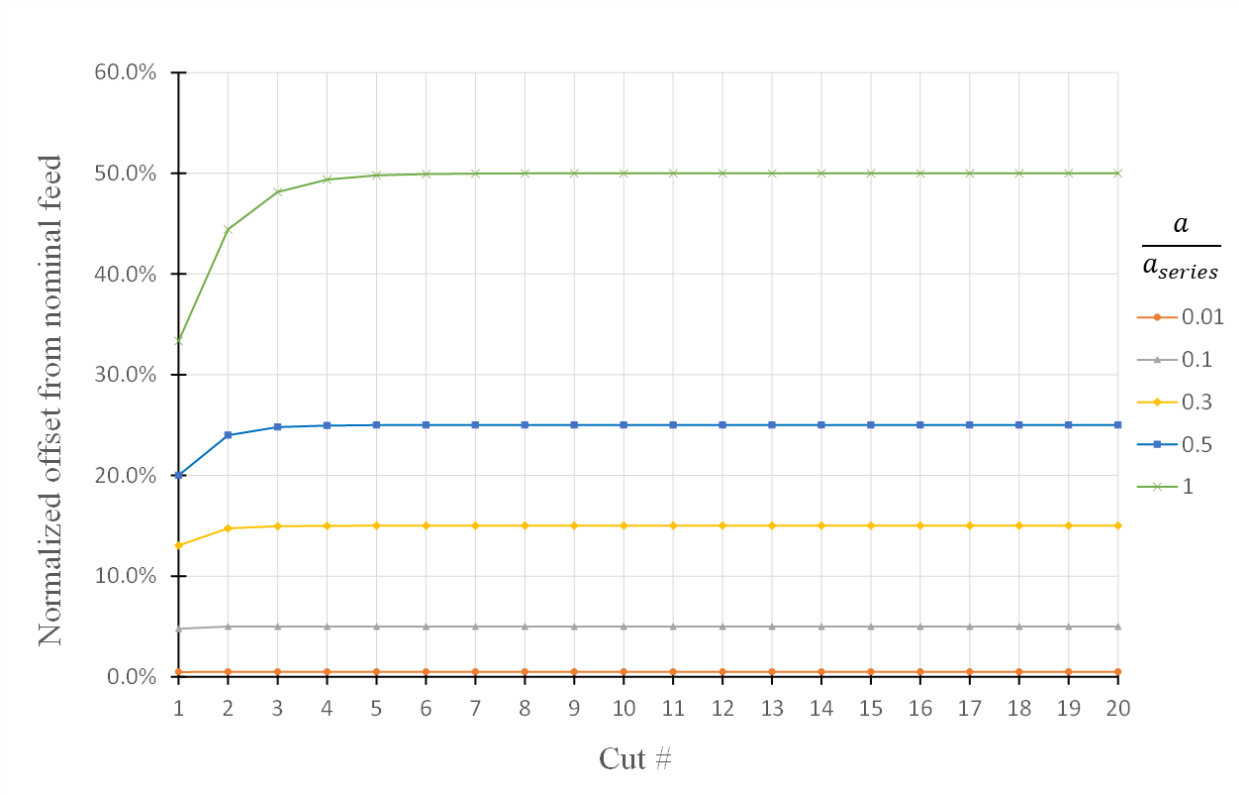


Figure 3.7: Plot of steady-state offset feed from nominal feed, versus cut number in a cutting sequence. Each line represents a series of cuts taken at a different normalized width of cut, normalized to the series stability limit. Such a limit doesn't exist for positive  $K_f$  but is still a useful normalization factor.

A practical consequence of this behavior which is not included in the model is that if the edge radius of the tool is considered, it is very likely that the true depth of cut (e.g., the amount of material being engaged by the tool) will become small enough that the cutting tool's edge radius will become important;  $K_f$  will increase and become more positive, and the tool will be pushed out of the cut completely and skim along the surface. Cut quality would likely be adversely affected due to the effective negative rake angles that would be encountered with the tool edge, as the section is effectively being ploughed and extruded ahead of the tool instead of cleanly cut.

### 3.2.3 Series cutting with negative $K_f$ : Thick-thin sectioning

With negative  $K_f$  the series will exhibit alternating thick/thin sections while the series is settling into a steady-state offset. If the width of cut is large relative to the maximum allowable series-stable width of cut, the thick-thin cuts will continue alternating for many cutting passes.

Qualitatively this sequence is described as follows:

1. The first cut attempts to make a cut at the nominal depth of cut; due to negative  $K_f$ , the knife is pulled in, resulting in more material being removed than intended. The result is a “thick” section.
2. The knife is fed in by the nominal feed, the depth of cut; because more material was removed during the previous cut, there is less material to cut during this pass. The knife is still pulled in, but to a lesser extent. This results in a “thin” section.

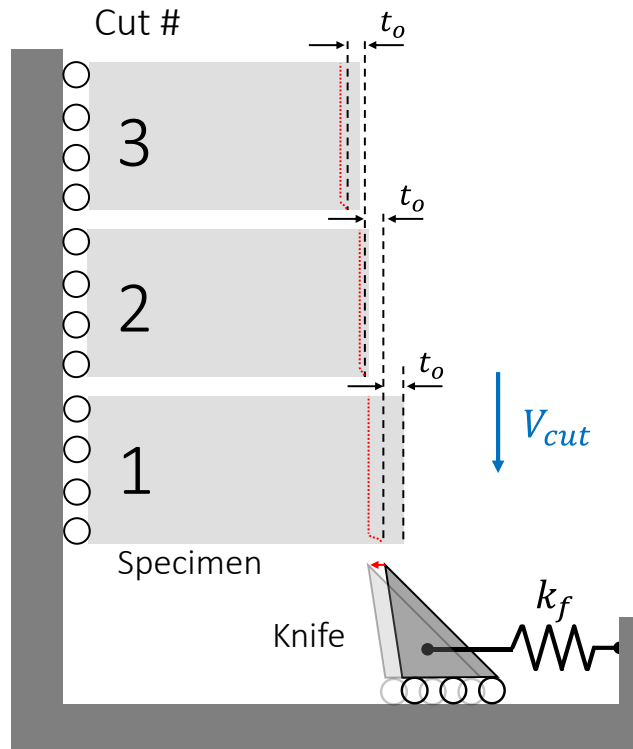


Figure 3.8: Schematic of thick/thin cutting, occurring when cutting with negative  $K_f$ . For each cut, the knife is fed in a constant feed  $t_o$ ; when the knife engages the material, it will be pulled in proportional to the feed. During the first cut, the knife is pulled in and removes additional material, resulting in a thick section. The next cut, cut #2, engages less material, and is pulled in less; a smaller section results. For a stable system, the thickness would eventually reach steady state.

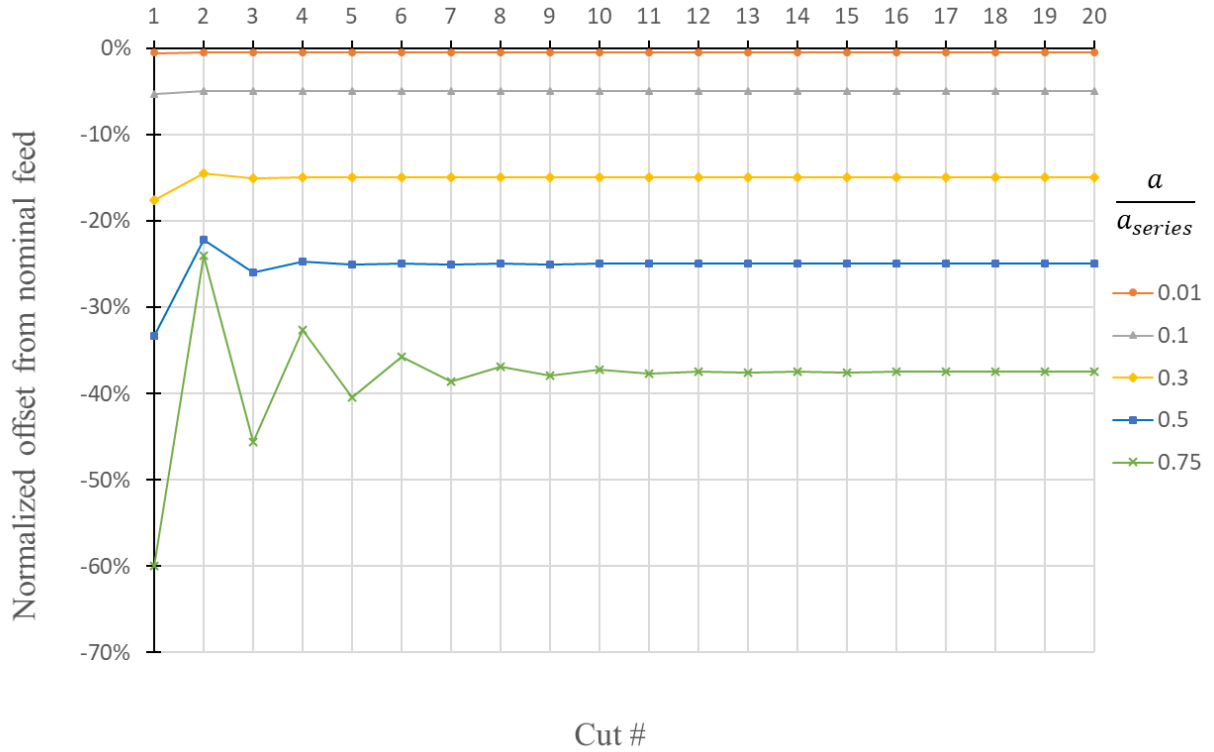


Figure 3.9: Series cutting at different widths, negative  $K_f$  case

When the system is series stable, the series will ultimately converge to a steady-state offset from the nominal depth of cut.

### 3.2.3.1 Instability onset for a series of cuts at fixed width: Skip sectioning

At the limit of series stability and at fixed cutting width, e.g., at the onset of instability when the cutting width is the same for the entire cutting run, the thickness of the “thin” section approaches zero – the cut will miss a section entirely. The cutting alternates between a thick section where the tool dives in one additional nominal feed’s worth of material, leaving no material for the next cut, resulting in a “thin” section of zero feed (Figure 3.10).

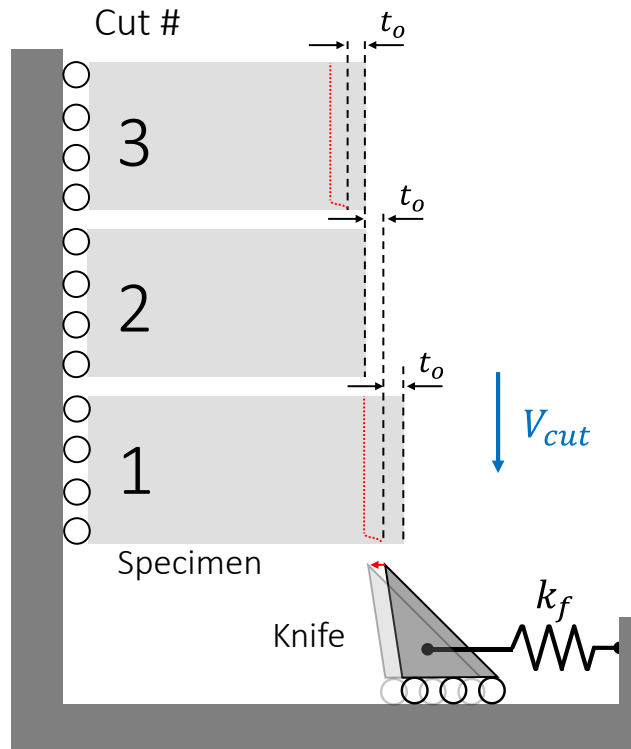


Figure 3.10: Schematic of skip-section cutting at the stability limit. The black dashed lines represent the nominal cutting depths, and the dotted red lines represent the knife's trajectory as it is pulled into the material. The first cut is pulled in one nominal feed's worth of feed ( $t_o$ ), for a total depth of cut of  $2t_o$ ; for the 2<sup>nd</sup> cut the knife is fed in  $t_o$ , however there is no material to cut; no material is removed during the second cut. The cycle repeats itself with the third cut, as the feed is once again  $t_o$ .

A numerical implementation of this behavior is shown in Figure 3.11, with the alternating thick and thin cuts.

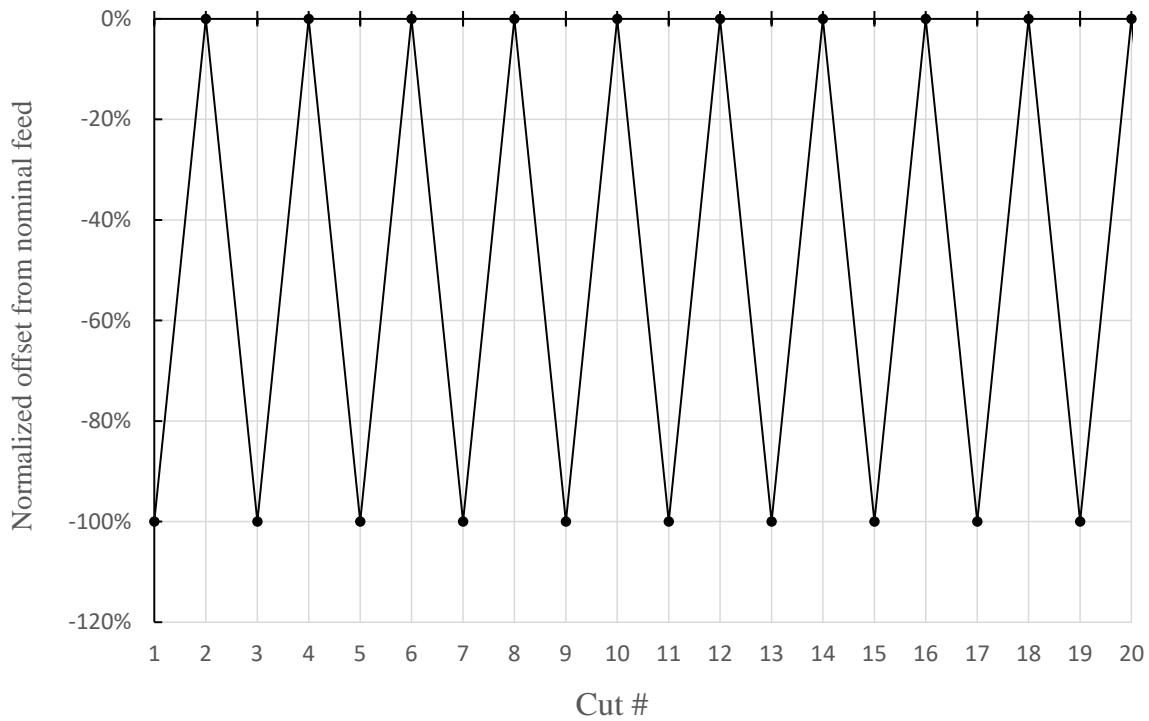


Figure 3.11: Cutting sequence with negative  $K_f$ , when the width is the series stable cutting limit. The cutting alternates between diving in an additional feed's worth of material, leaving no material for the next cut

### 3.2.3.2 *Instability onset for a series of cuts with incrementing cutting width*

The skip-sectioning behavior described in the previous section is only a valid signal of instability onset if the entire series of cuts has been performed at a fixed width. However, in the experiments performed in this work, cutting begins at an initial width of cut, proceeds for a set number of sections, and the cut width is incremented. In this case, the steady-state feed for the next series of cuts will depend on the steady-state offset from the series of cuts at the previous cutting width, and skip-sections are not observed in this case.

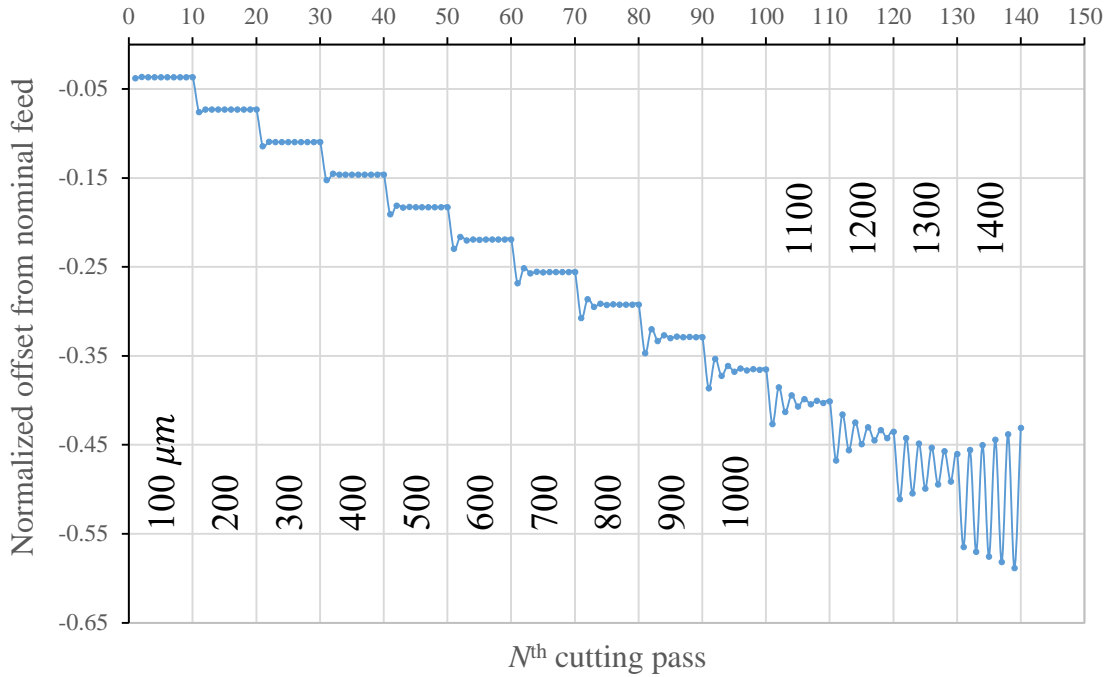


Figure 3.12: Numerical simulation of steady-state offset behavior for a sequence of cuts. The cutting width in microns of each cut is indicated in the inset numbers. The negative normalized offset indicates that this is a dig-in offset, meaning that the cut will be thicker than the nominal feed.

The parameters used to generate Figure 3.12 are shown in Table 3-1.

Table 3-1: Parameters used to generate plot of normalized offset from nominal feed for a sequence of cuts (Figure 3.12)

Parameter	Value	Unit	Description
<i>Inputs</i>			
$K_f$	-1.79E+07	$N/m^2$	Specific feed pressure
$k_f$	4.90E+04	$N/m$	Feed stiffness
$t_o$	1.00E-05	$m$	Nominal feed
$a_{min}$	1.0E-07	$m$	Starting cutting width
$a_{max}$	1.4E-03	$m$	Final cutting width
$N_{cuts}$	10		Cuts per pass
<i>Outputs</i>			
$a_{lim.s}$	1.37E-03	$m$	Series cutting stability limit

It is apparent from Figure 3.12 that skip-sections do not occur in the case of series cutting with incrementing width; i.e., the normalized offset never reaches  $-1.0$  while the cut is still stable. It can be shown that the steady-state offset at the threshold of stability under incrementing-width series cutting conditions is  $-0.5$ , however this is not necessarily usable for



signaling instability because when the cutting is close to the limit of stability, the cut will not settle down to  $-0.5$  unless a very large number of cuts are taken. If cutting is performed at the limit of stability, the offset will alternate indefinitely, and will never settle to the steady state offset of  $-0.5$ .

### 3.3 Depth of cut variance propagation model

The feed force and depth of cut variance propagation model uses the relationship between the knife's steady-state equilibrium position and several cutting parameters to model how perturbations in the cutting parameters, including the effect of variation on the previously cut surface on the next pass, change with each cutting pass. , it is also possible to consider how the knife's equilibrium position responds to changes in any of the parameters – i.e., its sensitivity to changes in the cutting or system parameters. The model predicts how much variation can be expected in the knife equilibrium position given the variation in the cutting parameters, and that the sensitivity of the system to perturbations increases as the system stability limit is approached.

#### 3.3.1 Derivation via equilibrium position and propagation of uncertainty

The derivation begins with the equilibrium offset from the nominal feed, i.e., how far from the nominal depth of cut the knife settles to, derived earlier in section 3.1.1.

$$x_{eq} = \frac{K_f a}{k_f + K_f a} (t_o + x_r) \quad (3.33)$$

It is assumed that the variances of the cutting parameters are independent. The variance in the equilibrium position is calculated:

$$\sigma_{x_{eq}}^2 = \left| \frac{\partial x_{eq}}{\partial K_f} \right|^2 \sigma_{K_f}^2 + \left| \frac{\partial x_{eq}}{\partial a} \right|^2 \sigma_a^2 + \left| \frac{\partial x_{eq}}{\partial t_o} \right|^2 \sigma_{t_o}^2 + \left| \frac{\partial x_{eq}}{\partial x_r} \right|^2 \sigma_{x_r}^2 + \left| \frac{\partial x_{eq}}{\partial k_f} \right|^2 \sigma_{k_f}^2 \quad (3.34)$$

The individual sensitivities must be derived; these are calculated and given below.

$$\frac{\partial x_{eq}}{\partial K_f} = \frac{k_f a}{(k_f + K_f a)^2} (t_o + x_r) \quad (3.35)$$

$$\frac{\partial x_{eq}}{\partial k_f} = -\frac{K_f a}{(k_f + K_f a)^2} (t_o + x_r) \quad (3.36)$$

$$\frac{\partial x_{eq}}{\partial x_r} = \frac{\partial x_{eq}}{\partial t_o} = \frac{K_f a}{k_f + K_f a} \quad (3.37)$$

$$\frac{\partial x_{eq}}{\partial a} = \frac{k_f K_f}{(k_f + K_f a)^2} (t_o + x_r) \quad (3.38)$$

The complete expression for  $\sigma_{x_{eq}}$  is too unwieldy for a compact algebraic result, but the expressions are implemented numerically via a program such as MATLAB or Excel. The regeneration term must be handled recursively; in a numerical implementation, the model can be set up as a sequence of cuts. The calculated value of  $\sigma_{x_{eq}}$  becomes the regenerative term  $\sigma_{x_r}$  for the next cutting pass – in this way, the growth in the system's feed variance can be modeled as a simulated cut progresses.

### 3.3.2 Stability limit and relation to dig-in stability limit

A useful question to ask is if a new stability criterion can be defined relevant to the uncertainty propagation, and its relationship to the dig-in stability limit examined. In this case, a useful definition of stability could be pass-over-pass growth in uncertainty; another way of expressing this is that the system has gone unstable when each pass' feed uncertainty is larger than the previous' feed uncertainty. Using this criterion and the uncertainty sensitivity model derived above in Section 3.3.1,

$$\frac{\sigma_{x_{eq}}}{\sigma_{x_r}} > 1 \quad (3.39)$$

$$\frac{\sigma_{x_{eq}}^2}{\sigma_{x_r}^2} = \left| \frac{\partial x_{eq}}{\partial K_f} \right|^2 \frac{\sigma_{K_f}^2}{\sigma_{x_r}^2} + \left| \frac{\partial x_{eq}}{\partial a} \right|^2 \frac{\sigma_a^2}{\sigma_{x_r}^2} + \left| \frac{\partial x_{eq}}{\partial t_o} \right|^2 \frac{\sigma_{t_o}^2}{\sigma_{x_r}^2} + \left| \frac{\partial x_{eq}}{\partial x_r} \right|^2 + \left| \frac{\partial x_{eq}}{\partial k_f} \right|^2 \frac{\sigma_{k_f}^2}{\sigma_{x_r}^2} \quad (3.40)$$

It doesn't appear that a simple closed-form solution will be possible due to the dependence on multiple input uncertainty variables. However, a baseline stability limit can be established by temporarily setting all uncertainty inputs except  $\sigma_{x_r}$  to zero and considering only the regeneration sensitivity  $\frac{\partial x_{eq}}{\partial x_r}$ , which is given in Eq. (3.37):

$$\frac{\sigma_{x_{eq}}}{\sigma_{x_r}} = \left| \frac{\partial x_{eq}}{\partial x_r} \right| = \left| \frac{K_f a}{k_f + K_f a} \right| > 1 \quad (3.41)$$

The inequality being solved is now exactly the same as the stability criterion solved for series dig-in stability in Eq. (3.26), therefore the same stability limit on the cutting width  $a$  applies here as well. In the presence of other uncertainties, the ratio will reach the critical threshold magnitude of 1 sooner, therefore the series dig-in stability limit represents a best-case stability criterion for pass-over-pass growth of the feed position uncertainty. Any uncertainty in the parameters will cause unstable uncertainty growth sooner than predicted by the series stability limit, though how much sooner depends on the uncertainty of the input parameters.

### 3.3.3 Discussion and model implications

It is possible via this approach to set a maximum allowable deviation from nominal, as an alternative to a stability criterion – one could assign the deviation to be no more than some fraction of the nominal feed. However, the user must know what the variances in each of the system parameters are.

An important takeaway from this analysis is that the system's sensitivity to variation in the cutting parameters increases as the stability limit is approached. An important metric of how poorly the cutting is behaving would be to track the standard deviation of  $x_{eq}$  normalized to the nominal feed  $t_o$ ; when the deviations in  $x_{eq}$  grow large enough, the tool would actually be disengaging from the material and the model would no longer apply. This generally happens before the cutting width has reached the series stability limit – in the cutting width regime leading up to the series dig-in stability limit, we can expect erratic cutting and large tool amplitudes even before the system has become unstable.

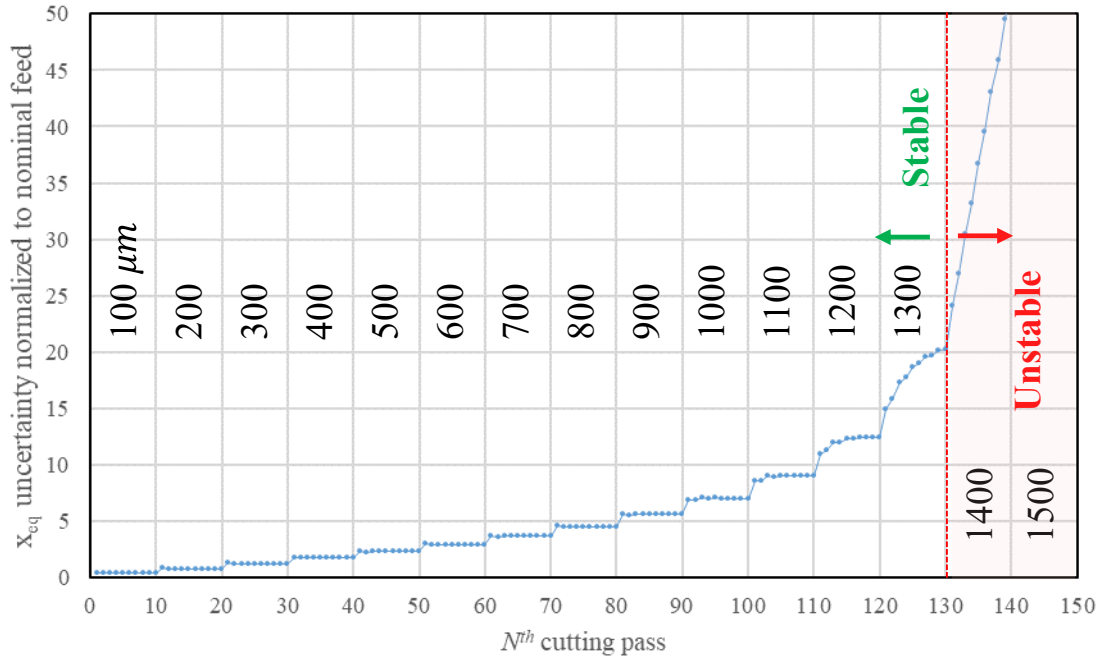
### **3.3.4 Numerical implementation**

The  $\sigma_{x_{eq}}$  propagation model was implemented in a spreadsheet, using the parameters in Table 3-2 to simulate how the variance in the tool equilibrium position evolves during a series of cuts as the width of cut varies. In this simulation, the cutting width remains constant for ten sections, after which the cutting width increments by  $100 \mu m$ . For this simulation the standard deviations were chosen to be 10% of the nominal values.

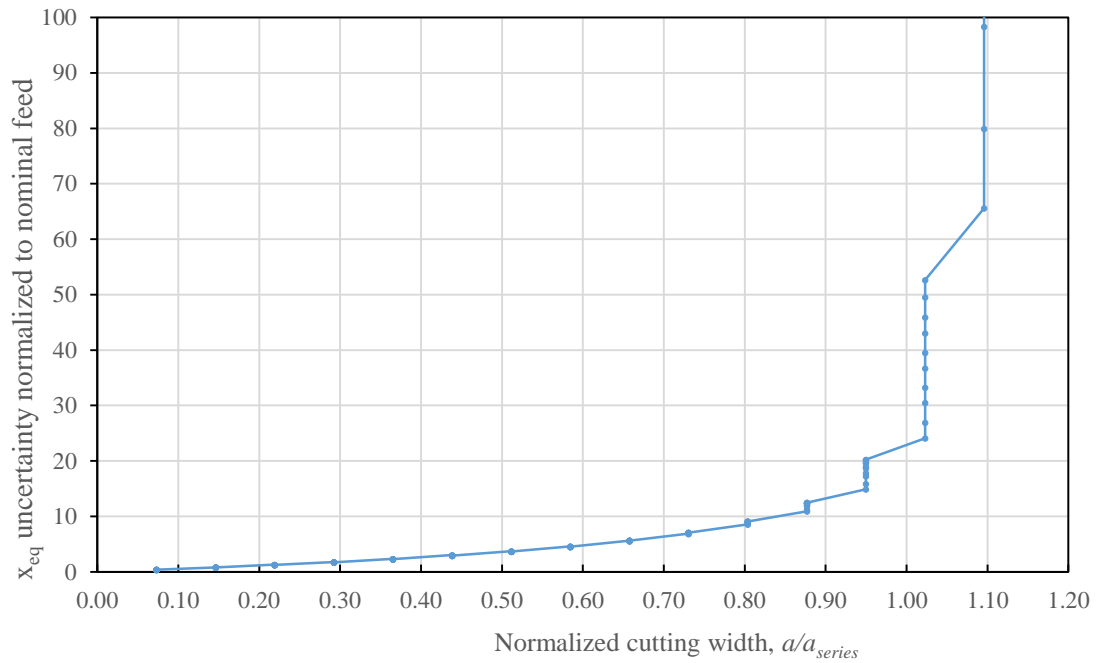
Table 3-2: Model inputs for variance propagation vs cutting width model; the resulting  $\sigma_{xeq}$  progression vs cutting width is shown in Figure 3.13

Parameter	Value	Unit	Description
<i>Model inputs</i>			
$K_f$	-1.79E+07	$N/m^2$	Specific feed pressure
$k_f$	4.90E+04	$N/m$	Feed stiffness
$t_o$	1.00E-05	$m$	Nominal feed
$\sigma_a$	1.00E-06	$m$	Cutting width standard deviation
$\sigma_{t_o}$	1.00E-06	$m$	Feed standard deviation
$\sigma_{k_f}$	4.90E+05	$N/m$	Feed stiffness standard deviation
$\sigma_{K_f}$	1.79E+06	$N/m^2$	Specific feed pressure standard deviation
$\sigma_r$	1.00E-06	$m$	Regenerative surface standard deviation
$a_{min}$	1.0E-07	$m$	Initial cutting width
$a_{max}$	1.4E-03	$m$	Maximum cutting width
$N_{cuts}$	10	-	Cutting passes at each width
$a_{inc}$	1.00E-04	$m$	Cutting width increment, after $N_{cuts}$ passes
<i>Model outputs</i>			
$a_{series}$	1.37E-03	$m$	Dig-in series stability limit

The  $\sigma_{xeq}$  progression against the  $N^{th}$  cutting pass is plotted in Figure 3.13a, and the  $\sigma_{xeq}$  progression against the cutting width normalized to the dig-in series stability limit is shown in Figure 3.13b. In both plots,  $\sigma_{xeq}$  is normalized against the nominal feed; when this ratio approaches unity, the tool will be more frequently hopping out of the cut, and the model will be less applicable.



(a)



(b)

Figure 3.13: Plots of equilibrium uncertainty propagation numerical simulation, with ten cutting passes at each cut width (a) Normalized position uncertainty against the  $N^{\text{th}}$  cutting pass, with cutting width shown overlaid on each series of cuts (b) Normalized position uncertainty against the normalized cut width

The equilibrium position standard deviation does not grow much within a single cutting width, except when the cutting width approaches the series stability limit. From these plots it is also evident that the system can exhibit much variation in the feed position (i.e., several multiples of the nominal feed) *before* the system has gone series dig-in unstable. After the system has gone unstable, the uncertainty grows after each cutting pass, instead of settling to a steady-state uncertainty value as when the system was cutting at a series-stable width.

### **3.4 Regenerative chatter in microtome serial sectioning**

The regenerative effect is believed to be the leading cause of chatter in machining, as was discussed in Section 2.7.1. This section discusses the generation of a model to model the conditions under which a microtome system would regenerate and become unstable. The section begins with a comparison between classical regenerative chatter stability theory from metal cutting, discusses why the model cannot be directly applied to microtome cutting, and proposes a modified model. The model is numerically implemented in MATLAB, and several numerical simulations are presented.

#### **3.4.1 Comparison to machining regenerative chatter stability theory**

In a machining operation, for example a turning operation, the tool position and velocity at the end of the previous cutting pass (a “cutting pass” in this context meaning cutting during one spindle revolution) become the initial conditions for the next cutting pass. However, in microtomy and serial sectioning, the end of one cut does not influence the conditions at the beginning of the next cut (assuming any machine vibrations die out by the time the knife is in position for the next cut). Classical regenerative stability theory in machining predicts the stable cut width at a given spindle period or frequency, but also predicts a global stability limit for the

width of cut: this would be the maximum width of cut for which the system is stable at all spindle periods. The regenerative chatter models developed for machining cannot be immediately applied to microtome cutting because of the lack of a cutting parameter-set time delay between the previous and current cutting pass. Furthermore, there is no periodic rotation providing a consistent source of excitation to the system. With these considerations, in this section a regenerative chatter model specifically for microtome-style cutting is derived, discontinuous and iterative orthogonal cutting. The conditions under which to expect regenerative instability are established based on a single degree of freedom model of the system's equation of motion.

### **3.4.2 Regenerative steady-state amplitude growth: two-pass model**

In this section a model is derived for the conditions under which the steady-state amplitude of a system's vibration increases, when excited by the surface variations left behind due to the vibrations of the previous cut. Specifically, an expression is derived for the maximum width of cut for which no forcing, regardless of frequency, would be amplified during a single cutting pass. The model is adapted from the delay-differential-equation (DDE) regenerative chatter model from machining [46], modified to eliminate the time-delay term. The goal of this analysis is to relate the system's cutting and dynamic parameters to the maximum allowable cutting width,  $a_{lim}$ , for which cutting will be globally stable (i.e., all input forcing frequencies leave a surface variation which reduces in amplitude after each pass).

The relationship between feed displacements in the current cut,  $x_2$ , and the feed forces caused by the feed displacements from the previous cut  $x_1$ , can be modeled in an equation of motion as



$$m\ddot{x}_2 + b\dot{x}_2 + k_f x_2 = F_f = K_f a(t_o - x_2 + x_1) \quad (3.42)$$

This equation of motion can be represented as a block diagram with two inputs (Figure 3.14), one being the nominal feed (a constant) and the other being the regenerative surface could generally contain some frequency-domain content:

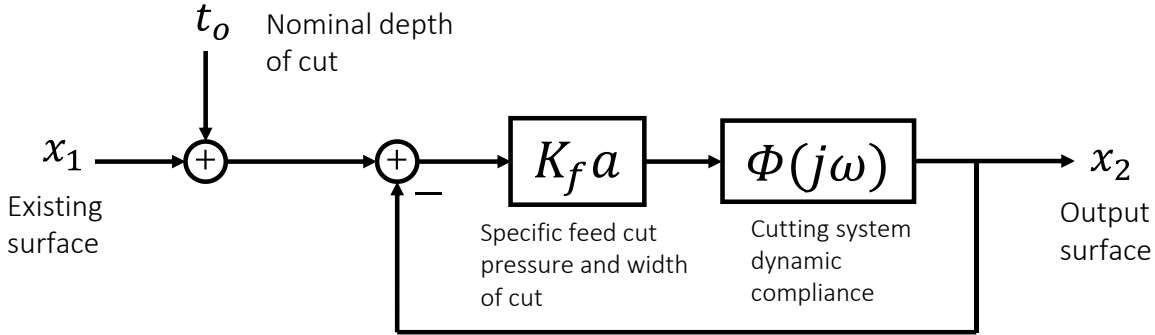


Figure 3.14: Block diagram representing the cutting equation of motion for the two-pass system

The relationship between the regenerative surface  $x_1$  and the output surface  $x_2$  can be expressed using the transfer function

$$\frac{X_2}{X_1} = \frac{K_f a \Phi}{1 + K_f a \Phi} \quad (3.43)$$

When the magnitude of this transfer function is greater than one, the response amplitude will be larger than the input - each cutting pass, this excitation will grow stronger, and system is unstable. Note that the system could be stable at some excitation frequencies and unstable at others, depending on the frequency response function (FRF)  $\Phi$ , which in general will be a function of frequency. The instability condition is written in (3.48):

$$\left| \frac{K_f a \Phi}{1 + K_f a \Phi} \right| > 1 \quad (3.44)$$

The modeling goal is to link system stability to the maximum allowable cutting width, so this expression must be expanded and solved for cutting width  $a$ ; however, it is a complex expression. To proceed, it will be helpful to define variables for the real and imaginary parts of  $\Phi$ :

$$G(\omega) = \text{Re}\{\Phi\} \quad (3.45)$$

$$H(\omega) = \text{Im}\{\Phi\} \quad (3.46)$$

To find the magnitude of the complex ratio (3.44), the magnitudes of the numerator and denominator are written out:

$$\text{Numerator magnitude: } K_f a \sqrt{G^2 + H^2} \quad (3.47)$$

$$\text{Denominator magnitude: } \sqrt{(1 + K_f a G)^2 + (K_f a H)^2} \quad (3.48)$$

Expanding the denominator and simplifying,

$$\text{Denominator magnitude: } \sqrt{1 + 2K_f a G + (K_f a)^2 (G^2 + H^2)} \quad (3.49)$$

Combining the numerator and denominator and simplifying further,

$$\frac{\sqrt{(K_f a)^2 (G^2 + H^2)}}{\sqrt{1 + 2K_f a G + (K_f a)^2 (G^2 + H^2)}} \quad (3.50)$$

The denominator magnitude is mostly identical to the numerator but also has additional terms, which will dictate the regenerative stability behavior. If

$$1 + 2K_f a G > 0 \quad (3.51)$$

then the resulting magnitude will be fractional – subsequent passes will have a smaller steady-state amplitude compared to the preceding one, so cutting vibrations will attenuate and the system is stable. If, however,

$$1 + 2K_f aG < 0 \quad (3.52)$$

Then the resulting magnitude ratio is greater than unity; each subsequent pass will have larger steady-state amplitude than the preceding one. This will continue until the cutting system experiences some unmodeled effect which arrests the vibration amplitude, for example, the vibration amplitude being large enough such that the tool disengages from the material, or some nonlinear stiffening of the workpiece or cutting machine. Note that the sign of  $K_f$  will change the stability analysis moving forwards – first, the positive  $K_f$  scenario is examined.

At the threshold of regenerative stability,

$$a_{lim} = -\frac{1}{2K_f G}, \quad K_f > 0 \quad (3.53)$$

The limiting width of cut must be a positive length, therefore only negative portions of  $G$  can amplify the vibrations. The smallest value of  $a_{lim}$  occurs at the minimum value of  $G$ ,  $G_{min}$ ; thus the system is expected to begin regenerating when the cutting width exceeds

$$a_{lim} = -\frac{1}{2K_f G_{min}}, \quad K_f > 0 \quad (3.54)$$

For a second-order, single degree of freedom system with damping  $G_{min}$  can be written out in terms of the system parameters. Expressions for  $G_{min}$ ,  $G_{max}$  and their corresponding frequencies  $\omega_1$ ,  $\omega_2$  are presented from [46]

$$G_{min} = -\frac{1}{4k_f\zeta(1+\zeta)} \quad (3.55)$$

This minimum value occurs at a frequency of

$$\omega_2 = \omega_n\sqrt{1+2\zeta} \quad (3.56)$$

This expression can be substituted into the expression for  $a_{lim}$  given in Eq. (3.54) to arrive at an expression for  $a_{lim}$  in terms of system parameters.

$$a_{lim} = \frac{2k_f\zeta(1+\zeta)}{K_f} \approx \frac{2k_f\zeta}{K_f} \text{ if } \zeta \ll 1; \quad K_f > 0 \quad (3.57)$$

In the case of negative  $K_f$ , the requirement on  $G$  to fulfill the instability condition in (3.52) changes to be that  $G$  must be a positive value. For a second order system,

$$G_{max} = \frac{1}{4k_f\zeta(1-\zeta)} \quad (3.58)$$

which occurs at a frequency of

$$\omega_1 = \omega_n\sqrt{1-2\zeta} \quad (3.59)$$

Using this expression for  $G_{max}$ , substituting into Eq. (3.52), and solving for  $a_{lim}$  results in an  $a_{lim}$  expression of

$$a_{lim} = \frac{2k_f\zeta(1-\zeta)}{K_f} \approx \frac{2k_f\zeta}{K_f} \text{ if } \zeta \ll 1; \quad K_f < 0 \quad (3.60)$$

For small values of damping, the  $a_{lim}$  expressions are identical and the worst-case frequencies occur very nearly at the same frequency (the system natural frequency).

### 3.4.3 Regenerative chatter model predictions

If the cutting width is smaller than the maximum allowable stable cutting width, i.e., if  $a < a_{lim}$ , then the system is *stable* – any applied forcing frequency results in a surface profile that attenuates each pass. If the cutting width is larger than the maximum allowable stable cutting width, i.e., if  $a > a_{lim}$ , then the system is *unstable* – there exist some forcing frequencies that, if applied to the system, will imprint a surface amplitude on the workpiece that will grow larger in amplitude each pass. The forcing frequencies that will begin to regenerate unstably after the cutting system crosses the  $a_{lim}$  threshold will be at and near the system's resonant frequency (where  $G_{min}$  is at its largest negative magnitude); the band of unstable frequencies will widen as the cutting width grows larger. Figure 3.15 shows a schematic comparing stable vs unstable regenerative cutting behavior.

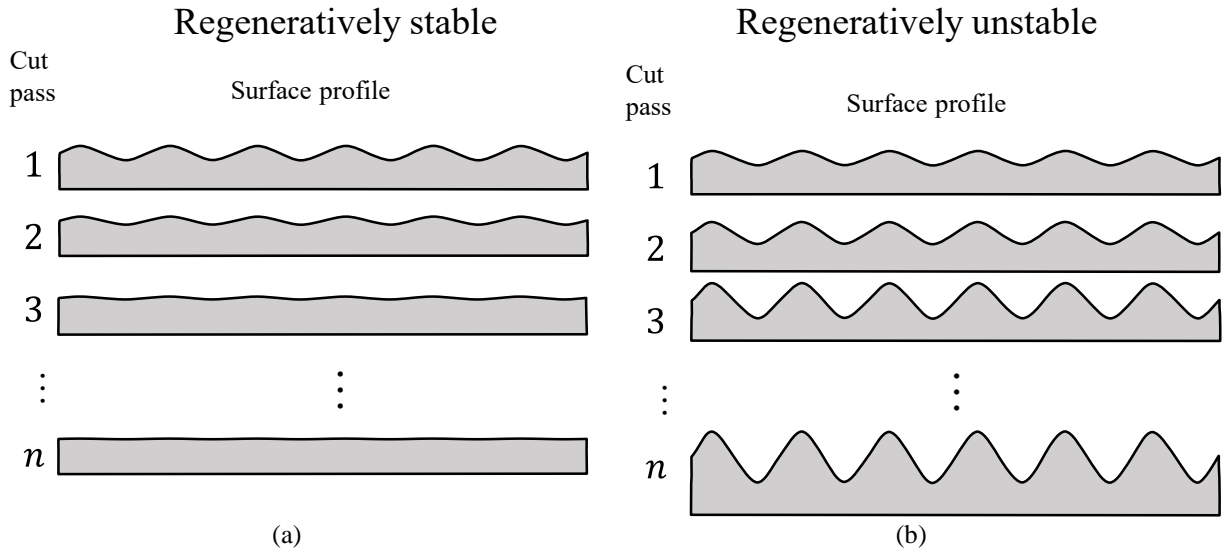


Figure 3.15: Stable versus unstable regeneration in serial sectioning. A sequence of cuts is visually represented, from top to bottom; each wavy surface represents a freshly cut surface. A surface profile has been imprinted on surface on the first cut. (a) For a regeneratively stable system, the amplitude of the surface will attenuate each cutting pass. (b) For a regeneratively unstable system, the surface profile will be amplified each cutting pass.

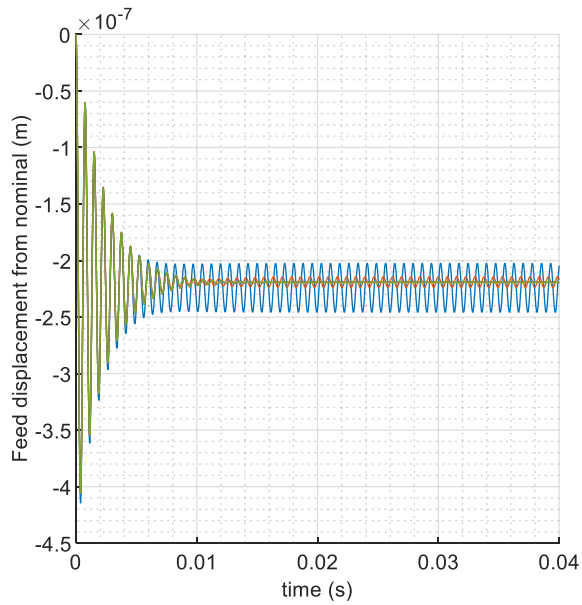
### 3.4.4 Numerical implementation

A MATLAB script was written to simulate the equation of motion Eq (3.42), including the regeneration effect - the  $x$  vector of each pass is saved and used to calculate forces for the next cutting pass. The cutting is initialized with a sinusoidal surface  $x_{init} = B \cos(\omega_{init} t)$ . The selected frequency  $\omega_{init}$  used is the modeled cutting system's natural frequency - while not the worst-case value, this value is close to the worst-case value where  $G_{max}$  occurs and is a practical frequency to select - a disturbance during cutting could initiate a vibration at the system's natural frequency and cause this surface to be imprinted, setting up potential regeneration. The initial seed surface amplitude  $B$  used in these simulations is  $0.1 \mu m$  (1% of the nominal feed).

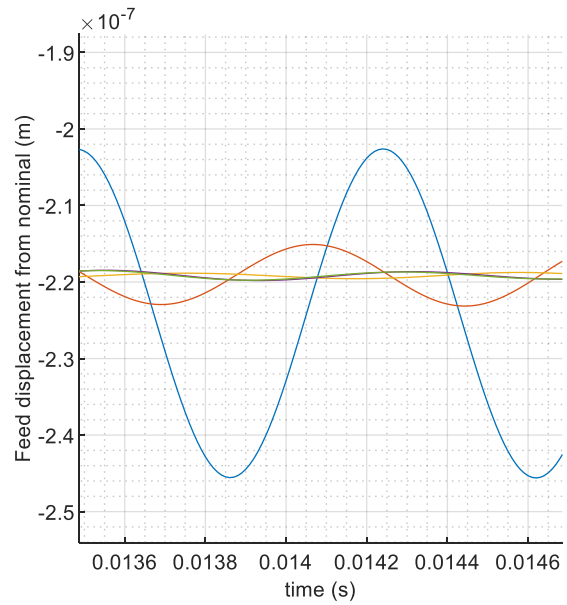
Figure 3.16 shows the simulated output surface profile of a sequence of five cuts when the cutting width is smaller than the maximum stable cutting width; for this simulation a cutting width of 10% of the maximum allowable width was used. Figure 3.16a shows the transient response and the steady-state response. Figure 3.16b shows a close-up of the steady-state portion

of the cut. It can be seen more clearly in this figure that the initial surface attenuates in amplitude with each subsequent pass. Figure 3.16c shows an FFT of the second half of the cut, the steady state portion of cutting; the downwards shift of the FFT indicates a reduction in amplitude.

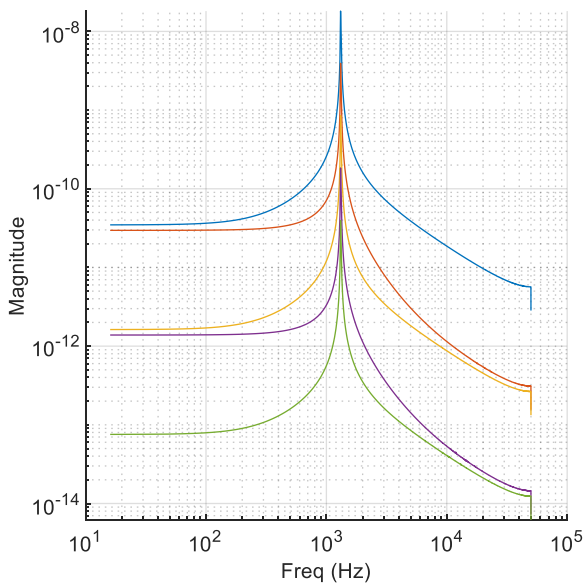
Figure 3.16d tabulates the parameters used in this simulation.



(a)



(b)



(c)

Parameter	Symbol	Value	Unit
Mass	$m$	0.7e-3	kg
Damping coefficient	$b$	0.6	kg/s
Feed stiffness	$k$	49e3	N/m
Width of cut	$a$	0.06e-3	m
Nominal feed	$t_o$	10e-6	m
Specific feed pressure	$K_f$	-17.9e6	N/mm <sup>2</sup>
Number of passes	$n$	5	

(d)

Figure 3.16: A sequence of 5 cuts overlaid on one another for a stable cut. The width of cut is 10% of the maximum allowable width of cut. (a) Entire simulated trace (b) a close-up showing attenuation of the different cuts (c) the FFT magnitude of each cut (d) Parameters used for simulation

In comparison, Figure 3.17 shows the output of a sequence of cuts when the cutting width is larger than the maximum stable cutting width – in these simulations a cutting width 110% of the maximum allowable width was used (10% higher than the maximum stable width). Figure 3.17a shows the transient response and the steady-state response – it can be seen here that the



response amplitude grows with each subsequent cutting pass. In addition to an amplification of the steady-state response, the initial transient response grows in amplitude as well as duration when cutting in the unstable regime. Figure 3.17b shows a close-up of the steady-state portion of the cut which more clearly shows the growth in amplitude compared to the initial seed surface. Figure 3.17c shows an FFT of the second half of the cut, the steady state portion of cutting – the magnitude at the system's natural frequency increases after every pass. Figure 3.17d tabulates the parameters used in the unstable regeneration simulation.

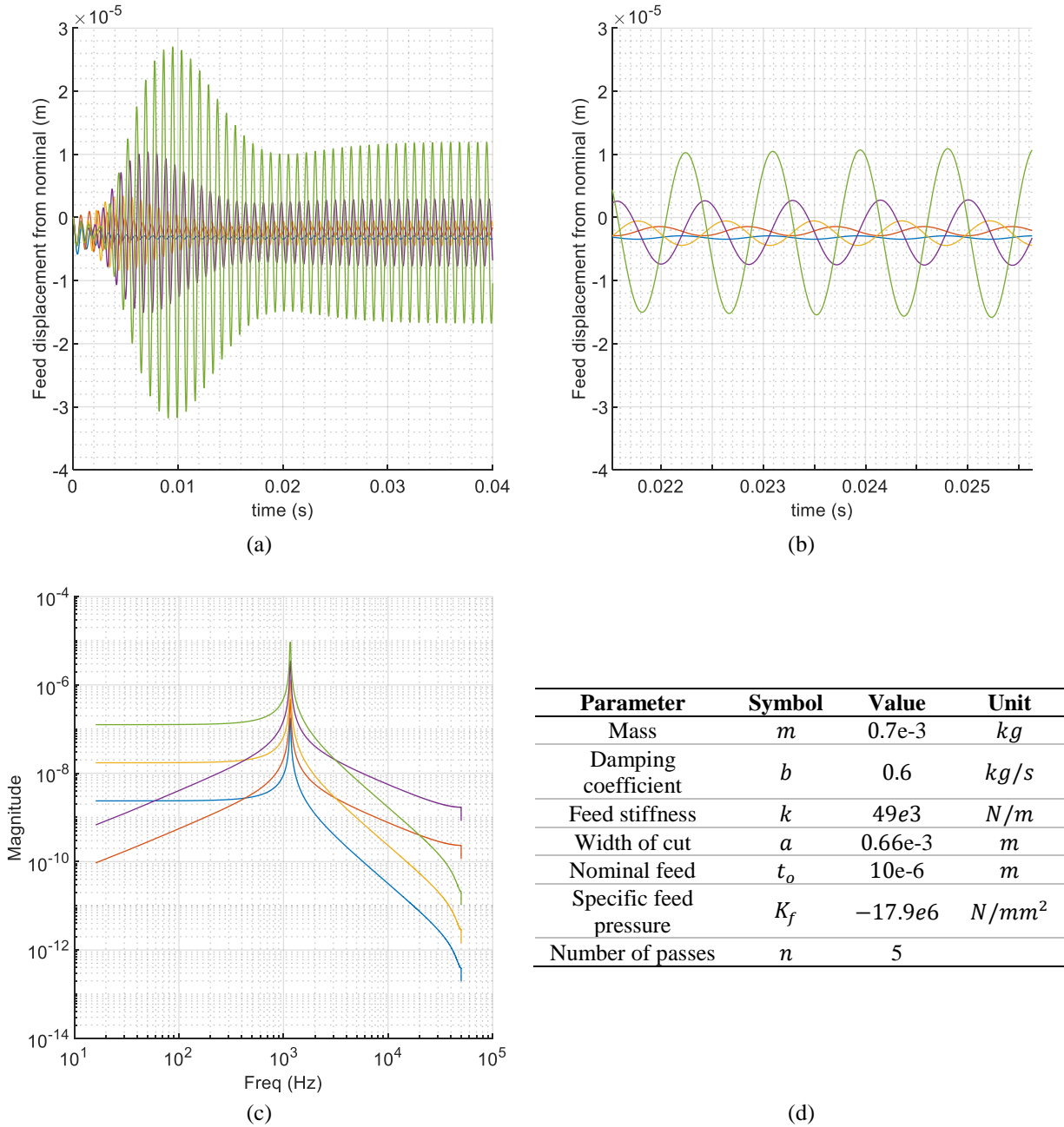


Figure 3.17: A sequence of cuts overlaid on one another for an unstable cut. The width of cut is 110% of the maximum allowable width of cut. (a) Entire simulated trace (b) a close-up showing attenuation of the different cuts (c) the FFT magnitude of each cut (d) Parameters used for simulation

### 3.5 Cantilevered knife tip compliance modeling

Understanding the net compliance of the cutting system is necessary in evaluating cutting stability, both for dig-in and regenerative chatter stability; the net compliance of a system with

compliances in series is dominated by the largest compliance, and the knife tip is a potential source of compliance. In this section a knife tip compliance model is developed and it is assessed whether or not the disposable knives used in the experiments in this work are potentially a significant source of compliance in the cutting system.

### **3.5.1 Knife tip deflection analytical model definitions**

Engineering handbooks contain tapered beam solutions tabulated in references such as [52], however, the ratio of the tip width to the base width is higher in this analysis is much higher than the tabulated values. A model for knife tip deflection is modeled here. The modeled portion of the knife is the portion of the knife that extends beyond the knife mount (or knife carrier) (Figure 3.18).

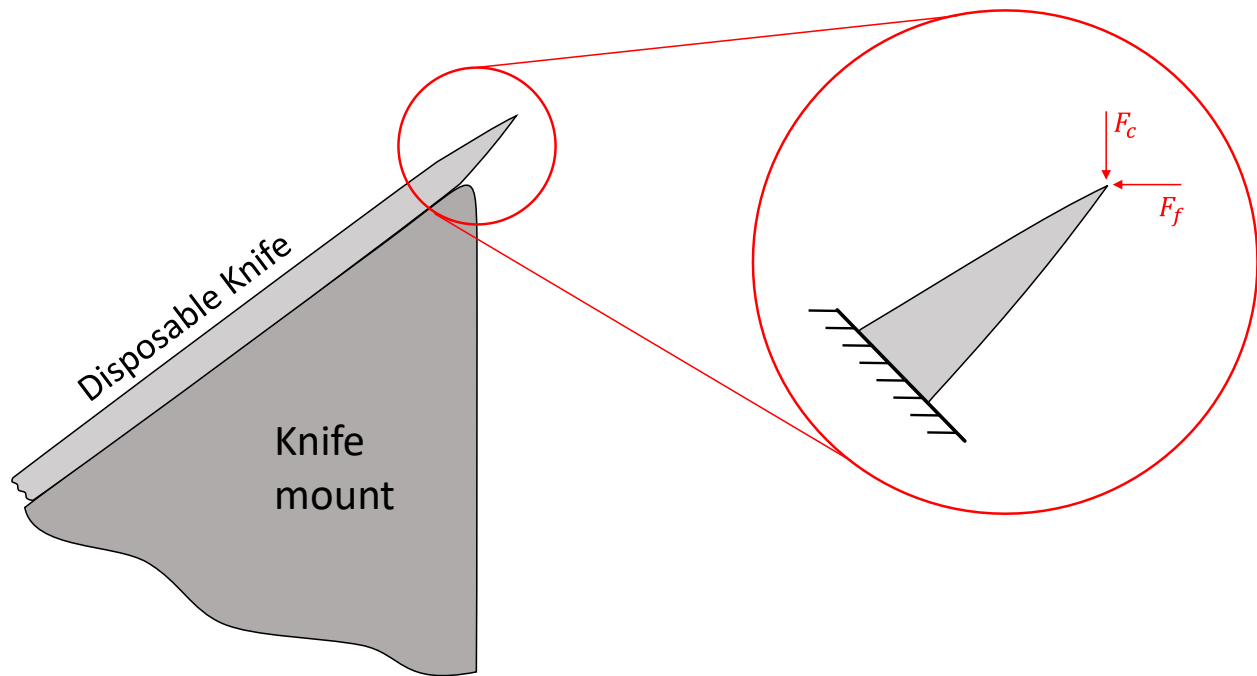


Figure 3.18: Schematic of disposable knife glue assembly used in cutting experiments in this work. A disposable microtome blade (disposable knife) is glued on to an aluminum substrate (the knife mount) and withstands cutting forces in the cutting velocity direction ( $F_c$ ) and in the feed direction ( $F_f$ ).

The knife tip is slender, and has a finite edge radius; this is modeled as a narrow symmetric wedge with a flat tip, with the flattened tip width being very small (Figure 3.19).

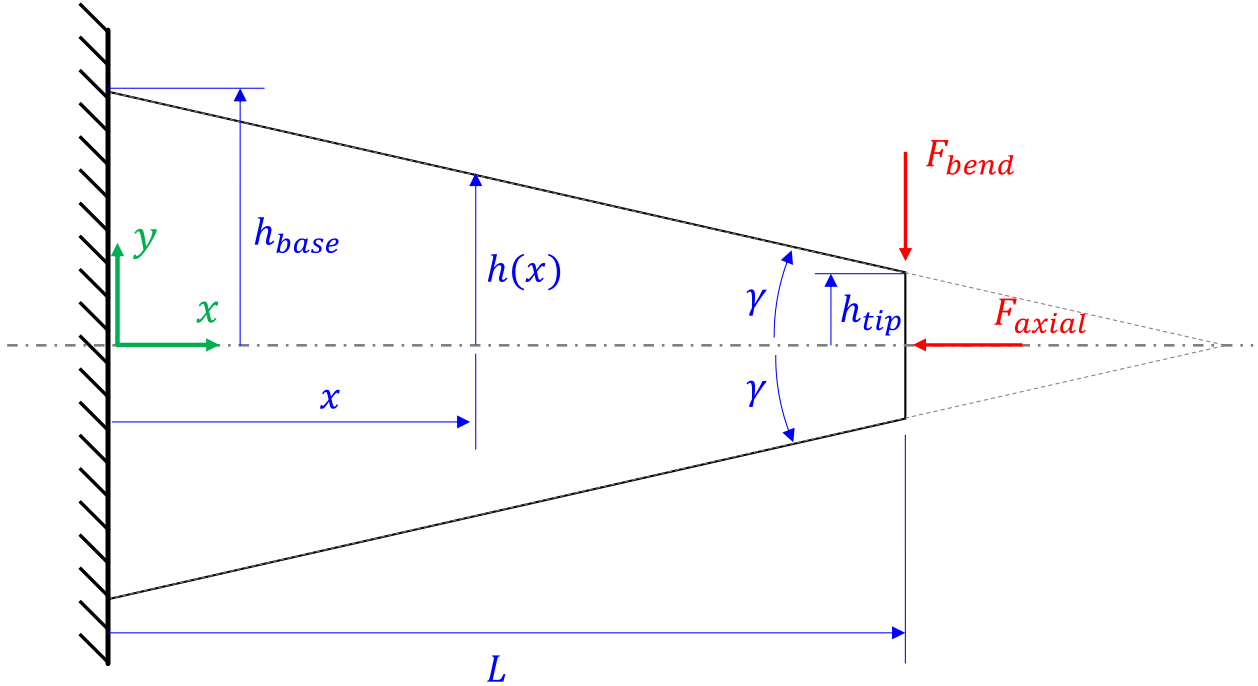


Figure 3.19: Narrow wedge truncated cantilever beam stiffness model and parameters

The half-height of the beam is written as a function of position along the beam measured from the wall, Eq. (3.61), and the area moment of inertia is subsequently defined as a function of this height. A MATLAB Live Script was written to assist with the algebra and calculus.

$$h(x) = h_{tip} + (L - x) \tan(\gamma) \quad (3.61)$$

$$I(x) = \frac{1}{12} b (2h(x))^3 \quad (3.62)$$

The moment function Eq (3.63) is written in terms of the input loads and geometry parameters, and integrated to obtain the beam angle, which is then integrated to obtain the deflection.

$$M(x) = F_{bend}(x - L) \quad (3.63)$$

$$\theta(x) = \int -\frac{M(x)}{E I(x)} \quad (3.64)$$

Zero slope and zero deflection boundary conditions were applied at the wall end ( $x = 0$ ). After solving the indefinite integrals and applying the boundary conditions, an expression for the deflection  $y_{tip}$  at the free end of the tapered beam can be written in terms of the parameters:

$$y_{tip} = \frac{3F_{bend}L^3 \cos^2 \gamma}{4Eb h_{tip} (L \sin \gamma + h_{tip} \cos \gamma)^2} \quad (3.65)$$

Values corresponding to the microscope-measured knife tips are presented in Table 3-3

Table 3-3: Parameters and outputs for truncated tapered beam deflection calculations

Parameter	Symbol	Value	Unit
<i>Inputs</i>			
Wedge tip half-height	$h_{tip}$	1	$\mu m$
Beam length	$L$	1	$mm$
Wedge half-angle	$\gamma$	6.75	deg
Wedge width	$b$	6.35	$mm$
Wedge elastic modulus	$E$	210	$GPa$
Applied bending load	$F_{bend}$	0.001	$N$
<i>Outputs</i>			
Tip deflection	$y_{tip}$	2.24	$nm$
Bending stiffness	$k_{bend}$	446	$N/mm$

### 3.5.2 Finite element analysis validation

A 2D plane-strain finite element analysis was set up in Solidworks Simulation to validate the analytical model. A high-density mesh control is used within a radius extending  $50 \mu m$  from the apex of the truncated cone (Figure 3.20a); the global mesh element size used was  $7.5 \mu m$  (Figure 3.20b), and a growth ratio of 1.01 was used to get a smooth transition between the high-density mesh zone and the global mesh zone (Figure 3.20c).

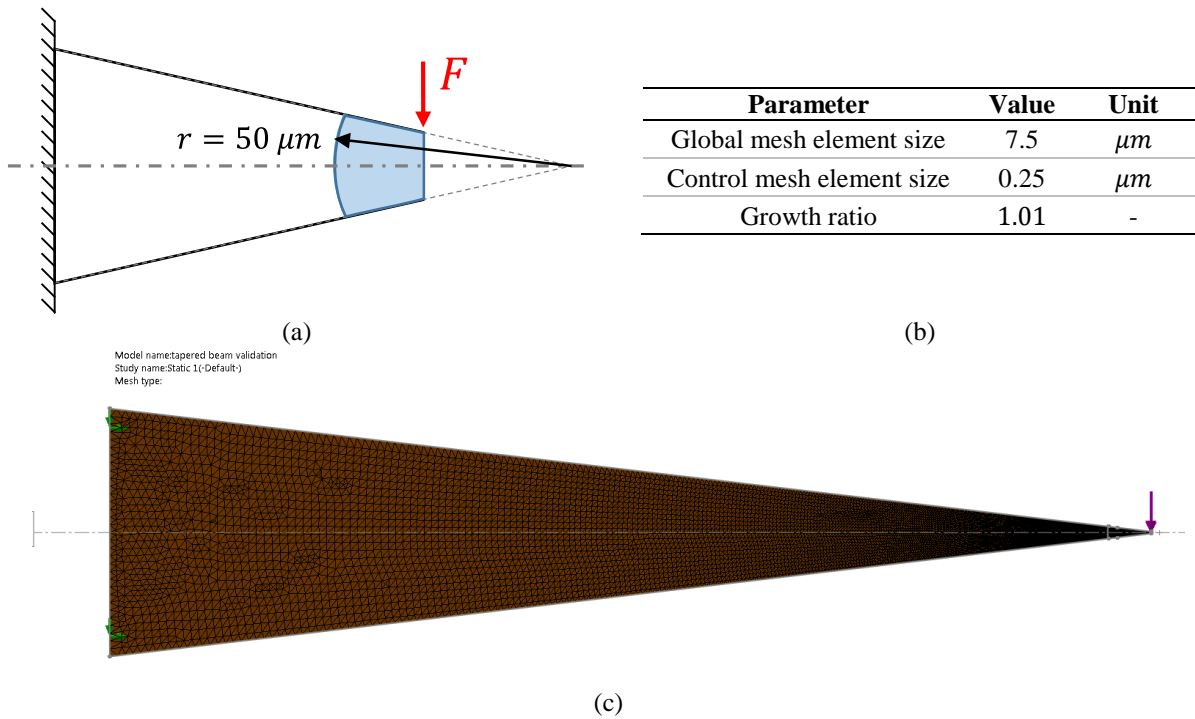


Figure 3.20: 2D plane strain knife tip deflection analysis setup. (a) a schematic of the high-density control mesh zone spanning a  $50 \mu m$  radius from the apex of the truncated wedge; the shaded region contains smaller elements (b) table of mesh element parameters (c) screenshot of the complete mesh.

Screenshots of the analysis results are presented for deflection (Figure 3.21a), von Mises stress (Figure 3.21b) and strain (Figure 3.21c). The tip deflection is measured by averaging the vertical displacement of the elements on the right-most side of the wedge.

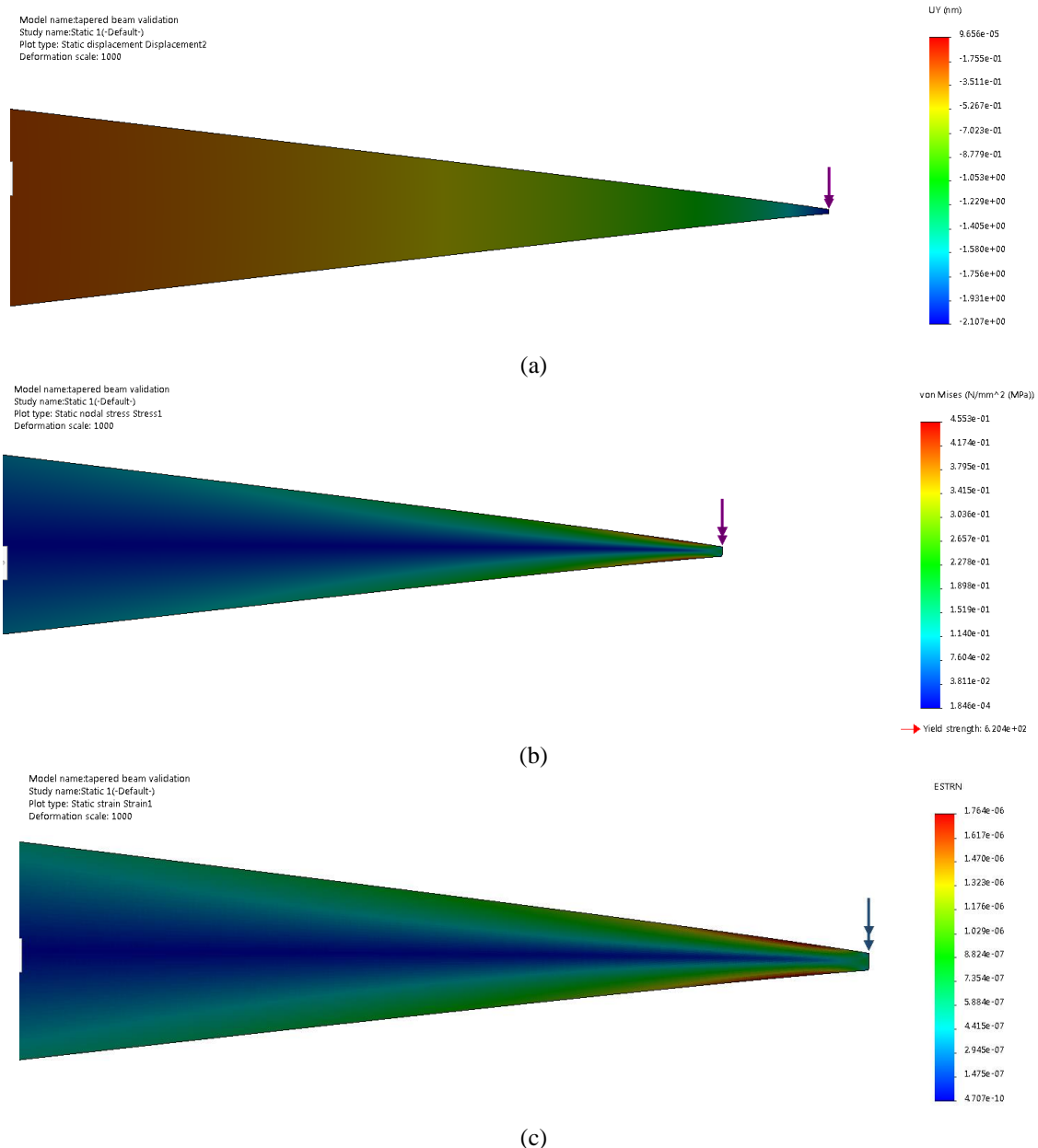


Figure 3.21: Truncated cantilevered wedge knife tip FEA results (a) Y deflection (b) von Mises stresses (c) equivalent strain

Taking the FEA value as the reference value, the analytical model overpredicts deflection by 6% (Table 3-4).



Table 3-4: Comparison between analytical model and FEA deflections for 2D truncated cantilever beam

<b>Parameter</b>	<b>Value</b>	<b>Unit</b>
Analytical model deflection	2.24	<i>nm</i>
FEA deflection	2.11	<i>nm</i>
% Error	6	%

This model is conservative, as it overpredicts compliance compared to the simulation, and is thus in line with typical precision engineering practice. However, in the course of this work it was found that this model oversimplifies the situation, and overpredicts the stiffness by about a factor of 50; not all of the width of the knife will resist the localized forces, and so local deformations must be considered as discussed in Section 6.4.2.

### **3.5.3 Knife tip deflection model discussion**

The deflections calculated here represent a worst-case scenario, with the load applied perpendicular to the wedge axis of symmetry – in a real cutting scenario, the knife will be inclined, so some of the applied force will be applied axially rather than in bending. This knife tip deflection model is used in designing the compliant knife cutting experiment (Section 5.1.2) – the knife carrier is designed such that it is an order of magnitude more compliant than this worst-case knife tip compliance to ensure that the system compliance is dominated by the compliant knife carrier.

## **3.6 Modeling workpiece deformation and compliance**

The goal of this analysis is to understand how geometry, material properties, and cutting parameters affect workpiece deformations and whether or not this localized compliance can be large enough relative to the other compliances in the system to dominate the net system compliance.

### 3.6.1 Localized workpiece deformations via Hertzian model

In this section, only localized workpiece deformations due to contact between the knife tip and workpiece are modeled – deflections due to workpiece shearing and bending are modeled in Section C.9 in the context of tallying up deflections and compliances in the cutting instrument design.

The Hertzian contact model enables an analyst to model deflections under loading for specific contact problems; in this section it will be used to roughly model workpiece deformation under the knife tip. For example, if the cutting is in the dig-in regime and the local stiffness at the cutting zone is low, the workpiece material can be pulled up towards the tool. Several assumptions are made in the Hertzian contact model [53]:

- Surfaces are continuous and non-conforming; the contact area radius is much smaller than the radius of the contacting elements:  $a \ll R$
- Deformations are elastic and strains are small
- Each solid is an elastic half-space:  $a \ll R_{1,2}, a \ll l$
- Surfaces are frictionless

During cutting many of these assumptions are violated, so the use of a Hertzian contact model is first-order approximation meant to assess whether or not localized elastic deformations could potentially be large enough such that the resulting stiffness is low enough to dominate the overall stiffness of the structural loop. The contact area radius is not much smaller than the knife edge, so the condition  $a \ll R$  is not met. These contact models will underpredict the contact stiffness when the surfaces are conforming [53], so these calculations would give a conservative contact stiffness estimate. Deformations are not solely elastic during cutting, rather a complex mixture of plastic shearing and elastic deformation. There is a zone of elastic material passing underneath the tool and pressing up against it as it passes by, since it is well documented in the

machining literature that some material “springs back” after being cut and contributes to tool flank wear. The friction force between the tool flank and the freshly cut surface could be large enough to plastically deform this surface (the freshly-cut surface may be “smeared” due to high local contact forces).

The knife tip and workpiece contact pair is modeled as a line contact – when the knife tip, modeled here as a cylinder, indenting the flat workpiece surface (Figure 3.22a), the resulting contact zone is modeled as forming a rectangular contact patch (Figure 3.22b). Cutting forces for cutting epoxy are estimated using measured feed-direction force-per-length from [39]. The line contact formulae Eq (3.66) through Eq. (3.73) are reproduced here from [54].

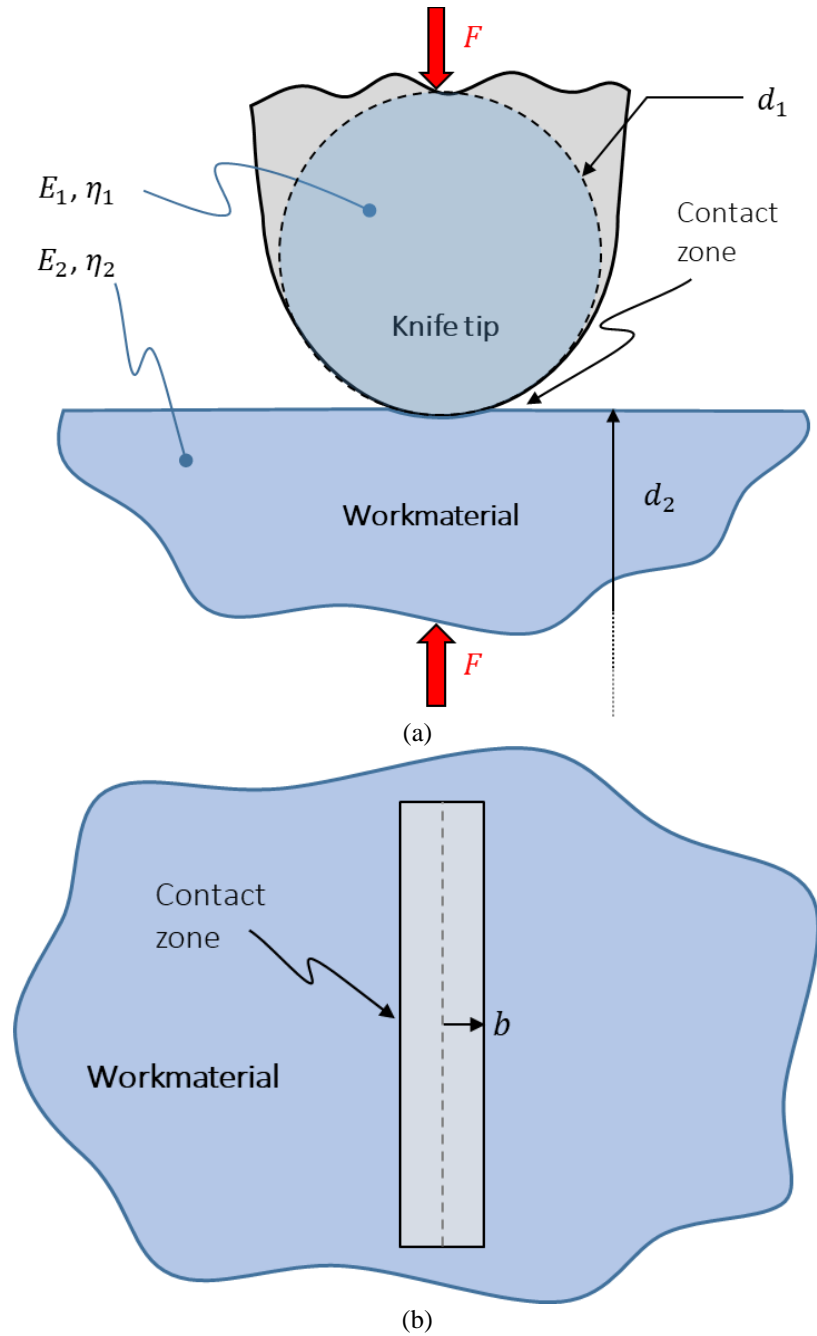


Figure 3.22: Hertzian contact model of knife tip indenting elastic workmaterial, used to get a first order estimate of how much deflection to expect in the workmaterial surface due to indentation forces (a) Side view showing the knife tip indenting the workmaterial (b) Top view, omitting the knife tip but showing the contact zone as an ellipse with high aspect ratio

To compute the knife tip displacements, the following calculation procedure is followed:

1. Calculate the contact modulus, Eq (3.66), and equivalent radius, Eq. (3.67)
2. Calculate the contact rectangle half-width, Eq. (3.68)
3. Calculate the deflection due to elastic deformation in the cylinder, Eq. (3.69), and due to the flat, Eq. (3.70)
4. Calculate the instantaneous stiffness, Eq (3.71)
5. Calculate the maximum contact pressure (3.72) and max shear stress (3.73)

$$\frac{1}{E_e} = \frac{1-\eta_1^2}{E_1} + \frac{1-\eta_2^2}{E_2} \quad (3.66)$$

$$\frac{1}{R_e} = \frac{1}{R_{1maj}} + \frac{1}{R_{1min}} + \frac{1}{R_{2maj}} + \frac{1}{R_{2min}} \quad (3.67)$$

$$b = \left( \frac{2Fd_1d_2}{\pi LE_e(d_1+d_2)} \right)^{\frac{1}{2}} \quad (3.68)$$

$$\delta_1 = \frac{2F}{\pi LE_e} \left( \ln \left( \frac{2d_1}{b} \right) - \frac{1}{2} \right) \quad (3.69)$$

$$\delta_2 = \frac{2F}{\pi LE_e} \left( \ln \left( \frac{2d_o}{b} \right) - \frac{\eta_2}{2(1-\eta_2)} \right) \quad (3.70)$$

$$k_{inst} = \frac{F}{\delta_1+\delta_2} \quad (3.71)$$

$$q = \frac{2F}{\pi bL} \quad (3.72)$$

$$\tau_{max} = 0.3q \quad (3.73)$$

In calculating the deflections, a reference value must be selected to integrate elastic deformation over; the reference value  $d_o$  used here is the cylinder diameter  $d_1$ . Parameters used for this modeling as well as the calculation outputs are provided in Table 3-5.

Table 3-5: Parameters used for Hertzian line contact model

Parameter	Symbol	Value	Unit
<i>Inputs</i>			
Knife tip (“cylinder”) diameter	$d_1$	2	$\mu m$
Workpiece diameter	$d_2$	$10^{10}$	$mm$
Knife elastic modulus	$E_1$	200	$GPa$
Workpiece elastic modulus	$E_2$	2.5	$GPa$
Knife Poisson ratio	$\eta_1$	0.28	-
Workpiece Poisson ratio	$\eta_2$	0.3	-
Contact zone length	$L$	10	$mm$
Applied normal load	$F$	0.1	$N$
<i>Outputs</i>			
Contact area rectangle half-width	$b$	0.069	$\mu m$
Knife tip elastic deformation	$\delta_1$	8.4	$nm$
Workpiece elastic deformation	$\delta_2$	9.0	$nm$
Instantaneous contact stiffness	$k_{inst}$	5.7	$N/\mu m$
Max shear stress	$\tau_{1max}$	93	$MPa$

The width of the cutting zone, i.e., the width of knife edge in contact with the cutting material, corresponds in this model to the contact zone length  $L$ . The relatively high stiffness value of  $5.7 N/\mu m$  compared to the stiffness of  $0.05 N/\mu m$  used for the compliant knife carrier, implies that elastic deformations due to knife tip and workpiece contact will not cause the dig-in instability in the experiments done in this work. However, the calculated stiffness is comparable in magnitude to the overall machine feed stiffness (of the order of  $1 N/\mu m$ ) and could present an ultimate limit in a future design with higher stiffness, if something else in the system doesn't restrict the system first. Further work in developing a force-displacement contact model for cutting conditions with experimental validation could assess whether or not the simple Hertzian model is adequate for this modeling task.

### 3.6.2 Bulk deformation modeling

Bulk deformations of the workpiece are estimated using uniaxial tension/compression (Figure 3.23a) and simple shear (Figure 3.23b) models.

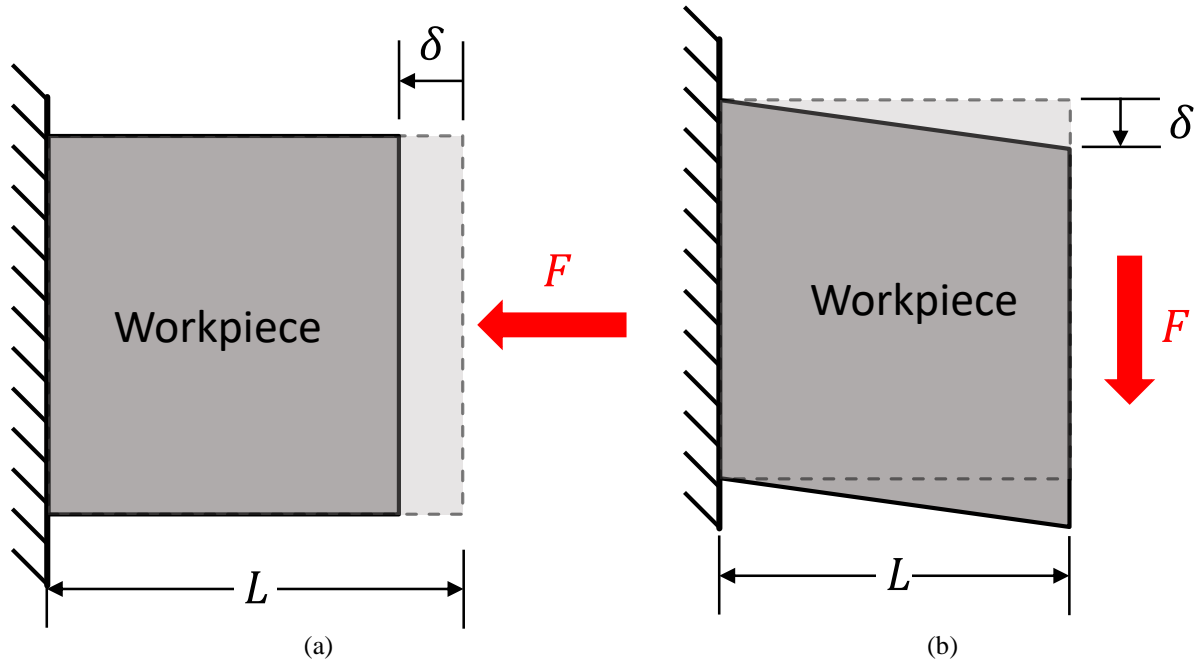


Figure 3.23: (a) Bulk workpiece tension/compression model, (b) bulk workpiece shear model

The deflections  $\delta_x$  and  $\delta_y$  can be calculated using the formulas shown in Eq (3.74) and Eq (3.75) respectively.

$$\delta_x = \frac{F_x L}{EA} = \frac{F_x L}{Eah} \quad (3.74)$$

$$\delta_y = \frac{F_y L}{GA} = \frac{F_y L}{Gah} \quad (3.75)$$

Workpiece stiffnesses are derived from these deflection formulas,

$$k_x = \frac{F_x}{\delta_x} = \frac{EA}{L} \quad (3.76)$$

$$k_y = \frac{F_y}{\delta_y} = \frac{GA}{L} \quad (3.77)$$

The stiffness scaling with volume is investigated first to understand how the workpiece stiffness would change with an increase of each dimension (if, for example, attempting to cut an entire mouse brain of scale  $\sim 10 \text{ mm}$  as opposed to a smaller tissue sample of scale  $\sim 1 \text{ mm}$ ). If a

cube specimen with side  $a$  is assumed, that is,  $a = L = h$ , then the stiffnesses above are written as

$$k_x = \frac{F_x}{\delta_x} = Ea \quad (3.78)$$

$$k_y = \frac{F_y}{\delta_y} = Ga \quad (3.79)$$

The overall stiffness of the specimen is expected to scale with the specimen size. Specific values of the deflections  $\delta_x$  and  $\delta_y$  are calculated to understand the scale of the deformations encountered during the cutting process. Parameters used for the deflection calculation are given in Table 3-6.

Table 3-6: Parameters used to calculate bulk specimen compression and shear deflections

Parameter	Symbol	Value	Unit	Comment
<i>Inputs</i>				
Workpiece elastic modulus	$E$	2.5	$GPa$	Cast epoxy average, from [55]
Workpiece shear modulus	$G$	0.94	$GPa$	Calculated from $E$
Width of cut	$a$	1	$mm$	from [39], estimated
Workpiece height	$h$	1	$mm$	from [39], estimated
Workpiece stick-out	$L$	1	$mm$	from [39], estimated
Cut force	$F_y$	0.06	$N$	from [39], at feed $0.22 \mu m$
Feed force	$F_x$	-0.01	$N$	from [39], at feed $0.22 \mu m$
<i>Outputs</i>				
Feed deflection	$\delta_x$	-4	$nm$	
Slice deflection	$\delta_y$	64	$nm$	
Feed stiffness	$k_x$	2.5	$N/\mu m$	
Slice stiffness	$k_y$	0.94	$N/\mu m$	

The calculated deflection in the feed ( $X$ ) direction is small, representing 1.8% of the nominal feed value; these are very small deflections for a reasonable workpiece size. The stiffness in the slice ( $Y$ ) direction (that is, parallel to the cutting velocity) is about a factor of 2.5 times smaller than the stiffness in the feed direction. Deflections in the slice directions will be generally higher since the workpiece stiffness is lower in this direction, and because the cutting forces will generally be higher in the slice direction than in the feed direction. However, these



deflections do not affect the section thickness directly. The consequences of too low a slice stiffness are currently unknown and are highlighted as an area for future work in Section 7.3.3.

## **3.7 Cutting zone thermal modeling**

The goal of this analysis is to assess how cutting parameters affect temperatures in the cutting zone – the tool, workpiece, and chip/section. In microtome cutting, the materials cut are typically thermal insulators, as compared to metal cutting, where the materials cut are generally good thermal conductors (compared to polymers). Sectioning at elevated temperatures has been shown to improve section quality especially in thicker sections, although too high of a temperature will cause distortion [24].

### **3.7.1 First-order section temperature modeling**

The section temperature is modeled by considering the power input to the system via the product of cutting force and cutting velocity, the thermal properties of the system, and the flow of mass into and out of the cutting zone. This model gives an upper bound, i.e., what the section temperature would be if all of the power was dissipated in the section, and does not specify what fraction of the power heats up the section compared to the workpiece.

The model assumes steady state cutting, a thin shear zone, and that the material is heated up as it passes through the shear zone, where the product of cutting force and cutting velocity continuously adds energy to the system. It is assumed that the material starts at room temperature. The mass flow rate through the shear zone is written in terms of the cut width, depth of cut, mass density, and cutting speed in Eq (3.80). Representative cutting forces are again taken from [39]. An expression for the temperature of the material after it passes through the shear zone is written, Eq (3.81).

$$\dot{m} = at_o\rho V \quad (3.80)$$

$$\theta_{out} = \frac{F_c V}{c_s \dot{m}} + \theta_{in} = \frac{F_c V}{c_s at_o \rho V} + \theta_{in} \quad (3.81)$$

Table 3-7: Parameters used in first-order chip temperature modeling, and calculation results

Parameter	Symbol	Value	Unit	Comment
<i>Inputs</i>				
Cutting speed	$V$	1	$mm/s$	from [39]
Cutting force	$F_c$	0.06	$N$	from [39]
Uncut chip thickness	$t_o$	0.225	$\mu m$	from [39]
Width of cut	$a$	1	$mm$	
Workpiece density	$\rho$	1250	$\frac{kg}{m^3}$	Cast epoxy average, [56]
Workpiece specific heat capacity	$c_o$	1000	$\frac{J}{kg K}$	Cast epoxy average, [57]
Initial section/chip temperature	$\theta_i$	293	$K$	Room temperature
<i>Outputs</i>				
Temperature change due to shear zone heat transfer	$\Delta\theta_s$	1.48	$K$	
Temperature change due to tool face heat transfer	$\Delta\theta_f$	-1.47	$K$	
Output section/chip temperature	$\theta_o$	293.01	$K$	

Under the cutting conditions in [39] and according to this model, the section temperature can potentially reach around  $200^\circ C$ , likely enough to significantly change the properties of the resin and possibly damaging it. However, this model represents an overly pessimistic worst-case scenario, that all of the cutting power goes into heating up the chip only, and neglects heat transfer to the bulk workpiece or the tool. The model employed in the next section includes these effects to get a more accurate prediction of what the highest temperatures in the section should be.

### 3.7.2 Including heat transfer to cutting tool and bulk workpiece

Modeling temperatures in the cutting zone has been a longstanding problem in machining analysis, and several models are available which could also apply to microtome cutting. The analysis here is an implementation of the analysis presented in [58] modeling temperatures in the machining cutting zone, which also models the effect of heat transfer into the bulk workpiece

and the cutting tool. The model is a two-source model (Figure 3.24): the first heat source is the shear plane, with heat entering the material as the material is sheared in the shear plane; the second source is friction at the tool rake face.

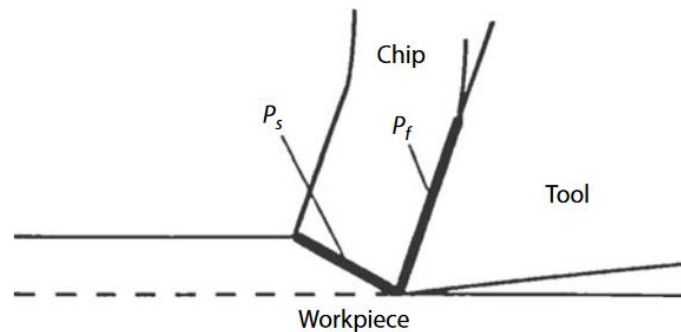


Figure 3.24: Two-source model for calculating chip (section) temperature in machining. Plastic deformation at the shear zone and the resulting power dissipated ( $P_s$ ) increases the temperature of the chip, and the power input from the power dissipated at the tool face due to friction ( $P_f$ ) further contributes to temperature rise. Figure from [58]

The assumptions made in the two-source model are listed here;

- The cutting achieves steady state
- The chip leaves the shear zone at uniform temperature
- Friction on the tool flank (the clearance face) is neglected

For detailed discussion of the model derivation and analysis, the reader is referred to [58], which also discusses model accuracy - the two-source model has successfully predicted rake face temperatures within approximately 20% of the measured values in steel and aluminum, so the assumptions made here are reasonably accurate for metal cutting. Steady-state cutting is a given, since the expectation is to cut smooth sections. Without detailed measurements of the temperature distribution it is unknown if the chip leaves the shear zone at uniform, but assuming a uniform distribution is a reasonable approximation. The remaining question is if the model still applies in polymer orthogonal cutting, which share the same geometry and kinematics as in

metal orthogonal cutting but differs in the workpiece material. The lack of a tool flank friction is likely not an issue, since the heat generated by this frictional power would be wicked away through the tool (a thermal conductor) rather than flowing through the polymer (a thermal insulator) and into the workzone.

The results and parameters used in the two-source analysis implementation are shown in Table 3-8.

Table 3-8: Two-source model implementation parameters and results.

Parameter	Symbol	Value	Unit	Comment
<i>Inputs</i>				
Cutting speed	$V$	1	$mm/s$	from [39]
Cutting force	$F_c$	0.06	N	from [39]
Rake angle	$\alpha$	40	deg	from [39] (estimated)
Uncut chip thickness	$t_o$	0.225	$\mu m$	from [39]
Width of cut	$a$	1	$mm$	
Workpiece density	$\rho$	1250	$\frac{kg}{m^3}$	Cast epoxy average, [56]
Workpiece specific heat capacity	$c_o$	1000	$\frac{J}{kg K}$	Cast epoxy average, [57]
Initial section/chip temperature	$\theta_i$	293	K	Room temperature
Tool thermal conductivity	$k_t$	43	$\frac{W}{m K}$	Carbon steel, [59]
Initial chip temperature	$\theta_i$	293	K	Room temperature
<i>Outputs</i>				
Temperature change due to shear zone heat transfer	$\Delta\theta_s$	1.48	K	
Temperature change due to tool face heat transfer	$\Delta\theta_f$	-1.47	K	
Output section/chip temperature	$\theta_T$	293.01	K	

The two-zone model predicts that the interface between the chip and tool is actually wicking away heat from the section, reducing the section temperature after it increases slightly after passing through the shear zone. This model suggests that the temperature of the offcut remains close to room temperature under microtome cutting conditions and no ill effects are expected, unlike in metal cutting where the offcut can rise to several hundred degrees C above room temperature.

### 3.7.3 The thermal (Peclet) number

The thermal, or Peclet number, Eq. (3.82), is a dimensionless number which characterizes is the ratio of the rate of material removal per unit width of cut, to the thermal diffusivity of the work material,

$$Pe = \frac{Vt_o\rho c_0}{k} \quad (3.82)$$

A high  $Pe$  number indicates that most of the heat is carried away in the chip, and not much heat flows into the tool and workpiece. A low  $Pe$  number indicates that the tool motion is slow relative to how quickly heat diffuses away from the section into the tool and workpiece. In metal cutting and conventional machining, Peclet numbers of around 10,000 - 100,000 are the norm [58]. In the latter case, the workpiece typically remains cool as most of the heat is carried away by the offcut, however in the former case the workpiece heats up due to heat transfer between the chip and workpiece. A Peclet number is calculated for microtome cutting,

Table 3-9: Calculating a Peclet number for microtome cutting

Parameter	Symbol	Value	Unit	Comment
<i>Inputs</i>				
Cutting speed	$V$	1	$mm/s$	from [39]
Uncut chip thickness	$t_o$	0.225	$\mu m$	a.k.a. feed
Workpiece density	$\rho$	1250	$\frac{kg}{m^3}$	Cast epoxy average, [56]
Workpiece specific heat capacity	$c_0$	1000	$\frac{J}{kg K}$	Epoxy average, [57]
Workpiece conductivity	$k$	0.35	$\frac{W}{m K}$	Epoxy average, [59]
<i>Outputs</i>				
Peclet number	$Pe$	$8.0e-4$	-	

The Peclet number computed for this reference microtome cutting is smaller than what is typical in machining by a factor of  $1e7$ ; this suggests that that the speed of the tool with respect to the workpiece is small compared to the thermal diffusivity of the material, and a large portion

of the heat generated during cutting has time to diffuse into the workpiece (and most likely, the tool and ambient environment).

### **3.7.4 Workzone thermal modeling discussion**

The analysis presented here suggests that the heat generated during cutting is removed from the section by conduction via the tool and the bulk workpiece material. It is also possible (though not modeled) that heat can be removed from the cutting zone by the ambient environment (i.e., via convection to air and any fluid bath the cutting may take place in). Experiments showing the effect of cutting parameters on resulting section, workpiece, and tool temperature would be a useful avenue of future research.

# CUTTING INSTRUMENT DESIGN AND CHARACTERIZATION

---

This chapter is an in-depth discussion of the design of the instrument used to carry out the cutting dig-in stability experiments in this thesis. The chapter opens with a summary of the instrument's salient features, then segues to a detailed discussion of the instrument modules. Additional modeling details are described in Appendix D.

## **4.1 Instrumented sectioning visualizer design summary**

The cutting instrument was designed to be able to measure cutting forces in three degrees of freedom while recording cutting video, with an emphasis on the instrument having a deterministic feed stiffness. Table 4-1 summarizes important features of the instrumented cutter.

Table 4-1: Instrumented cutting visualizer capabilities summary table

<b>Specification</b>	<b>Value</b>	<b>Unit</b>
Range of motion (slice and feed)	~50	<i>mm</i>
Position resolution	40	<i>nm</i>
Position accuracy	75	<i>nm</i>
Position repeatability	40	<i>nm</i>
Cutting speed range	0.1-10	<i>mm/s</i>
Feed (X axis) stiffness	2	<i>N/μm</i>
Slice (Y axis) stiffness	2	<i>N/μm</i>
Force sensitivity	<1	<i>mN</i>
Maximum $F_y$ , at $F_x = 0$	9.5	<i>N</i>
Maximum $F_y$ , at $F_x = 5$	2.8	<i>N</i>
Force measurement DOFs	3	-
Natural frequency	100	<i>Hz</i>
Video record frame rate	170	<i>frame/s</i>

The modeled error contributions in the sensitive direction (i.e., the feed, or X, direction) calculated from the load-induced error modeling are presented in Figure 4.1.



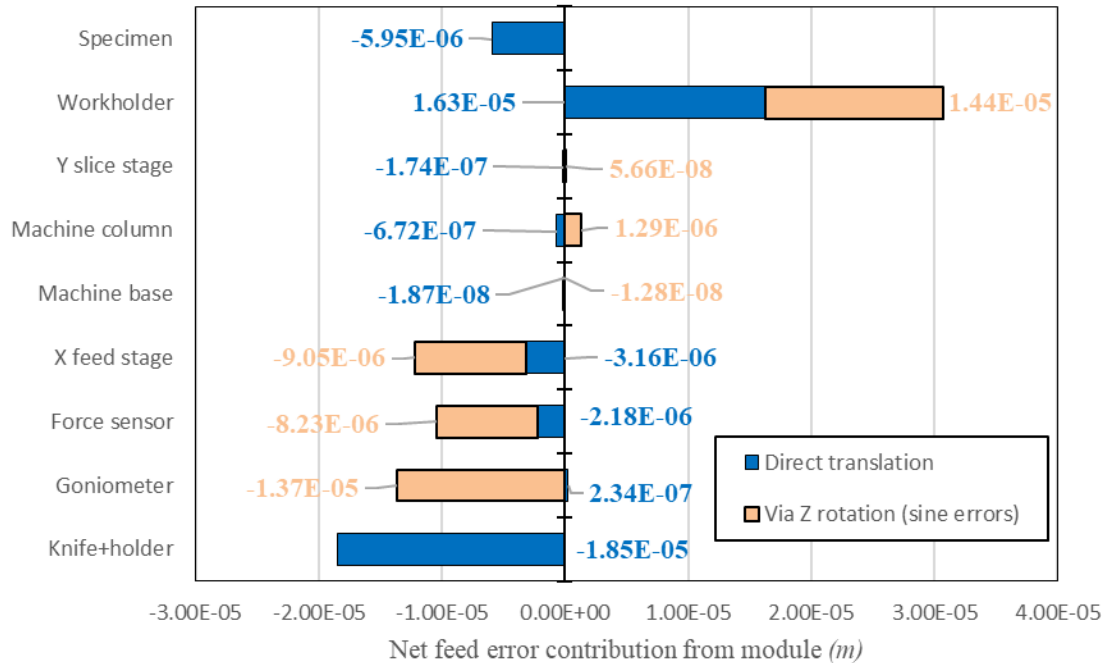


Figure 4.1: Analytical model load-induced feed error at the point of interest (the relative displacement between the specimen tip and the knife tip) broken down into contributions from the instrument modules. Each module's error contribution is further broken down into the direct translation error, and the error induced by each module's rotations and the subsequent lever effect (the sine errors)

An open frame C-frame design was chosen over a gantry-type (closed frame) due to several advantages. The C-frame allows excellent operator access to the workzone, which is important in work where frequent adjustments to the work zone are going to be required for experimental work. The open access to the workzone also allows for greater flexibility for any auxiliary equipment (for example, the loading frame used to calibrate the force sensor) due to the additional space around the work area, which is especially important for a research instrument where additional hardware may be necessary as the work progresses. A closed-frame design leads to a more complex design leading to issues with alignment and overconstraint if countermeasures are not taken (mitigating overconstraint is possible, but requires additional design work and hardware). The C-frame also requires fewer parts and less materials, leading to a more economical design. The main advantage of the gantry design is that higher stiffnesses are

possible. In the following sections, it will be shown that the stiffness specification could be met with the simpler C-frame design, thus the C-frame concept was chosen.

## 4.2 Motivation for combined force and video recording

Understanding the relationships between cutting parameters and cutting behavior requires first defining what is meant by ‘cutting behavior’, and subsequently how it can be measured. Cutting that results in a smooth, flat surface is considered to be good quality cutting. The ideal measurement system would be a multi-axis force sensor combined with a sensor that could map out the surface topography immediately after cutting, but this wasn’t feasible. Instead, cutting force is used as a proxy for cutting surface quality, as the cutting force is expected to be proportional to the depth of cut, and the cutting force measurement is supplemented with cutting videos from a video microscope. The cutting force measurements are supplemented with videos providing qualitative and, to a lesser extent, quantitative information; cutting videos can be used to supplement and explain anomalous force data – for example, if a piece of material is torn out of the workpiece, and gets stuck between the knife and work, the associated cutting force would be difficult to explain without the videos. The videos can also be used to provide some degree of measurement ability via pixel counting. An important decision was made early on in the work to focus on cutting at scales of between 1-10  $\mu m$ , despite the ultramicrotomy process typically taking place at scales of between 10-100  $nm$ . Cutting at the micron scale allows the use of an inexpensive optical microscope and commonly available digital cameras with reasonably high frame rates, as opposed to requiring an electron microscope, and needing to fit all of the cutting and sensing hardware inside of the SEM’s vacuum chamber, which is a much more difficult and resource-intensive design task, see for example [60] for an in-SEM cutting instrument designed to study nanomachining for single-point diamond turning. Fundamentally, nanometer and micron

scale cutting will have in common two key characteristics relevant to dig-in stability: first, that the cutting system will have some finite stiffness, and two, that negative feed cutting forces will be generated pulling the tool into the workpiece. The first point is universally true and the second point is known to be true based on the microtome cutting force measurements in [39], therefore we can study the dig-in phenomenon at the micron scale without the additional burden of requiring nanometric scale cutting, measurement, and visualization.

It's generally more difficult and expensive to achieve high bandwidth with video microscopy than with force measurement – a force measurement system can easily and relatively cheaply measure a few kHz, whereas an equally high-bandwidth high-speed camera setup would impose difficulties with lighting, triggering, data throughput and storage. The compromise in this work is to use high-bandwidth force sensing supplemented with moderately fast video (170 frames per second) with a CMOS digital microscope camera.

As a more practical matter, the digital microscope is indispensable for setting up and running the experiments (e.g., setting up the tool approach to the workpiece, and setting the start and end of the cuts), general troubleshooting, and sanity-checking.

### **4.3 First-order instrument analysis and design**

The purpose of the first-order analysis is to obtain first-pass approximations for structural and bearing stiffnesses, the general size of the machine, the magnitude of errors to expect under force and thermal loading, and to get an idea of how bearing layout will contribute to error at the machine's tooltip. These are interrelated (for example, the general size of the machine increasing based on increased spacing between bearings), so the design process is expected to be iterative.

### 4.3.1 Cutting forces estimation

Estimating the cutting loads is required for setting the stiffness-related functional requirements, and later to model the load-induced errors in a first-order model of the system (Section 4.3.3.1). Cutting forces were estimated using cutting force data measured for embedding epoxy in [39]. The cutting data was used to calculate specific feed and cutting pressures (Table 4-2), which are then used to calculate cutting loads at other cutting widths and feeds. An approximation is made here that the specific feed pressures remain constant with these parameters.

Table 4-2: Estimating cutting forces for modeling. Measured data from [39]

<b>Parameter</b>	<b>Value</b>	<b>Unit</b>
Measured cut force per unit width	60	$N/m$
Measured feed force per unit width	-10	$N/m$
Depth of cut (feed)	0.22	$\mu m$
<i>Outputs</i>		
Specific feed pressure	-46	$N/mm^2$
Specific cutting pressure	273	$N/mm^2$

Once the specific feed pressures were calculated, they were used to calculate loads at other depths and widths of cut (Table 4-3).

Table 4-3: Estimating cutting forces used for first-order modeling

<b>Parameter</b>	<b>Value</b>	<b>Unit</b>
<i>Inputs</i>		
Depth of cut (feed)	10	$\mu m$
Width of cut	1	$mm$
<i>Outputs</i>		
Cutting force	2.7	$N$
Feed force	-0.5	$N$

### 4.3.2 Functional requirements

Design work begins with by listing functional requirements for the instrumented cutter; these are shown in Table 4-4, followed by a description and brief discussion of each entry in the table.

Table 4-4: Functional requirements for  $\mu m$ -scale cutting visualizer; discussion of the numbers selected in the body text can be found in the following paragraphs

Functional requirement	Specification	Unit
Slice (Y axis) range of motion	~6.35	mm
Feed (X axis) range of motion	~6.35	mm
Feed position resolution	100	nm
Feed position accuracy	100	nm
Feed position repeatability	100	nm
Size constraints	Must fit around optics	-
Max cutting speed	10	mm/s
Min cutting speed	0.1	mm/s
Slice (Y axis) stiffness	1	N/ $\mu m$
Feed (X axis) stiffness	1	N/ $\mu m$
Force resolution	1	mN
Motion resolution	100	nm
Maximum force	10	N
Force measurement DOFs	3	-

**Range of motion** refers to the overall travel each linear stage will require. For the **Slice (Y axis) range of motion**, the slice stage would need to sweep the knife over the entire face of the specimen. The slice length must be long enough for the cut to reach steady-state, but not so long that the video recording file grows excessively large. The specimens used will be standard 8 mm cylinders (BEEM 00 size), which will be then machined down to a controlled geometry. For the **feed (X axis) range of motion**, the number of desired sections needs to be considered. The expected slice thickness is between 1 – 10  $\mu m$ , and for a given specimen, anywhere between 10-100 cutting videos are expected. On the high end of 10  $\mu m$  feed, 100 sections would require an X travel of 1 mm. As a practical consideration, some extra travel will be required to move the

knife into a convenient position for changeouts, therefore for now the X axis range of motion is set to also be 6.35 mm [0.25 in].

**Size constraints** are the overall dimensions of the instrument. The main requirement for this is that the instrument must fit around the video recording optics. Additionally, the machine should have unobstructed operator access to the cutting area, since the operator will be likely swapping out specimens and tools frequently.

**Max cutting speed** is the maximum speed at which the slice stage is expected to move. Similarly, **Min cutting speed** is the minimum speed at which the slice stage is expected to move. These values are based on observations of commonly used microtome cutting speeds; typical cutting speeds are around 1 mm/s, and slower for serial sectioning where high accuracy and precision are required.

**Stiffness** is the stiffness of the machine at the cutting zone, further subdivided into feed stiffness and slice stiffness. In either case, there are no guidelines in the microtome cutting literature for reasonable or effective values of the slice and feed stiffness (exploring this is a central motivation of this work). In the feed direction, the **feed stiffness** target is estimated as follows: Feed cutting loads of up to 1 N were expected at 10  $\mu\text{m}$  feed, and a target maximum allowable deflection of 10% is assigned. This requires a minimum stiffness of 1 N/ $\mu\text{m}$ . The system **slice stiffness** does not have an obvious constraint, as deflections in the slice direction are not in a sensitive direction. In theory, if the machine deflects a large amount only in the slice direction, this would not affect the section thickness so long as the cut finishes. In practice, it is very likely that excessive slice deflection will lead to some error in the feed direction due to coupling between the two axes, or to cyclical cutting behavior with the slice stiffness storing energy instead of using the input power to cut material. For this design, and in the absence of a

better model for slice-stiffness effects, a balanced stiffness is chosen matching the slice stiffness to the feed stiffness.

**Force resolution** is the minimum force increment the instrument can discriminate. In the literature, instrumented microtomes have been able to achieve  $mN$  resolution (for example, [39]).

**Maximum force** is the maximum load the instrument is expected to withstand. The expected cutting loads reviewed briefly in Section 4.3.1. At a  $1\text{ mm}$  width of cut, for a feed of  $1\ \mu\text{m}$ , projected cutting forces are a slice force of  $0.27\text{ N}$  and a feed force of  $-0.044\text{ N}$ . For a feed of  $10\ \mu\text{m}$  with the same cut width, the forces are expected to be a slice force of  $2.7\text{ N}$ , and a feed force of  $-0.44\text{ N}$ . Conservatively, this number can be placed at  $10\text{ N}$  for the slice force, and about  $2\text{ N}$  for the feed force.

**Force DOFs** are the number of degrees of freedom for force measurement; 2 would be the minimum, measuring in the slice and feed directions; adding in a 3<sup>rd</sup> sense direction would allow for improved diagnostics and troubleshooting (for example, a significant force component in the out-of-plane direction could indicate a misaligned knife).

### 4.3.3 Loads and thermal structural loop analysis

First-order sizing estimates for structural components were made by first estimating the length of the machine's structural loop. The length of the structural loop was estimated by summing the range of motion of each axis, and adding an 'overhead' factor based on an estimate of how much extra space would be needed to mount actuators, sensors, and structural components.

#### 4.3.3.1 Structural load-induced deflections

Structural components were initially sized by calculating a required stiffness, given the budgeted amount of allowable deflection and the applied cutting loads. An overall stiffness of

about  $10\text{ N}/\mu\text{m}$  was estimated to be required in the previous section. General sizing of components can begin using this stiffness. The required structure geometry is estimated by modeling the structural loop as a single cantilevered beam with the cutting loads acting on the end, and calculating different combinations of materials and cross-sectional areas that would achieve this stiffness. Figure 4.2 (a) and (b) are schematics of a planar microtome with two axes of motion; (a) shows the structural loop at its largest length when the specimen has the largest overhang, and (b) when the knife has moved through its full range of motion and the specimen is at its shortest length.

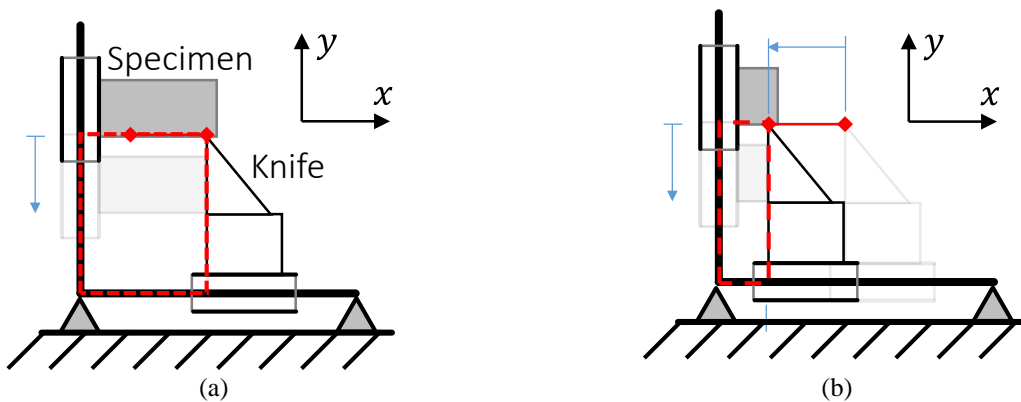


Figure 4.2: Schematic of the machine structural loop for a simple planar two-axis machine. (a) The structural loop (dashed red line) is longest at one extreme of the  $X$  range of motion and (b) is a minimum at the opposite end of the  $X$  range

The case shown in Figure 4.2 (a) is used to estimate structural requirements because it represents the worst-case for stiffness due to the longer structure required. Estimating the structural loop length begins with the required range of motion; if the bearings and support hardware were infinitely compact, the length of the structural loop in the worst case would be twice each axis' range of motion. In reality, the machine will require additional space for the components required to perform the required motions; this is added in as an additional per-axis length (Figure 4.3). For estimation purposes, this “overhead” length is taken as a multiple of each axis' range of motion.



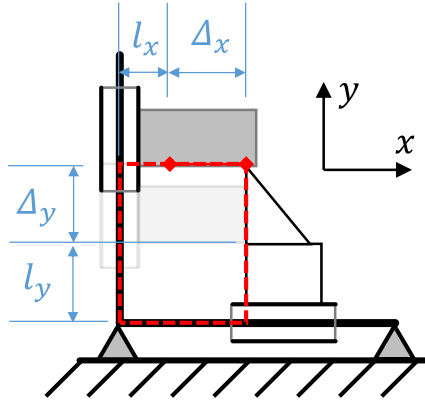


Figure 4.3: Estimating the structural loop length: if the machine can provide the required motion without adding any bulk, then the worst-case structural loop length would be the perimeter of the square formed by the two ranges of motion  $\Delta_x$  and  $\Delta_y$ ; however, the machine will need “overhead” space to include motion and structural components, and sensors. This overhead length is added to each range of motion  $l_x$  and  $l_y$ . For a first order estimate, the overhead lengths are estimated to be a multiple of the range of motion.

The estimate of the structural loop length is given by

$$l_{loop} = 2(\Delta_x + l_x) + 2(\Delta_y + l_y) \quad (4.1)$$

This was further simplified by assuming that the amount of overhead is a multiple  $n$  of the axis range of motion. The structural loop length can then be written as

$$l_{loop} = 2(\Delta_x + \Delta_y)(1 + n) \quad (4.2)$$

After establishing an estimated structural loop length (red dashed line in Figure 4.4(a)), several simple loop stiffness models are created. The cantilever beam model is made by ‘unfurling’ the structural loop, Figure 4.4(b) and (c), and calculating the deflections with the estimated input loads for different materials and cross-sections. A more refined estimate models the machine’s structural loop as a C-frame “hoop” and calculates the stiffness using Castigliano’s method. Given the deflection target, different materials and geometries are used to calculate the required dimensions needed to meet the target.

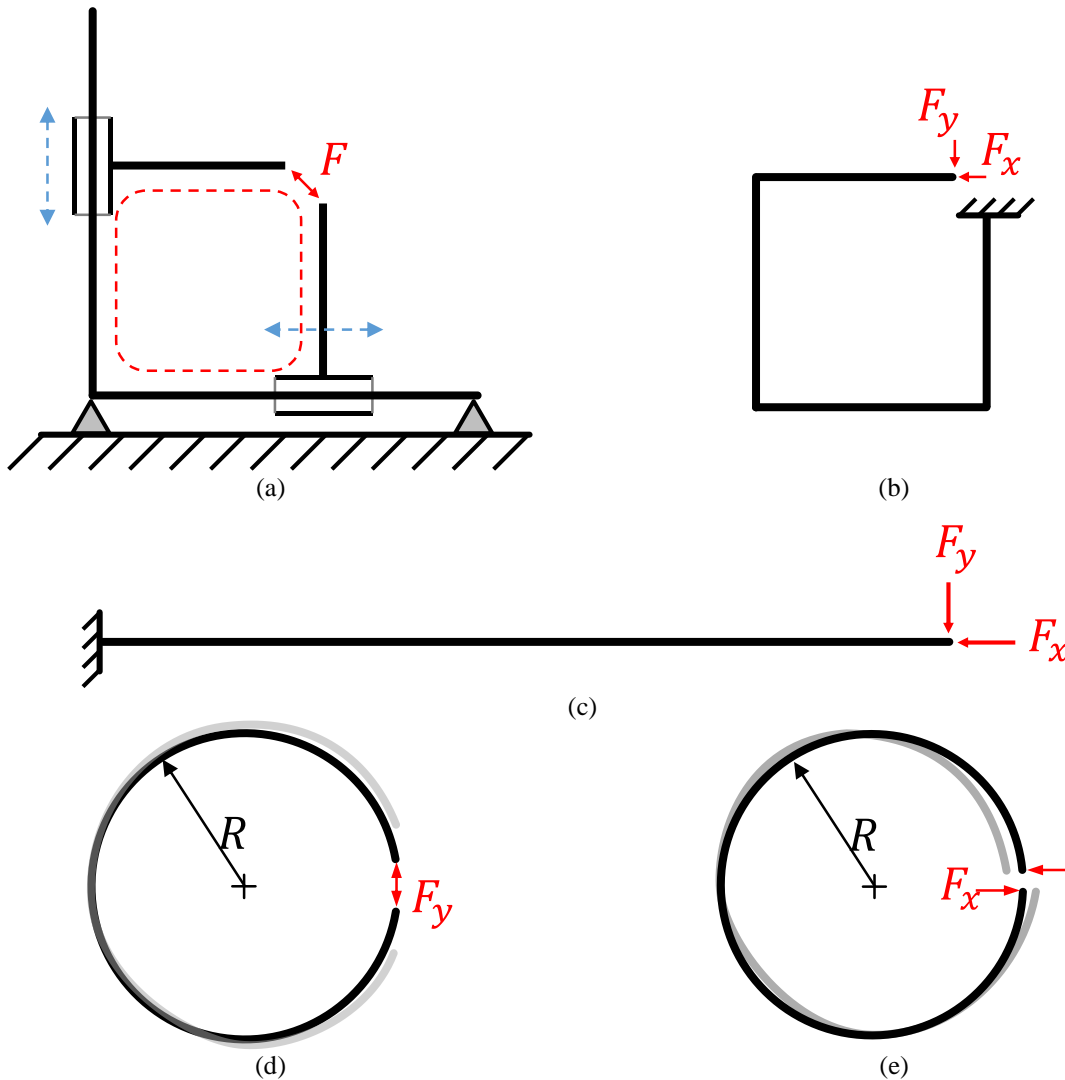


Figure 4.4: First-order estimation of the required stiffness. (a) Schematic of a general two-dimensional machine, with two axes of motion (dashed arrows). A process force is generated at the interaction point between the two axes, and this load must be carried by the machine’s structural loop (dashed red loop). (b) The elements in the structural loop can be modeled as a single continuous structure. (c) For a rough, conservative estimate of the required stiffness, the structure can be “unfurled” into a cantilever beam of equivalent length, and the deflections calculated. An alternate approach is to model the structural loop as an open ring, with forces attempting to spread the hoop open (d) or shear the hoop in-plane (e).

Calculation inputs and results are shown in Table 4-5. The calculations assume the structural elements are circular tubes, with a wall thickness of about 10% of the diameter (this gives a good parametric approximation to commonly available tube sizes; a lookup table with specific sizes could also be used). Calculations are performed for both aluminum and steel as the structural material. In addition to the equivalent cantilever beam and C-frame stiffness, the

calculation is also performed for a ‘closed’ frame, i.e., a machine frame with two C’s arranged front-to-front such that the structural loop is symmetric and the load path flows symmetrically through each C frame. This modeling assumes 10 mm of motion for both axes.

Table 4-5: First order sizing of structural components in aluminum and steel, with the equivalent cantilever beam model and open/closed C frames.

	Equivalent		C frame			
	Cantilevered beam		Open		Closed	
	Aluminum	Steel	Aluminum	Steel	Aluminum	Steel
<i>Required stiffness (N/μm)</i>				10		
<i>X travel (mm)</i>				10		
<i>Y travel (mm)</i>				10		
Wall thickness factor				10%		
Per-axis overhead factor				3		
<i>Loop structural length (mm)</i>				160		
<i>Required section inertia (mm<sup>4</sup>)</i>	1.98E05	6.83E04	7.52E03	2.59E03	2.45E4	1.30E03
<i>Equiv. beam tube diameter (mm)</i>	51	39	30	17	30	15
<i>Tube cross sectional area (mm<sup>2</sup>)</i>	739	434	144	85	260	60
<i>C frame radius (mm)</i>	-	-		25		

The required stiffness can be handily achieved with aluminum tubes of about 60 mm cross-section diameter with about 5 mm wall thickness. The same results in steel can be achieved with smaller tubes. This will be used as a starting point for the detailed structural design.

#### 4.3.3.2 Thermal error first-order analysis

The purpose of the first-order thermal analysis was to estimate thermal errors, given the approximate estimated size of the machine, candidate structural materials, and potential thermal loads, and assess if this will be a potential problem area to focus design effort on. The machine was to be used within an enclosure in a temperature-controlled lab; temperature variations were estimated at 1 °C. The analysis assumes that one arm of the structural loop is subjected to a thermal load, and expands in the sensitive direction (in this case, the direction that would change the feed of the cut, the X direction).

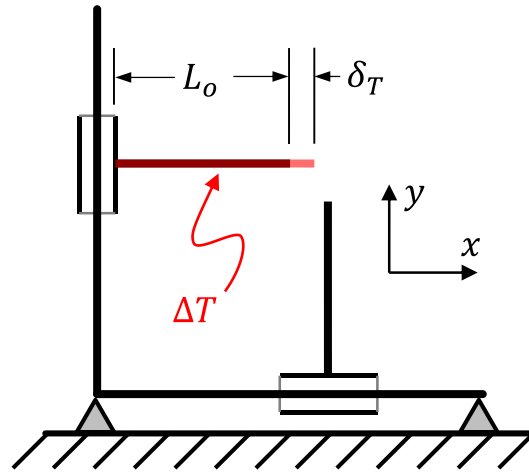


Figure 4.5: Errors in the sensitive direction introduced with thermal loading; for estimation it was assumed that in the worst case, only a part of the structure expands so that symmetry would not cancel out the thermal error.

The analysis results are presented in Table 4-6.

Table 4-6: First order thermal error analysis results with aluminum, steel, and Invar as candidate structural materials

Parameter	Unit	Value		
Loop structural length	mm	160		
Expansion length	mm	40		
Temperature variation	°C	1		
Material	-	Aluminum	Steel	Invar
CTE	$\frac{\mu m}{m \cdot ^\circ C}$	22	10	2
X expansion	$\mu m$	0.88	0.4	0.08

The results cautioned that care needed to be taken with thermal errors during design detailing – possible countermeasures include selecting a thermally insensitive structure layout, using low-expansion materials such as invar or super invar, tighter control of the thermal environment, and in general a better understanding of the thermal loadings of the system (for example, how much change could be expected over a given period of time).

## 4.4 Module design and analytical load-induced error model

The machine is subdivided into the following subsystems/modules:

- Force sensor
- Feed stage (X stage)
- Slice stage (Y stage)
- Workholder
- Knifeholder
- Goniometer and knife edge adjustment
- Optics
- Chassis
- Instrumentation

For each module, a design summary is presented, followed by a discussion of concept generation and selection, and its incorporation into the error model. Detailed module analysis is briefly discussed, and more detailed analysis can be found in the appendices.

An error budget in conjunction with an analytical error model are design tools used to quantitatively assess the amount of error individual subsystems are contributing to a point of interest, as a function of system inputs and design parameters (such as bearing spacing or structural characteristics). The analytical error model used in this work is based on a modified version of an error modeling spreadsheet developed by Professor A. H. Slocum and used in the MIT Mechanical Engineering course 2.70/2.77 Fundamentals of Precision Product Design. The coordinate systems used to model the machine compliances and load-induced errors are shown overlaid on a schematic of the machine in Figure 4.6, and the major compliance contributions modeled in each coordinate system are summarized in Table 4-7.

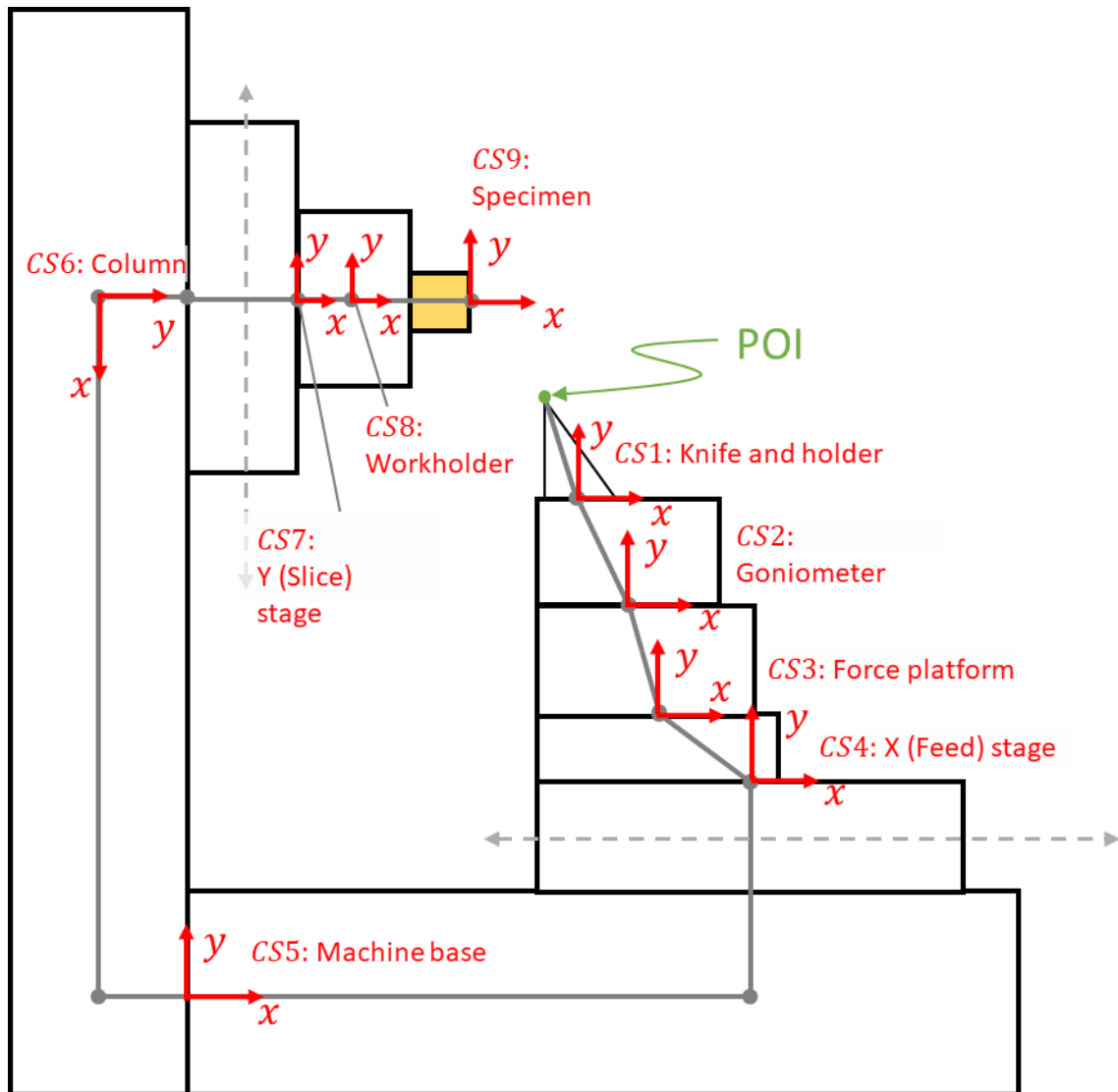


Figure 4.6: Schematic of machine structure with error modeling coordinate systems labeled. Detailed geometry is given in Appendix C

Table 4-7: List of coordinate systems used for load-induced error modeling, and the primary compliance modeled

Coordinate system (CS)	Compliance modeled
1	Knifeholder mount contacts
2	Goniometer contacts
3	Force sensor assembly
4	Feed stage and drive
5	Basebeam structure
6	Column structure
7	Y stage and drive
8	Vise contacts
9	Specimen

## 4.4.1 Force sensor

The force sensor must be sensitive enough to measure cutting forces at the required resolution, while minimizing its contributions to load-induced error (and, equivalently, to overall system compliance). In this design, three single-axis force sensors are mounted to a platform to sense forces in three directions (Figure 4.7); a thin sheet flexure absorbs shear loads, and shunts some of the force intended to be measured by the single-axis. The decision to build rather than buy a force sensor is discussed in Section 4.4.1.2. The sensor assembly is calibrated after being assembled onto the machine, with details of the calibration discussed in Section 4.9.1.

### 4.4.1.1 Force sensor functional requirements

Functional requirements were generated to guide force sensor selection (Table 4-8) and are discussed in-depth in this section.

Table 4-8: Functional requirements for force sensor

Functional requirement	Specification	Unit
Force resolution	1	$mN$
Repeatability	3	$mN$
Cross-talk (YX)	2.2	%
Accuracy	2.5	%
Stiffness	5	$N/\mu m$
# of directions	3	-
Drift	1	$mN/s$
Bandwidth	2500	$Hz$

Previous microtome cutting force dynamometers were based on strain-gauge technology, requiring compliant elements to deflect in order to generate a strain signal, though later designs such as in [39] used piezoelectric sensing elements to maintain high stiffness and high sensitivity. A tradeoff with piezoelectric sensors however is that the DC component of the signal decays due to charge leakage in the signal conditioning electronics (this is evident in [39] as a significant DC offset between the start and end of the cutting force signals).

The stiffness of the overall force sensor assembly will depend on the stiffness of the individual force sensors, their physical layout, and the load application point. The approach taken here was to select sensors that had high sensitivity and high stiffness, and create a draft force sensor assembly design; the stiffness characteristics of this design were then entered into the load-induced error model to assess how much error the draft force sensor design added to the system both via direct deflections and via sine errors. Similarly, it was important to minimize the overall dimensions of the force sensor assembly; keeping the sensor assembly compact reduces the structural loop length of the machine, which reduced sine error contributions from other downstream modules.

#### *4.4.1.2 Force sensor concept*

The decision to build a custom force sensor came only after searching for a commercially available appropriate sensor. The best combination was the Kistler Type 9119AA1 3-axis force platform paired with a Type 5080A signal conditioner; this combination would have met the force resolution specification of 1 *mN* in a compact package and with very high stiffness of around 1,000 *N/μm*. However, the combined cost of the sensor and signal conditioner was greater than what was budgeted for the entire instrument. Similar electrical performance could be attained at a fraction (about 0.17) of the cost by using 3 single-axis Type 9217 sensors with a Type 5073 signal conditioner, but the tradeoff would be a custom build and calibration, a larger physical package, and a lower stiffness (the 9217 has a stiffness of 15 *N/μm* along its sense axis). This was deemed a manageable tradeoff, and design work moved forward with the built-up sensor.



The inspiration for a high-stiffness multi-axis force sensor comes from previous work done in instrumented microtomy [61]. In this work the authors built a custom microtome workholder with two piezo force sensors built into the chuck.

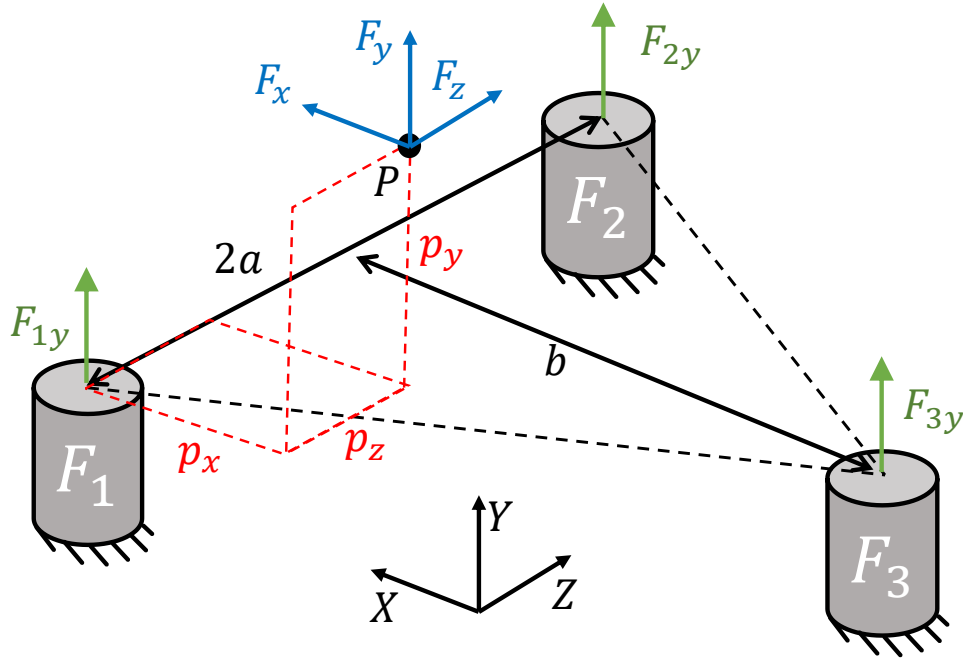


Figure 4.7: Schematic of 3-axis force sensor built up from three single-axis piezo force sensors – the tops of the cylinders are rigidly mounted to a sensing platform, and also to a sheet that shunts shear loads to ground (not shown). Each sensor can measure in the Y direction only.  $F_x$ ,  $F_y$ , and  $F_z$  are the applied loads at  $P$ , which in use will correspond to the knife edge.

An analytical formula for the sensor gain was derived using static equilibrium. The nominal sensor gain is given by

$$\begin{bmatrix} F_x \\ F_y \\ F_z \end{bmatrix} = \begin{bmatrix} \frac{p_x}{p_y} & \frac{p_x}{p_y} & \frac{p_x}{p_y} - \frac{b}{p_y} \\ -1 & -1 & -1 \\ -\frac{p_z}{p_y} & \frac{2a}{p_y} - \frac{p_z}{p_y} & \frac{a}{p_y} - \frac{p_z}{p_y} \end{bmatrix} \begin{bmatrix} F_{1y} \\ F_{2y} \\ F_{3y} \end{bmatrix} \quad (4.3)$$

In principle, the force sensor's gain could be set using this matrix computed from nominal part geometry, individual sensor gains, and loading point lever arms, but errors in each of these would erode the accuracy of the sensor; thus, the sensor should be calibrated before use. The analytical model was useful during the design process to trade off force sensor sensitivity with increases in deflection-related pitching errors due to the increasing moment arms, always with the intention of in-situ calibration. This sensor must be loaded at the same location at which it was calibrated (point P in the figure), otherwise the sensor gain will be different and error will be introduced. Such a design was far more economical than a pre-calibrated multi-axis piezo-based sensing platform and allows for introducing gain via the moment arms, at the cost of larger physical size and requiring calibration and associated hardware.

The sensors are designed to withstand a certain amount of bending and shearing loads, however a discussion with a Kistler representative convinced the author that extra robustness was required; the representative recounted that these sensors are very attractive due to their combination of low price and high sensitivity, but with the sensitivity comes a damage vulnerability tradeoff; they are frequently damaged due to their off-axis load limit being exceeded. Therefore it was decided to err on the side of robustness, and a shear force shunting mechanism was designed to isolate the sensors from bending and shear loads while minimally affecting the sensitivity of the sensor. A schematic of the force-shunting mechanism in two dimensions to demonstrate the concept is shown in Figure 4.8, and is discussed in detail in section C.3.3.

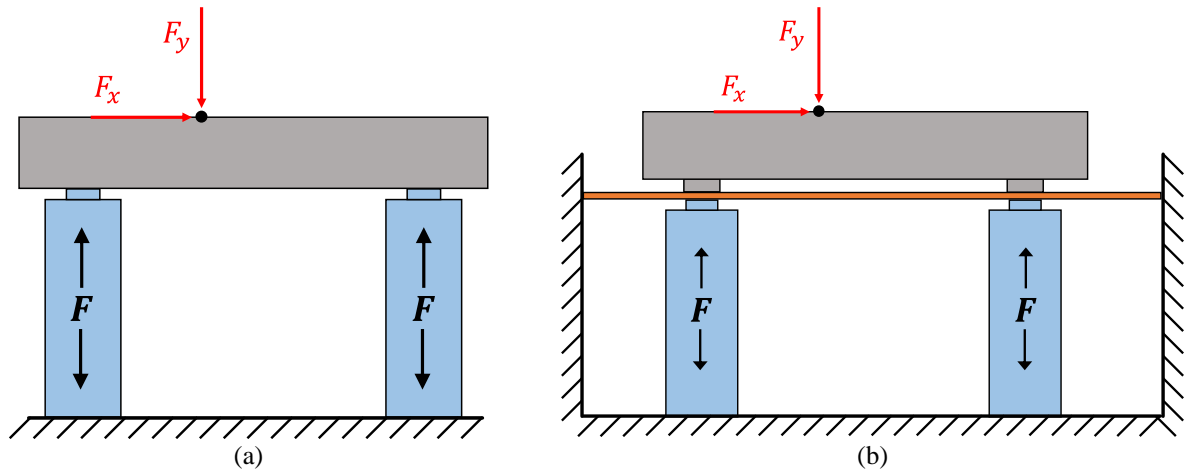


Figure 4.8: Schematic of force platform (a) with and (b) without a force shunting membrane. Each force sensor senses force along its longitudinal axis only, bending and shearing forces can damage the sensors and contribute to cross-talk noise. With the addition of a membrane which is compliant in its out-of-plane direction, but rigid in its in-plane direction, the shear and bending loads are shunted to ground with minimal decrease in sensitivity.

#### 4.4.1.3 Force sensor design analysis

The goal of the analysis is to establish a sensor gain matrix relating the applied forces at the loading point and the reaction loads measured at each sensor. This matrix can be used to calculate the sensitivity to errors in the load placement, and the effective stiffness of the force sensor at the load application point. The coordinate system and nomenclature used for the analysis is shown below in Figure 4.9.

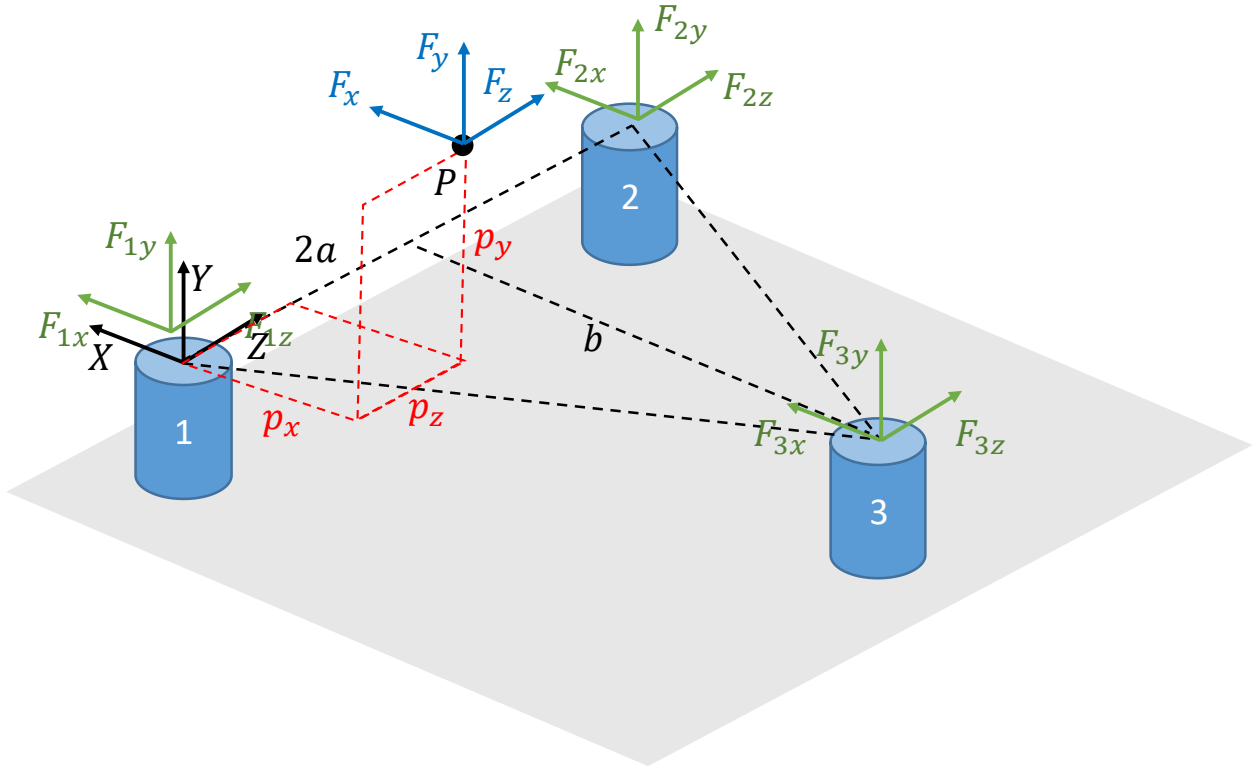


Figure 4.9: Coordinate system and variables used for force sensor assembly modeling

Input loads  $F_x, F_y, F_z$  in each Cartesian direction are applied at loading point  $P$ , and three reaction forces are generated at each of the three anchoring sites. The  $y$  component of each sensor is the sensed force component; other components are to be shunted to mechanical ground. Given the three force measurements  $F_{1y}, F_{2y}, F_{3y}$ , the loading forces  $F_x, F_y, F_z$  which satisfy equilibrium are calculated. The equilibrium conditions in all six degrees of freedom, consistent with the coordinate system in Figure 4.9 are shown below.

$$\Sigma F_x: F_{1x} + F_{2x} + F_{3x} + F_x = 0 \quad (4.1)$$

$$\Sigma F_y: F_{1y} + F_{2y} + F_{3y} + F_y = 0 \quad (4.2)$$

$$\Sigma F_z: F_{1z} + F_{2z} + F_{3z} + F_z = 0 \quad (4.3)$$

$$\Sigma M_x: -F_{2y}2a - F_{3y}a + F_z p_y - F_y p_z = 0 \quad (4.4)$$

$$\Sigma M_y: F_{2x}2a + F_{3x}a + F_x p_z + F_{3z}b + F_z p_x = 0 \quad (4.5)$$

$$\Sigma M_z: -F_{3y}b - F_x p_y - F_y p_x = 0 \quad (4.6)$$

After algebraic manipulation, the input loads can be written as

$$F_x = -\frac{1}{p_y}(F_{3y}b + F_y p_x) \quad (4.7)$$

$$F_y = -(F_{1y} + F_{2y} + F_{3y}) \quad (4.8)$$

$$F_z = \frac{1}{p_y}(F_y p_z + F_{3y}a + F_{2y}2a) \quad (4.9)$$

Equilibrium of the in-plane force components  $F_{xn}$  and  $F_{zn}$  is used to rewrite the force components as follows:

$$F_{1x} = -\frac{F_x}{3} - a \frac{(3F_z b - 9F_z p_x)}{6(3a^2 + b^2)} \quad (4.10)$$

$$F_{2x} = \frac{a(3F_z b - 9F_z p_x)}{6(3a^2 + b^2)} - \frac{F_x}{3} \quad (4.11)$$

$$F_{3x} = -\frac{F_x}{3} \quad (4.12)$$

$$F_{1z} = \frac{F_z b p_x - \frac{F_z b^2}{3}}{2(3a^2 + b^2)} - \frac{F_z}{3} \quad (4.13)$$

$$F_{2z} = \frac{F_z b p_x - \frac{F_z b^2}{3}}{2(3a^2 + b^2)} - \frac{F_z}{3} \quad (4.14)$$

$$F_{3z} = \frac{F_z(a^2 + b p_x)}{3a^2 + b^2} \quad (4.15)$$

The  $F_n$  components can be written as functions of the sensor forces  $F_{yn}$  as follows:

$$F_x = F_{3y} \left( \frac{p_x}{p_y} - \frac{b}{p_y} \right) + F_{1y} \frac{p_x}{p_y} + F_{2y} \frac{p_x}{p_y} \quad (4.16)$$

$$F_y = -(F_{1y} + F_{2y} + F_{3y}) \quad (4.17)$$

$$F_z = F_{2y} \left( \frac{2a}{p_y} - \frac{p_z}{p_y} \right) + F_{3y} \left( \frac{a}{p_y} - \frac{p_z}{p_y} \right) - F_{1y} \frac{p_z}{p_y} \quad (4.18)$$

Several ratios show up in the output, which can be used for design purposes. Some of these parameters are fixed in the sensor layout, and some are dependent on where the load is applied.

#### 4.4.1.4 Force sensor load-induced error contributions

The force sensor contributes to error at the final POI through its compliance deflection in two major ways, via direct translation superposition at the POI, and via rotation deflections propagating through the rest of the system. The compliance of the force sensor subassembly is modeled in-depth in Appendix C.3.2, and the results are used here to present the load-induced error contributions. The direct translation error refers to the load-induced deflection's translation directly adding to the POI final error, after transforming errors in the local CS (in this case CS3) to the reference CS (the final CS, CS8); in this case the two CS's are already in the same orientation so the transformation doesn't change the CS3 error vector, but in general this needs to be considered and is taken into account in the spreadsheet (e.g, the user must make sure that a  $\delta_x$  translation error corresponds to a  $\delta_x$  error at the POI in the reference coordinate system). With the input loads used at CS1, the final error contributions from the force sensor stiffness model in CS3 are given in Table 4-9.

Table 4-9: Force sensor (CS3) load-induced error contributions

<b>POI Error</b>	<b>Via direct translation (<i>nm</i>)</b>	<b>Via lever arm and <math>\epsilon_z</math> rotation (<i>nm</i>)</b>	<b>Total contribution (<i>nm</i>)</b>
$\delta_x$	-2	-8	-10
$\delta_y$	-5	-3	-8

#### 4.4.2 Feed stage

The feed stage subassembly is highlighted in Figure 4.10. The feed stage is responsible for positioning the knife to a cutting position and holding in place during a cut.

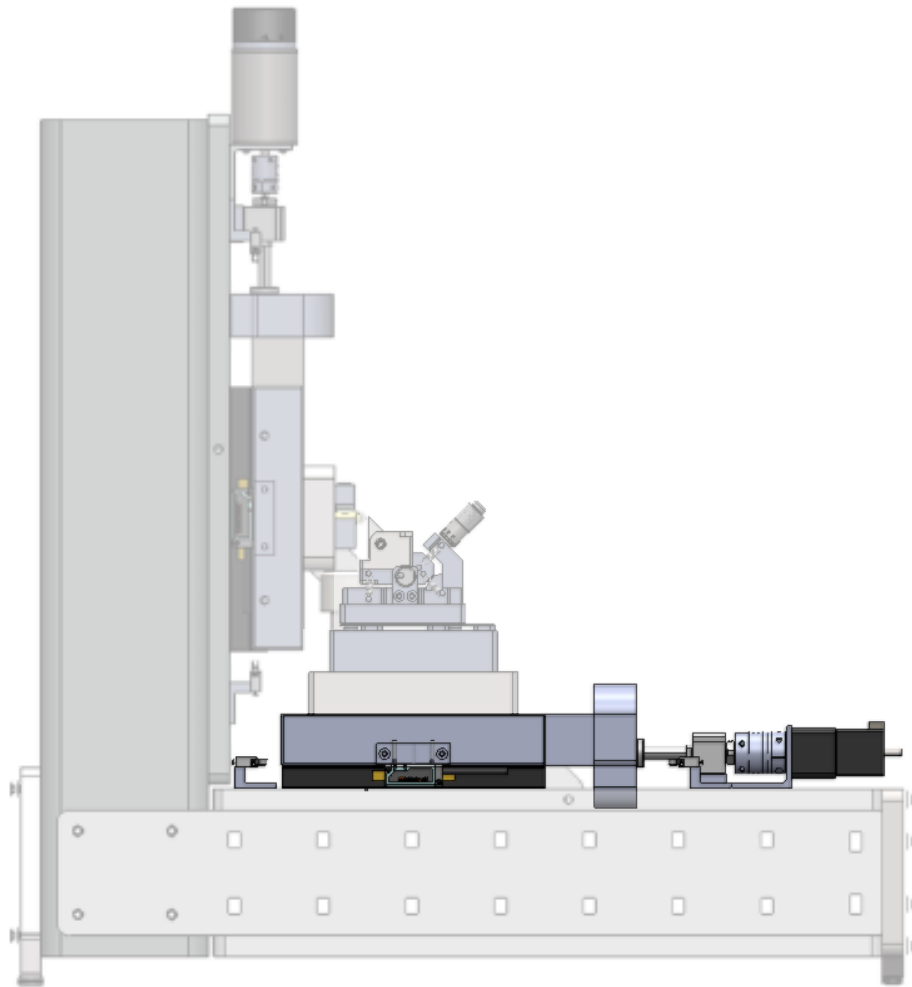


Figure 4.10: The feed stage subassembly, highlighted within the full assembly

Figure 4.11 is an annotated diagram showing the different components in the feed stage subassembly, and component descriptions are given in Table 4-10. A crossed-rollers linear stage provides linear motion with high stiffness against off-axis loading and pitching/yawing moments. The stage is driven by a 1 mm lead ballscrew and preloaded nut (THK BNK0801-3G0 screw with 115LC3Y nut), with a two-stage decoupling flexure to reduce precision and alignment requirements of the assembly and mitigate the effects of misalignment introduced during assembly (details of the decoupler design are provided in appendix D.3). The ballscrew is



supported by an angular contact bearing pair (THK EK6 support unit). The ballscrew is driven by a stepper motor with a harmonic gear reduction (Oriental Motor PK523HPB-H50S), with an off-the-shelf decoupler between the motor and ballscrew support bearing unit (Stock Drive Products S50MSCMA25H06H08).

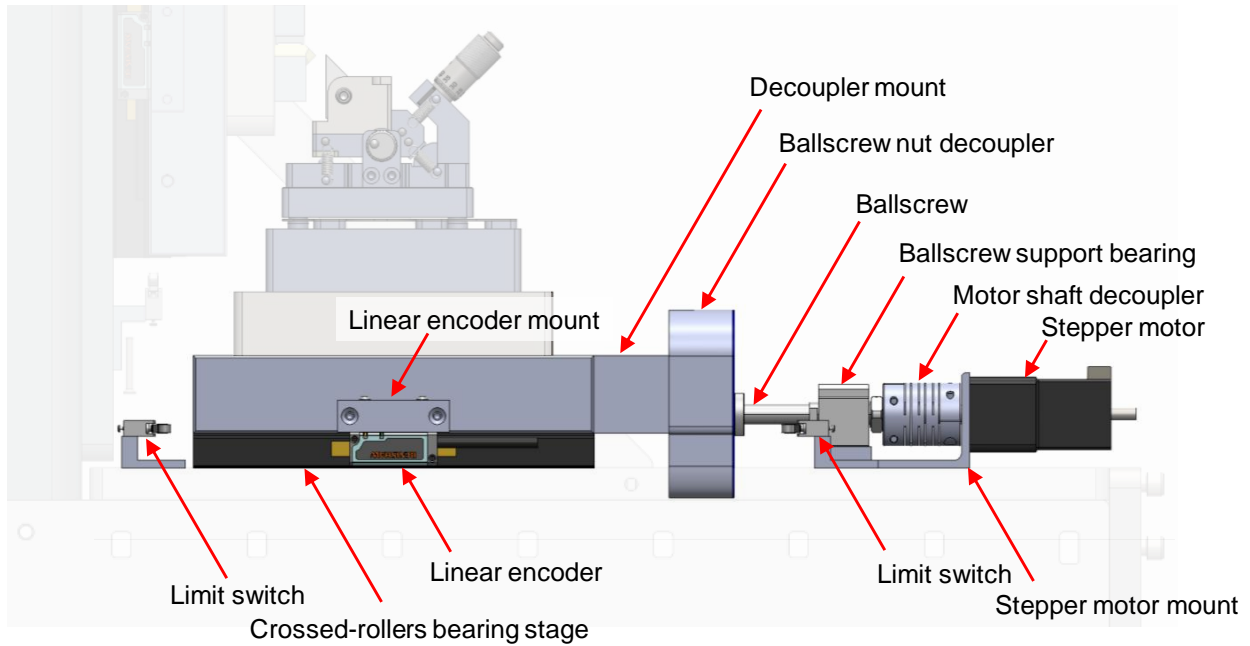


Figure 4.11: Feed stage subassembly with components labeled

Table 4-10: Feed stage component summary

Component	Description
Drive ballscrew	1 mm lead ballscrew
Ballscrew support	Angular contact bearing pair
Drive motor	Stepper motor with harmonic gear reduction stage
Stage	Crossed-roller bearing linear stage
Feedback encoder	Linear encoder and scale
Motor coupler	Allows some misalignment between motor and ballscrew
Limit switches	Provide end-of-travel signal to software; homing reference
Leadscrew decoupler	Mitigate effect of misalignment between leadscrew nut, linear stage

#### 4.4.2.1 Feed stage error contribution modeling

An initial draft design for the feed stage subsystem was selected based on the physical dimensions of the force sensing platform, whose dimensions were also in flux during design iteration. The THK bearing stage stiffness specifications were input into the error model, and the

amount of error at the POI was assessed. It was found that the bearing stage’s pitching stiffness was the primary bottleneck, and the bearing stage was upsized multiple times throughout the design process to reduce the error contribution from the feed stage. Details of the feed stage stiffness model are provided in Appendix C.1. The final calculated deflections using the VRU 6160 stage under the modeled input loads are given in Table 4-11

Table 4-11: Feed stage (CS4) load-induced error contributions to the POI

<b>POI Error</b>	<b>Via direct translation (<i>nm</i>)</b>	<b>Via lever arm and <math>\epsilon_z</math> rotation (<i>nm</i>)</b>	<b>Total contribution (<i>nm</i>)</b>
$\delta_x$	-3	-9	-12
$\delta_y$	-1	-2	-3

### 4.4.3 Slice stage

The slice stage is responsible for moving the specimen across the knife at a controlled and smooth velocity. The slice stage module is highlighted in Figure 4.12. An electrically commutated motor (Maxon 283867) drives a 1 *mm* lead ballscrew (THK BNK0801-3G0 screw with 115LC3Y nut and EK6 bearing support unit). The motor is commutated using a high-resolution rotary sine encoder (Heidenhain ERO 1480) configured for 4 million counts per revolution. Commutation and motor driving is performed with a Galil DMC31012 motion controller, which interpolates the encoder signal with a 16-bit interpolator. The drive motor is decoupled from the ballscrew via a standard motor shaft decoupler (Stock Drive Products S50MSCMA16H06H06). The ballscrew drives the crossed-roller bearing stage (VRU 6160) via a custom two-stage flexure decoupler (identical to the one used for the feed stage). Stage position is read out by linear encoders (Renishaw T1001 TONIC readhead with TI2000A interface) giving a 40 nm signal period with a resolution of 10 nm.

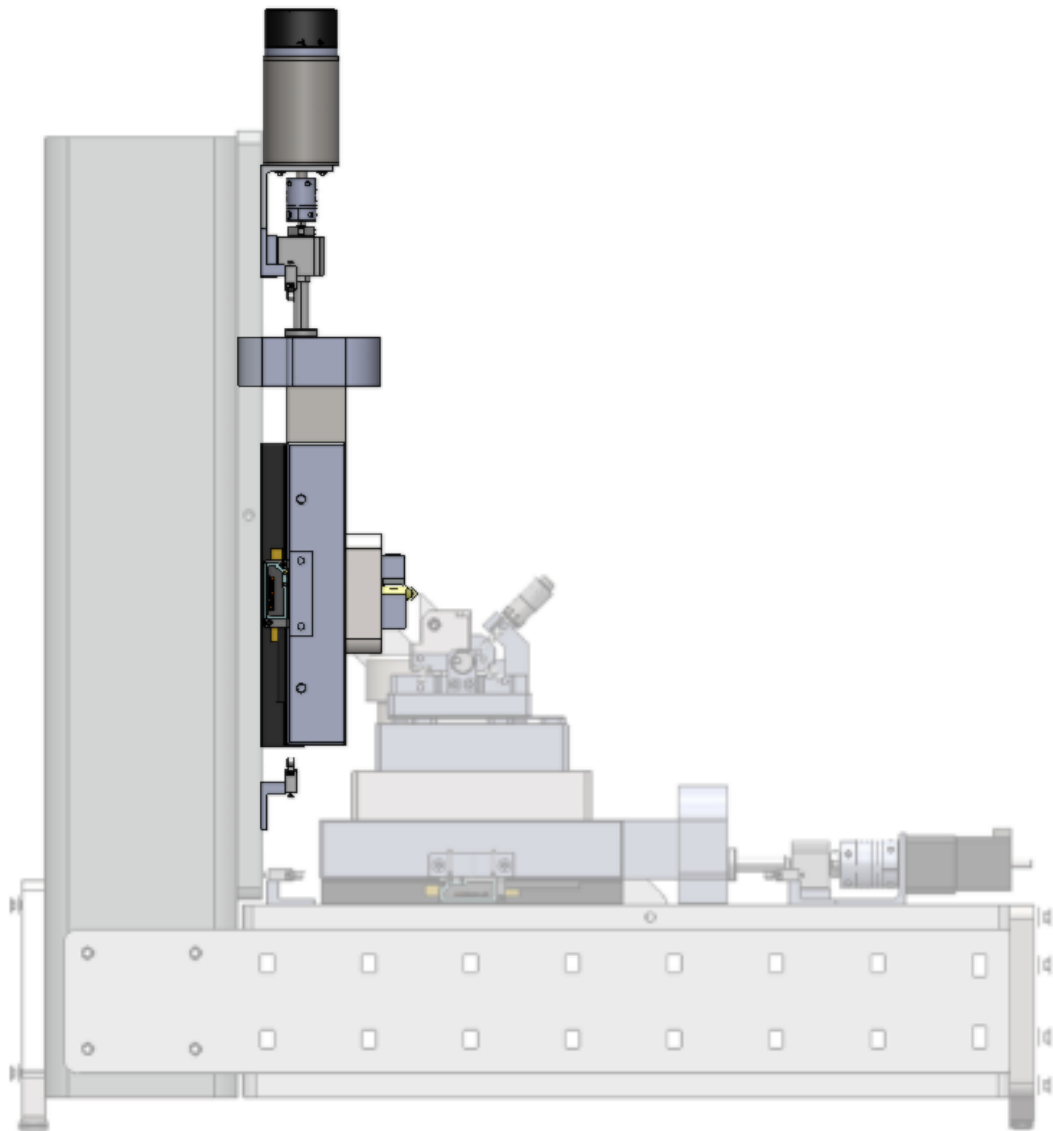


Figure 4.12: The slice stage subassembly, highlighted in the context of the full assembly

Figure 4.13 shows an annotated diagram of the slice stage component layout, and Table 4-12 provides brief descriptions for the components. A

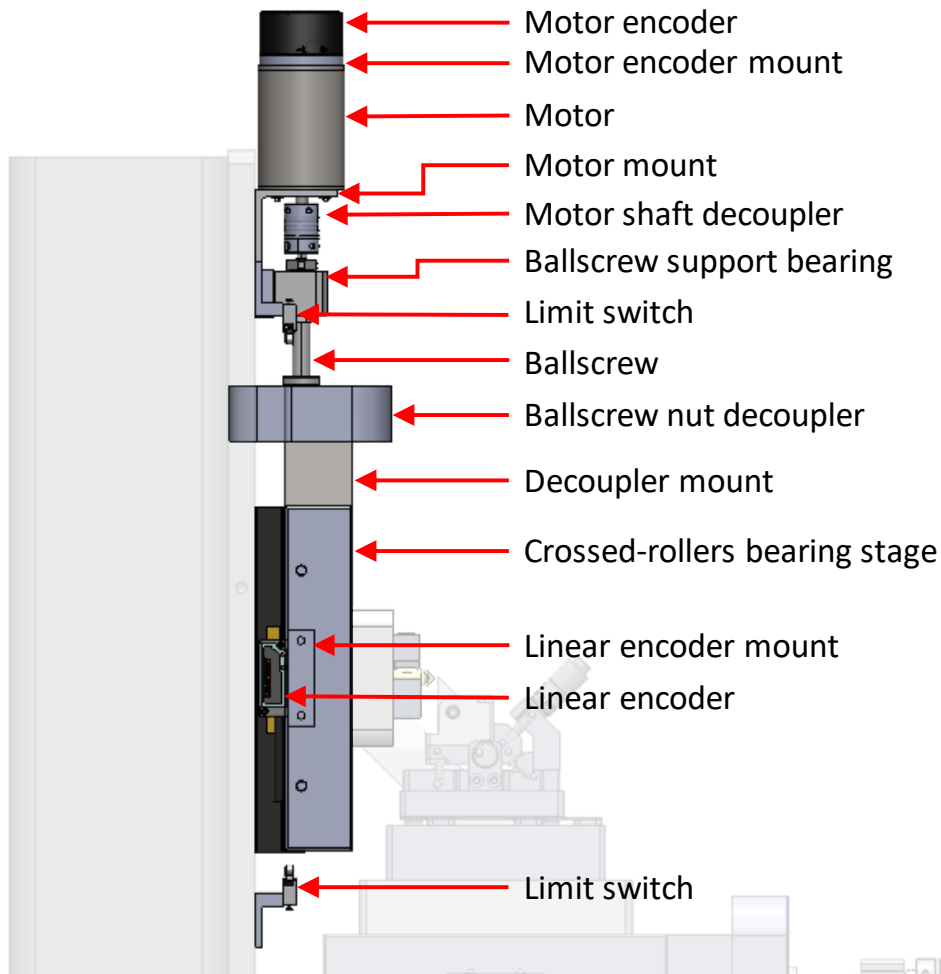


Figure 4.13: Annotated slice stage component diagram

Table 4-12: Slice stage component summary

<b>Component</b>	<b>Description</b>
Drive ballscrew	1 mm lead ballscrew
Ballscrew support	Angular contact bearing pair
Drive motor	Brushless, slotless motor
Linear stage	Crossed-roller bearing linear stage
Linear encoder	Provides linear positioning feedback
Motor coupling	Mitigate effect of misalignment between motor shaft, leadscrew end
Limit switches	Provide end-of-travel signal to software; homing reference
Rotary encoder	Provides motor feedback for brushless motor control
Leadscrew coupling	Mitigate effect of misalignment between leadscrew nut, linear stage

#### 4.4.3.1 Slice stage error contribution modeling

The results of the slice stage load-induced error modeling are summarized in Table 4-13, and details of the slice stage stiffness models are presented in C.5. Overall, the slice stage contributes negligible error in the feed direction. The slice stage has the same stiffness characteristics as the feed stage, but is rotated 90 degrees, presenting a higher stiffness in the feed direction. In addition, the lever arm between the slice stage and the final POI is smaller, so angular errors caused by stage pitching are smaller.

Table 4-13: Slice stage (CS7) load-induced error contributions

<b>POI Error</b>	<b>Via direct translation (<i>nm</i>)</b>	<b>Via lever arm and <math>\varepsilon_z</math> rotation (<i>nm</i>)</b>	<b>Total contribution (<i>nm</i>)</b>
$\delta_x$	-0.2	0.07	-0.13
$\delta_y$	-17	-3	-20

#### 4.4.4 Camera and optics module

The magnification optics subassembly provides microscope video recording of the cutting process and provides valuable qualitative information about the cutting process. Quantitative analysis is also possible via calibrated pixel measurement on post processed video frames. Figure 4.14 below highlights the optics subassembly within the context of the entire instrument.

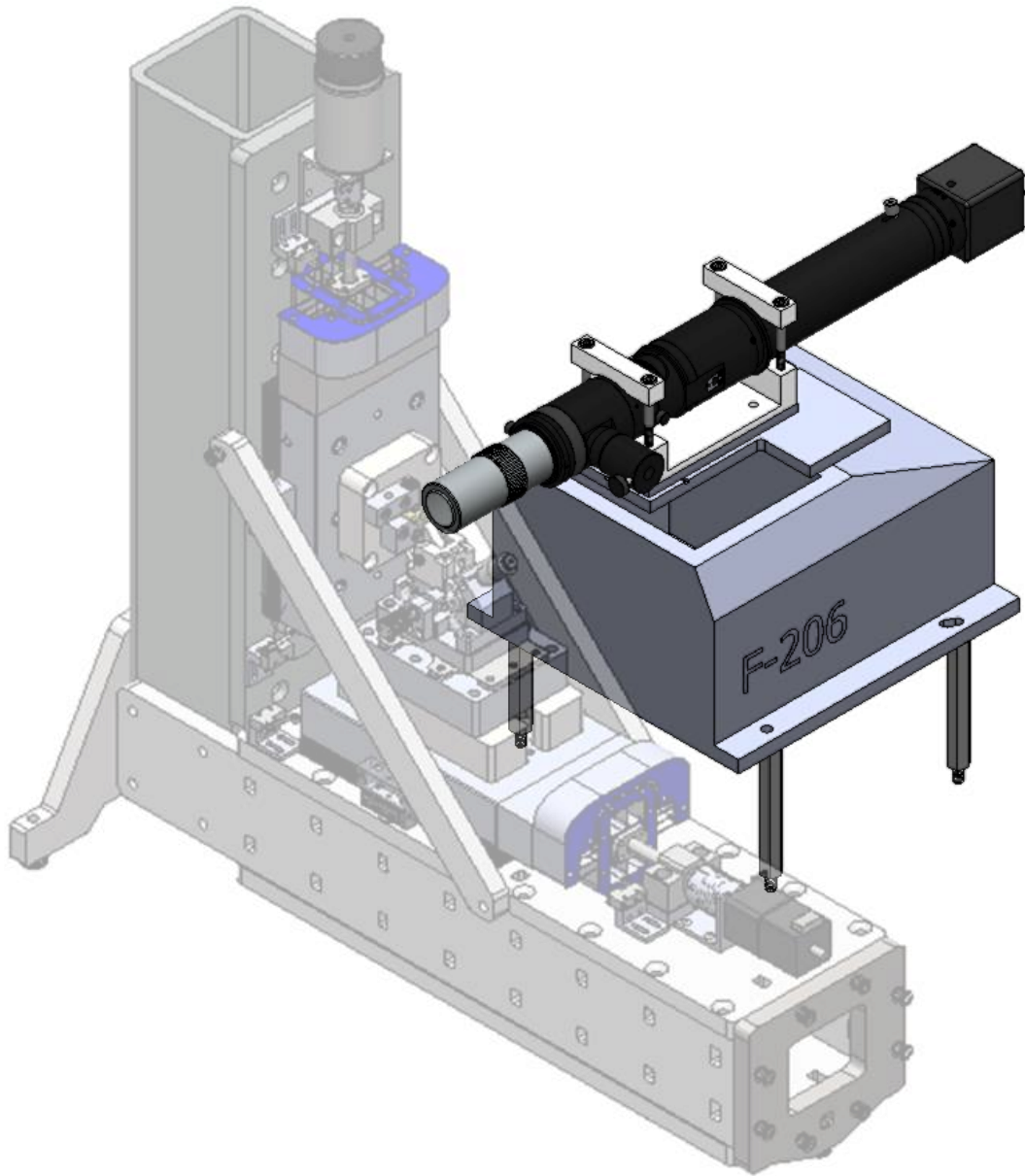


Figure 4.14: Optics subassembly. A long working distance objective lens mounted on a zoom lens and recorded at 170 frames per second. The entire optical column is mounted on a hexapod allowing fine positioning of the optical column.

For flexibility in choosing depth of field, field of view, and resolution, a modular zoom lens system was selected (Navitar 12x Ultrazoom), and to adjust the microscope position it is mounted on a Physik Instrumente F206 hexapod. The objective lenses used are a Mitutoyo 50x

and Motic 20x both with long working distances of ~10 mm; currently the 20x objective is in use for its larger depth of field. For recording video, a Lumenera LT225 monochrome CMOS camera shoots 170 fps at full HD (1920 x 1080 pixels).

Table 4-14 Configuration summary for optics

Parameter	Specification	Unit
Magnification	11.08x-133.25x	-
Resolution	1920x1080	px
Frame rate	170	frame/sec
Field of view	1 – 0.08	mm
Max resolution	0.7	um
Min Depth of field	1.6	um

A detailed configuration summary is shown in Figure 4.15 and Table 4-15

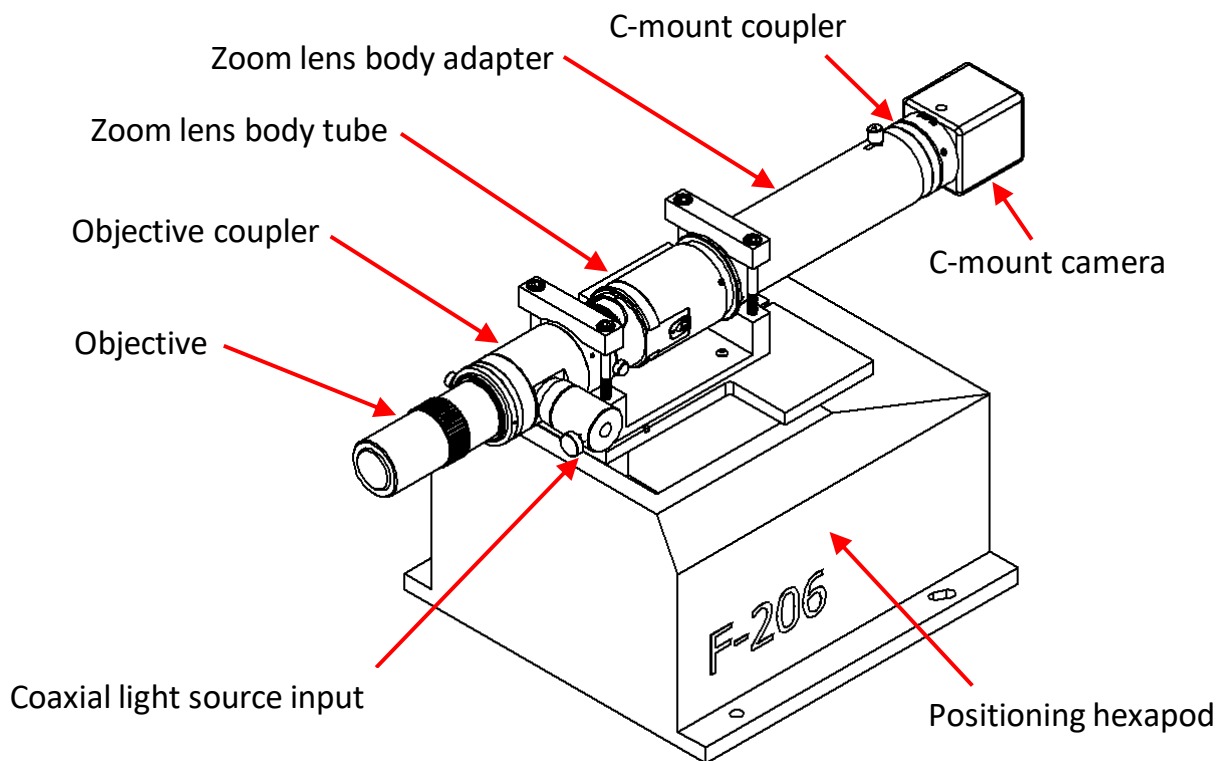


Figure 4.15: Annotated optical column components

Table 4-15: Optics subassembly system configuration

<b>Component</b>	<b>Description</b>	<b>Part number</b>
Objective	20X ELWD ICO	Navitar 1-62830
Zoom lens body	12x UltraZoom body tube	Navitar 1-50503D
Zoom lens body adapter	2.0x UltraZoom body adapter	Navitar 1-6030
C-mount coupler	Camera mount adapter	Navitar 1-6010
Camera	USB 3.0 170 fps HD camera	Lumenera LT225
Hexapod	Optical column positioning	Physik Instrumente F-206

#### **4.4.5 Knifeholder**

The knifeholder secures 45°-45°-90° triangle wedge knives 25.4 mm [1"] per side, standard for ultramicrotome glass knives. The force sensor design requires that the force is applied at the calibrated point, therefore it is necessary for the knife to repeat to the same position. The quasi-kinematic clamp allows for deterministic knife-clamp contact, avoiding the problem of knife rocking and compromised stiffness due to uncertainty in exactly where the knife clamp contacts the knife. Clamping pressure is applied via a swivel-tip ¼-20 setscrew to allow self-alignment of the clamping pad to the knife surface. The knife is lightly pressed against the locating contacts with a fingertip during tightening to ensure that the knife is properly seated during clamping.



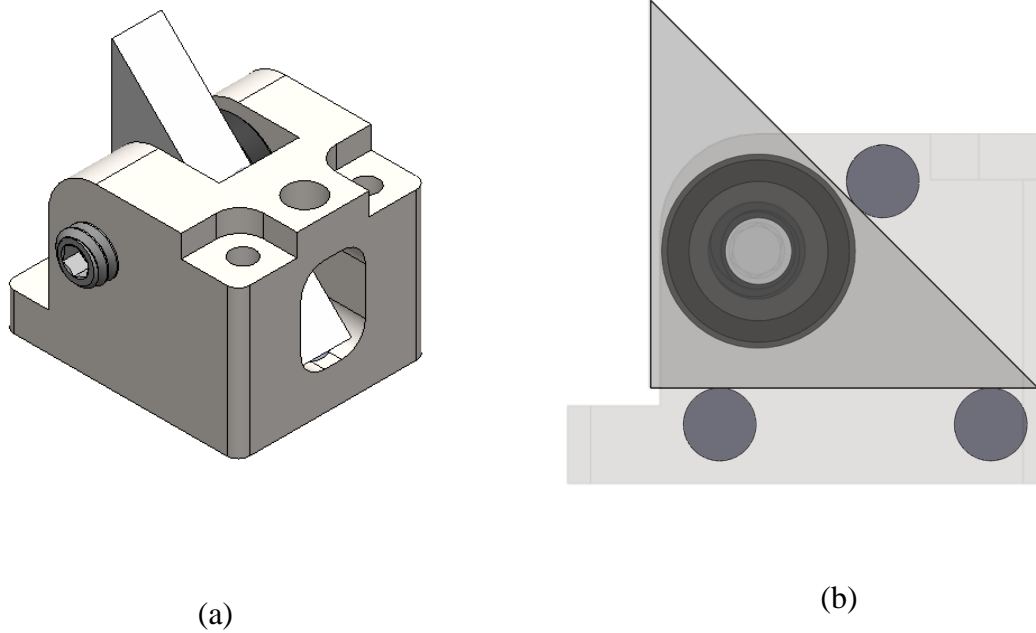


Figure 4.16: Quasi-kinematic knifeholder (a) full subassembly CAD model (b) quasi-kinematic contacts shown from side view

The knifeholder error contributions to the POI are given in Table 4-16. Note that for the first CS there are no additional errors due to pitching, since the POI is defined in CS1 and there is no lever arm to propagate the angular error through.

Table 4-16: Knifeholder (CS1) load-induced error contributions

<b>POI Error</b>	<b>Via direct translation (nm)</b>	<b>Via lever arm and <math>\varepsilon_z</math> rotation (nm)</b>	<b>Total contribution (nm)</b>
$\delta_x$	-35	0	-35
$\delta_y$	-16	0	-16

Details of the stiffness model are presented in Appendix C.1.

#### 4.4.6 Workholding

The workholding module supports the specimen and holds it in place firmly during cutting. The workholder subassembly CAD model is shown highlighted in Figure 4.17a with a

specimen in place. The workholder is designed to hold an 8 mm diameter cylindrical specimen, the BEEM 00 form factor used in microtomes.

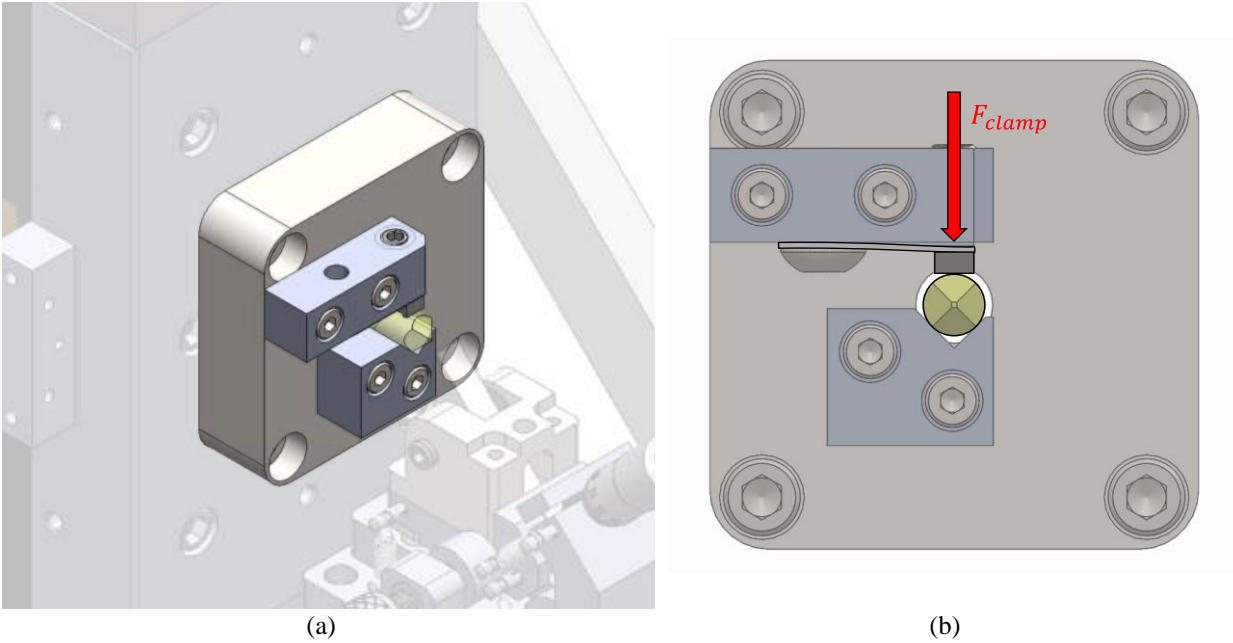


Figure 4.17: (a) Specimen workholding module CAD model. An 8 mm cylindrical specimen sits in a V-slot and is clamped with a setscrew from above. (b) Workholder clamping mechanism detail. A swivel-tip setscrew applies clamping pressure on the back side of a leaf spring and clamping pad.

The specimen sits in a V-groove and is clamped from above (Figure 4.18a); a clamping pad with an undercut in the middle transfers the clamping load to the front and the back of the specimen to provide improved pitching resistance (Figure 4.18b). The clamping pad's motion is guided by a blade flexure, and the pad is epoxied to the tip of the flexure (Figure 4.17b). The clamping force comes from a set-screw with a self-aligning swivel tip pressing against the backside of the flexure. Axial constraint is provided by friction, and by the clamping pad feet slightly digging in to the specimen.

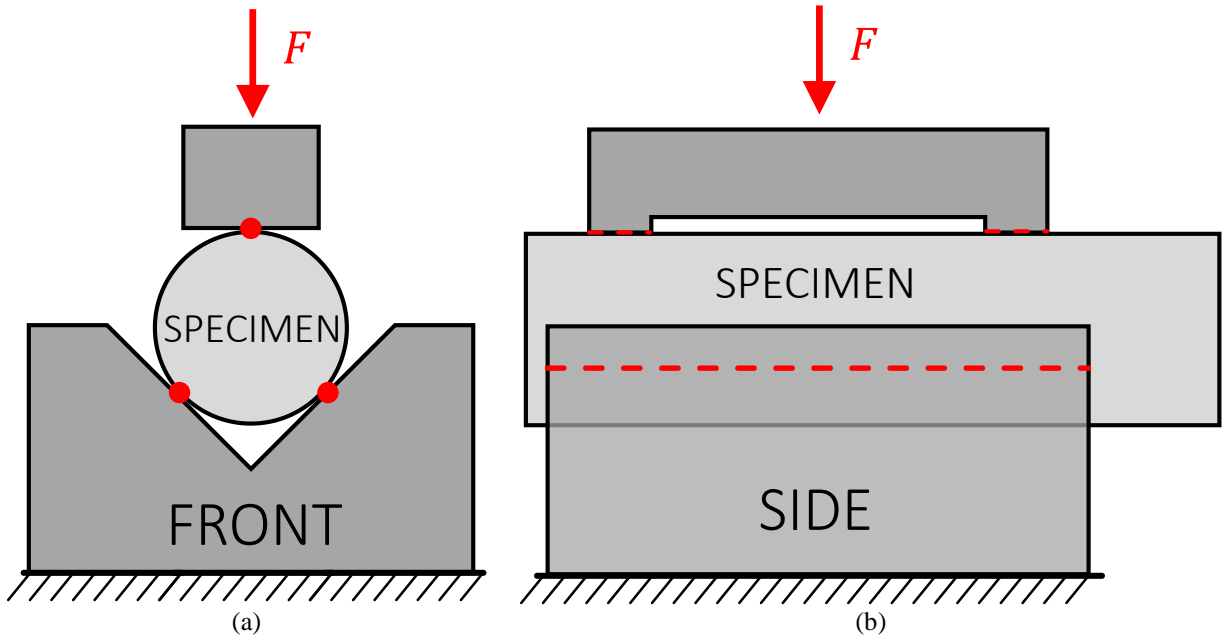


Figure 4.18: Schematic front and side views of workholding module with mounted specimen (a) Front view shows specimen nested in V-groove and three lines of contact (b) Side view, showing undercut on the top clamping pad. Clamping on the front and back of the specimen improves pitching resistance.

The detailed CS geometry definitions and compliance analysis is covered in Appendix C.8. The main stiffnesses modeled were the contact stiffnesses between the specimen and the vise, modeled as line contacts. The error contributions due to the workholder compliance is summarized in Table 4-17.

Table 4-17: Workholder (CS8) load-induced error contributions

POI Error	Via direct translation (nm)	Via lever arm and $\varepsilon_z$ rotation (nm)	Total contribution (nm)
$\delta_x$	16.3	14.4	30.7
$\delta_y$	355	-540	-185

#### 4.4.7 Goniometer and knife edge adjustment

A small amount of angle adjustment is typically necessary to add or remove clearance on the trailing edge of the cutting tool; in the worst case, the clearance face of the tool interferes with the freshly cut worksurface, resulting in increased feed forces pushing the tool out of the cut

and surface marring. In this work, a custom goniometer was designed that allowed for small (less than  $5^\circ$ ) rotations about the knife tip, while allowing knife edge translation to select a fresh part of the knife edge, and avoided any slop or backlash by using preloaded contacts. It is designed to be as compact as reasonably possible, and have well-defined stiffness characteristics via the preloaded contacts, which can be used for load-induced error modeling. The goniometer module is shown highlighted in the context of the full assembly in Figure 4.19.

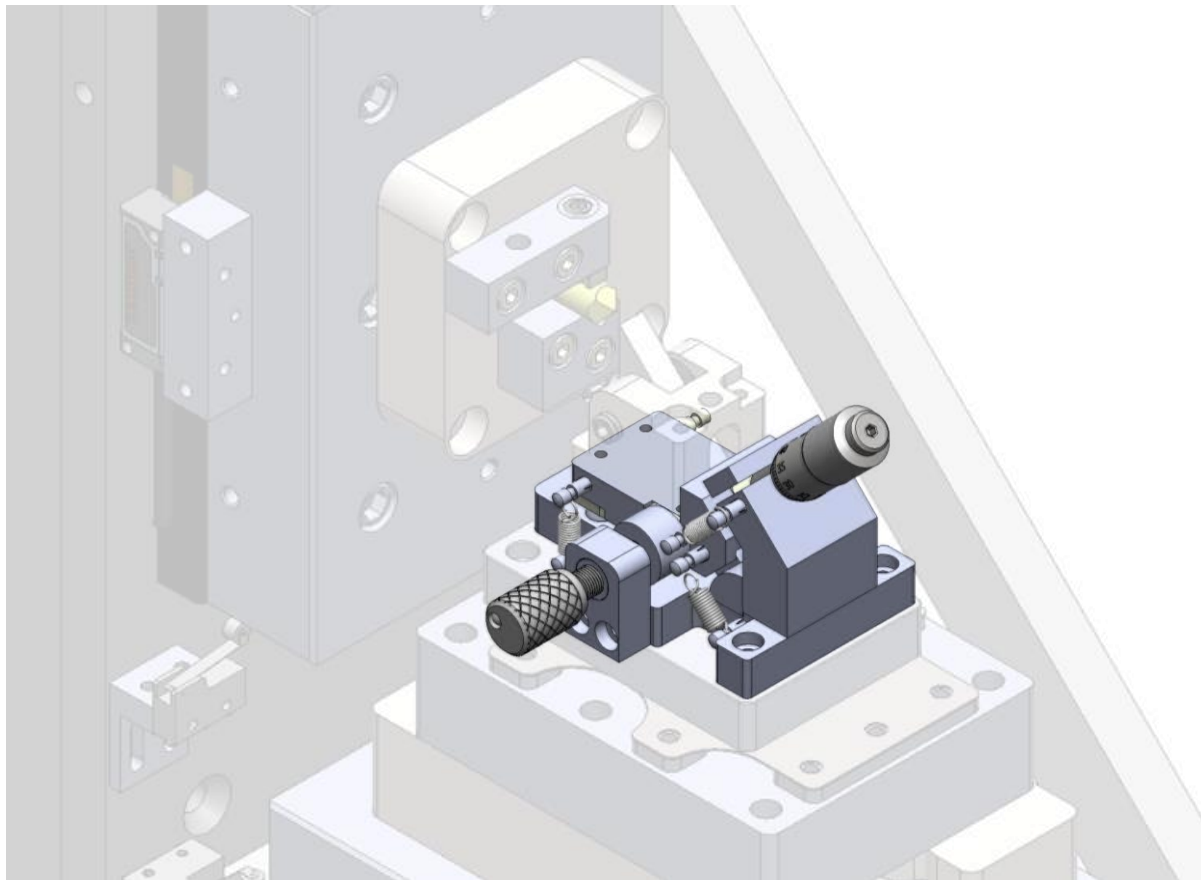


Figure 4.19: Goniometer and knife edge adjustment module, shown in full assembly

#### 4.4.7.1 *Goniometer concept*

The knife cutting edge represents the input to the force sensor platform, e.g., the loading point. With the microscope focused on the cutting tool edge, any angle adjustments should ideally cause rotation about the cutting tool tip, else adjusting the knife angle will both rotate the

tool and also translate it, cause the tool edge to move away from the intended loading point as well as the microscope's field of view. The force sensor accuracy relies on the input loads being placed at the same point at which the sensor was calibrated; deviations from this loading point will cause force measurement errors. Therefore, it was important that the goniometer's instant center of rotation and the cutting edge be coincident.

An exactly-constrained kinematic goniometer design is used to adjust the clearance angle of the knife while keeping the knife point at a particular point (Figure 4.20); this gives the designer flexibility to choose the physical layout of the goniometer, and to ensure backlash-free operation via preloaded kinematic contacts.

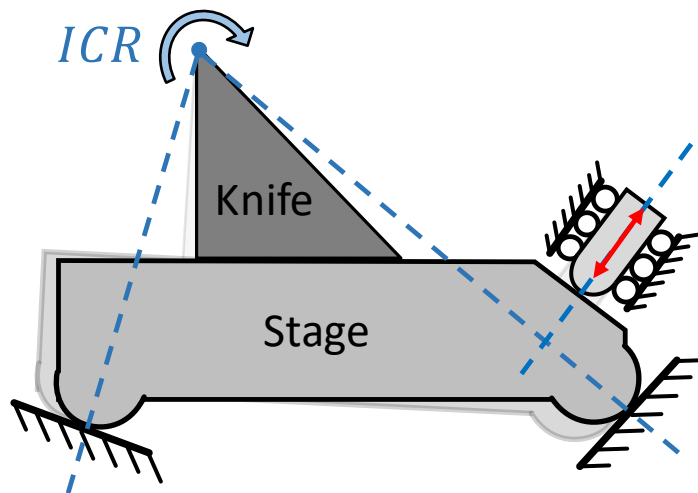


Figure 4.20: Kinematic goniometer concept, shown in 2D. The instant center of rotation of the rigid body lies at the intersection of the instantaneous surface normals; a third movable contact rotates the rigid body. Valid for small displacements. Friction is the main performance limiter for such a mechanism.

The module utilizes four ball-on-flat contacts and one cylinder-on-flat contact. A CAD model of the implementation is shown in Figure 4.21. Different knifeholders can be mounted on the goniometer stage, and the current knifeholder is designed to hold  $25.4\text{ mm} \times 25.4\text{ mm}$   $45^\circ$  degree wedges.

A kinematic design was chosen with one line contact and four point contacts. The point contacts were made of polished tungsten carbide epoxied into a steel body, except for the movable contact, which was the rounded tip of a micrometer head.

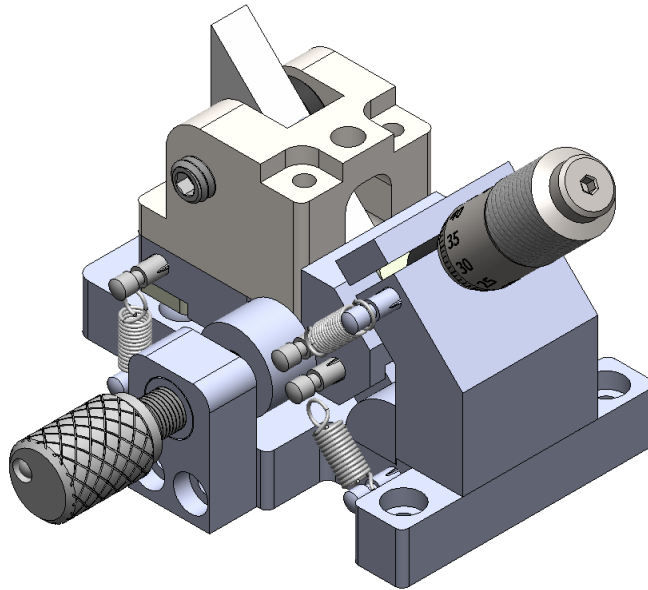


Figure 4.21: Detail of kinematic goniometer and knife edge adjustment module. A magnetically preloaded screw allows for edge translation to use different parts of the cutting edge. The other contacts are preloaded with extension springs. This design is good for a range of approximately 10 deg and is primarily limited by friction.

#### 4.4.7.2 *Error contribution*

The overall goniometer compliance matrix was arrived at via the stiffness transformation method and used to compute the load-induced error contributions; the results are summarized in below in Table 4-18, and details of the analysis are provided in Appendix C.2

Table 4-18: Goniometer (CS2) load-induced error contributions

<b>POI Error</b>	<b>Via direct translation (nm)</b>	<b>Via lever arm and <math>\epsilon_z</math> rotation (nm)</b>	<b>Total contribution (nm)</b>
$\delta_x$	0.2	-13.7	-13.5
$\delta_y$	-7	-6	-13

#### 4.4.7.3 Fabrication notes

Polished tungsten carbide flats were not available off-the-shelf in the desired geometries, so these were custom made starting from a bar of C2 tungsten carbide 1/16" thick, 1/2" wide, 6" long. The carbide hardness was rated Rockwell C80, making any kind of machining and shaping challenging, but feasible with the correct techniques and tools. The contacts were roughed by scoring the bar stock with a diamond scribe, clamping the stock in a vice, and breaking off pieces with pliers; they were shaped to final size using a rotary tool with diamond burr grinders. The contact surfaces were lapped to a mirror finish using diamond grit lapping film as recommended in a lapping and polishing handbook [62]; a progression of several grits of diamond lapping film were used to sequentially lap/polish the tungsten carbide contacts.

- 30 um
- 9 um
- 1 um
- 0.1 um

Lapping was accomplished by placing the lapping film on a clean granite surface plate, applying light viscosity cutting fluid on the lapping film to remove swarf, and sliding the contacts across the lapping film in a figure-eight pattern until scratches from the previous coarseness are removed. The contacts were periodically inspected under a microscope to observe progress. After final lapping, the contacts were taken to a white light interferometer (Zygo

NewWave 5000) and measured for surface roughness by measuring each contact at three sites (chosen at random). Measured roughness  $R_a$  values were between 4 and 12 *nm rms*. Figure 4.22a shows the three polished tungsten carbide contacts, with one of them crisply reflecting a nearby label. Figure 4.22b shows the contacts epoxied in the goniometer stage.

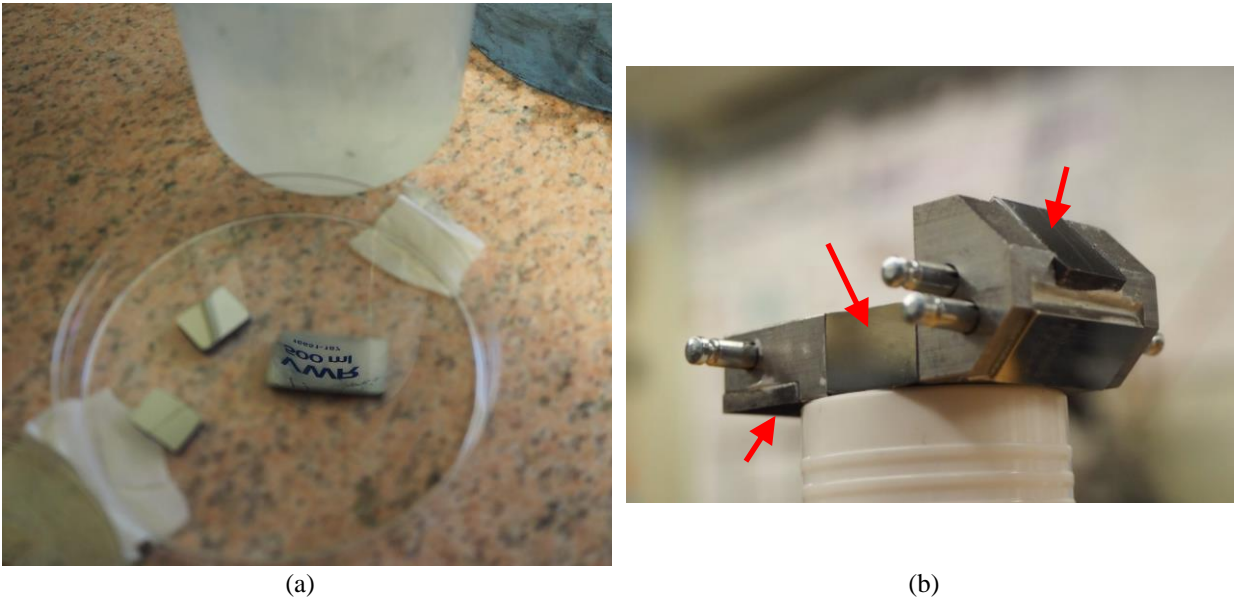


Figure 4.22: (a) Polished tungsten carbide contacts in plastic tray; a reflection off of a nearby container is visible in the reflection of one of the contacts (b) the polished tungsten carbide contacts (red arrows) mounted in the goniometer stage

#### 4.4.8 Chassis

The chassis is the platform on to which the other modules are mounted; its main functions are to provide enough structural rigidity to avoid introducing excessive deflection error from the cutting loads, to be thermally stable enough to avoid introducing excessive thermal errors, and to provide convenient mounting points for the other subassemblies. For modeling and fabrication purposes, the design is subdivided into two subassemblies: the basebeam module and the column module (Figure 4.23). The following sections discuss the subassemblies in detail.



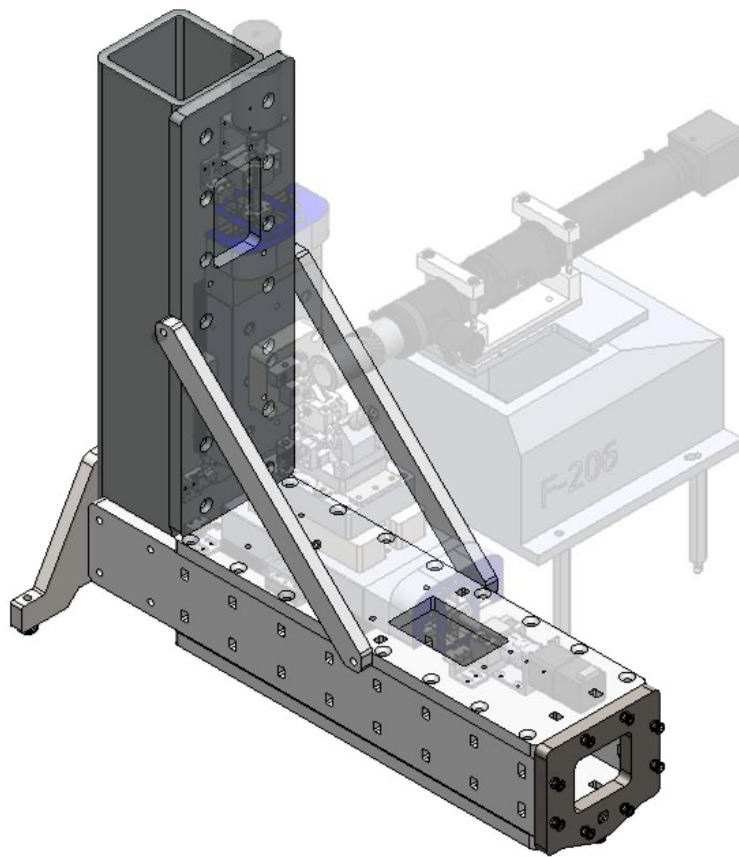


Figure 4.23: Instrumented cutter chassis subassembly, consisting of the basebeam and column subassemblies. Diagonal braces are shown, but were not used in the final assembly.

#### 4.4.8.1 *Base beam*

The base module is a built-up box beam made of  $\frac{1}{2}$ " thick Invar 36 plate. The box beam structure (i.e., a rectangular tube built up of individual plates) was selected based on its combination of good stiffness properties, material efficiency, relatively simple fabrication, and the ability to provide mounting surfaces for the other subassemblies. The box beam cross section is convenient for fabrication as it allows the Invar, which was more readily available in plate stock than in tube stock, to be cut out of plate stock on an abrasive waterjet and then assembled

into a box beam.

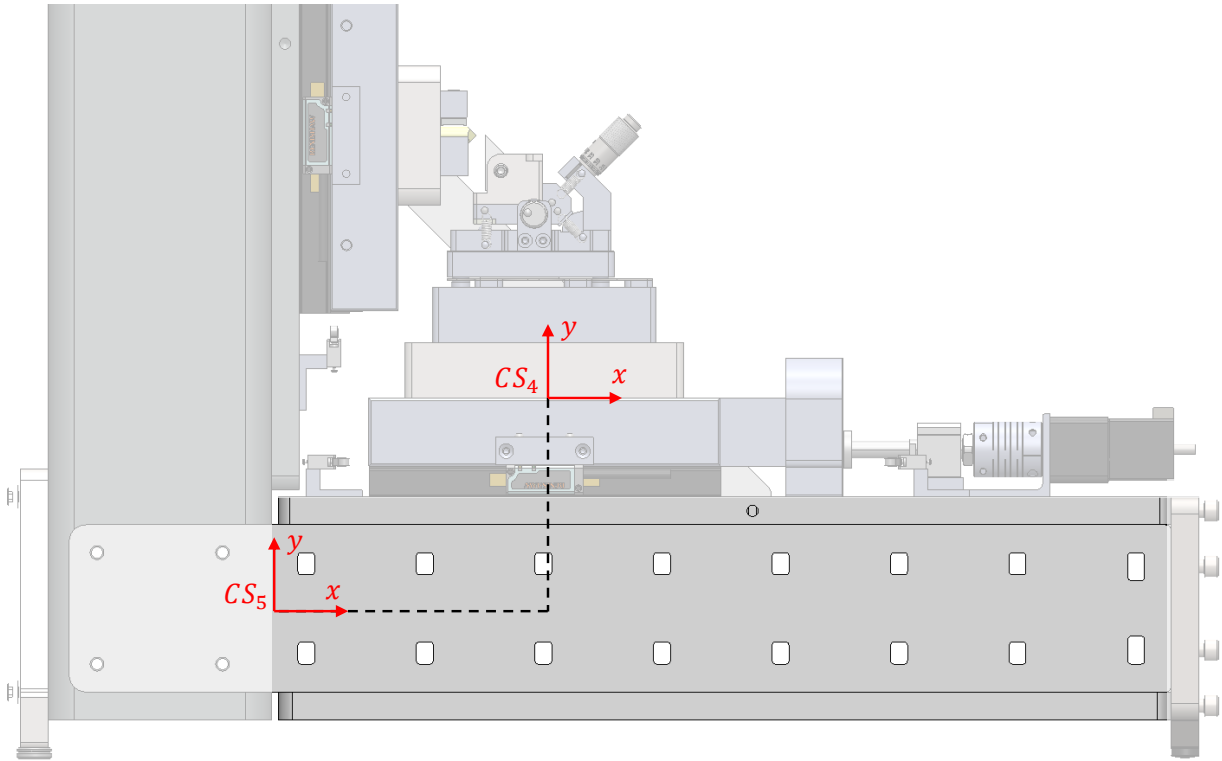


Figure 4.24: Error modeling coordinate systems used for the machine base – CS4 is taken as the point-of-interest for CS5

The decision to use Invar instead of steel (such as the A36 and cold-rolled steel used in the column) was made to provide additional thermal stability against temperature swings and gradients, although this is a partial solution since it was not feasible to make everything in the structural loop out of low-expansion alloy (for example, the bearing stages, the knife, and the specimen). If a uniform thermal expansion was expected, then it would introduce less error to have the whole structure made of a single material (e.g., the less expensive steel), assuming the structure expands freely and uniformly. However, this is not a reliable assumption, as the friction at the machine feet will provide resistance, and any expansion/contractions will be erratic and unpredictable. The low-expansion alloy reduces these errors by a factor of 10 compared to the

steel frame. An alternative design would have been to use a bearing which freely allows contraction/expansion of the machine frame while supporting the machine weight.

Under the expected thermal loads, the introduced errors due to temperature swings are expected to be insignificant. The machine was designed to be used within an enclosure, therefore drafts are not expected to contribute to temperature changes (except via the occasional opening of the enclosure door). Temperature measurements in the lab showed temperature changes with a peak-peak amplitude of  $2.2\text{ }^{\circ}\text{C}$  and a period of about 24 hours (86,400 s). If a triangular profile for the temperature swing is assumed, then for half the day the temperature is increasing towards the peak value, and the other half of the day the temperature is returning to the baseline. The rate of change is therefore approximately  $(2.2\text{ }^{\circ}\text{C} / 43,200\text{ s}) = 5.09\text{e-}5\text{ }^{\circ}\text{C/s}$ . A single cut, assuming a speed of  $1\text{ mm/s}$  over a (fairly large)  $10\text{ mm}$  cut, requires  $10\text{ s}$  to complete. The temperature change expected during this cut would be  $5.1\text{e-}4\text{ }^{\circ}\text{C}$ . This would induce a thermal expansion of  $(13\text{ }\mu\text{m}/^{\circ}\text{C})(0.085\text{ m})(5.1\text{e-}4\text{ }^{\circ}\text{C}) = 5.6\text{e-}4\text{ }\mu\text{m}$

The stiffness model of the basebeam used a compliance matrix which assumed an Euler-Bernoulli (E-B) beam, however as the design iterated towards its final value, the geometry of the basebeam moved away from what could be considered an E-B beam. The compliance matrix based on the E-B beam was still used, and a finite element analysis was performed to “spot check” the deflections introduced in CS5 by the basebeam deflections. The deflections were higher than predicted by the E-B compliance matrix, however the overall error contributions were still miniscule. The load-induced error contributions are given in Table 4-19. Details of the basebeam stiffness modeling are provided in Appendix C.5.

Table 4-19: Chassis basebeam (CS5) load-induced error contributions

<b>POI Error</b>	<b>Via direct translation (<i>nm</i>)</b>	<b>Via lever arm and <math>\epsilon_z</math> rotation (<i>nm</i>)</b>	<b>Total contribution (<i>nm</i>)</b>
$\delta_x$	-0.012	-4e-3	-0.016
$\delta_y$	-0.05	-1e-3	-0.05

#### 4.4.8.2 Column

The column subassembly is composed of a hot-rolled A36 steel tube with a steel plate bolted on to one face (Figure 4.25) to provide a platform for mounting the slice stage components; this also serves to provide additional bending stiffness.

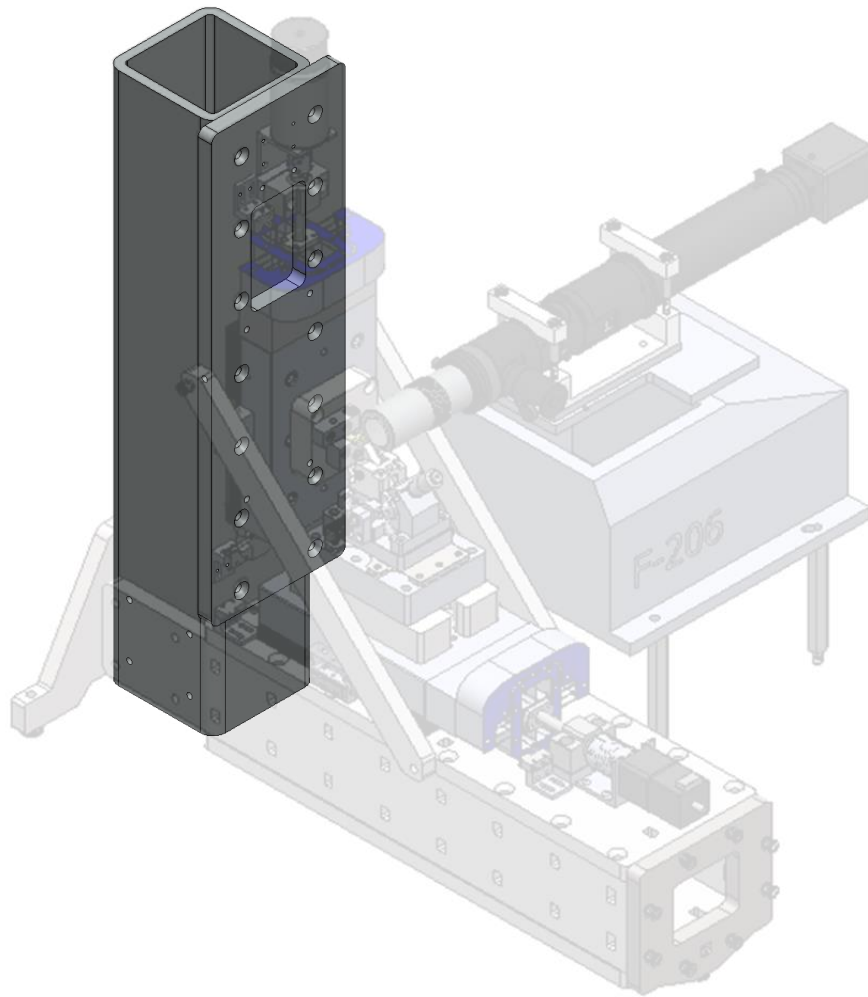


Figure 4.25: Chassis column subassembly

A summary of the load-induced errors contributed by chassis column deflections are presented in Table 4-20 and a figure of the coordinate system definitions used to compute the deflections is shown in Figure 4.26.

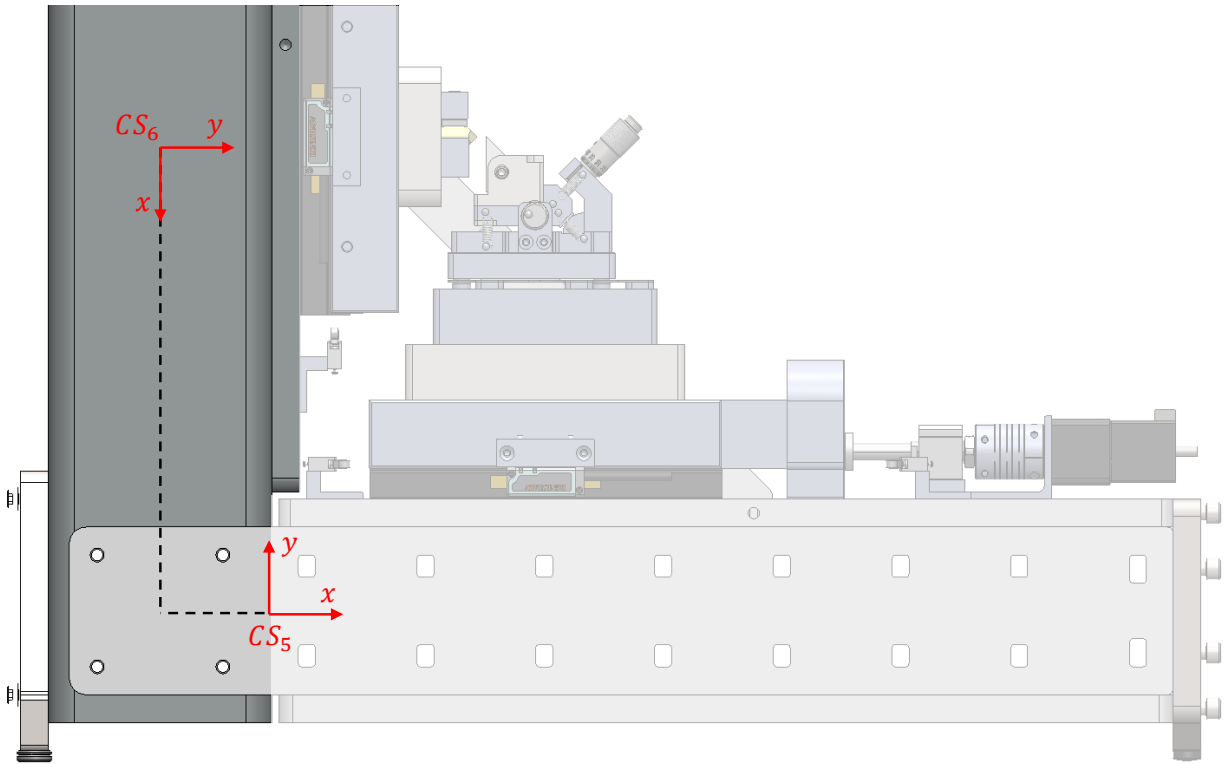


Figure 4.26: Error modeling coordinate systems between CS6 (Column) and CS5 (Basebeam)

Table 4-20: Chassis column (CS6) load-induced error contributions

<b>POI Error</b>	<b>Via direct translation (nm)</b>	<b>Via lever arm and <math>\epsilon_z</math> rotation (nm)</b>	<b>Total contribution (nm)</b>
$\delta_x$	-0.7	1.3	0.6
$\delta_y$	-0.4	-0.6	-1

Details of the load-induced error modeling, including geometry descriptions and compliance matrix information are given in appendix C.6.

## 4.5 Instrumentation and data acquisition hardware

The instrumentation used for data acquisition and the signal flow through the different system instrumentation modules is shown in Figure 4.27, with a more detailed list of the modules in Table 4-21.

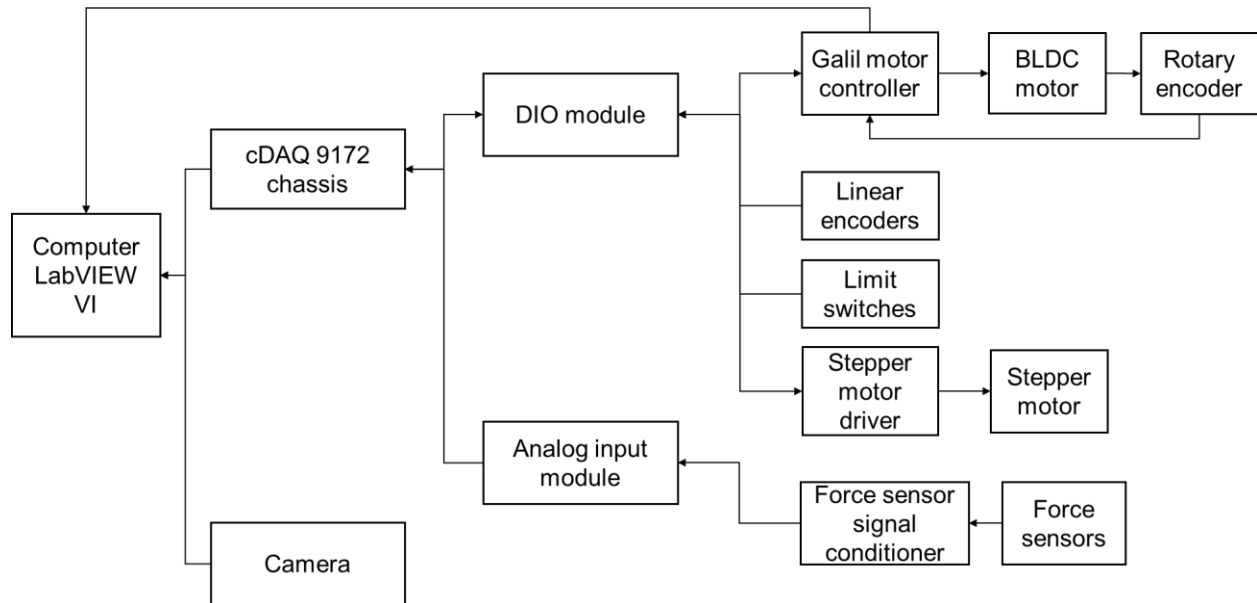


Figure 4.27: Instrumentation block diagram with arrows indicating signal flows

Table 4-21: Instrumentation summary

Instrumentation description	Make	Model
Instrumentation module chassis	National Instruments	9172
Digital I/O module	National Instruments	9401
24-bit analog input module	National Instruments	9239
Force sensor signal conditioner	Kistler	5073
Force sensors	Kistler	9217A
Camera	Lumenera	Lt225
Rotary encoder	Heidenhain	ERO 1480
Single-axis motor controller	Galil Motion Control	DMC-31012
Stepper motor driver	Oriental Motor	CRD5107HP
Limit switches	McMaster-Carr	7193K2
Linear encoder readhead	Renishaw	T1001
Linear encoder interface	Renishaw	TI2000A
Linear encoder tape	Renishaw	RGSZ20

The instrument is controlled via a single LabVIEW program (or “virtual instrument”, VI) running on a Dell Precision 7510 laptop running Microsoft Windows 7.

Three single-axis piezo sensors (Kistler 9217A) are arranged to provide a three-axis force measurement. The charge output from these sensors is converted into  $\pm 10 V$  signal voltages by a Kistler Type 5073 3-channel charge amplifier into, which is read into a National Instruments 9239 24-bit ADC.

Rotary position feedback for the brushless motor's sine commutation is provided by a Heidenhain ERO 1480 sine encoder, currently configured for 4,000,000 counts per revolution. This feedback is used by a Galil DMC31012 motion controller with 16-bit encoder interpolator to control a Maxon EC-Max 283867 brushless motor. Linear position feedback for both the slice and the feed stages is provided by Renishaw T1001 linear encoders with TI2000A interfaces, which give a 40 nm signal period and a max resolution of 10 nm (4X counting).

The limit switches on the machine have two functions, to provide an absolute reference for homing capability and to prevent the machine from overrunning its travel limit and potentially damaging something. The limit switch wiring is configured such that if the switches ever lose connectivity (such as to a cut wire or faulty connection) the output will be triggered, which will be registered as a limit switch being tripped, and the machine will not run without some kind of intervention, alerting the operator to a fault. During normal operation (switch is not tripped), current flows through the circuit and the signal will be low; when the switch is tripped, the switch disconnects and current flow ceases; the circuit output becomes high.

## **4.6 Fabrication and assembly**

This section covers the feeds and speeds used for the different machining operations in Invar 36, followed by the general the cutting instrument assembly procedure.



### 4.6.1 Invar machining

The custom-machined parts were CNC machined without incident. Of special interest, however, was the Invar 36 machining – as a nickel-iron alloy, this material work-hardens significantly during cutting and can be a challenge to machine.

Parts were roughed from the Invar 36 raw stock (½” hot rolled plate, Ed Fagan Inc) on a waterjet cutter (OMAX 2652) using the OMAX pre-sets for Invar. Feed and speed selections for the different machining operations were set based on recommendations provided by the Invar manufacturer (Ed Fagan, Inc.), and machining was immediately successful with the recommendations. Invar 36 feeds and speeds are given in Table 4-22. A vertical machining center (Haas VF2 VMC) was used to mill the parts down to final size and to drill and countersink holes. Milling the parts down to final size was done using a 5-tooth 3” face mill with Kennametal TiAlN PVD coated carbide inserts (HNPJ0604ANSNGD KC725M grade). Threaded holes were tapped on a smaller bed mill (Prototrak RX2) using a self-reversing tapping head (Tapmatic) and cutting fluid designed for work-hardening materials.

Table 4-22: Feeds and speeds used for Invar 36 machining operations

Operation	Tool Material	Coating	Feed (U.S.)	Feed (Metric)	Speed (U.S.)	Speed (Metric)
Milling	Carbide	TiAlN	0.006 in/tooth	153 $\mu$ m/tooth	100 sfpm	30.5 m/min
Drilling	HSS	TiN	0.002 in/rev	51 $\mu$ m/rev	40 sfpm	12.2 m/min
Countersinking	HSS	TiN	0.002 in/rev	51 $\mu$ m/rev	40 sfpm	12.2 m/min
Tapping	HSS	TiN	manual	manual	11 sfpm	3.4 m/min

### 4.6.2 Instrument assembly

The cutting instrument was assembled on a granite slab reference surface, using a precision Starrett square, 1-2-3/2-4-6 blocks, and a set of gauge blocks (Shars Tool Co) to align parts as needed. For the chassis frame parts prior to assembly, the bolted joint contact surface

areas around drilled holes were scraped down with a carbide scraping tool (A&W Precision Anderson scraper) to remove the high spot “mound” left around the drill site until the scraping tool removed material uniformly with the area around the hole. Screw torques were controlled with a torque wrench (CDI Torque Products 1501MRRH) and a torque driver (CDI Torque Products 61NSM) for smaller screws and torques.

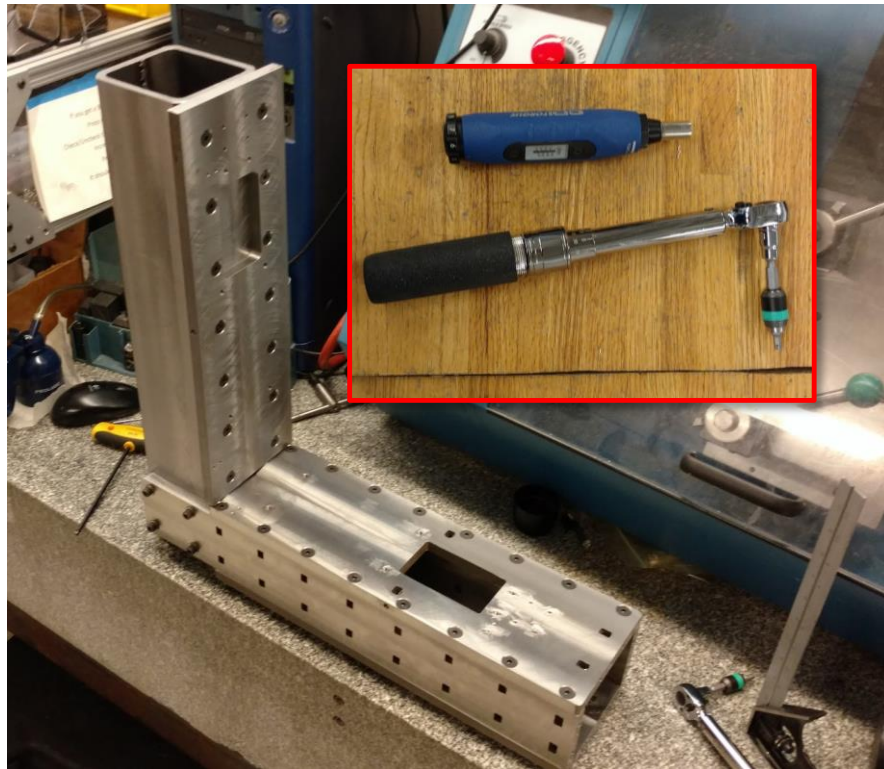


Figure 4.28: Assembled cutting instrument column and basebeam. *Inset:* torque screwdriver and torque wrenches used for assembly. Starrett square visible in foreground.

Bolted joints were generally tightened in three stages, each time in a star pattern; first to snug, then to half of the final torque, then to full torque. Bolt torques were selected based on 75% of proof load for socket head cap screws (SHCS) meeting the ASTM A574 standard, and similarly for metric Class 12.9 fasteners meeting DIN 912 and ISO 4762 standards. All screws were utilized without additional lubrication unless otherwise indicated. Bolt torques for different bolt sizes and types are given in Table 4-23.

Table 4-23: Bolted joint bolt torque table

<b>Bolt size</b>	<b>Bolt type</b>	<b>Torque (Metric) (N-m)</b>	<b>Torque (U.S.) (in-lbf)</b>
¼-20	SHCS, FHCS	17	150
M3	SHCS	2	18
M3	BHCS	0.8	7.1
M4	SHCS	5.2	46
M5	SHCS	8.5	75
M6	SHCS	16.3	144

The Kistler force sensors were torqued using manufacturer-recommended tightening torques of 2 N-m [17.7 in-lbf] for the M10 mounting thread and 0.1 N-m [0.89 in-lbf] for the M3 force sensor input.

## 4.7 Instrument control software

The instrument is controlled via a LabVIEW 2017 Virtual Instrument (VI). The code structure is composed of multiple independent loops running in parallel, with queues used to send messages between the loops. The VI runs on a Dell Precision 7510 laptop running Microsoft Windows 7 (Figure 4.29). The control VI runs five parallel loops running independently and communicating with one another via message queues; loop responsibilities are summarized in Table 4-24.

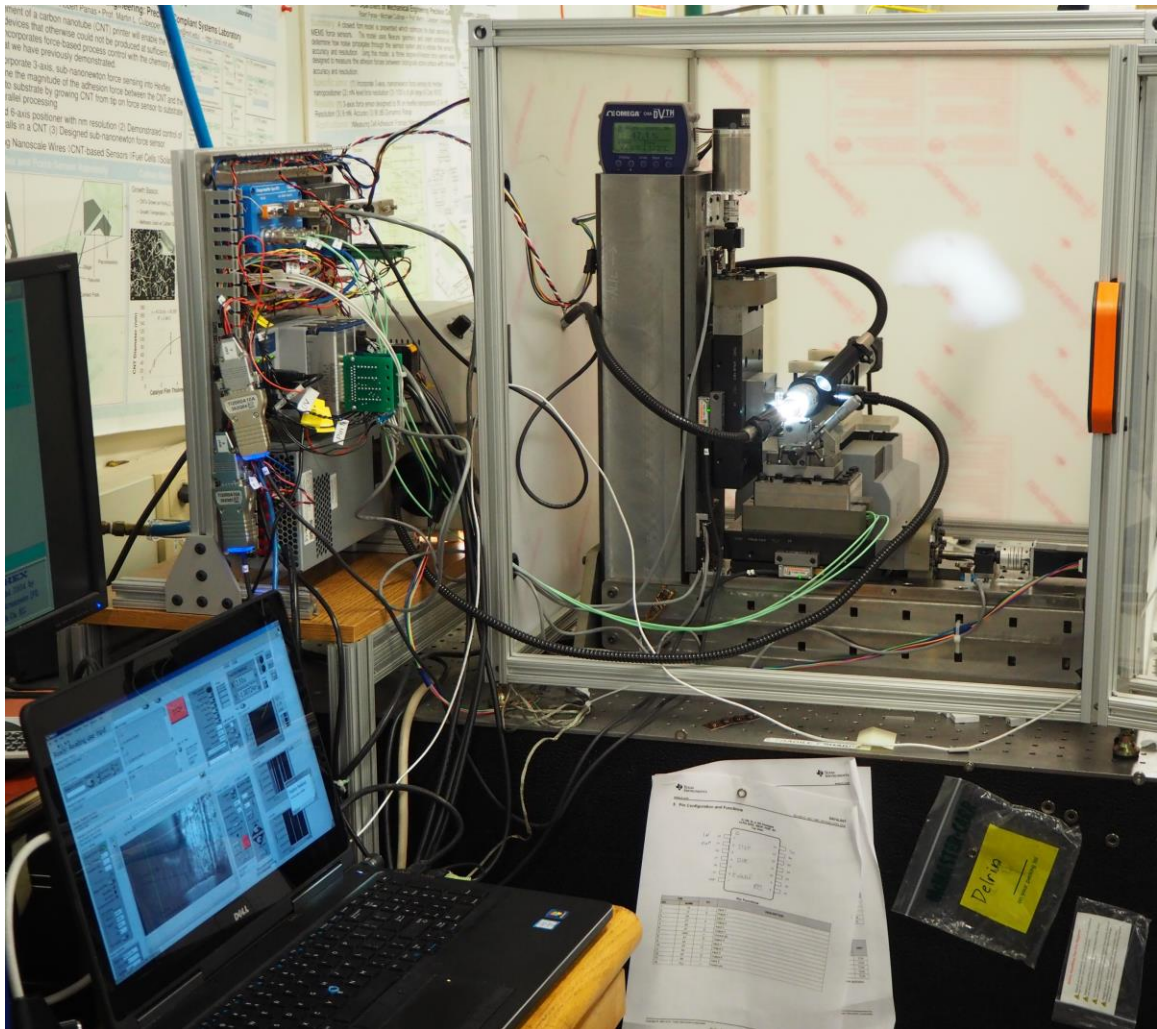


Figure 4.29: Instrument control VI (visible in lower left) running on control laptop. The control VI centralizes communications between the different modules, displays instrument status to the operator, and allows the operator to jog the machine and set experiment parameters (such as video recording length and feed)

Table 4-24: Summary of LabVIEW instrument control VI parallel loop responsibilities

<b>Loop</b>	<b>Loop responsibilities</b>
Main	Event handling, GUI updates (i.e., button presses)
Camera	Image and video acquisition and saving
DAQ	Data acquisition module input/output commands, saving data
Slice servo	Communication with slice motor controller
Feed positioning	Generates motion commands to stepper motor driver

## 4.8 Data acquisition, analysis, and post-processing

This section discusses how the data is collected, processed, and prepared for analysis as is relevant for dig-in stability or feed force variation propagation analysis.

### 4.8.1 Data acquisition

Raw output voltages from the Kistler signal conditioner are recorded from the analog cDAQ module. LabVIEW converts the sensor outputs from the signal conditioner into calibrated forces, and writes these into a `.lvm` file along with timestamp information. Every cut which recorded video data was programmed to write a new line into the metadata database `.csv` file, the metadata collected is described in Table 4-25.

Table 4-25: Metadata collected for each recorded cutting experiment

Metadata field	Unit	Description and comments
Video filename	-	The unique filename for the cutting <code>.avi</code> video
Objective lens used	-	Which objective lens was used to record the video
Microscope zoom level	-	Which index on the zoom lens was used when recording data
Type of lighting used	-	Coaxial, versus external gooseneck lamps, or both
Light intensity	-	Low/Med/High, corresponding roughly to different thirds of the light intensity knob
Feed	$\mu m$	The depth of cut the machine was set to, in
Knife type	-	What style of knife used (e.g., a triangular glass knife, vs disposable steel)
Knife included angle	$^{\circ}$	The nominal “wedge angle” of the knife being used
Specimen material	-	Which material is being cut
Cutting speed	$mm/s$	The cutting speed
Cutting width	$\mu m$	The width of the specimen being cut
Comment	-	A catch-all field to store miscellaneous comments
Date	-	A human-readable date field, in MM/DD/YYYY format
Time	-	A human-readable time field, hh:mm AM/PM format
Timestamp	-	A machine-readable timestamp, in MM/DD/YYYYhh:mm:ss.sss format

Video data was saved using LabVIEW drivers provided by Lumenera. Camera data was saved at 170 frames per second, simultaneously as the force data. Though the camera was capable of filming in full HD (1920 x 1080 pixels), a region-of-interest (ROI) was set up to cut

out unnecessary data and make the files smaller. The saved portion of the video was the central portion of the field of view, 1080 by 1080 pixels

#### **4.8.2 Data post-processing**

The goal of the data post-processing is to extract force vs time data from the LabVIEW files, to plot the force vs time vectors, to run useful calculations of the force vs time data, and to save figures for later review and integration into slideshows and presentations. The software written to accomplish these tasks are described in this section.

The LabVIEW-output `.lvm` file containing force and time vector data is imported into MATLAB and extracted into four vectors: a time vector  $t$ , and three force channels  $F_x$ ,  $F_y$ , and  $F_z$ . The LabVIEW timestamps are converted into a relative time vector, with the initial time as  $t = 0$ . A MATLAB script was written to import the force and time vectors as well as the relevant metadata from the experiment database `.csv` file; all of these are loaded into the MATLAB workspace. Once the force variables are in the workspace, a second MATLAB script calculates force statistics and saves figures in pre-set formats for integration into slides and documents. A single cutting run generated dozens of force/video datafiles, so a batch processing MATLAB m-file was written to automate processing a set of datafiles and generate plots for the full force vs time data for each cut.

For each data set, a second set of plots was saved with additional processing. Another MATLAB script programmatically loaded force and time data from a target `.fig` file (generated using the scripts from the previous paragraph) into the MATLAB workspace, trimmed the signal to remove most of the non-cutting portion before and after the cut, and optionally extracted the steady-state portion of cut (i.e., further trim out the entry and exit portions of the cut). Trimming the active cutting portion of the data is done via a force threshold; the script looks for cutting

force magnitudes larger than the threshold value and will remove portions of the signal before the threshold value while keeping a pre-set number of data points before the threshold event. Similarly, when the cutting force drops down below the threshold file, the script will trim away the rest of the file except for a preset number of data points after the threshold event. This is done to remove the data points associated with motion before and after the cutting when the specimen is approaching and moving away from the knife. If requested, the autobrusher script will further trim a percentage off of the beginning and end of the extracted force signal; this is done to remove entry/exit transient effects and only run calculations based on the steady-state portion of the cutting forces; typically, removing the first 10% and the last 10% of the signal vector (after the signal had been extracted via the thresholding event) successfully extracted the steady-state portion of the cut. After the relevant variables have been loaded into the workspace, a processing script is run to perform calculations on the extracted forces such as statistics and to save figures.

### **4.8.3 Data organization and review**

Running the MATLAB data processing scripts on the cutting data generated two sets of figures for each cutting test, one set being figures for the cutting forces vs time plots of the entire recorded cut. The second set of figures was plots of cutting forces vs time for the steady-state portion of the cut, and also FFTs of the steady-state forces. From this second set of figures, the mean and standard deviation for each steady state portion of the cutting forces were compiled into a Microsoft Excel spreadsheet for review and analysis with regards to dig-in stability and the variance propagation.

For regenerative chatter analysis, the FFT of each cut's steady-state forces was examined by re-opening sequences of `.fig` files and scrolling through to look for consistent growth in the frequency spectrum; in some cases, it was useful to create a Microsoft Powerpoint to create a

slideshow with several figures to allow for scrolling through a set of cuts (an improvised animation).

Cutting video for each cutting test was examined using MATLAB's `implay` function from the Image Processing Toolbox; `implay` was used to play videos at a slowed down playback from the original 170 frames-per-second capture, and to allow frame-by-frame analysis. Video frames of interest were exported and saved using `imtool`, and any image analysis (such as pixel counting lengths) was done using the ImageJ software package.

## **4.9 Commissioning and characterization**

The hardware and procedures developed for force sensor calibration are described in Section 4.9.1. The subsequent sections discuss characterization tests performed to verify instrument operation after assembling the machine and instrumentation; these include testing the minimum motion increment, instrument stiffness, and machine temporal stability.

### **4.9.1 Force sensor calibration and commissioning**

Calibrating the force sensor assembly required applying a set of known loads in each of three measurement directions, in both positive and negative directions, and recording the outputs of each force sensing element in response to each load vector. These inputs and responses were then used to calculate the best-fit sensor gain matrix (Section 4.9.1.2). This calibration task necessitated designing dedicated hardware (Section 4.9.1.1) and test procedures (Section 4.9.1.2); the implemented calibration module concept is shown in Figure 4.30.



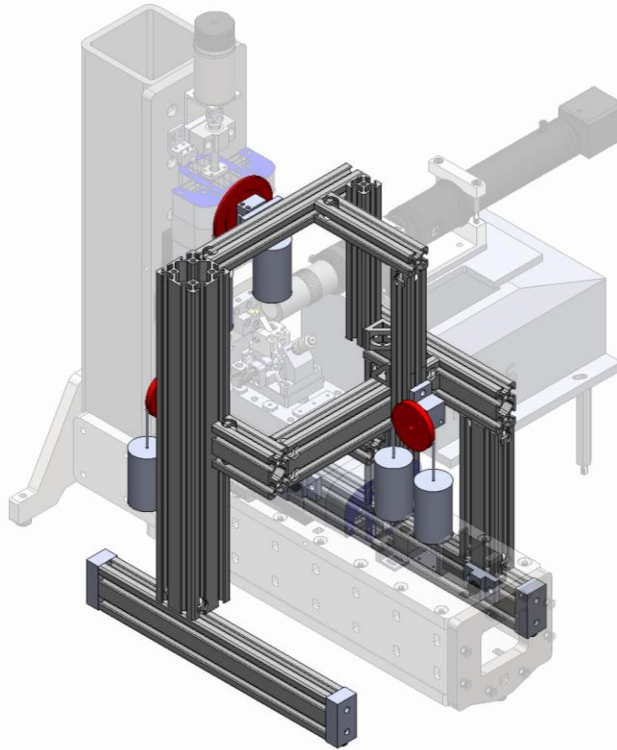


Figure 4.30: Calibration module assembly overlaid on full cutting instrument assembly. The module consists of a frame holding three pulleys (shown simplified as red discs), each of which can be loaded with a dead weight in one of two positions to allow for bidirectional loading. A wire (not shown) couples the pulley output to the force sensor. The frame locates against the machine such that the module can be placed without requiring any instrument disassembly.

The hardware implementation of this concept is discussed in-depth in the following sections.

#### 4.9.1.1 Force sensor calibration hardware

Gravity and laboratory calibration weights provide a simple, accurate, and consistent force source; however, these loads can only be applied parallel to the gravity vector. Calibrating the force sensor required applying bidirectional loads in three directions; to accomplish this bidirectional load application using gravity as the load source, the X and Z directions (orthogonal to gravity) utilized a bell crank concept (Figure 4.32a) and the Y direction (parallel to gravity) utilized a lever concepts (Figure 4.32b). With these concepts, the load mass can be applied in one of two positions to allow for bi-directional loading.

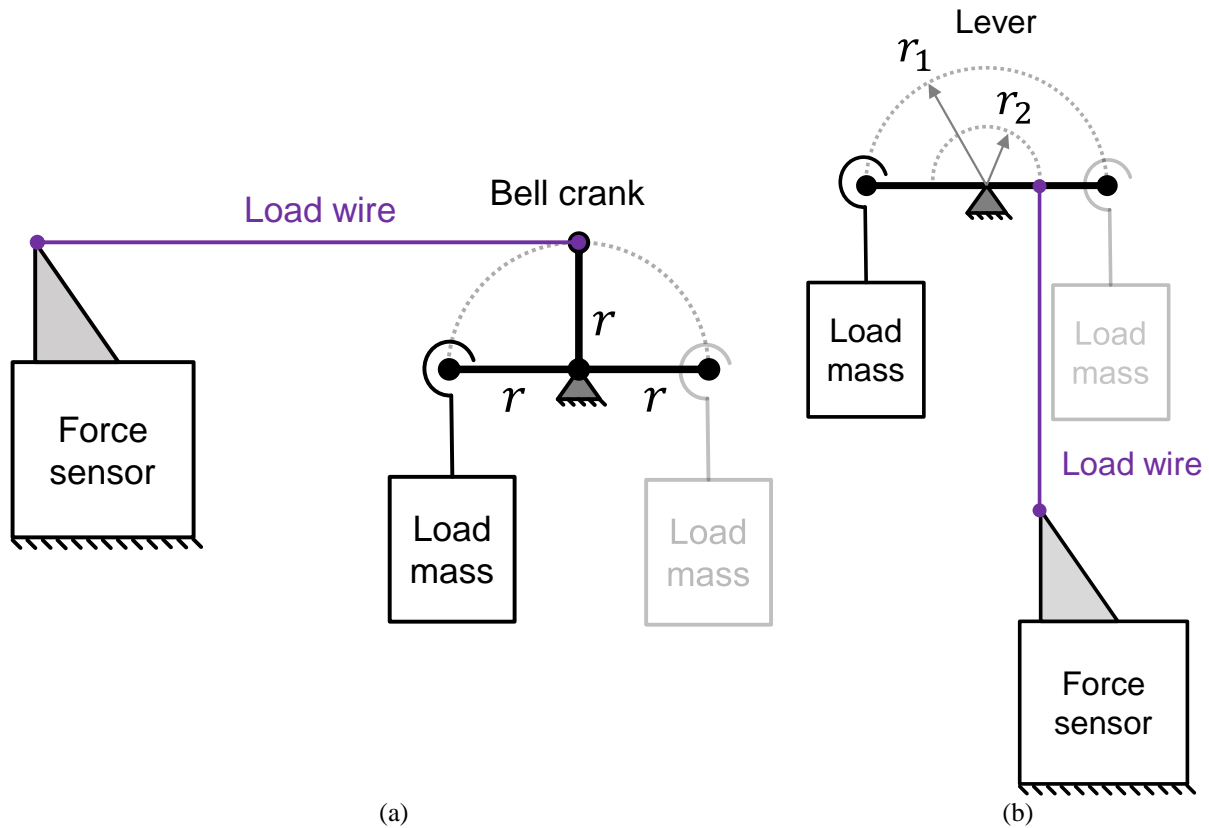


Figure 4.31: Force application loading mechanism schematic (a) Schematic of force sensor bidirectional bell crank loading arrangement for applying loads in the X and Z directions (b) Lever mechanism used for applying bidirectional loads in the Y direction (parallel and antiparallel to gravity vector). For both concepts the load can be applied on either arm of the loading crank pulley to apply loads bi-directionally.

Both flexure pulley designs were 3D-printed from PLA material on a Sindoh 3DWox.

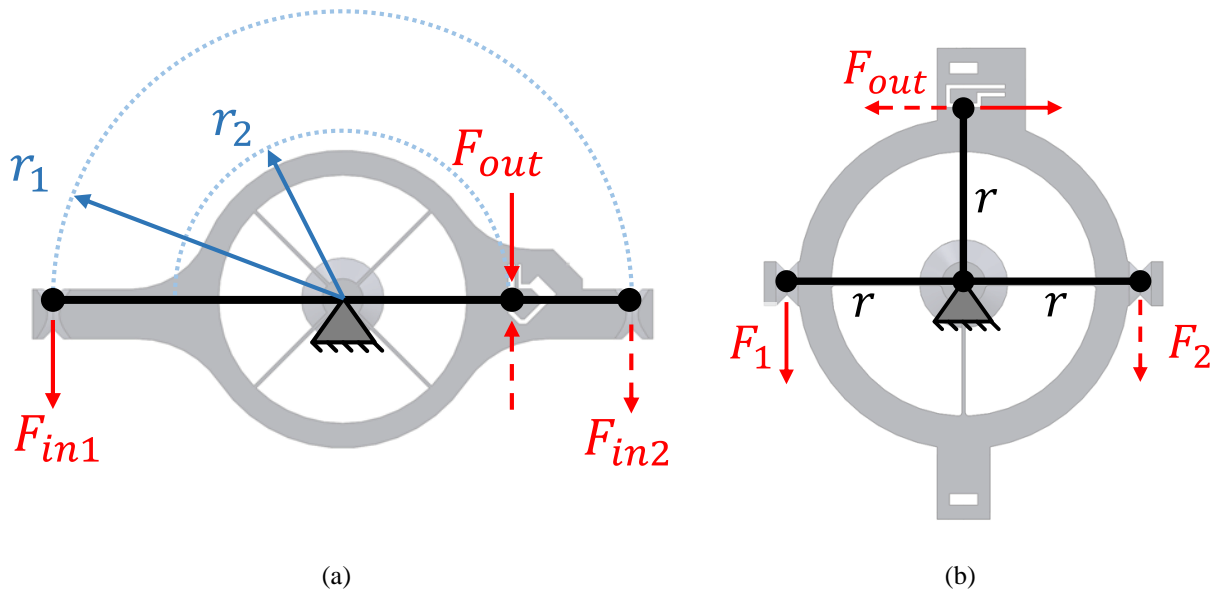


Figure 4.32: (a) Schematic of Y-direction (parallel and anti-parallel to gravity) loader, overlaid on CAD model of implementation via flexure pivot. This implementation has a gain of  $(r_2/r_1)$ , currently 1.5 and (b) Bell-crank converts a gravity dead-weight load ( $F_1$  or  $F_2$ ) into a load at the output rotated 90 degrees. This implementation has unity gain and is used to apply X and Z direction loads.

Ball-bearing, knife-edge, and flexure pulleys were evaluated for accuracy and precision in a test setup which transferred the pulley’s output via a load wire to a Futek LSM300 strain gauge force sensor, which itself was calibrated with dead weights. Flexure pulleys were ultimately chosen due to their superior precision (the only pulleys with precision higher than LSM300), with the potential tradeoff of low accuracy if the output stiffness is too low (e.g., if the torsional stiffness of the pulley entirely reacts the dead weight load). The load cell output was not observed to drift after a load had been applied (loads were applied for around 30 seconds), allaying concerns of PLA stability during loading. The stiffness of the force sensor is much higher than that of the flexure pulley, and the expected error due to this is approximately half a percent.

To transfer the load from the loading pulleys to the force sensor, a calibration “dummy knife” (Figure 4.33) was designed to clamp the load wire and transfer the load to the force sensor. Music wire of 0.762 mm (0.030”) diameter (selected to avoid buckling for the loads

used) is used to transfer both tensile and compressive loads from the pulley to the sensor's loading point. The clamp successfully lifted a 1 kg weight without slipping in each orientation.

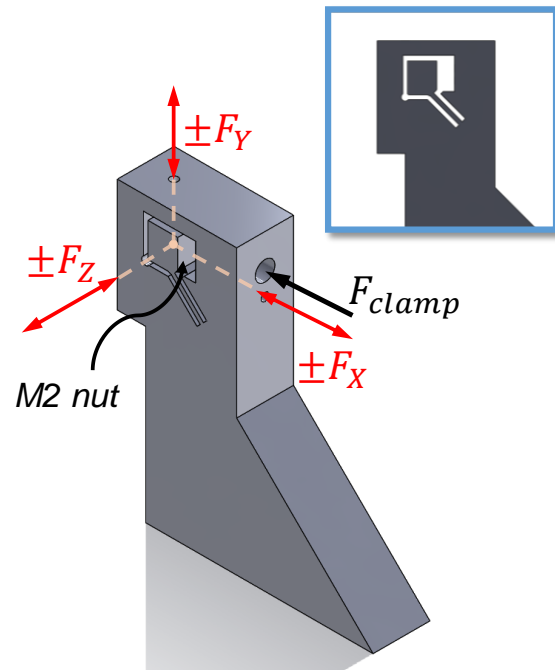
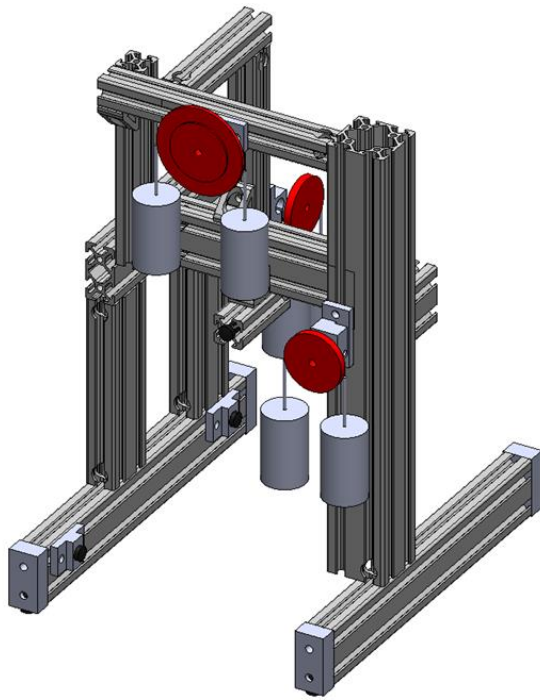
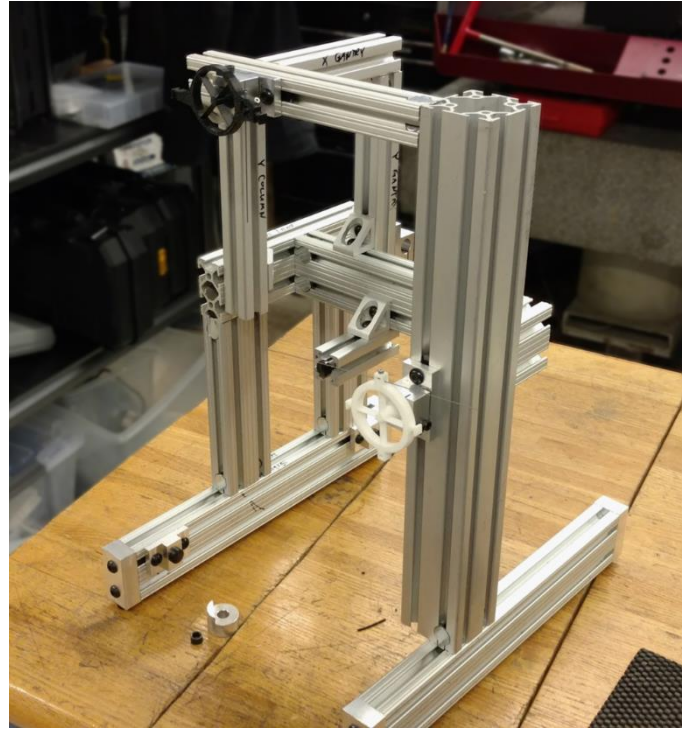


Figure 4.33: CAD model of load-transferring dummy knife for force sensor calibration. The clamping force is applied via an M2 screw which threads into an M2 nut inserted into a pocket. INSET: side view showing the clamping pad guided by a simple flexure bearing. This dummy knife allows for bidirectional load application in any of the three directions without requiring the knife to be removed from the force sensor knifeholder.

A frame was designed to position the three pulleys around the force sensor while providing enough clearance to apply the dead weights. The frame slides over the machine without requiring any disassembly or otherwise disturbing the hardware, and fits inside the machine enclosure.



(a)



(b)

Figure 4.34: Loading frame module CAD model (a) and assembly (b)

The loading frame registers to the instrument with three kinematic contacts, and to the optical table via four kinematic contacts. This set of four contacts is potted in place with epoxy while in contact with the optical table to minimize overconstraint (a three-footed exactly-constrained design was desirable but was unfeasible due to space constraints – the loading frame base could not be made large enough to avoid tipping). These kinematic contacts allow the frame to be removed when calibration is complete so as not to interfere with normal operation, and to apply loads at the same location if recalibration is later deemed necessary. The frame is designed with one kinematic contacting the feed stage, so that the calibration results do not depend on the feed stage position (the calibration frame “travels” with the feed stage). The frame is designed so

that calibration can be carried out from the front of the instrument, without removing the instrument enclosure.

#### *4.9.1.2 Force sensor calibration procedure*

The main instrument control VI was upgraded with a calibration control cluster containing features to streamline calibration. The operator set metadata about each data snapshot via drop-down and Boolean controls. The relevant metadata was whether the loading was in the X, Y, or Z direction, the load mass, whether the loading was negative or positive, and if the current data snapshot was a reference data snapshot (e.g., no loading has been applied). When a measurement snapshot was requested, the VI captured 5000 samples at 5000 Hz sample rate, and computed the captured waveform's average and standard deviation. The processed data, the initial data point timestamp, and the user-entered metadata were all written to a text file. Subsequent snapshots are appended to the same text file.

Hooked laboratory weights (Troemner Class 7 Hook Weight Set) between 0.02 – 0.200 kg were used to provide the input load (due to space constraints, the larger masses in this set could not be used). Loads were applied bidirectionally in all three directions, one at a time. The masses used were 20g, 50g, 100g, 200g. Each loading was repeated three times. Immediately prior to each loading, a reference measurement snapshot was taken. A small monofilament loop settles into the pulley loading point groove, and allows for easier hooking of the weights on to the pulley (see arrows in Figure 4.35 inset). The pulley was then loaded, and the force sensor outputs were recorded. The difference between the loaded output and the reference measurement was taken as the sensor response to the input load.

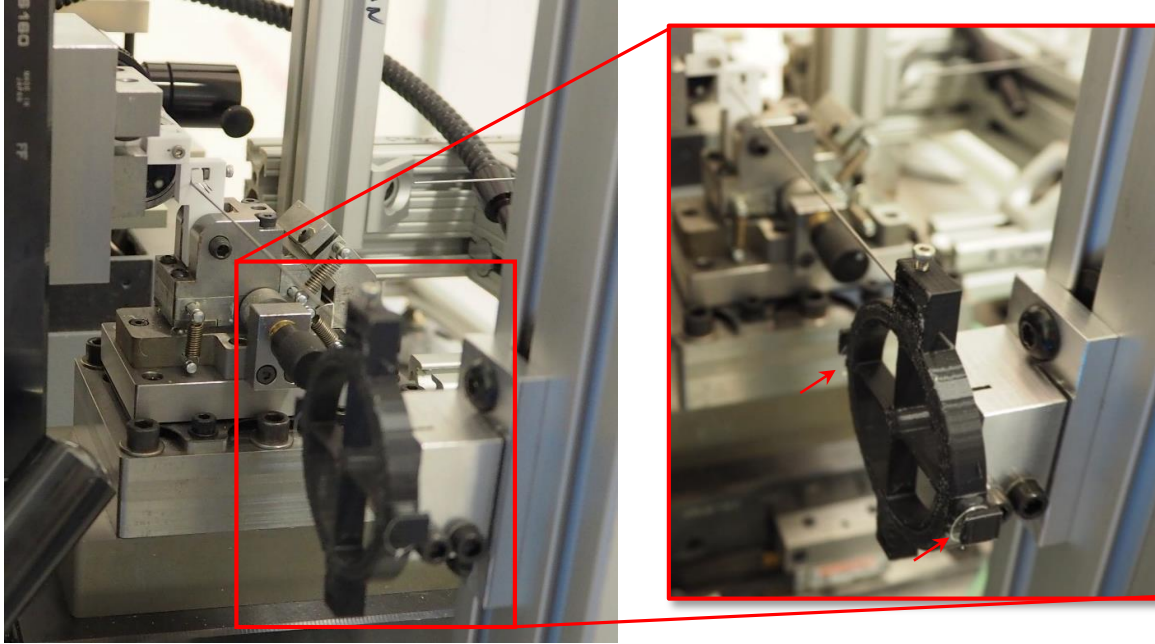


Figure 4.35: Force sensor calibration module in place over the cutting instrument, configured to apply  $Z$  loads. Inset zoom: focus on  $XZ$  loading pulley. Arrows show monofilament loops for hooking weights on. Also shown is a wire clamping module mounted in the vise in place of a specimen, but this was not used for calibration.

The goal of the force sensor calibration is to calculate the sensor calibration matrix  $\mathbf{C}$  which calculates the applied loads at the force sensor input  $\mathbf{m}$  for a given set of force sensing element output loads  $\mathbf{z}$ ,

$$\mathbf{Cz} = \mathbf{m} \quad (4.19)$$

The method used here to compute the best-fit sensor gain matrix was the least-squares pseudoinverse method as summarized in [63], and the nomenclature used here for the load/response vectors and sensor gain is consistent with their nomenclature.

The input load vectors  $\mathbf{m}_i$  are assembled into a known-load matrix  $\mathbf{M}$ ; similarly, the output sensor loads  $\mathbf{z}_i$  are assembled into sensor response matrix  $\mathbf{Z}$ ,

$$\begin{bmatrix} \mathbf{z}_1^T \\ \vdots \\ \mathbf{z}_n^T \end{bmatrix} \mathbf{C}^T = \begin{bmatrix} \mathbf{m}_1^T \\ \vdots \\ \mathbf{m}_n^T \end{bmatrix} \quad (4.20)$$

The best-fit calibration matrix  $\mathbf{C}$  is calculated via the pseudoinverse matrix,

$$\mathbf{C}^T = \mathbf{Z}^+ \mathbf{M} \quad (4.21)$$

where  $\mathbf{Z}^+$  is the pseudoinverse of  $\mathbf{Z}$ . The pseudoinverse calculation was performed in MATLAB using the built-in function `pinv(A)`, where  $\mathbf{A}$  is the matrix to be pseudo-inverted.

#### 4.9.1.3 Force sensor calibrated matrix results

The calibration matrix calculated using the collected load/response data and the method described in the previous section is shown in Table 4-26.

Table 4-26: Force sensor calibration matrix converts sensor loads  $F_n$  to applied loads  $F_{xyz}$  units are  $N$

$$\mathbf{C} = \begin{bmatrix} 0.0989 & 0.0935 & -0.3703 \\ -0.4686 & -0.4693 & -0.4684 \\ -0.1309 & 0.1745 & 0.0174 \end{bmatrix}$$

This calibration matrix converts a vector of individual force sensor outputs  $\mathbf{z}_n = [F_1 \ F_2 \ F_3]^T$  to the applied loads at the calibrated force sensor assembly input  $\mathbf{m}_{xyz} = [F_x \ F_y \ F_z]^T$

#### 4.9.1.4 Load limits before saturation – usable force range

Applying loads at the force sensor's input will generate reaction loads (the sense loads) in each of the three force sensors supporting the force platform; a large enough combination of input loads will cause one or more of the sensors to saturate. A numerical approach is used to compute the sensor's usable range; the inverse of the force sensor calibration matrix is used to back out the individual force sensor loads at each applied load. At a given X load, the largest magnitude of Y load is found (to the nearest 0.1 N) that will not saturate any of the three force



sensors. Only negative Y loads are of interest, since these correspond to cutting loads; under normal cutting circumstance, the force sensor should not register a positive load.  $F_x$  values larger than 5 N would saturate a force sensor regardless of  $F_y$ , and values more negative than  $-5$  require a positive cutting force to avoid saturation, which is not a realistic cutting scenario.

Table 4-27: Maximum allowable cutting load ( $F_y$ ) at a given level of feed force ( $F_x$ ) to avoid saturating any force sensors and causing a measurement error. Assumes that  $F_z$  is zero (no out-of-plane load)

$F_x$ (N)	Max $F_y$ (N)
-5	2.8
-4	-2
-3	-6.9
-2	-11.8
-1	-10.6
0	-9.5
1	-8.4
2	-7.3
3	-6.2
4	-5.1
5	-2.8

#### 4.9.2 Force sensor noise floor

The force sensor noise floor was characterized by measuring the force sensor output under quiescent conditions for approximately 40 seconds and calculating the mean and standard deviation of the force signals. The typical cutting test was expected to take about 3-4 seconds (covering a distance of 3 mm at a speed of around 0.75 – 1.5 mm/s), so this was approximately ten times longer than the typical cut. The average ( $\mu$ ) and standard deviation ( $\sigma$ ) were calculated. The  $\pm 2\sigma$  ( $4\sigma$ ) value, representing the 95% confidence interval, was also calculated. Results of the quiescent measurement are tabulated in Figure 4.36.

<b>Force Direction</b>	<b><math>\mu</math> (N)</b>	<b><math>\sigma</math> (N)</b>	<b><math>4\sigma</math> (N)</b>
$F_x$	2.3e-4	1e-3	4e-3
$F_y$	2.8e-3	2.4e-3	9.6e-3
$F_z$	8.1e-4	6.8e-4	2.7e-3

Figure 4.36: Results of quiescent force sensor noise floor measurement with 95% noise confidence interval ( $4\sigma$  value)

Force measurements were also recorded with the slice stage in motion at 0.75 mm/s, moving down against gravity approximately 8 mm, holding position at the bottom for a few seconds, and then returning back to its original position. The recorded length was 29 seconds. The resulting mean and standard deviation of the data are presented in Figure 4.37.

<b>Force Direction</b>	<b><math>\mu</math> (N)</b>	<b><math>\sigma</math> (N)</b>	<b><math>4\sigma</math> (N)</b>
$F_x$	-1.1e-3	1.4e-3	5.6e-3
$F_y$	-1.4e-4	2.3e-3	9.2e-3
$F_z$	-4.6e-5	7.2e-4	2.9e-3

Figure 4.37: Results of force sensor noise floor measurement with slice stage in motion, with 95% noise confidence interval ( $4\sigma$  value)

The resulting noise values during the in-motion noise test are higher for  $F_x$  but are slightly lower for  $F_y$  and  $F_z$ . This could be due to the longer recording length of the quiescent noise test capturing more noise spikes in the quiescent test, combined with the structure being more sensitive to X- and Z-direction excitation. The  $4\sigma$  value is taken to be the minimum value below which any force measurement cannot be distinguished from noise.

### 4.9.3 Minimum motion increment

In this experiment, capacitance probes with a higher resolution than the linear encoders are positioned to measure motion along the X and Y axes. The minimum discernible motion as well as its repeatability are compared to theoretical values.

#### **4.9.4 Microscope objective calibration**

The MOTIC 20x objective lens was calibrated at zoom level 2 (this zoom level was found to give the best balance between image brightness, depth of field, and resolution) via the following procedure: first, a reference image was acquired. The feed stage was then moved a fixed amount. A second image was acquired; then the pixel shift was computed in MATLAB using the phase correlation between the two images. The ratio of input distance to pixels shifted gives a calibration value useful for taking pixel measurements of video frames.

#### **4.9.5 Instrument stiffness**

As part of the instrument commissioning, it was important to verify that the machine's stiffness characteristics were as designed – in a structure composed of modules transferring load in series, it only takes one “weak link”, e.g., one item which introduces compliance, to drop the effective stiffness of the *entire* serial chain. The instrument stiffness between the specimen and knife was measured by characterizing the stiffness of half of the machine at a time. Measuring the stiffness of the structural loop requires applying a known “prying” force within the structural loop, and measuring the resulting relative displacements between the loaded points (Figure 4.38a); such measurements are difficult to implement in practice, so a simplified approach was taken in this work. Instrument stiffness was instead measured by characterizing each half of the structural loop separately, and then adding the stiffnesses in series; one of these half-loop stiffness measurements is shown schematically in Figure 4.38b.

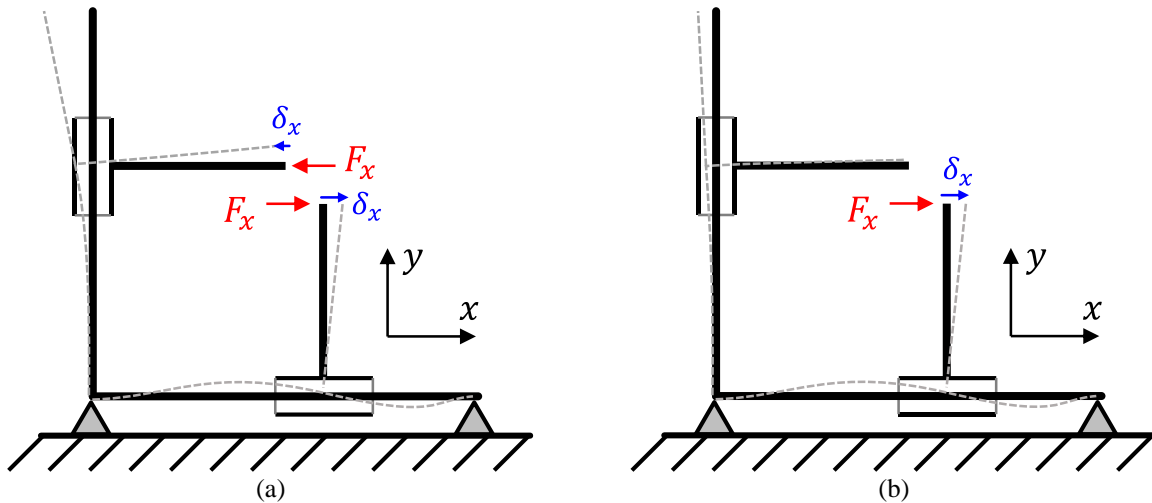


Figure 4.38: Schematic of structural loop stiffness measurement, shown with X direction load and resulting X deflection. (a) During cutting,  $F_x$  is generated and acts on each end of the structural loop, causing X deflections (b) In the simplified approach, loads are applied on one “half-loop” of the structural loop at a time, and are reacted by the table; deflections are measured with respect to the table (the ‘ground’ frame). The two stiffnesses are then added in series.

The same load-application apparatus was used in this characterization as was used to calibrate the force sensor, however some modification was required to transfer the load to the specimen and the wedge glass knife. Load-transferring elements were designed and shown schematically in Figure 4.39(a-d); for the slice arm, a load wire was sharpened to a point and reinforced by gluing additional load wires around it; prior to loading, a small dimple was made in the plastic specimen, and the load wire was set such that the tip rested in the dimple (Figure 4.39 a and c). To transfer loads through the wedge knife and into the feed arm, toothpicks were carved into small hooks that rested on the knife edge and could pull (X load configuration, Figure 4.39b) or push down on the knife edge (Y load configuration, Figure 4.39d). These wooden hooks were then glued to the load wires; half of the toothpick was cut away, and the load wire itself was used to form a small channel in the wood where it was then glued in place.

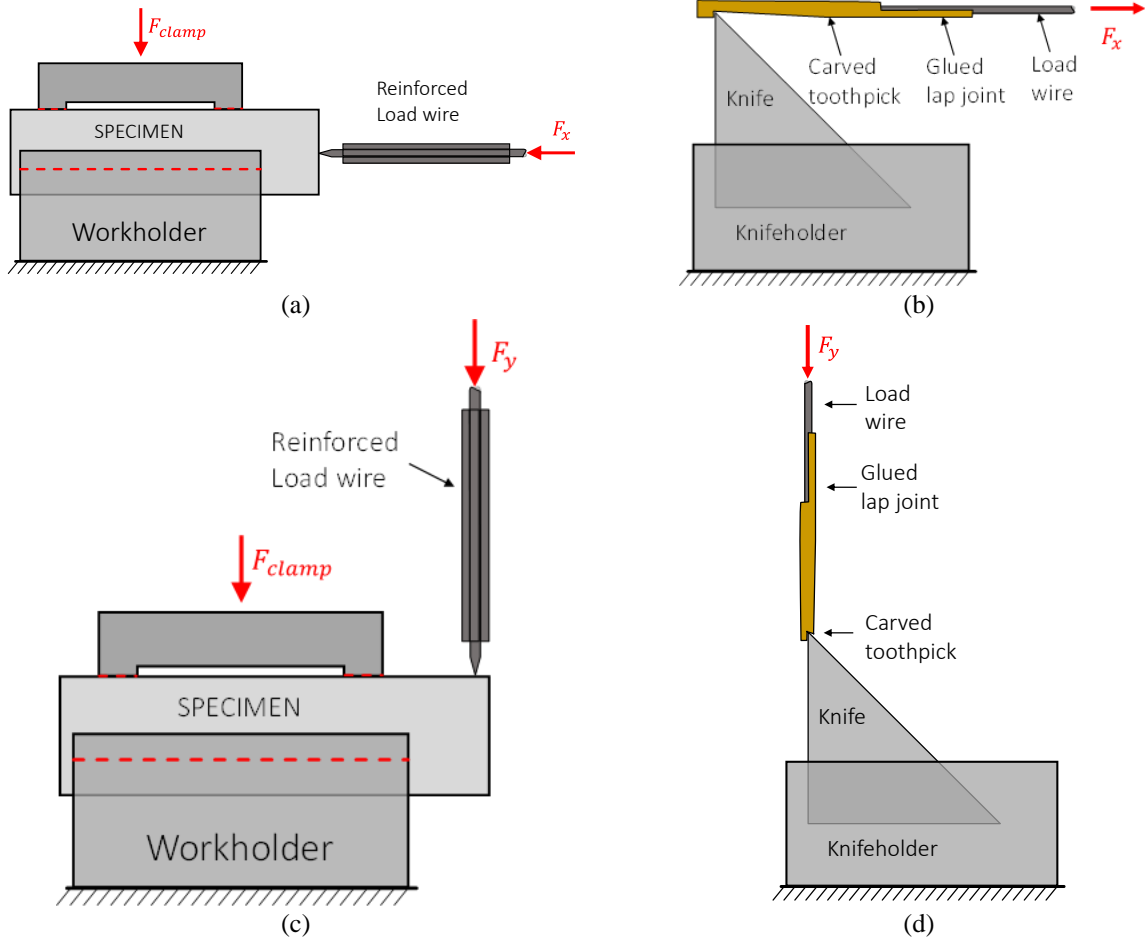


Figure 4.39: Detail schematic of load-transferring to the slice and feed arms. (a) Slice arm loading, X direction (b) Feed arm loading, X direction (c) Slice arm loading, Y direction (d) Feed arm loading, Y direction

The physical implementation for two of these loading scenarios are shown in figs Figure 4.40a and Figure 4.40b.

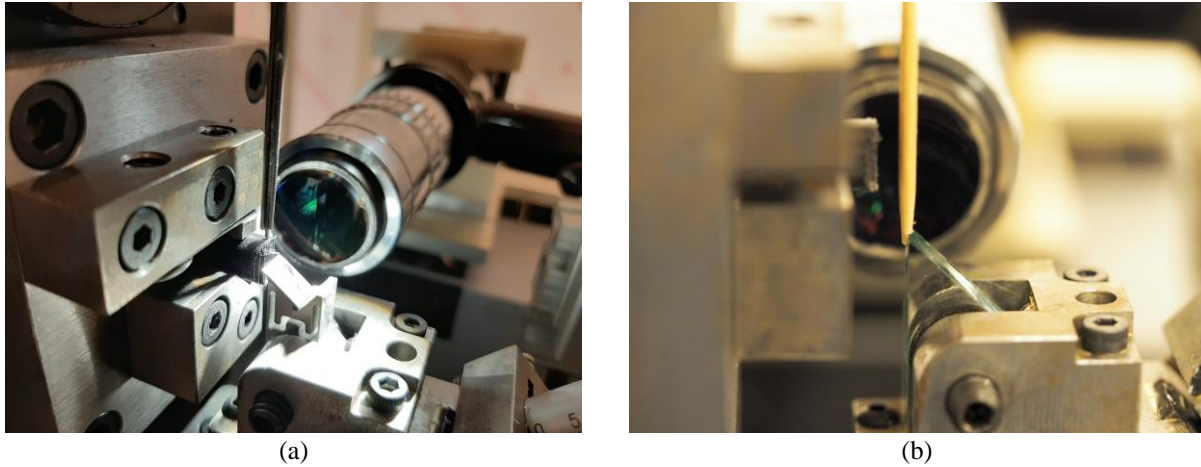


Figure 4.40: Physical implementation of two of the loading configurations (a) Y-direction loading on the specimen to characterize slice arm stiffness and (b) Y direction loading on the knife feed arms of the structural loop to characterize feed arm stiffness

200g weights were used, corresponding to loads of 1.96 N for X and 2.94 N for Y (higher for the Y direction due to a built-in gain due to the loading pulley design), and the loads were applied 5 times. Deflections were measured optically with the microscope by focusing on the specimen side or the knife tip for the slice arm and feed arm characterizations, respectively. A reference image was taken before each loading, and a second image was taken after loading. The MATLAB Image Processing Toolbox function `imregtform` is used to compute the  $(x, y)$  pixel shift between the reference and loaded images. The compliances of the feed arm and slice arm of the machine are added in series to obtain the total structural loop compliance, and this is inverted to obtain the net structural loop stiffness.

Table 4-28: Compliance measurements and stiffness calculations, for the feed and slice arms of the structural loop (measured separately)

Direction	X Load (N)	X Displacement ( $\mu\text{m}$ )	X Compliance ( $\mu\text{m}/\text{N}$ )	X Stiffness ( $\text{N}/\mu\text{m}$ )	Y load (N)	Y Displacement ( $\mu\text{m}$ )	Y compliance ( $\mu\text{m}/\text{N}$ )	Y Stiffness ( $\text{N}/\mu\text{m}$ )
Feed (X)	1.96	0.86	0.439	2.27	-2.94	-0.626	0.213	4.7
Slice (Y)	-1.96	-0.192	0.098	10.2	-2.94	-0.983	0.334	3.0
<b>Net</b>			<b>0.537</b>	<b>1.86</b>			<b>0.547</b>	<b>1.83</b>

The stiffness predicted by the analytical error model is obtained by applying an input load in one direction at a time, then dividing the input load by the calculated output displacement. Results are summarized in Table 4-30.

Table 4-29: Analytical error model stiffness predictions

Input X Load (N)	Output X Displacement ( $\mu\text{m}$ )	X Stiffness ( $\text{N}/\mu\text{m}$ )	Input Y load (N)	Output Y Displacement ( $\mu\text{m}$ )	Y Stiffness ( $\text{N}/\mu\text{m}$ )
-0.05	-0.027	<b>1.85</b>	-0.3	-0.239	<b>1.26</b>

The net measured stiffness is then compared to the predictions made by the analytical error model (Table 4-29).

Table 4-30: Measured vs analytical error model predictions, with percent error relative to analytical model predictions

Direction	Measured stiffness ( $\text{N}/\mu\text{m}$ )	Predicted stiffness ( $\text{N}/\mu\text{m}$ )	% error
Feed (X)	1.86	1.85	0.5
Slice (Y)	1.83	1.26	45

The measured stiffness matches the analytical model in the feed direction, which is the sensitive direction. The measured slice stiffness however is larger than that predicted by the analytical model; the analytical model thus yields a conservative estimate. This characterization confirms that there is no unexpected addition of compliance from the cutting instrument and that its stiffness characteristics are as designed.

*(this page intentionally left blank)*



## DIG-IN STABILITY EXPERIMENTS

---

The goal of the experimental work was to validate the models developed in sections 3.2 and 3.2.3.2, for series dig-in stability and dig-in sensitivity, respectively. Section 5.1 describes the hardware and procedures used to test the series dig-in stability and feed force variance propagation models; both dig-in stability and sensitivity can be assessed from the same experiment in post-processing. Section 5.2 describes the data analysis and post-processing required to present the data. Section 5.3 discusses the signals that were used to assess when a cutting system has entered the unstable regime.

### **5.1 Series dig-in stability test via stepped-width specimen cutting and compliant knives**

A system having a single degree of freedom with a known compliance and a known width of cut is used to test the dig-in stability model. The known-compliance system cuts a workpiece at different width of cuts, taking several cuts at each width of cut; the width of cut is then incremented and the process is repeated. These cuts are performed while measuring cutting forces and viewing the cutting on a microscope. A schematic of the experiment in side-view is shown in Figure 5.1, and a front view showing a schematic of the increasing width of cut is shown in Figure 5.2

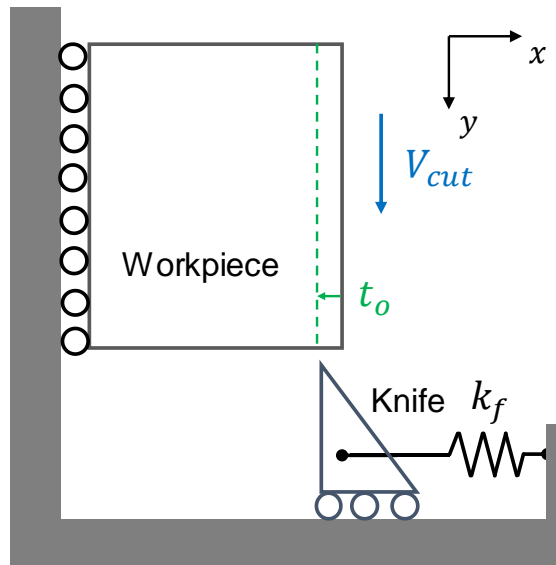


Figure 5.1: Schematic of dig-in stability experiment cutting.

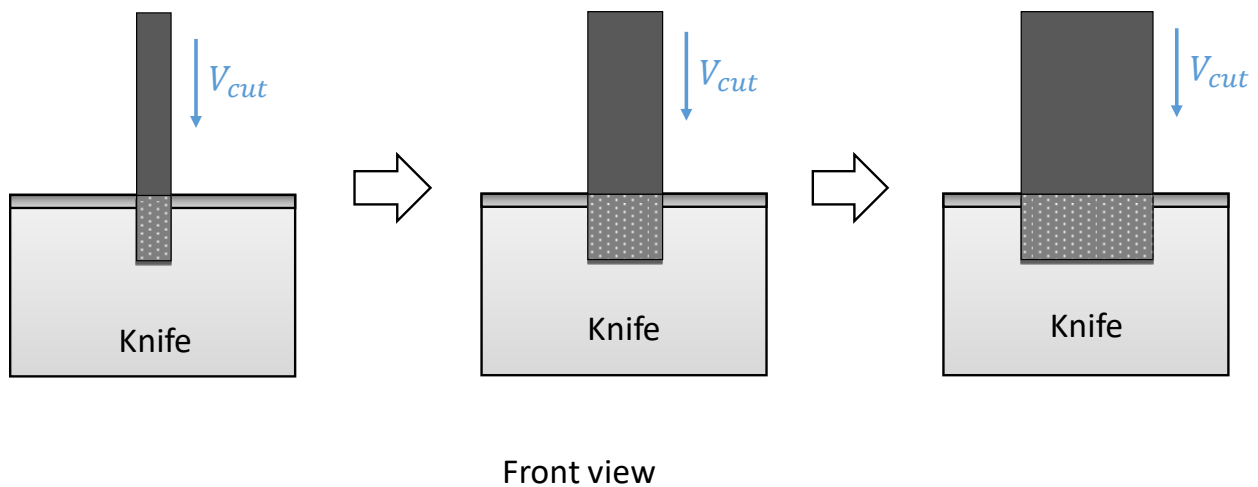


Figure 5.2: Front view of dig-in stability experiment concept. Cutting is attempted at increasing widths of cut until instability is evident.

In order to perform this experiment, the following are required:

1. A well-defined single degree of freedom compliant system
2. A series of specimens with well-defined and increasing width of cuts

The following sections discuss how each of these was achieved.

### 5.1.1 Changing the width of cut using a stepped specimen

To perform cutting tests at various specimen widths without requiring refixturing and interaction with the machine between each cutting width increment, a stepped specimen was designed that would increase in width after several cuts. This specimen is fixtured and aligned with the microscope once at the beginning of the run; with this concept, several cuts can be performed at a constant width of cut before incrementing the width of cut. Force data is recorded for each cut, and is analyzed after the experiment. The stepped specimen is shown below in Figure 5.3

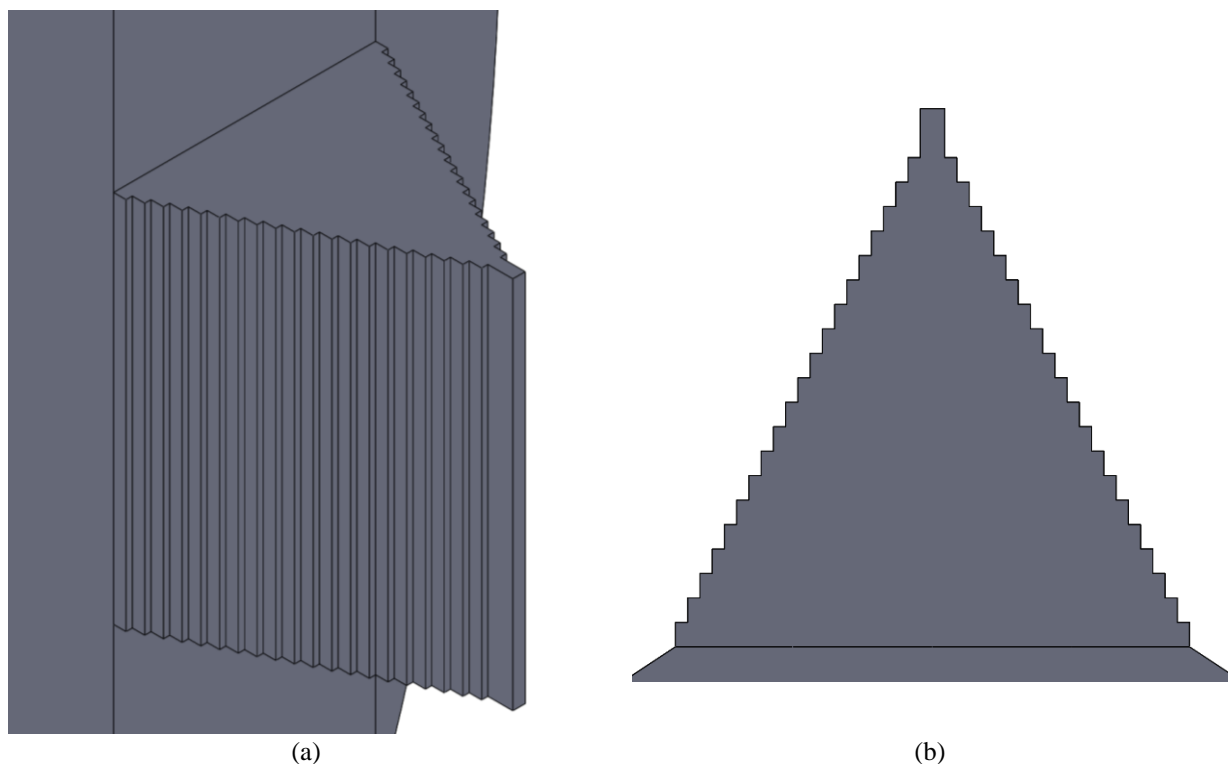


Figure 5.3: Stepped specimen design machined from rod (cylinder) stock, (a) isometric view (b) front view

The widths of each step for the specimens used in this work are given in Table 5-1. The following sections discuss why these widths were chosen.

Table 5-1: Stepped specimen step widths

Step level	Width ( $\mu\text{m}$ )	Step level	Width ( $\mu\text{m}$ )
1	100	11	1100
2	200	12	1200
3	300	13	1300
4	400	14	1400
5	500	15	1500
6	600	16	1600
7	700	17	1700
8	800	18	1800
9	900	19	1900
10	1000	20	2000

### 5.1.1.1 Stepped specimen concept constraints

The minimum specimen width is constrained by fabrication method limitations, the force sensor's sensitivity, and the requirement that the initial cuts are of a small enough width that the initial cuts can be treated as nominal cutting, and aren't affected by being too close to the stability limits. To generate the geometry used for the experiments in this work, the specimen was machined on a micromilling machine (i.e., a cutting machine using small end-mill cutters, not to be confused with a MEMS micromilling process). Too small of a width coupled with too tall of a wall would leave a poor surface finish due to the wall deflecting under the machining cutting loads, or might just break off entirely. The smallest width must also be large enough to generate a detectable force signal from the force sensor.

The maximum width of the specimen is constrained by the force sensor's saturation limit, the knife width, and the expected max stable cutting width. Too wide of a cut would increase the cutting forces past the force sensor's maximum limit and would require resetting the force sensors. As a practical matter, if the specimen width is too wide, it will be wider than the knife width. In addition, too many cutting widths beyond when the specimen is expected to go unstable would be a wasted opportunity to fit more widths leading up to the instability regime.

### 5.1.1.2 Specimen material selection

A polymer model material was chosen to test the dig-in stability model to avoid introducing additional variables such as variation within a cut due to tissue inhomogeneity, and variation due to epoxy mixing and curing or tissue prep. The chosen material needed to cut smoothly, since the embedding resins are specifically mixed to have the right combination of brittle and plastic to yield smooth-cutting sections. Delrin® acetal homopolymer<sup>1</sup> thermoplastic was chosen as the specimen material. Acetal is a highly machinable polymer and will yield smooth cuts under most cutting conditions, and cutting data is available from the machining literature, which was useful for designing experiments (for example, in selecting a rake angle to use). A caveat with the existing machining literature data is that there was no cutting data available for the specific feeds and speeds planned in these experiments, so a  $K_f$  measurement would still be necessary.

Whether or not the mechanical properties of acetal are similar to embedded tissue is currently unknown, as there is no cutting data available for resin-embedded tissues in the literature. The existing instrumented microtomes have either only cut epoxy blanks, or have cut tissue specimens embedded in wax instead of resin. During embedding, the epoxy resin infiltrates the tissue, so it is likely that mechanical properties such as the Young's modulus of the embedded tissue lie somewhere between the properties of the fresh tissue and the resin, likely leaning towards the latter because the goal of embedding is to rigidify the tissue enough so that it cuts smoothly. This allows us to make one relevant comparison between embedded tissue and

---

<sup>1</sup>Delrin® is a registered trademark of DuPont de Nemours, Inc.

Delrin cutting - they are both materials that cut smoothly, so their combination of rigidity, strength, and fracture resistance are just right to allow for good sections.

### 5.1.1.3 Specimen fabrication

The stepped specimens were machined on a Microolution 363-S micro machining center using a 1/16” carbide end mill from Performance Micro Tool. A custom fixturing pallet was fabricated to hold 8 mm OD cylindrical stock (Figure 5.4a), and a close-up shot of a freshly machined Delrin stepped specimen is shown in Figure 5.4b.

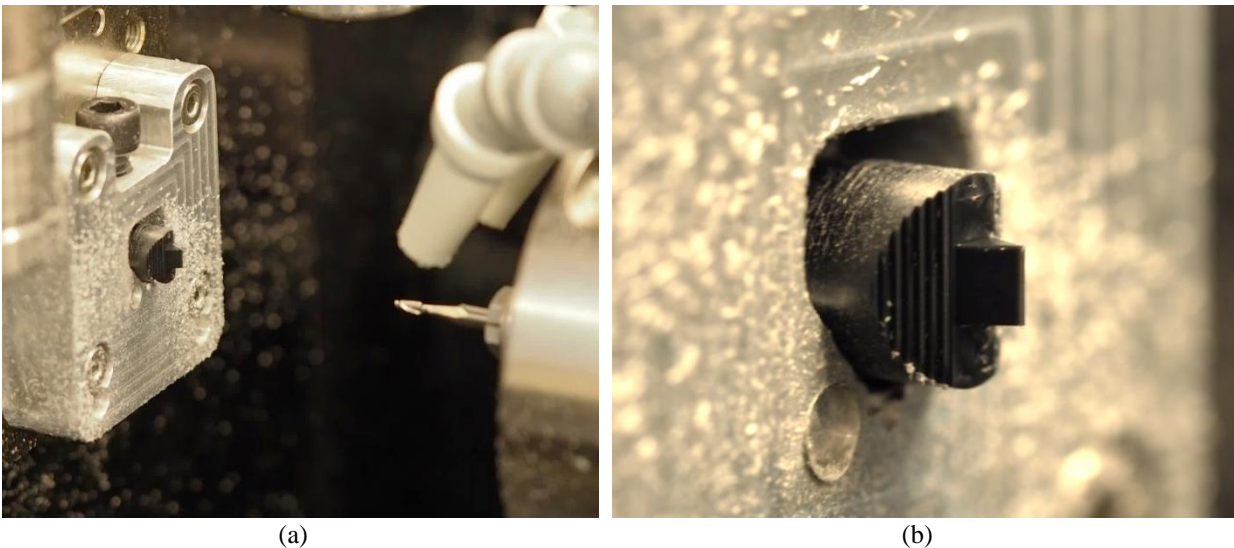


Figure 5.4: Delrin stepped specimen machining in custom pallet fixture in a Microolution 363-S micromachining center. (a) The stepped specimen just after machining and (b) close up of the specimen

General micromachining values for polymers were provided in Machinery’s Handbook [43] (note that the section on micromachining was added in the 28<sup>th</sup> edition) and from the tooling manufacturer (Performance Micro Tool) and were used as a starting point; the final feeds and speeds used for machining are provided in Table 5-2.

Table 5-2: Feeds and speeds used for machining stepped specimen

<b>Roughing</b>			<b>Finishing</b>		
<b>Parameter</b>	<b>Value</b>	<b>Unit</b>	<b>Parameter</b>	<b>Value</b>	<b>Unit</b>
Spindle RPM	38,381	<i>rev/min</i>	Spindle RPM	24,446	<i>rev/min</i>
Surface speed	191	<i>m/min</i>	Surface speed	121	<i>m/min</i>
Feedrate	3911	<i>mm/min</i>	Feedrate	1245	<i>mm/min</i>
Chipload per tooth	51	<i>μm/tooth</i>	Chipload per tooth	25.4	<i>μm/tooth</i>
<i>Common parameters</i>					
1.59 mm [1/16"] two flute square carbide endmill					
Air coolant					

#### 5.1.1.4 Specimen characterization

Initially the specimen was inspected on a microscope (Amscope HD1080-TP18) to inspect for gross imperfections and general quality level. The microscope had been calibrated by optically measuring the width of a gauge block at the various zoom levels. After tweaking the speeds and feeds, the specimen was then characterized by pixels measurements in ImageJ from images acquired from the microscope at the highest zoom level. The first ten thicknesses were measured by optically measuring the widths using ImageJ.

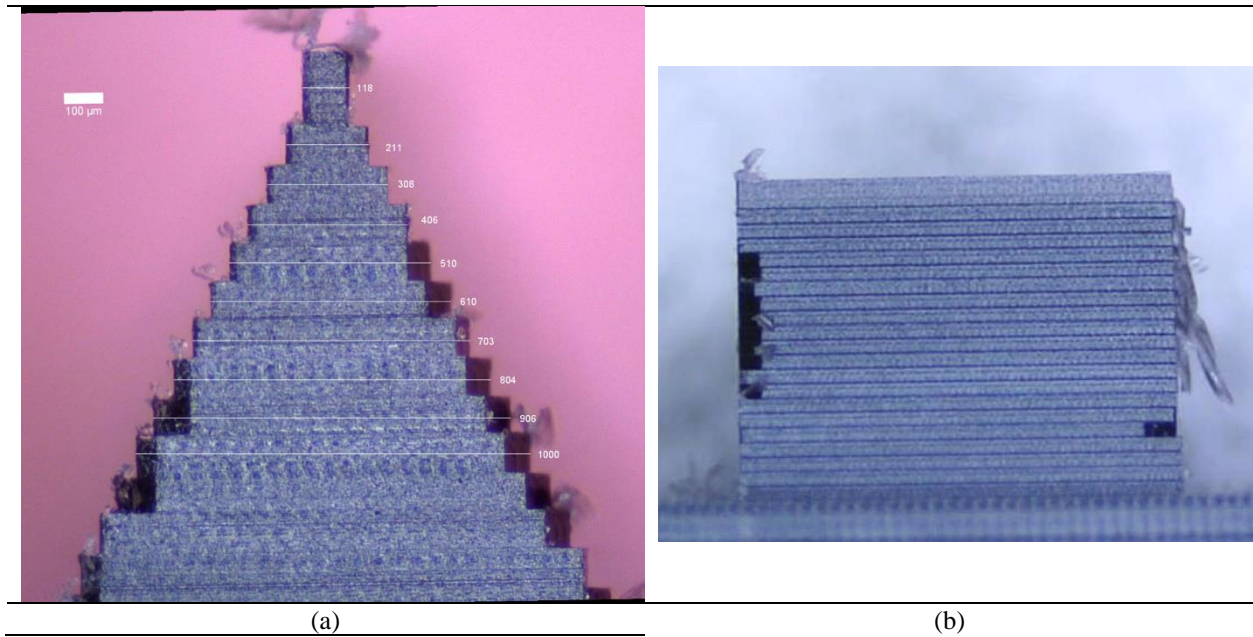


Figure 5.5: Microscope images of machined thinwall specimen (a) Specimen profile with ImageJ measurements of wall thicknesses (b) side profile image taken at a lower zoom level, to inspect for gross imperfections. Some parts of the sidewall are rounded off, this appeared to be due to a toolpath error and was consistent among specimens.

#### 5.1.1.5 Specimen materials

The same knife used for cutting different materials gives different values for the specific feed pressure, both in magnitude and importantly for studying the effects of dig-in stability, in sign. The compliant knife cutting Acrylic results in a positive specific feed pressure – the feed forces generated are such that the tool is being pushed out of the cut. The compliant knife cutting Delrin results in a negative specific feed pressure – the feed force generated during cutting is such that the cutting tool is pulled into the material.



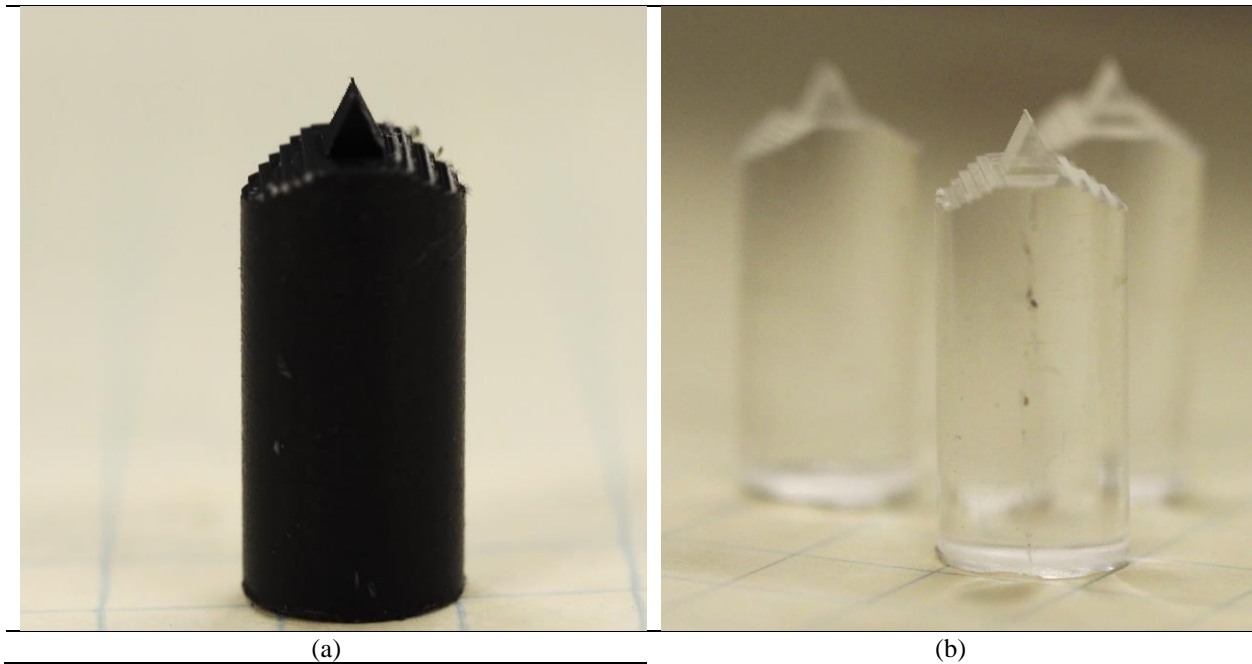


Figure 5.6: Machined thin-wall specimens (a) acetal (b) Acrylic

### 5.1.2 Introducing a known feed compliance using a compliant knife carrier

The second important experimental requirement for testing dig-in stability was having a known compliance in the feed direction, a single-degree of freedom system that would allow the knife to deflect in the feed direction. A feed-compliant knife which fits in the existing knifeholder was designed to meet this experimental requirement. This section discusses the design, and the design drivers that led to the design shown in Figure 5.7.

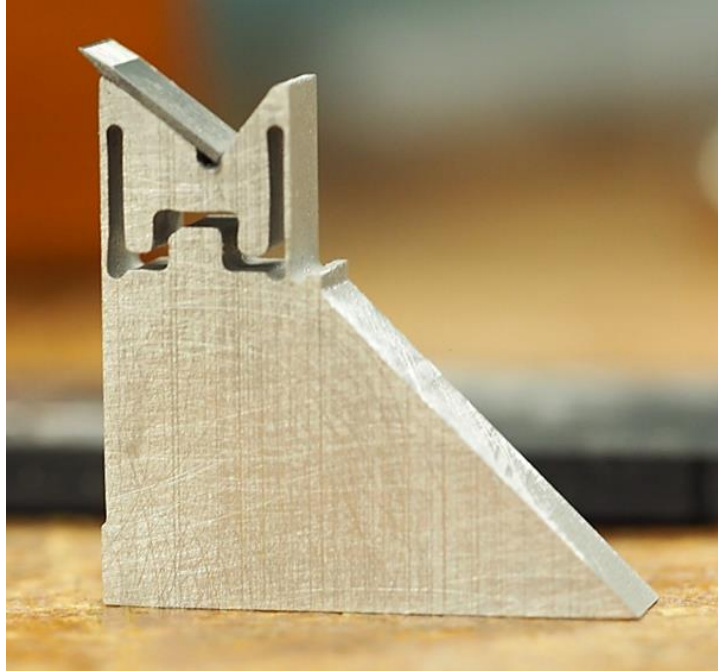


Figure 5.7: Compliant knife used for dig-in stability testing. The body contains a set of flexures providing single-degree-of-freedom motion in the feed direction, and the cutting edge is a glued-in insert cut from a commercially available microtome blade.

A variant of this design which omits the flexures was also fabricated, and discussed in Section 5.1.2.7.

#### 5.1.2.1 *Compliant knife requirements*

The dig-in stability experiment requires a known feed stiffness; this was done by introducing a “weak link” in the machine’s structural loop via a compliant knife. The stiffness of the knife must be chosen such that the transition in behavior between stable and unstable behavior is observable before the force sensor saturates. The requirements are summarized in the following bullet list, and are discussed in-depth in the next paragraphs.

- The design should result in dig-in cutting forces, i.e., the feed force generated during cutting should pull the knife into the workpiece.
- The design should be a single degree of freedom system, and be compliant only in the feed direction.

- The design stiffness should be such that dig-in instability behavior is observed before force sensor saturation.

The available cutting data from sources such as [44] and [51] are useful for getting a general idea of cutting behavior in polymers, but not necessarily for making accurate quantitative predictions about cutting forces, since the cutting conditions reviewed in these studies were for machining conditions. Microtome cutting conditions are going to be at much smaller depths of cut and at lower cutting speeds. Reviewing cutting data in acetal resin from [44] suggests that digging-in depends on the rake angle, depth of cut, and cutting speed. For the range of depths and cutting speeds closest to those relevant to sectioning, the critical rake angle is expected to be at around 19°; higher rake angles have a larger negative specific feed pressure (i.e., they generate a larger pull-in force per unit width and depth of cut). Reviewing the Delrin cutting data from [51] suggests that specific feed pressures of around -10 to  $-20 \frac{N}{mm^2}$  are expected for rake angles of 25 and 30 deg, respectively. Initial cutting tests with the instrumented cutter measured a specific feed pressure of  $-26.3 \frac{N}{mm^2}$  and a specific cutting pressure of  $141 \frac{N}{mm^2}$  with a rake angle of 45 deg. The latter set of specific feed pressures were chosen as they would yield a more conservative design with regards to force sensor saturation.

The design stiffness should be such that the dig-in behavior is observed before the force sensor's saturation limit is reached (force sensor saturation limits were discussed in Section 4.9.1.4). To know if the saturation limit will be reached, the specific cutting pressure is required in addition to the specific feed pressure, since both the feed and cut forces contribute to reaching the saturation limit. A target feed (a.k.a. depth of cut, or uncut chip thickness) must be chosen to calculate the predicted forces; during preliminary testing with Delrin specimens with negative specific feed pressures, reducing the feed would ultimately cause the sign of the specific feed

pressure to change and increase in magnitude. Feeds smaller than about  $1 \mu m$  would not be observed to remove material, and had high positive feed forces; cutting videos suggested that the knife was rubbing the surface of the workpiece rather than cutting. This effect is most likely due to the knife's edge radius as the depth of cut approaches the size of the edge radius. This effect was observed to occur for feeds smaller than about  $5 \mu m$ . Too small of a feed is also difficult to observe on the microscope. Too large a feed is also undesirable, since fewer cuts could be taken from a specimen, and could also cause earlier force sensor saturation. Ultimately a feed of  $10 \mu m$  was chosen to strike a balance between these.

As a practical concern, the design should be usable in the machine without requiring significant retooling or recalibration; i.e., the knife tip of the compliant knife should be at the same location as it would be for a  $25.4 \text{ mm} \times 25.4 \text{ mm}$  (1" by 1") wedge triangle knife, where the force sensor was originally calibrated. The design should also be reasonably simple to fabricate, in the event that iteration was required.

The different design criteria were entered into a spreadsheet to generate an acceptable range of target stiffness design values. Choosing a series stability limit between 1 and 2  $mm$  width of cut was ideal. These resulted in feed stiffnesses of  $53 \frac{N}{mm}$  and  $105 \frac{N}{mm}$ , respectively. The next step was then to design a concept for the compliant knife with a stiffness in this range, and whether or not this would be feasible to fabricate while still fulfilling the other requirements.

#### *5.1.2.2 Compliant knife design and stiffness model*

The compliant knife carrier is a parallelogram leaf spring flexure stage. To obtain the stiffness of the knife carrier the stage is modeled as being supported by two fixed-guided beams in parallel.

Aluminum was chosen over steel because using steel and also obtaining the required stiffness would have made the geometry too small for the waterjet to produce the required features reliably.

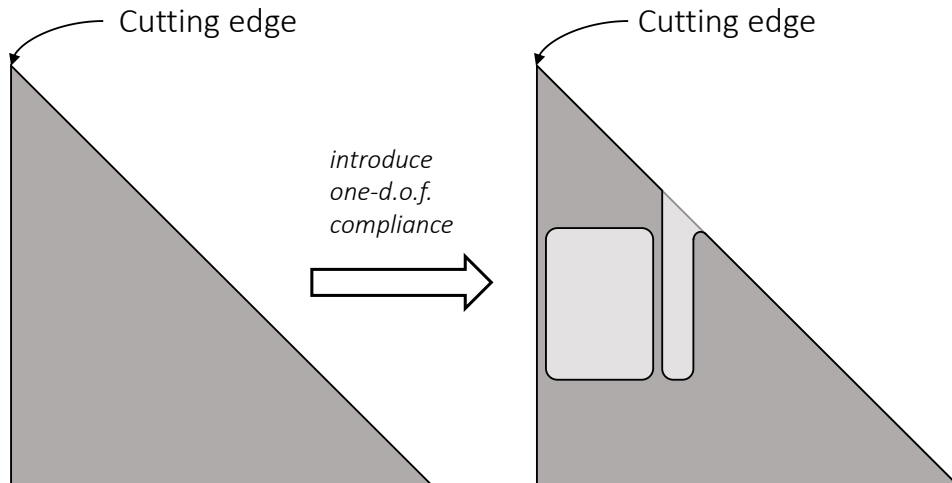


Figure 5.8: Compliant knife concept – introduce a single degree-of-freedom compliance while maintaining the profile of a 45°-45°-90° wedge knife. This avoids modification to the knifeholder hardware or force sensor recalibration

The analytical model for the stiffness of the compliant knife was derived by modeling the compliant knife as two fixed-guided beams acting in parallel; each beam's stiffness is given by

$$k_{FG} = \frac{12EI}{L^3} \quad (5.1)$$

With two beams acting in parallel, the net feed stiffness is given by

$$k_f = 2k_{FG} \quad (5.2)$$

Note that because the beams are deep compared to their thickness, the plane-strain Young's Modulus formula is used in the stiffness calculation [52]:

$$E_{Al.ps} = \frac{1}{1 - \nu^2} E_{Al} \quad (5.3)$$

The full list of parameters and outputs are given below in Table 5-3

Table 5-3: Compliant knife design parameters

<b>Parameter</b>	<b>Value</b>	<b>Unit</b>	<b>Description</b>
$E_{Al}$	69	$GPa$	Young's modulus, aluminum
$b$	6.4	$mm$	Beam depth
$L$	7.1	$mm$	Beam length (includes fillets)
$t$	0.3	$mm$	Beam thickness
Intermediate calculations			
$I$	0.015	$mm^4$	Area moment of inertia
$E_{AL,PS}$	76.9	$GPa$	Plane strain Young's modulus, aluminum
$k_{FG}$	38.5	$N/mm$	Stiffness of single fixed-guided beam
Output Calculations			
$k_f$	76.9	$N/mm$	Net feed stiffness of compliant knife

### 5.1.2.3 Compliant knife body fabrication

The body of the compliant knife was cut on an OMAX Micro-Max abrasive waterjet from 6.35 mm (1/4" inch) 6061-T6 aluminum plate stock. After waterjetting, both sides of the knife carrier were lightly sanded against 200 grit sandpaper backed by a granite surface plate until the scratches were uniform across the surface; this was done to remove the non-uniformity present in the extruded plate stock (the plate is slightly dished and is higher at the edges than at the center of the plate).

### 5.1.2.4 Disposable knife insert fabrication

The compliant knife cutting edge was cut from commercially available microtome blades, Sturkey Premium High Profile microtome blades, and glued to the compliant knife bodies using Loctite 401 adhesive. To cut the blades, a sacrificial fixture was designed that would hold the blades in place with double-sided tape while the inserts were cut on the abrasive waterjet (Figure 5.9a). The cartridge would remain in one piece after cutting (Figure 5.9b), and the cut blades

would be peeled away from the cartridge using a pair of tweezers (with a drop of isopropyl alcohol, if the tape offered too much resistance) prior to being assembled on to a compliant knife.



(a)



(b)

Figure 5.9: Microtome cutting blades on sacrificial waterjet cutting fixture (a) before being cut (b) after being cut. Knives remain stored on the fixture until they are needed.

The sacrificial cartridges are printed on a Sindoh 3DWox 3D printer out of black PLA. The fixture was designed with three bumps to locate the blade. A small bar magnet was found to be extremely useful for handling and positioning the blades; special care was taken to ensure to not touch the edge against anything, both for safety reasons and to prevent damaging the edges. The blades are carefully wiped with soap and then isopropyl alcohol; they are then pressed into the cartridge and held firmly in place by the tape. The cutting path was set up such that the knife

and fixture would remain in one piece after cutting (i.e., no parts would come loose).

Immediately after being cut on the waterjet, the cartridge was rinsed with tap water to remove any residual abrasive, and a paper towel was blotted on top of the cartridge to soak up the water; the cartridge was then gently air dried with compressed air. Each cartridge yielded eleven usable cutting inserts.

#### *5.1.2.5 Compliant knife assembly*

To remove a knife insert, the knife would be soaked in isopropyl alcohol (IPA) for a few minutes, after which the used blade was pried off with tweezers. The bulk of the remaining glue on the compliant knife body would be peeled off with tweezers, and any remaining glue would be rubbed off with IPA. The knife insert contact area was then lightly roughened with 180 grit sandpaper, followed by cleaning with soap (Simple Green Crystal) and an IPA rinse.

To prepare a new knife insert for gluing, a fresh insert was removed from the blade cartridge with a pair of tweezers. Subsequently, all handling of the blade was performed by using a small stick magnet of about 3 mm by 3 mm by 25 mm to avoid having the edge come into contact with anything. The face of the knife insert which was the exit side of the waterjet cutter is lightly deburred with sandpaper to remove the burr left behind from waterjetting. The contact face of the knife insert is then lain flat against the sandpaper and roughened up. The insert is then cleaned with soap and IPA.

Once both surfaces have been prepped, the compliant knife and knife insert are both lain flat against a granite surface plate with a sheet of parchment paper on top to provide a non-stick surface. A drop of adhesive is placed on the compliant knife body contact face, and the knife insert is slid into place. Pressure is applied to the joint from both sides for about 30 seconds. The



assembly is then left to cure for 24 hours. A schematic of the gluing assembly is shown in Figure 5.10.

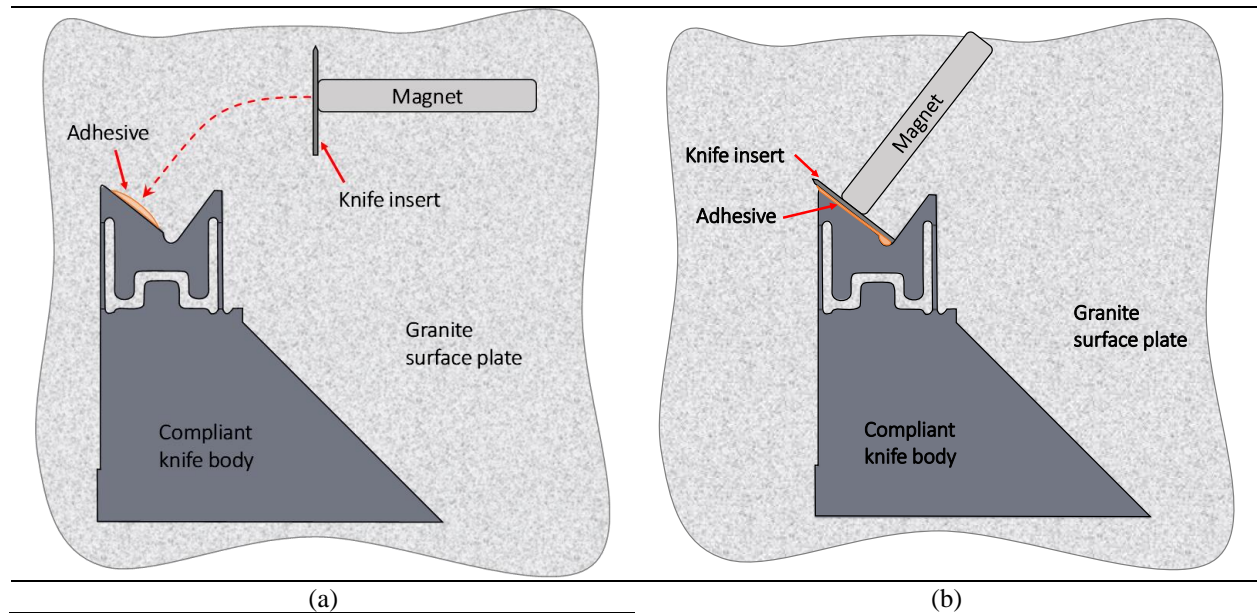


Figure 5.10: Schematic of compliant knife and knife insert assembly process

This process could potentially be optimized with the use of a gluing jig, but this manual method was found to work well for the low quantities involved.

#### 5.1.2.6 Compliant knife characterization

To measure the compliant knife's stiffness, the knife would be excited across a range of frequencies to find the knife's resonant frequency, and the stiffness would be derived based on the system's mass properties. Simultaneous force application and displacement measurement was required this; to fulfill this need, a co-located force application and displacement measuring apparatus was designed. A small forcing coil was wrapped around a capacitive displacement probe; these would both be mounted in a body that would hold the capacitive probe relative to the force coil, and could be clamped in place in the workholder. A flat square magnet (K & J

Magnetics B4401) 6.35 mm [1/4"] side width and 0.794 mm [1/32"] thick provided both a measurement target for the displacement probe (LION Precision C6 probe feeding into a DMT-22 signal conditioner), and a magnetic field to push against. A schematic of the apparatus is shown in Figure 5.11.

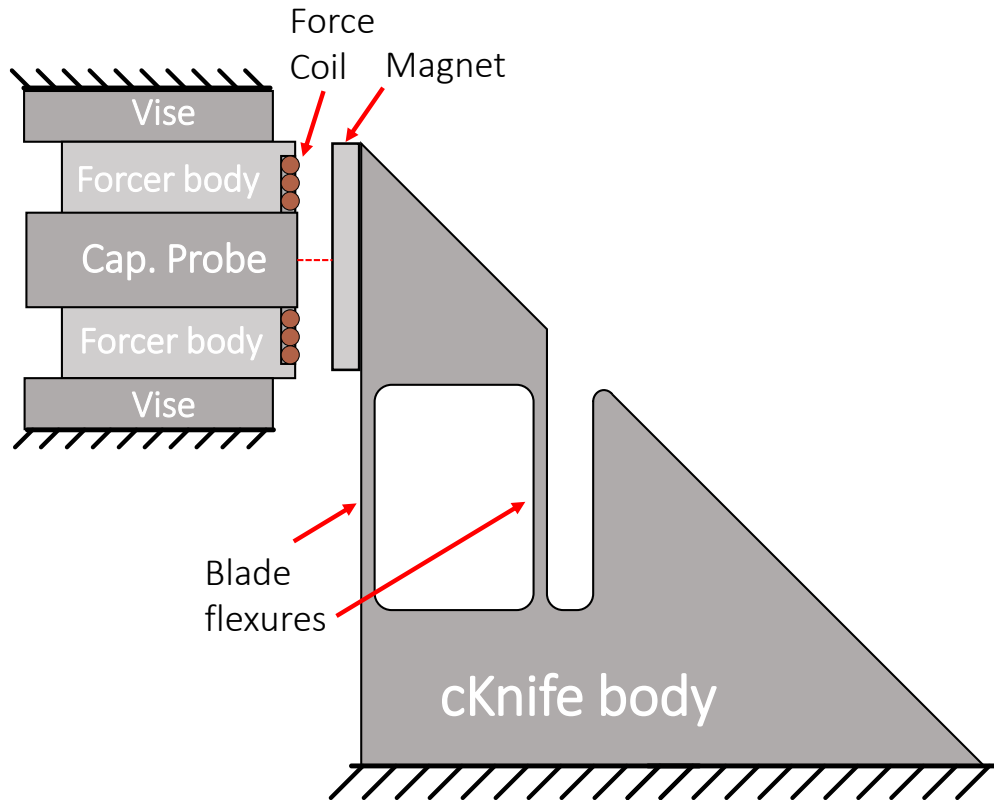


Figure 5.11: Schematic of compliant knife characterization setup. A small electromagnetic coil wrapped around a capacitive displacement probe provides excitation and measurement to characterize the cKnife's resonant frequency

An HP 35665A Dynamic Signal Analyzer was used to generate the frequency sweep, an OPA548 amplifier was used to drive the forcing coil, and the compliant knife's displacement response was recorded using the capacitive probe. The frequency sweep range was selected based on where the resonant peak of the compliant knife was expected to be based on modeled stiffness value and where the stiffness could be given plausible manufacturing error. The

frequency sweep range was set to 300 Hz – 2200 Hz, with 400 points (4.75 Hz increment). A signal generator was also used to fine-tune the exact location of the resonant peak.

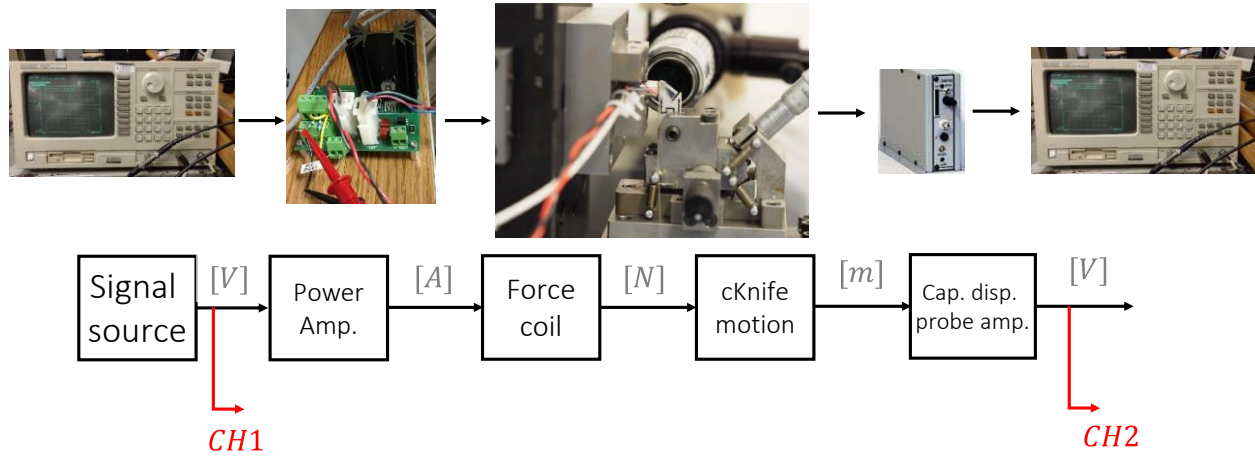


Figure 5.12: Compliant knife stiffness characterization setup signal block diagram

Figure 5.13 is a photograph of the forcer, sensor, and compliant knife.

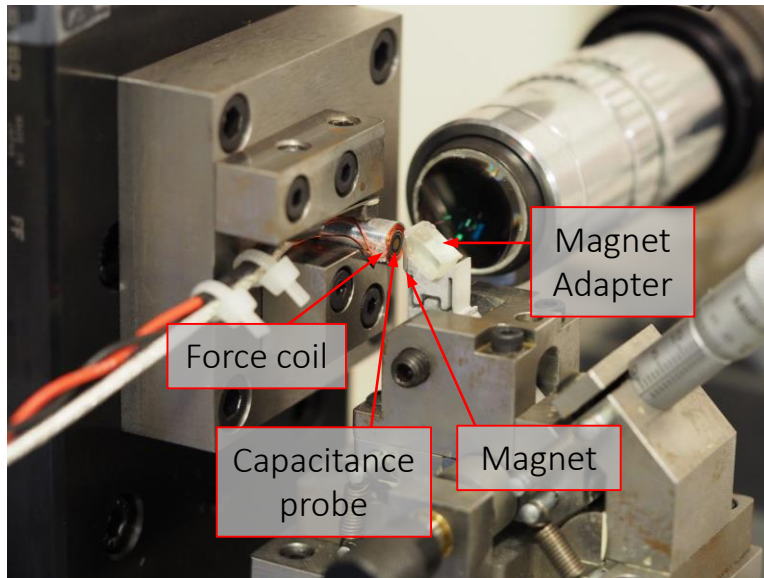


Figure 5.13: Photograph of compliant knife characterization setup: the exciter is clamped in the vise where a specimen would be during cutting, and the compliant knife with magnet adapter instead of a knife insert is clamped in the knifeholder. The gap has been exaggerated to show the forcer and capacitance probe more clearly.

The transfer function of the compliant knife is shown in Figure 5.14. A single resonance is evident at 1022 Hz.

## Compliant knife dynamic response magnitude

*TRAC105.MAT, 1 V source*  
*pk*

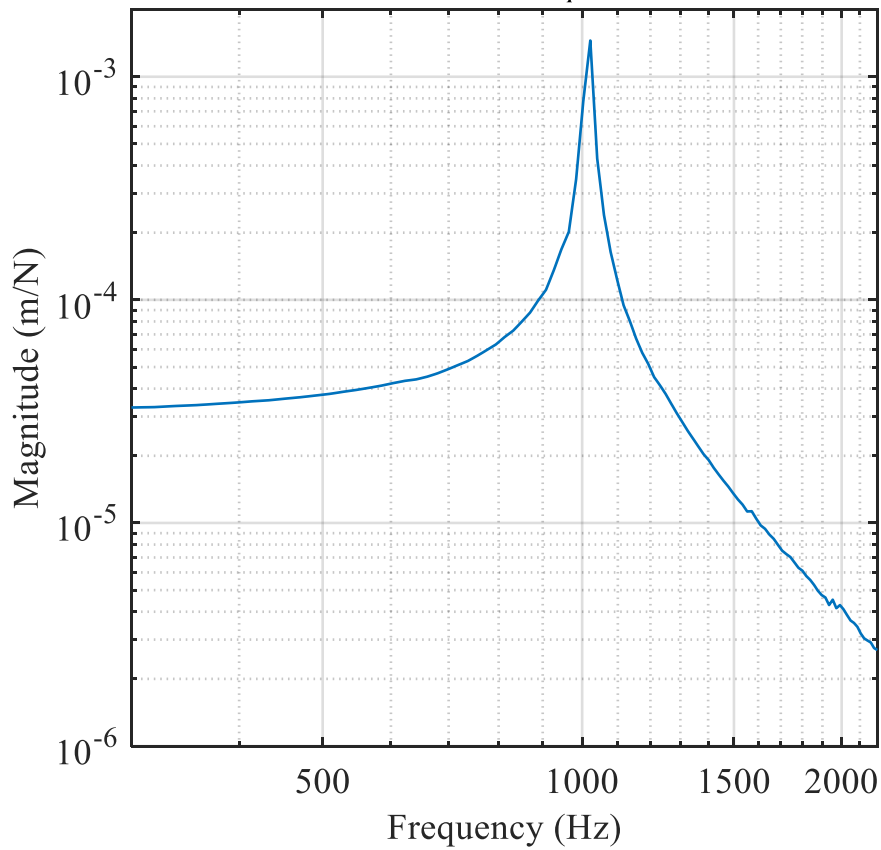


Figure 5.14: Compliant knife dynamic response magnitude. The resonant peak occurs at 1022 Hz.

Manual measurement using a function generator to provide the source and oscilloscope to measure the response confirmed 1017 Hz as the resonant peak. The stiffness is calculated from the resonant frequency,

$$k = m\omega_n^2 = 4m(\pi f_n)^2 \quad (5.4)$$

The vibrating mass must be known prior to calculating the stiffness. The moving mass breakdown for the compliant knife is given in Table 5-4.

Table 5-4: Contributors to compliant knife moving mass, to be used in stiffness calculation

Part	Mass (g)	Comment
Magnet and adapter	0.5	Measured using a lab scale
Adhesive drop	0.055	Approximated as 1 metric drop; specific gravity of Loctite 401 = 1.1
Compliant knife moving body	0.61	Calculated in CAD model, density 1200 kg/cu m (6061-T6 Al)
Half of compliant knife flexures	0.031	Assume only half of the mass of the flexures participates in the motion
TOTAL	1.2	

With these values, the measured stiffness of the compliant knife is calculated to be 49.0 N/mm.

### 5.1.2.7 Knife carrier without added compliance

A variant of the compliant knife design was also designed and fabricated, which omits the flexures and so avoids the additional feed compliance, but is otherwise identical (Figure 5.15).

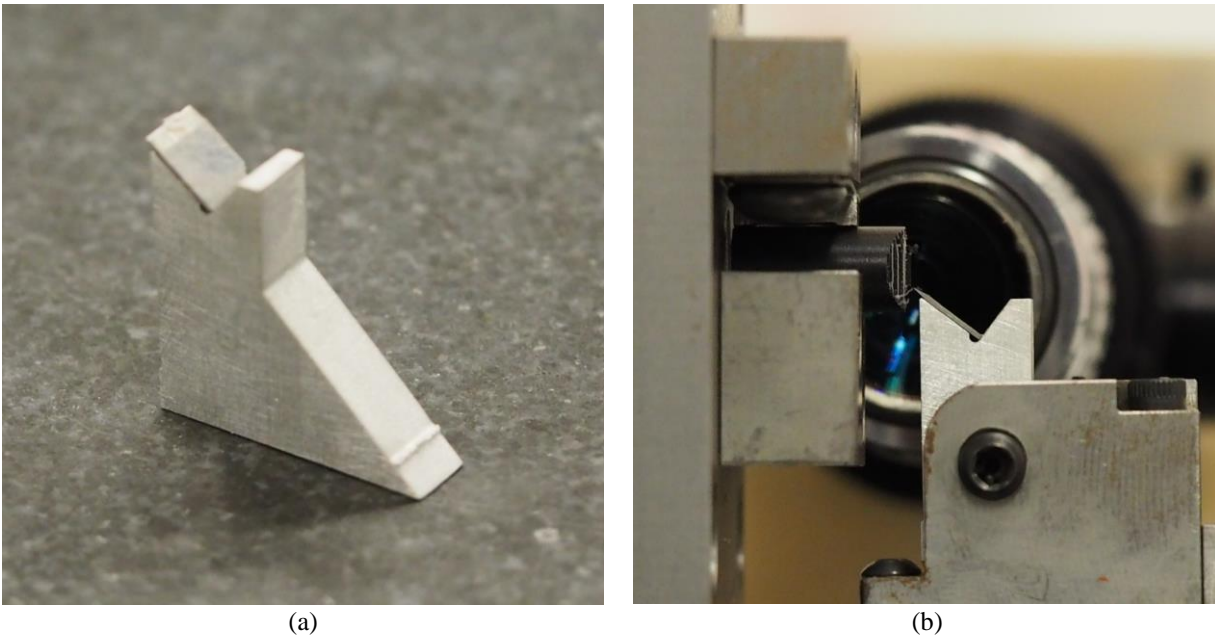


Figure 5.15: Knife carrier without added compliance (a) freestanding, shown with some Acrylic cutting debris (b) shown mounted in cutting machine while cutting an acetal resin sample

## 5.2 Stepped-width specimen cutting experiment data processing

The force data gathered in the cutting experiments is used to assess the dig-in stability and to quantify the dig-in sensitivity via the change in force variance with cutting width. The following sections describe how the data is analyzed in each case.

### 5.2.1 Specific feed pressure ( $K_f$ ) measurement

As a preliminary step, the specific feed pressure for the cutting run must be calculated as the exact value of the specific feed pressure is not known in advance. The forces generated during the cuts made at the smaller cutting widths are used to calculate the specific feed pressure (too large of a width would cause the depth of cut to change as the compliant knife deflects, introducing error into the calculation).

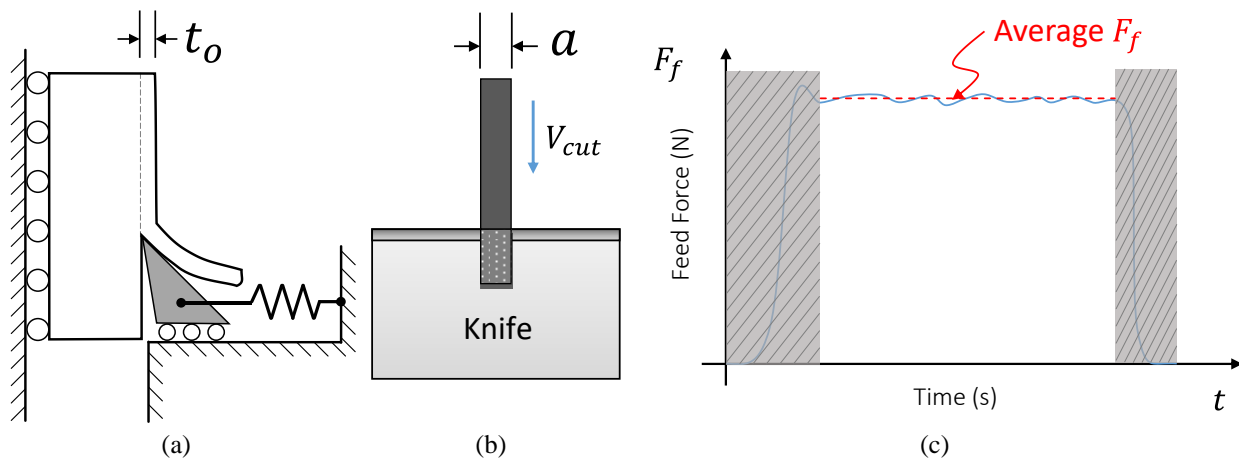


Figure 5.16: Calculating the specific feed pressure from measured cutting forces. (a) Side view of the calibration cut, showing the nominal feed  $t_o$  (b) Front view of the cut, showing the width of cut  $a$  (c) Resulting force trace. The entry and exit portions of the trace are trimmed. The average of the remaining data points,  $F_{f,avg}$  is used to calculate  $K_f$  together with  $a$  and  $t_o$

The specific feed pressure is then calculated from

$$K_f = \frac{F_{f,avg}}{at_o} \quad (5.5)$$

where  $a$  is the cutting width,  $t_o$  is the depth of cut (feed), and  $F_{f,avg}$  is the feed force.

## 5.2.2 Cutting variance increase with cutting width

A second effect predicted to occur when cutting in the dig-in (negative  $K_f$ ) regime is that the cutting system will become more sensitive to variation in the cutting parameter; for example, a change in  $K_f$  (perhaps due to material inhomogeneity, hitting a “hard spot”) will cause a much larger change in the knife position (and the resulting local section thickness) at a larger width of cut than for a smaller width of cut; this effect was described and modeled in Section 3.2.3.2. The sensitivity of the feed force and feed position to parameter variation is expected to increase with the cutting width. A schematic of the expected behavior is shown below in Figure 5.17. As the cutting width progresses, the standard deviation is expected to increase with increasing width of cut.

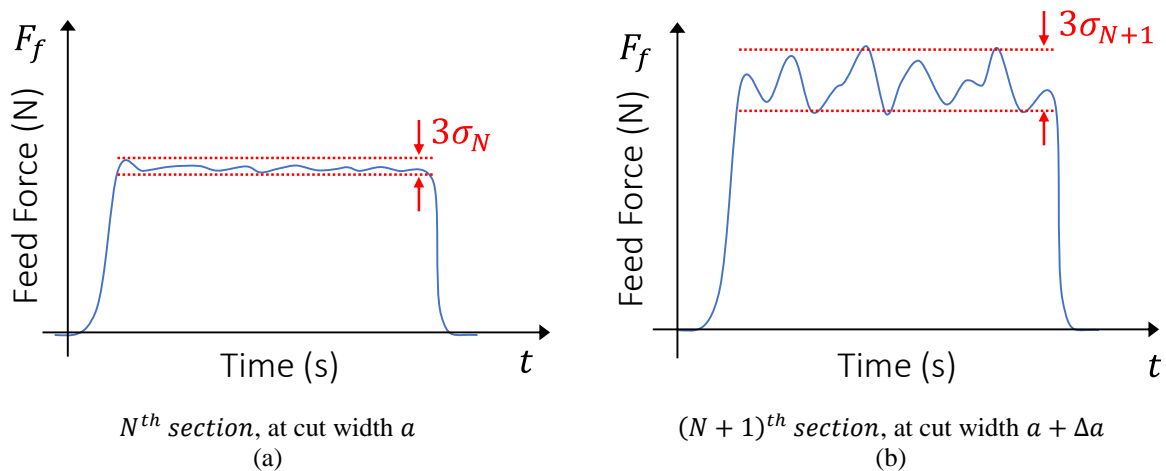


Figure 5.17: Schematic of force traces with increasing feed force variation as cut width increases (a) force trace of cutting on the  $N^{th}$  section, at a cut width of  $a$ ; (b) force trace of cutting on the  $(N + 1)^{th}$  section, with a larger cut width  $a + \Delta a$ . In the latter force trace, the force swings are larger, and the average force magnitude has increased.

The feed force mean and standard deviation is calculated for each cut, excluding the entry and exit portions of the cut. The standard deviation of the cut is then plotted against the cutting width, and compared against the expected behavior, Figure 5.18 shows a schematic of the



expected progression of the feed variance as cutting width increases. The green line represents the largest feed position standard deviation at a given cut width, and the red line represents the smallest feed position standard deviation at a given cut width.

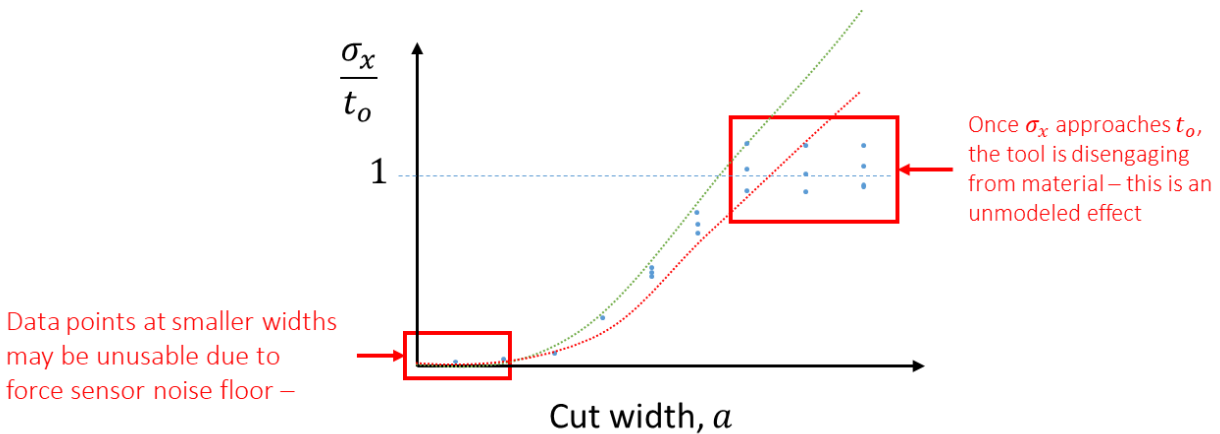


Figure 5.18: Schematic of the expected cutting variance progression with cutting width. The vertical axis plots the ratio of the standard deviation of the cut, to the nominal feed. At lower widths of cut, the cutting width may be small enough that the resulting forces aren't significantly higher than the noise floor. At larger widths of cut, the amount of variations exceeds the nominal feed, which means the tool will be disengaging from the material, which is not a modeled effect.

In building the plot, reasonable estimates of parameter variations have to be made.

### 5.2.3 Uncertainty estimates and measurements

To numerically implement the uncertainty propagation model requires measurements or estimates of the variances of the variables involved. Table 5-5 summarizes the uncertainty estimates used to numerically implement the feed position uncertainty propagation model for the stepped-width experiment.

Table 5-5: Summary of uncertainty estimates for modeling feed variance propagation

Parameter	Value	Unit	Description
$\sigma_{Kf}$	1.5	$N/mm^2$	Specific feed pressure uncertainty
$\sigma_{kf}$	0	$N/mm$	Feed stiffness uncertainty
$\sigma_{to}$	0.5	$\mu m$	Nominal feed uncertainty
$\sigma_a$	1.4	$\mu m$	Cutting width uncertainty
$\sigma_{xr}$	1.0	$\mu m$	Initial surface standard deviation

The following sections discuss how these estimates or measurements were performed.

### 5.2.3.1 Feed stiffness uncertainty $\sigma_{kf}$

The feed stiffness variance  $\sigma_{kf}^2$  is assumed to be zero for the initial variance propagation model. In Section 6.4 this assumption is revisited, and reasoning is given for why this variation is more important than was initially assumed, due to unmodeled effects.

### 5.2.3.2 Nominal feed uncertainty $\sigma_{to}^2$

The value for the nominal feed uncertainty is taken from the slice stage's running parallelism specification; the VRU 6160 crossed roller table is specified for  $3 \mu m$ . Assuming the error is randomly normally distributed, this error range corresponds to potential deviations of  $\pm 3\sigma_{to}$  or a total of  $6\sigma_{to}$ . Setting this equal to the running parallelism specification and solving for  $\sigma_{to}$  yields  $\sigma_{to} = 0.5 \mu m$ .

### 5.2.3.3 Cutting width variance $\sigma_a^2$

The variance in the cutting width  $\sigma_a^2$  is estimated by inspecting the machined specimen sidewalls with the microscope. Machining marks are apparent on the surface, and it is possible to focus on the high and low spots of the machined surface by moving the microscope along the optical axis using the hexapod; the recorded displacement required to shift focus from the high spots to the low spots is taken as the measurement of the surface height. A rough scan of a specimen sidewall at the  $100 \mu m$  cutting width, stopping to measure whenever a larger

machining mark is apparent, measured the largest peak-to-valley distance at approximately  $5 \mu m$ . If we assume that this corresponds to the  $6\sigma$  value for one side, then the standard deviation of one side of the specimen is  $0.83 \mu m$ . Considering that both sides of the specimen will have this variation, the net variance in the specimen width is  $2 (0.83 \mu m)^2 = 1.4 \mu m^2$ , corresponding to a  $\sigma_a$  value of  $1.4 \mu m$ .

#### 5.2.3.4 Initial surface variance $\sigma_r^2$

An initial regenerative variance  $\sigma_{xr}^2$  is required for the numerical implementation of the variance propagation; after the first cutting pass, the resulting net variance  $\sigma_{xeq}^2$  in the steady-state feed equilibrium position is taken as the  $\sigma_{xr}^2$  of the following pass. The initial value corresponds to an initial roughness of the surface that would contribute to offset from the nominal feed. If the cutting system is series stable, the effect of this initial uncertainty quickly dissipates (within a few cutting passes). For numerical modeling, the initial seed value is assumed to be due to the initial roughness of the surface from machining. The same surface measurement value from the  $\sigma_a$  measurement for one side of the specimen, rounded up, is used for the initial value of  $\sigma_{xr}$ .

#### 5.2.3.5 Specific feed pressure variance $\sigma_{Kf}^2$

The  $K_f$  uncertainty was estimated by finding the magnitude of  $\sigma_{Kf}$  that would explain the observed feed force measurement variance, given measurements and estimates for  $\sigma_a$ ,  $\sigma_t$ , and the measured noise in the sensors. For this estimation it is assumed that the total feed  $t$  is equal to the nominal feed  $t_o$ ; that is to say, there is no additional “dig-in” or “push-out” due to cutting system compliance.

$$F_f = K_f a t + F_{f.noise} = K_f a t_o + F_{f.noise} \quad (5.6)$$

The feed force variance is given by

$$\sigma_{F_f}^2 = (a t)^2 \sigma_{K_f}^2 + (K_f t)^2 \sigma_a^2 + (K_f a)^2 \sigma_{t_o}^2 + \sigma_{F_f.noise}^2 \quad (5.7)$$

All of the quantities in this expression are known or measured except for  $\sigma_{K_f}$ , therefore this expression was rearranged to solve for  $\sigma_{K_f}$ :

$$\sigma_{K_f}^2 = \frac{\sigma_{F_f}^2 - (K_f t)^2 \sigma_a^2 - (K_f a)^2 \sigma_{t_o}^2 - \sigma_{F_f.noise}^2}{(a t)^2} \quad (5.8)$$

This estimation was performed for two datasets, the non-compliant knife cutting test. Other parameters used were  $t_o = 10 \mu m$ ,  $\sigma_a = 1.4 \mu m$ ,  $\sigma_{t_o} = 0.5 \mu m$ .

Table 5-6: Specific feed pressure variance calculation, rigid knife dataset

$a$ (mm)	$\sigma_{F_f}$ (N)	$K_f$ (N/mm <sup>2</sup> )	$\sigma_{K_f}$ (N/mm <sup>2</sup> )
0.1	0.0028	-14.9	1.75
0.2	0.003	-14.6	1.48
0.3	0.0034	-13.5	1.38
0.4	0.0049	-16.5	1.36
0.5	0.0045	-9.6	1.62
0.6	0.005	-9.4	1.59
0.7	0.0054	-10	1.43
0.8	0.0061	-10.3	1.4
0.9	0.0065	-10.3	1.34
1.0	0.007	-10.3	1.31
<i>AVG</i>			1.47
<i>STDDEV</i>			0.14

The average value of  $\sigma_{K_f} = 1.5 \text{ N/mm}^2$  is taken as the estimate of the variation in the specific feed pressure.

## **5.3 Series cutting instability onset indicators**

This section discusses the expected cutting behavior indicative of the onset of unstable series cutting to be used in analyzing the data generated from the stepped-width specimen cutting experiment. Of the signaling criteria, only skip sections are immediately obvious in real time; tracking the trends in the mean cutting force could in principle be done immediately after cutting each section, but for these experiments they were done via post-processing analysis of the data after the entire dataset was collected. Series cutting with alternating thick and thin sections is noticeable indication of a cutting system approaching (but not yet past) the series cutting stability limit.

### **5.3.1 Skip sections**

Skip sections will only occur when the system has already become series-unstable; see for example Figure 3.12. This criterion is not useful for signaling the onset of instability, however; depending on the degree of instability (that is, how much wider the current cutting width is compared to the series stability limit), this may take a few to many cuts to manifest. This criterion is the most useful and obvious for real-time stability assessment, but may take several cuts to become apparent.

General skip-section behavior was described in Section 3.2; the primary characteristic to look for is a complete drop in the cutting force magnitude between a pair of successive cutting forces, the latter cutting pass having a cutting force magnitude of zero for the entire duration of the cut. Figure 5.19 shows a schematic of the behavior of the feed force when a skip-section occurs.

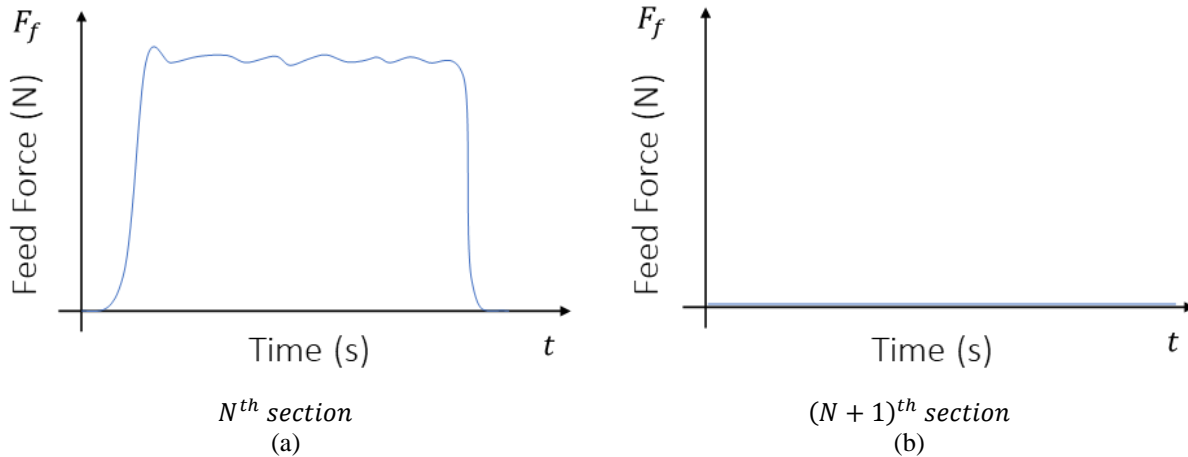


Figure 5.19: Schematic of force traces expected for a skip-section event, which would only occur after the series has gone unstable. (a) A typical feed force vs time plot (b) The subsequent section, which has zero or near-zero force, due to the previous section removing more than a nominal feed's worth of material

Physically, what has happened is that due to the dig-in phenomenon, the former cut has “dug in” and removed at least one extra nominal feed. After the former cut completes and the machine moves forward one feed's worth for the next cut, there is no material for the knife to engage because this material was removed during the prior pass. The cutting width at which the skip-section event occurs is compared to the maximum stable cutting width prediction made in Equation (3.32(3.22)). The cutting videos are used to confirm whether or not the cutting tool has completely missed the material.

### 5.3.2 Increasing magnitude of mean force difference between successive sections

Once the system cutting width passes the threshold for stable series cutting, the mean force will no longer converge to a steady-state value; the offset from the nominal feed will continue to oscillate with increasing magnitude. This behavior could be measured by calculating the magnitude of the difference between the mean feed force of successive cut; when the system has gone unstable, this value will continually increase. One potential issue with this however is that the mean feed force may not be clearly defined as the stability limit is approached – the

increasing variance of the feed force may lead to erratic cutting and a poor mean force measurement.

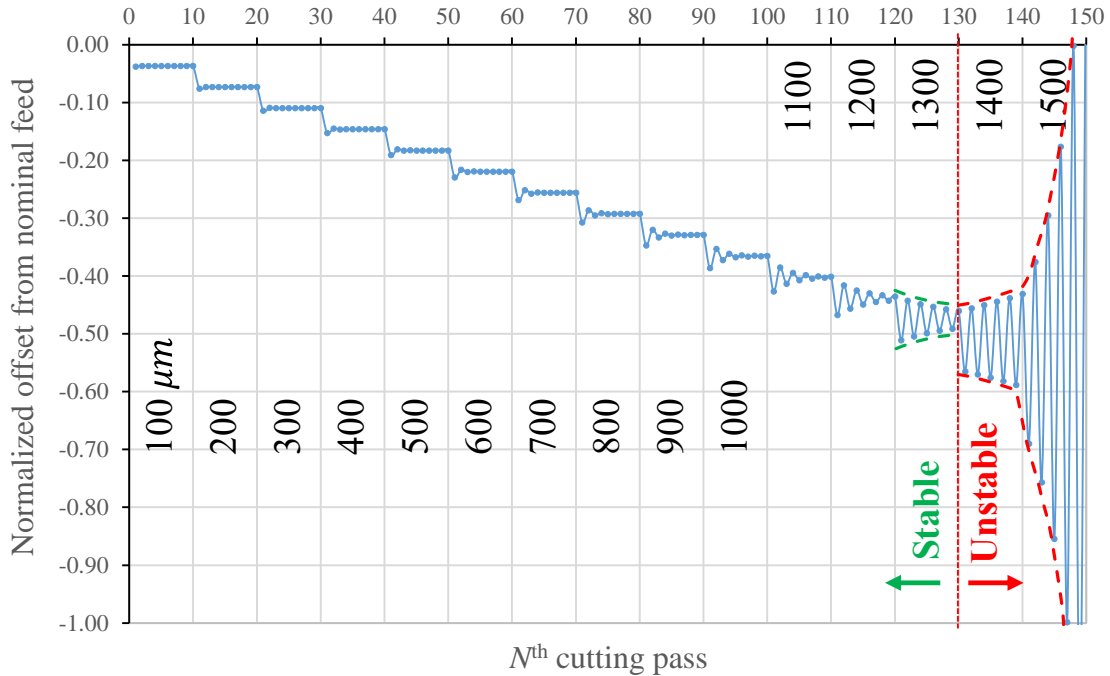


Figure 5.20: Numerical implementation of the normalized offset from nominal feed for incrementing width of cut, versus cutting pass. Cutting width (in  $\mu m$ , shown inset) is held constant for 10 cuts, and is then incremented by  $100 \mu m$ . As the system approaches stability, the steady state offset takes more cuts to settle down (green dashed line).

### 5.3.3 Feed position standard deviation increases each cut

The last signal uses the fact that the feed force variance, once the system has crossed into the unstable regime, will monotonically increase pass-over-pass – contrast this to a stable system, where the variance should eventually reach a steady state value. As the stability limit is approached it may be difficult to differentiate between a stable system that is taking many passes to stabilize to a steady-state value, and a system that has gone unstable and is increasing each cutting pass.

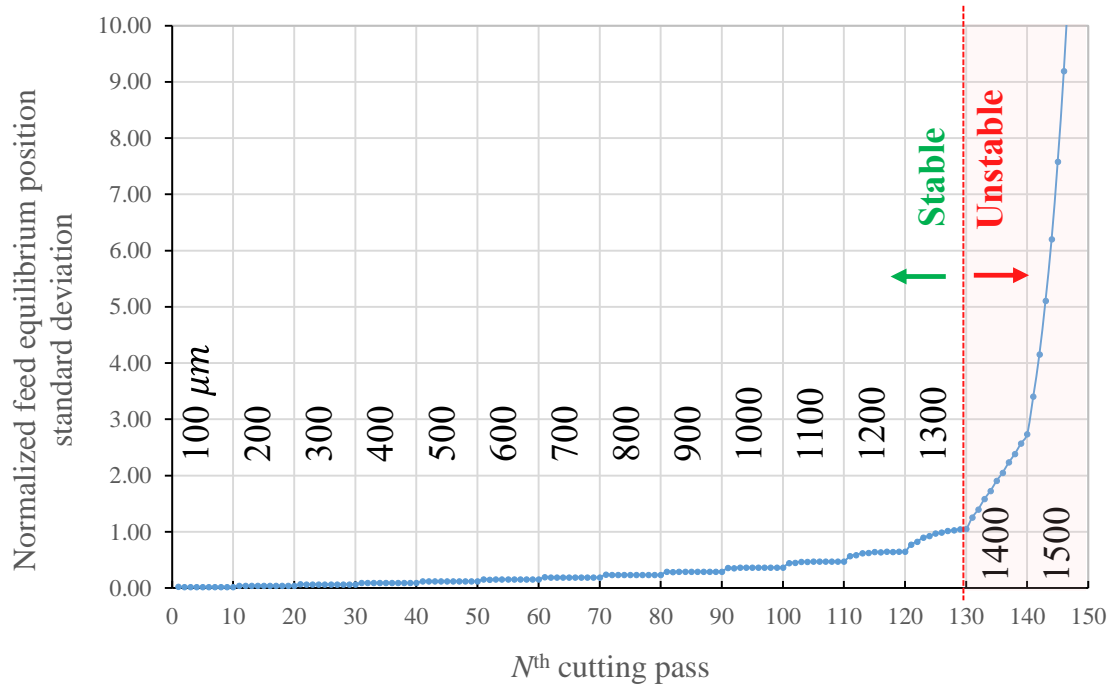


Figure 5.21: Numerical implementation of the normalized feed position standard deviation vs cutting pass. The standard deviation is normalized against the nominal feed  $t_o$ . Cutting width (in  $\mu m$ , shown inset) is held constant for ten cuts, then incremented by  $100 \mu m$ . Note that values of the standard deviation approaching 1.0 are troublesome, as this would imply that the tool is potentially exiting the cut, and deviations from modeled behavior would be expected here. When the system is unstable, the standard deviation will monotonically increase, pass-over-pass, and this growth is faster depending on how far over the stability limit the cutting width is.

Parameters for both Figure 5.20 and Figure 5.21 are given below.



Table 5-7: Parameters used to generate Figure 5.20 and Figure 5.21

<b>Parameter</b>	<b>Value</b>	<b>unit</b>	<b>Description</b>
$Kf$	-1.79E+07	$N/m^2$	Specific feed pressure
$kf$	4.90E+04	$N/m$	Feed stiffness
$a_{min}$	1.00E-04	$m$	Cutting width, min
$a_{max}$	1.5E-03	$m$	Cutting width, max
$a_{inc}$	0.1E-04	$m$	Cutting width increment
$N_{pass}$	10		Cutting passes per cutting width
$t_o$	1.00E-05	$m$	Nominal feed
$\sigma_a$	1.00E-05	$m$	Cutting width standard deviation
$\sigma_{Kf}$	8.95E+06	$N/m^2$	Specific feed pressure standard deviation
$\sigma_{kf}$	4.90E+03	$N/m^2$	Feed stiffness standard deviation
$\sigma_{xr}$	2.00E-06	$m$	Initial regenerative surface ('seed')
$\sigma_{t_o}$	1.00E-06	$m$	depth of cut stddev

## 5.4 Dig-in stability test without additional compliance

To compare the behavior of a system with a feed compliance and one without, the same stepped-specimen dig-in stability test as described in Section 5.1 is run, except that the flexureless version of the knife carrier is used instead of the knife carrier with flexures. This system is not expected to exhibit instability characteristics in the tested range of widths before saturating the force sensor.

## 5.5 Cutting with positive $K_f$ , in the push-out regime

The same test is run as described in Section 5.1 with the compliant knife, except that the workpiece is made of Acrylic instead of Delrin. This is expected to result in a positive specific feed pressure, based on cutting force measurements from [44]. The series stability model developed in Section 3.2.2 makes predictions about series cutting behavior when cutting with positive  $K_f$ , specifically that there is no dig-in series instability in the positive- $K_f$  regime.

## 5.6 Regenerative chatter cutting tests

The goal of these cutting tests was to test the regenerative chatter model developed in Section 3.4.2, and uses the same compliant knife carrier and stepped-width specimens as was used for the dig-in stability tests. A compliant knife with characterized dynamic characteristics was loaded into the cutting machine, and repeatedly cuts through a Delrin stepped-width specimen. After cutting through enough material, the specimen width will increase. Once the cutting width increased past the maximum stable width of cut given by Eqs (3.57) and (3.60) (for positive and negative specific feed pressures, respectively), it was expected that vibrations around the compliant knife's natural frequency would regenerate unstably – vibrations at this amplitude would continue to grow in amplitude and dominate the dynamic response of the

system, and continue to grow each pass. The vibrations should grow to the point where they could be heard audibly by the machine operator, and should leave visible waves on the cut surface.

However, a major difficulty with this model is that the damping ratio of system vibrations must be known in order to make predictions about the stability limit. Measuring the damping ratio of the compliant knife while it was vibrating in air was not adequate, as its vibration characteristics are likely different when the tool is in contact with the material (but could provide a worst-case value). A characterization experiment was devised to measure the damping ratio of the compliant knife when in contact with material.

### **5.6.1 Measuring damping ratio with acetal and compliant knife**

The cutting tool was cut into a Delrin specimen with a width of  $0.9\text{ mm}$ , at the usual feed of  $10\ \mu\text{m}$  but stopped approximately halfway through the cut to leave the tool in the workpiece. The back of the compliant knife was tapped several times with a small improvised mallet (a small Allen wrench was found to give clean hits and give good control) (Figure 5.22) while recording force sensor data; a sequence of several hits and responses was captured.

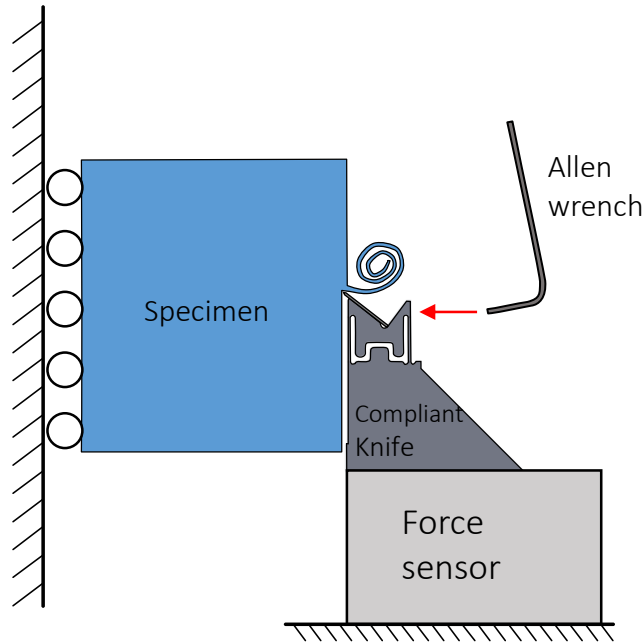


Figure 5.22: Schematic of buried-tool damping characterization; a cutting test with a compliant knife cutting a Delrin specimen was stopped approximately halfway through the cut, leaving the tool engaged in the material. A small Allen wrench is used as a mini-mallet to tap on the backside of the compliant knife; the resulting vibrations are recorded and used to measure the damping ratio for the vibrations during cutting.

The data was imported into MATLAB and inspected. Clean responses were extracted (mallet impacts with multiple bounces were excluded). The decaying transient exponential of the impulse response of the form (5.9) was used to calculate the system damping ratio. Each impulse response had a best-fit decay exponential envelope fitted to the data and had its natural frequency calculated. The damping ratio was then calculated from (5.10).

$$e^{-Bt} = e^{-\zeta\omega_n t} \quad (5.9)$$

$$B = \zeta\omega_n \quad (5.10)$$

A best-fit decay exponential was fitted to the data by using `findpeaks()` from the MATLAB Signal Processing Toolbox was used to locate signal peaks, then using `lsqnonlin()` from the MATLAB Optimization Toolbox to find the best-fit parameters for a decay envelope for each impulse data trace (Figure 5.23). The system's natural frequency was

calculated from the FFT by the frequency with the largest magnitude response. A damping ratio for each impulse response was calculated using each trace's natural frequency and best-fit decay coefficient  $B$ . The aggregated calculations are presented in Table 5-8.

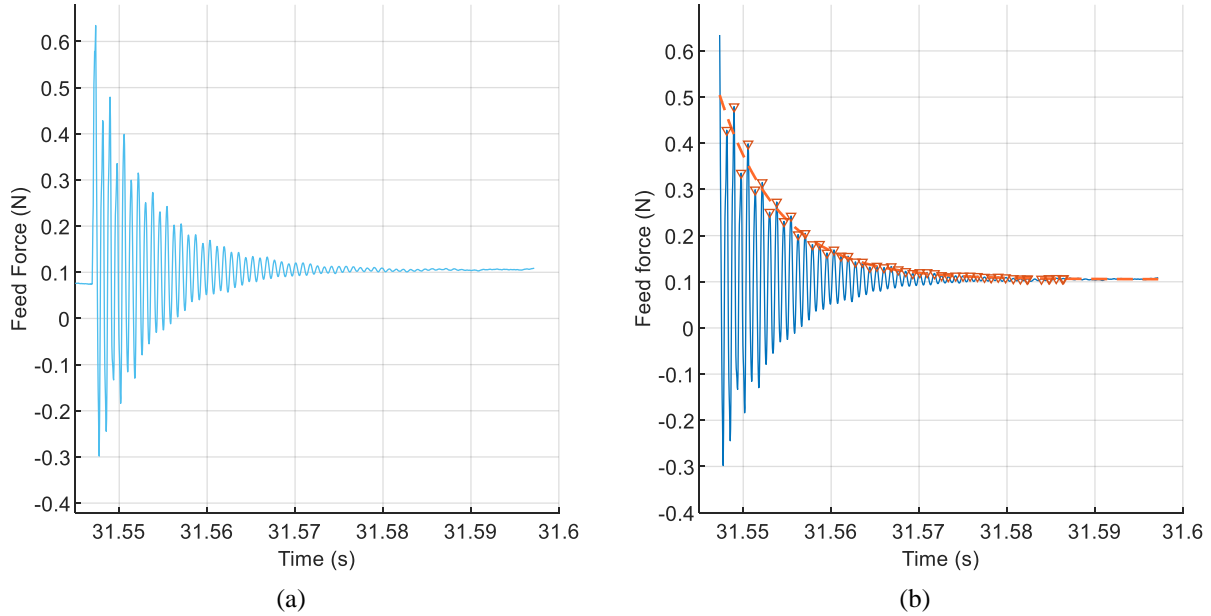


Figure 5.23: Impulse response of compliant knife, with knife buried in a Delrin specimen (a) an extracted impulse response from a series of mallet taps. (b) The same impulse response with a best-fit decay curve overlaid and peaks identified

Table 5-8: Measured experimental damping ratio for buried-tool vibrations measurement

Parameter	Value	Unit	Description
$N$	14	-	Number of traces included in calculations
<i>Natural frequency</i>			
Average	1227	Hz	Vibration response frequency, average
Standard deviation	6.5	Hz	Vibration response frequency, standard deviation
<i>Damping ratio</i>			
Average	0.0196	-	Calculated damping ratio average; 1.96%
Standard deviation	0.0030	-	Calculated damping ratio standard dev; 0.30%

The measured damping ratio could now be used as a better estimate of the system damping and could be used to model the maximum stable width of cut, in conjunction with the system feed stiffness  $k_f$  and the specific feed pressure  $K_f$  for the cut.

*(this page intentionally left blank)*

## DIG-IN STABILITY RESULTS AND DISCUSSION

---

The results of dig-in stability testing are presented in a roughly chronological order. The system was observed to be dig-in unstable at a cutting width between 400  $\mu\text{m}$  and 500  $\mu\text{m}$  corresponding to stability widths 71% to 63% smaller than predicted by the series dig-in stability model. After reviewing cutting videos and tracking down sources of additional compliance, this discrepancy was resolved to between 2% and 21%. An initially unmodeled localized tip compliance was determined to be responsible for the additional system compliance. The cutting behavior of the compliant knife is compared to the cutting behavior of a control knife which has no added compliance. Additional results for cutting that was not specifically related to dig-in stability, positive- $K_f$  cutting and regenerative chatter, are presented and discussed in Appendices A and B, respectively.

### 6.1 Cutting force data from dig-in stepped width cutting experiments

This section presents cutting force data from two datasets: cutting with a compliant knife and a stepped-width specimen, and cutting with a control knife with no added compliance and a stepped width specimen. For each dataset, three force vs time traces per width of cut are shown in all three directions; the degradation in cutting behavior can be seen in the cutting traces in the

former dataset. Cutting statistics, specifically the cutting force mean and standard deviation for the steady-state portion of the cut are also presented. The cutting force sign convention for the recorded data is shown in Figure 6.1

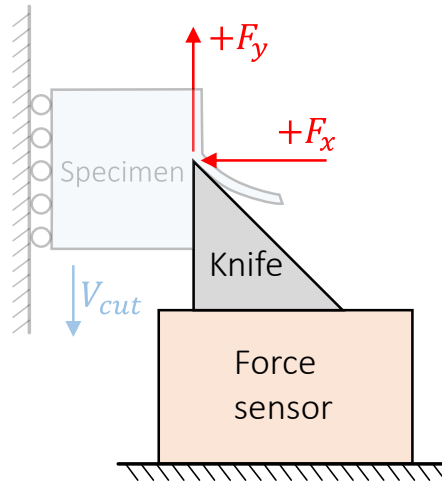


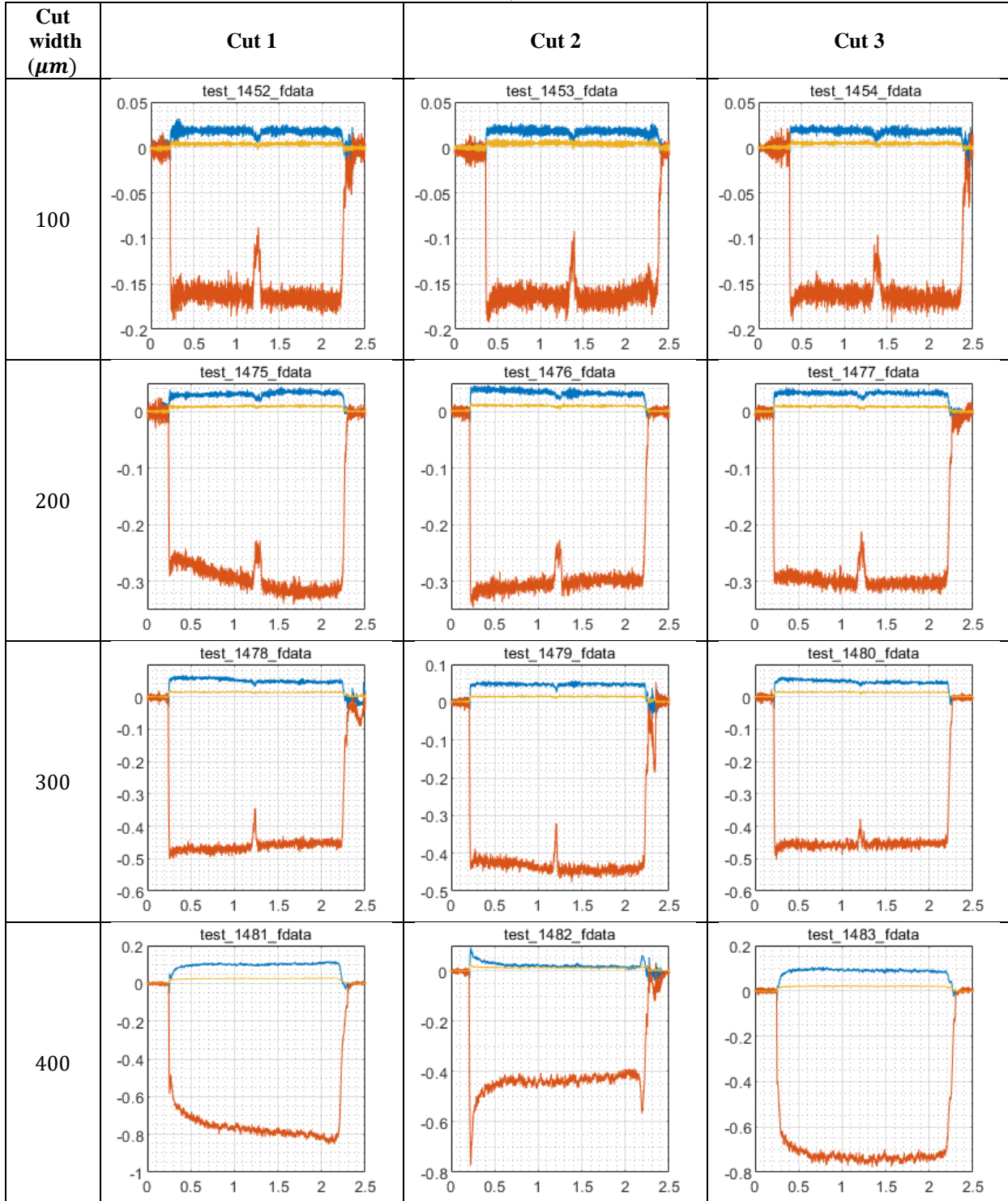
Figure 6.1: Cutting force sign convention for  $F_x$ , the feed force, and  $F_y$ , the cutting force.

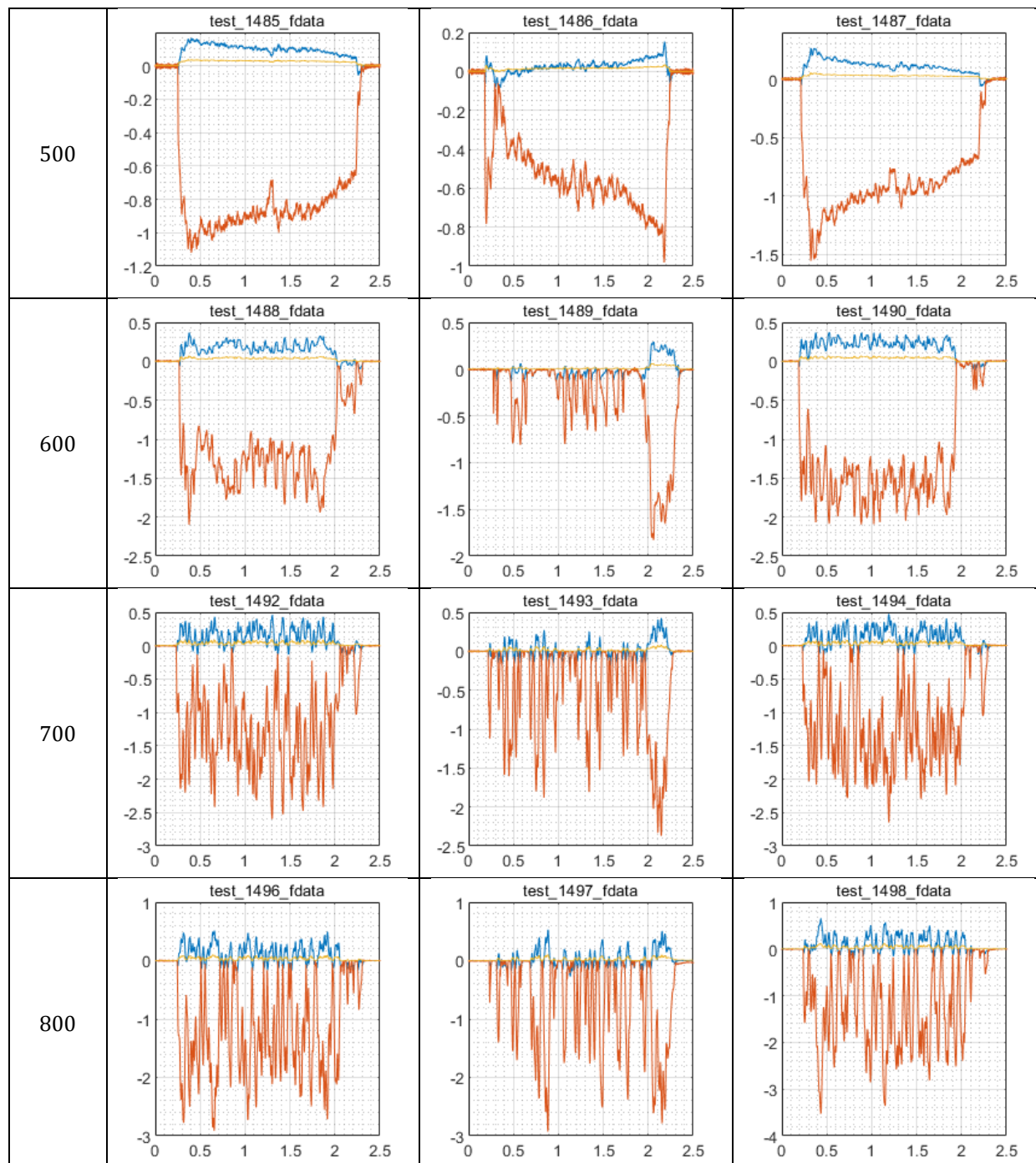
### 6.1.1 Dig-in regime cutting with feed compliance

Cutting force data for the stepped-width specimen cutting is presented in a grid format in **Table 6-1**. Each grid row is a cutting width, and each column presents cutting data for sequential cuts. All three cutting force directions are shown in the plots. The test was stopped at a cutting width of 1.3 mm, at which point the force sensor was saturating due to deep digging-in.



Table 6-1: Cutting force plot at each cutting width with compliant knife and negative  $K_f$ .  $F_x$  blue,  $F_y$  red,  $F_z$  yellow. The feed force is nominally positive, indicating a dig-in force with the coordinate system in Figure 6.1. Units on the horizontal axis are seconds, units on the vertical axis are Newtons.





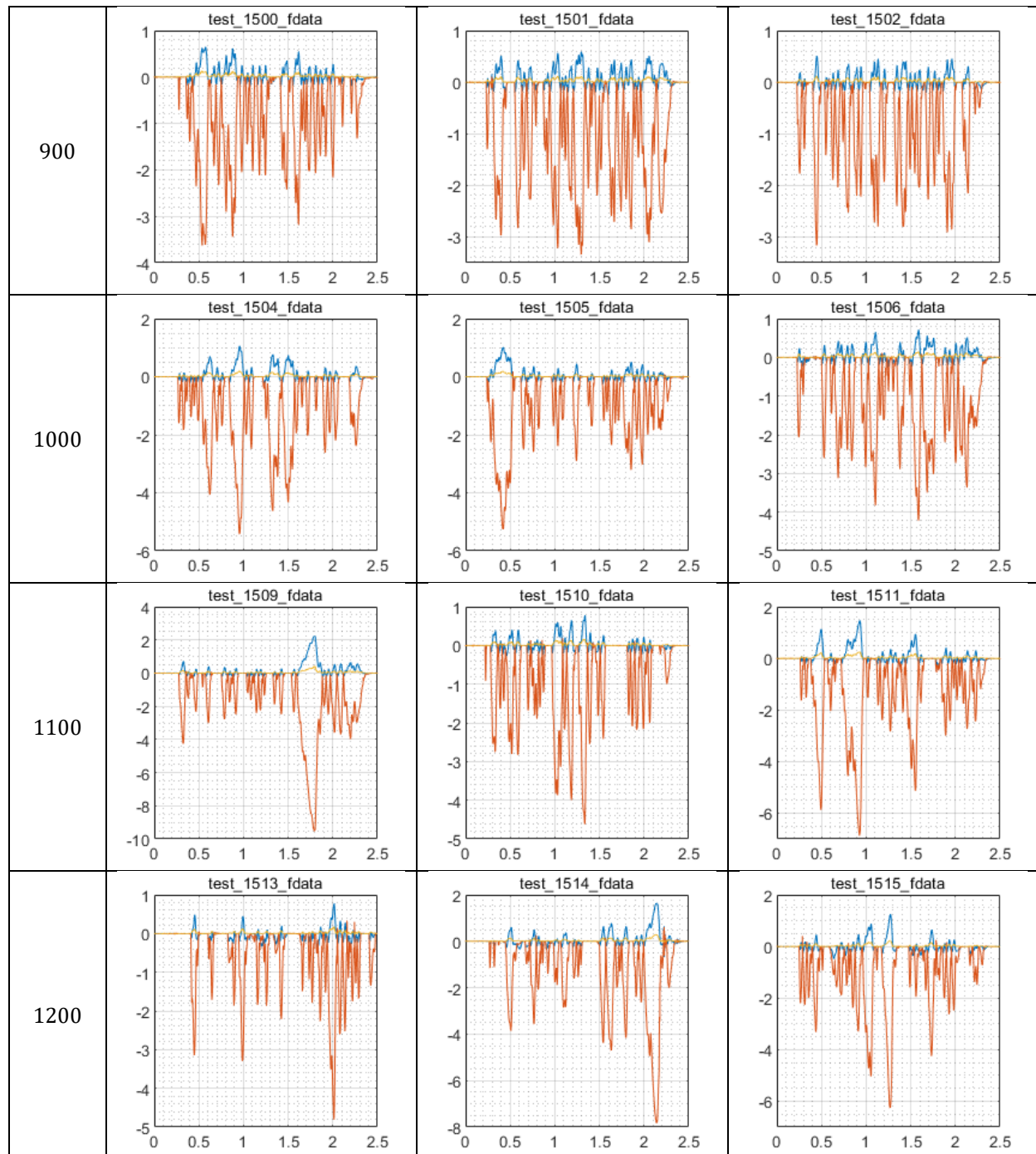


Table 6-2 presents aggregated statistics on the cutting forces. Each row represents a cutting width, ordered sequentially from thinnest cut width to widest. The number of cuts with recorded data is presented in the  $n$  column. Columns 3, 5, and 7 are the averages of the average cutting force at each cutting width for  $F_x$ ,  $F_y$ , and  $F_z$ , respectively. Similarly, Columns 4, 6, and 8

are the averages of the standard deviations of the cutting forces at each cutting width for  $F_x$ ,  $F_y$ , and  $F_z$  respectively. Calculations were not performed for widths past 1000  $\mu m$  due to the increasing erraticness and more frequent “deep-dive” dig-ins.

Table 6-2: Statistics from cutting forces – means and standard deviations of cutting forces. Units are in Newtons.

Cutting width ( $\mu m$ )	$n$	$\mu_x$	$\sigma_{Fx}$	$\mu_y$	$\sigma_{Fy}$	$\mu_z$	$\sigma_{Fz}$
100	8	0.018	0.003	-0.163	0.009	0.005	0.001
200	3	0.032	0.004	-0.299	0.016	0.009	0.001
300	3	0.048	0.005	-0.451	0.014	0.014	0.001
400	4	0.060	0.005	-0.607	0.022	0.018	0.001
500	3	0.083	0.027	-0.800	0.111	0.025	0.004
600	4	0.092	0.081	-0.801	0.416	0.024	0.013
700	4	0.068	0.113	-0.890	0.574	0.027	0.019
800	4	0.072	0.149	-1.020	0.773	0.030	0.026
900	4	0.054	0.170	-1.059	0.909	0.031	0.031
1000	5	0.070	0.207	-1.189	1.114	0.035	0.037

### 6.1.1.1 Specific feed pressure calculation

The specific feed pressure  $K_f$  for this dataset was calculated by applying Eq. (5.5) to each cutting pass at 100  $\mu m$  cutting width, at 10  $\mu m$  feed (Table 6-3). A  $K_f$  value is calculated for each cutting pass using that pass’ average feed force, and the nominal values for width and feed. A negative value is added to  $K_f$  to indicate that this is a pull-in (dig-in) quantity. Then the average and standard deviation of the set of calculated specific feed pressures is calculated to get an aggregated  $K_f$  value. This resulting aggregated value of  $K_f$  is  $-17.6 \pm 1.4 \frac{N}{mm^2}$ .

Table 6-3: Cutting data used to calculate specific feed pressure ( $K_f$ ) for the stepped-width cutting experiment.

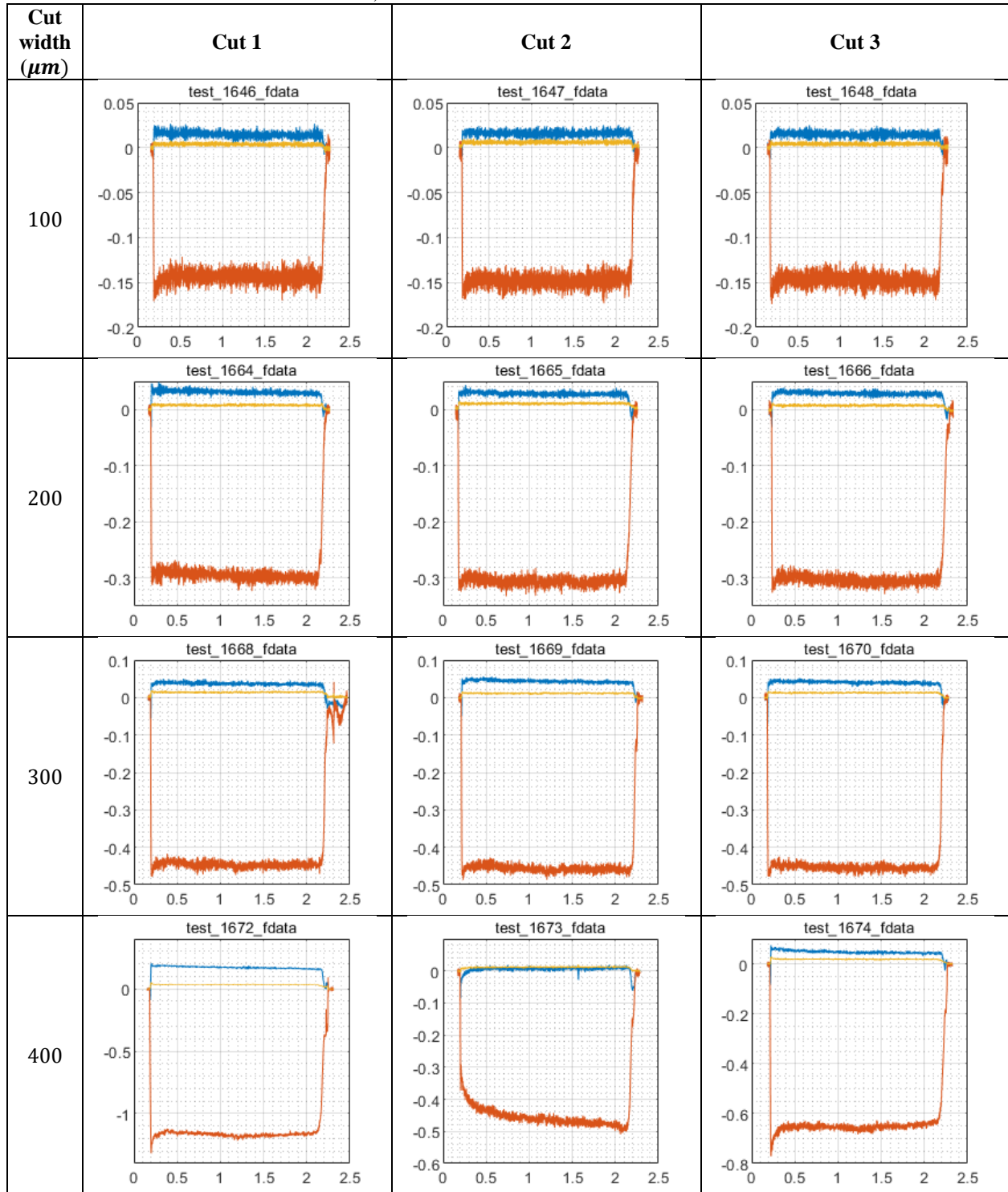
Cut ID #	Feed ( $\mu m$ )	Cut width ( $\mu m$ )	$F_{f,avg}$ (N)	Calculated $K_f$ ( $N/mm^2$ )
1452	10	100	0.0179	-17.9
1453	10	100	0.0178	-17.8
1454	10	100	0.0179	-17.9
1455	10	100	0.0148	-14.8
1456	10	100	0.0172	-17.2
1457	10	100	0.0164	-16.4
1458	10	100	0.0189	-19.0
1459	10	100	0.0201	-20.1
<b>AVERAGE</b>				<b>-17.6</b>
<b>STANDARD DEV.</b>				<b>1.5</b>

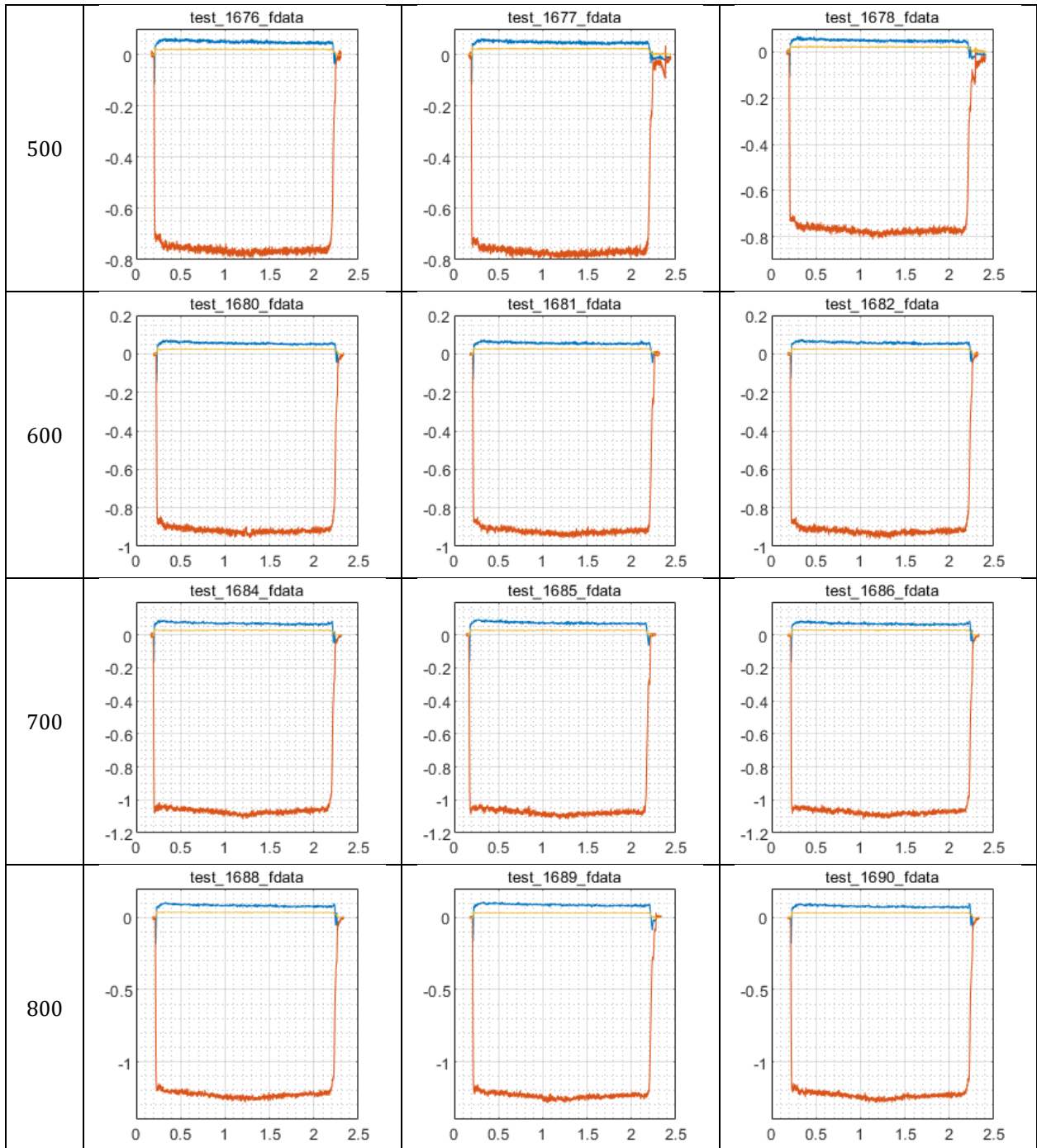
This calculated experimental  $K_f$  is compared against feed force cutting data in acetal resin machining, Figure 8 in [51]; Rao et al measured a specific feed pressure of approximately  $-14 N/mm^2$  at a feed of  $75 \mu m$ , a rake angle of  $20^\circ$  (same nominal value as for this cutting experiment), a cut speed of  $1610 mm/s$ , and a width of cut of  $4.8 mm$ . The value measured here is approximately 25% higher than the  $K_f$  measured by Rao, though an exact match is not necessarily to be expected since the cutting conditions aren't exactly the same, but it does serve as a good sanity check. No information is provided on how much variation there is in the feed force (and by extension,  $K_f$ ) between cuts. Understanding the factors behind  $K_f$  variation, both within a single cutting pass and between cutting passes, is highlighted as an area of future work in Section 7.3.1.

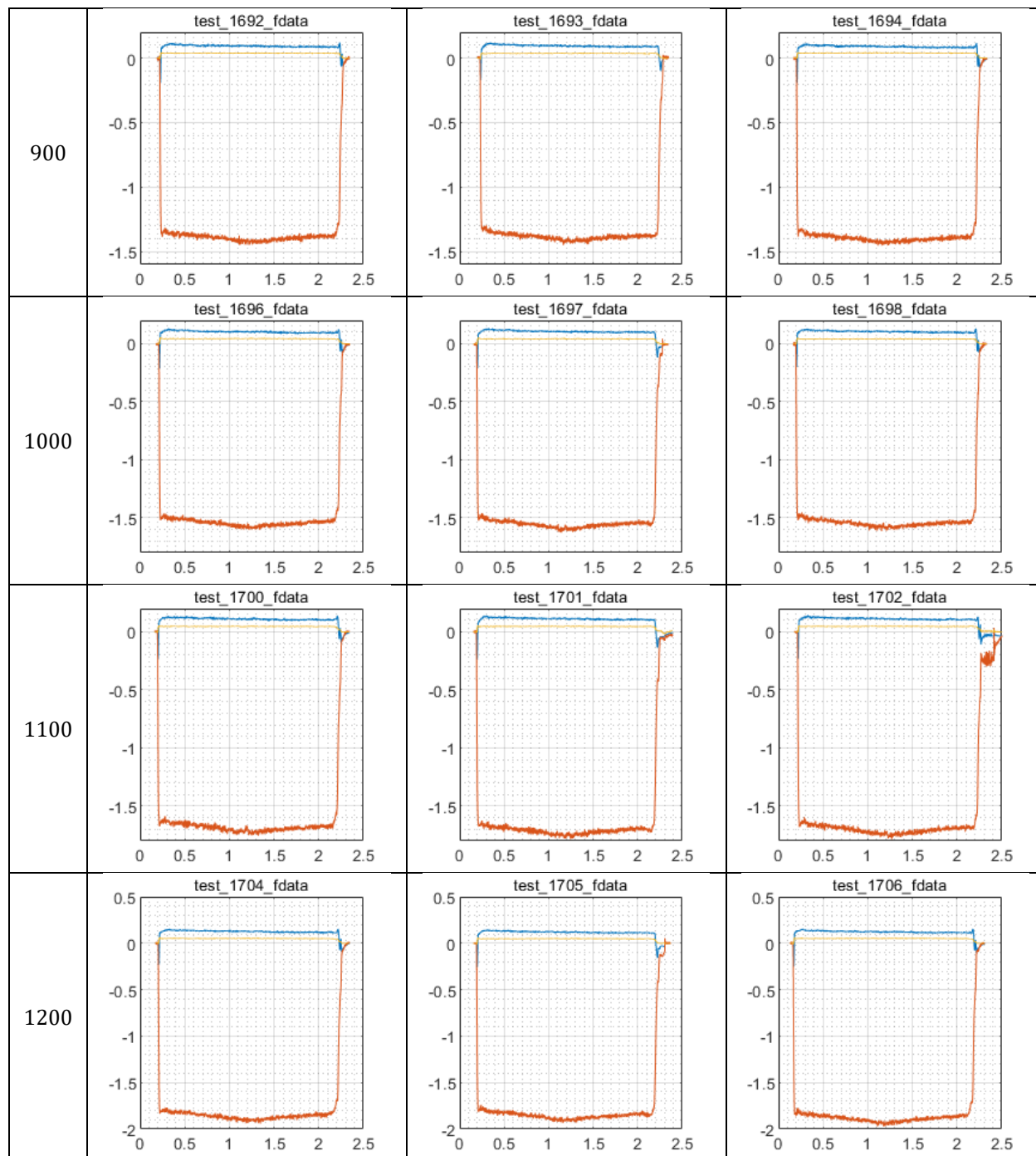
### 6.1.2 Dig-in control cutting; cutting with a knife with no added compliance

Cutting data is presented in the same fashion for the dig-in control cutting dataset as was done for the dig-in regime cutting dataset. Each row of Table 6-4 contains force vs time plots for three sequential cuts at a fixed width of cut.

Table 6-4: Control knife cutting dataset force plots.  $F_x$  blue,  $F_y$  red,  $F_z$  yellow. The feed force is nominally positive, indicating a dig-in force with the coordinate system in Figure 6.1. Units on the horizontal axis are seconds, units on the vertical axis are Newtons.









Cutting statistics for the flexureless knife dataset are summarized below in Table 6-5.

Table 6-5: Cutting force mean and standard deviation in each direction for the flexure-less knife. Units are in Newtons.

Cutting width ( $\mu\text{m}$ )	$n$	$\mu_x$	$\sigma_{Fx}$	$\mu_y$	$\sigma_{Fy}$	$\mu_z$	$\sigma_{Fz}$
100	18	0.015	0.0028	-0.154	0.006	0.005	0.001
200	4	0.029	0.0030	-0.304	0.007	0.009	0.001
300	4	0.041	0.0034	-0.454	0.007	0.013	0.001
400	4	0.066	0.0049	-0.722	0.012	0.020	0.001
500	4	0.048	0.0045	-0.771	0.010	0.021	0.001
600	4	0.056	0.0050	-0.924	0.011	0.025	0.001
700	4	0.070	0.0054	-1.078	0.014	0.029	0.001
800	4	0.082	0.0061	-1.240	0.017	0.033	0.001
900	4	0.093	0.0065	-1.397	0.019	0.037	0.001
1000	4	0.103	0.0070	-1.556	0.022	0.042	0.001

### 6.1.2.1 Specific feed pressure calculation

The specific feed pressure for this dataset is calculated in the same manner as was done for the dig-in cutting in Section 6.1.1.1. The mean and standard deviation of each 100  $\mu\text{m}$  width cut is presented in Table 6-6, with an aggregated value of the mean and standard deviation at the bottom. This dataset resulting in a  $K_f$  of  $-15.0 \pm 1.8 \frac{\text{N}}{\text{mm}^2}$ .

Table 6-6: Cutting data used to calculate specific feed pressure ( $K_f$ ) for the stepped-width cutting experiment, flexureless knife.

Cut ID #	Feed ( $\mu m$ )	Cut width ( $\mu m$ )	$F_{f,avg}$ (N)	Calculated $K_f$ (N/mm <sup>2</sup> )
1646	10	100	0.0147	-14.7
1647	10	100	0.0158	-15.8
1648	10	100	0.0146	-14.6
1649	10	100	0.0134	-13.4
1650	10	100	0.0131	-13.1
1651	10	100	0.0162	-16.1
1652	10	100	0.0142	-14.2
1653	10	100	0.0146	-14.6
1654	10	100	0.016	-15.4
1655	10	100	0.016	-16.0
1656	10	100	0.014	-14.1
1657	10	100	0.0121	-12.2
1658	10	100	0.0157	-15.7
1659	10	100	0.0163	-16.3
1660	10	100	0.0171	-17.1
1661	10	100	0.0184	-18.4
1662	10	100	0.0167	-16.7
1663	10	100	0.0104	-10.4
<b>AVERAGE</b>				<b>-15.0</b>
<b>STANDARD DEV.</b>				<b>1.8</b>

## 6.2 Series dig-in instability assessment

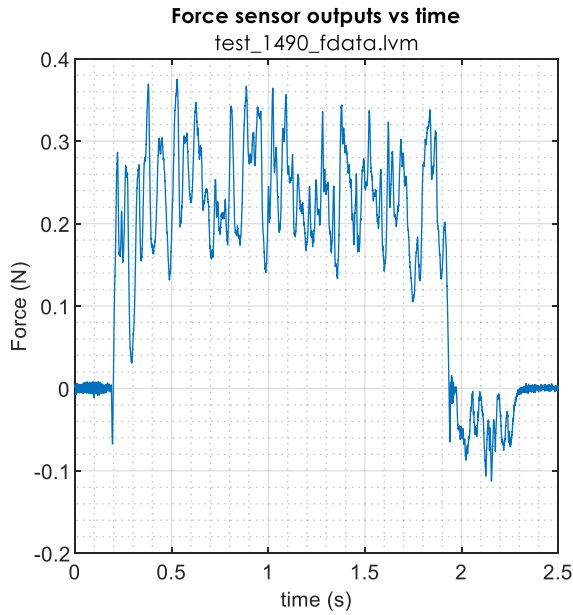
The series instability criteria discussed in Section 5.2.3 were applied to the dig-in regime cutting dataset to assess at what cutting width the system became unstable. Each stability criterion and its application to the stepped-width/compliant knife experiment is discussed in the following subsections.

### 6.2.1 Detecting instability via skip-sections

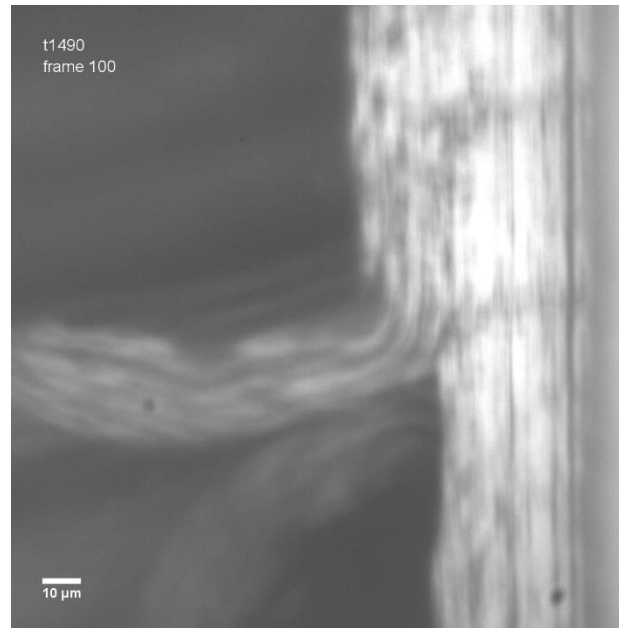
Skip sections should not be observed in a series-stable system when performing a series of cuts whose initial cutting width is a stable width, as in this experiment (Figure 3.12). In the stepped-specimen and compliant knife cutting experiment performed here, skip-sections are taken as an indication that the system has already become unstable, and deviations from modeled

behavior are certain due to unmodeled effects such as the knife leaving the cut entirely, and edge effects (if the depth of cut is smaller than the edge radius, the knife edge will “skate” along the surface instead of engaging the material).

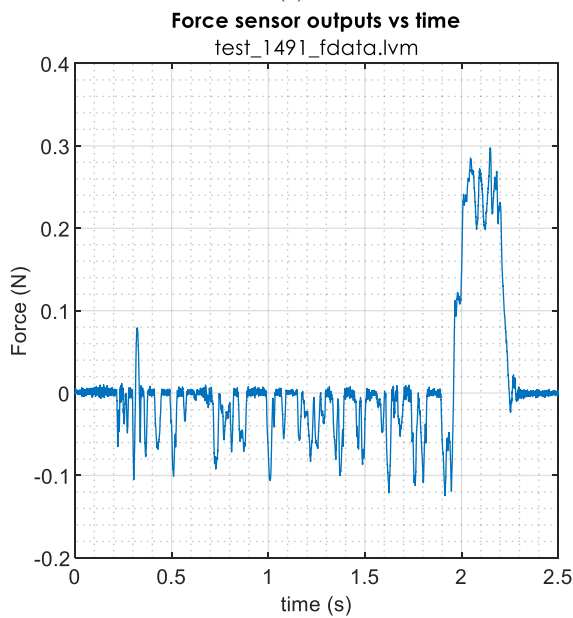
In this experiment, skip-sections were observed at  $600\ \mu\text{m}$  cutting width. Two sequential cuts and corresponding images from the cutting videos are shown in Figure 6.2. The cut corresponding to Figure 6.2(a,b) shows that the knife is heavily engaged in the material – more so than the nominal feed of  $10\ \mu\text{m}$  based on the captured image, so the cut is digging in. The feed forces are positive, corresponding to a dig-in force, and a significant amount of variation is observed. The subsequent cut, corresponding to Figure 6.2(c,d) has feed forces that switch sign – the knife is being pushed out of the cut, and only engages material towards the end of the cut. The captured video frame corresponding to this cut confirms that the knife is not engaged in the material, and rubs along the surface, occasionally ploughing up a wispy chip, until the end of the cut, where the knife is able to engage the material due to sufficient material being left behind on the previous cut. There is a minimum feed required for the knife to begin cutting the material – too shallow of a cut, and the knife will be pushed out of the cut and skim the surface of the material instead of removing a section.



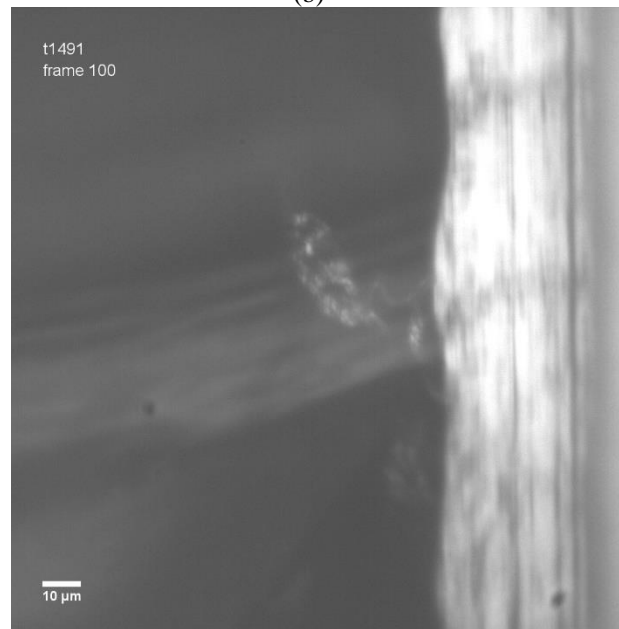
(a)



(b)



(c)



(d)

Figure 6.2: Feed force cutting data for two sequential cuts at  $600\ \mu\text{m}$  cutting width. Cutting force vs time plots (a) and (c), and corresponding video stills (b) and (d). The feed force in (c) drops to near zero, with occasional rubbing. It is evident from the video (d) that the knife is not engaged in the material, and only removes wisps of material. This skip section is indicating that the system is already unstable.

From this it was concluded that the cutting system was already unstable at the  $600\ \mu\text{m}$  cutting width, though this skip-section identification doesn't identify exactly when the system became unstable.

### **6.2.2 Detecting instability via divergent steady-state offset per pass**

A second signal of a serial cutting system becoming series unstable is that the magnitude of the steady-state mean offset will increase, pass over pass (see Section 5.3.2 for modeling of this phenomenon). A stable system at a given width of cut would settle to a steady-state offset from nominal feed, corresponding to the mean force eventually stabilizing after a number of cuts. An unstable system will oscillate between thick and thin sections with increasing amplitude.

The average feed force per cutting pass for the stepped specimen and compliant knife cutting experiment is shown in Figure 6.3. From this data it can be inferred that the system is at the threshold of instability at  $400\ \mu m$  cutting width, and unstable at  $500\ \mu m$  and beyond.

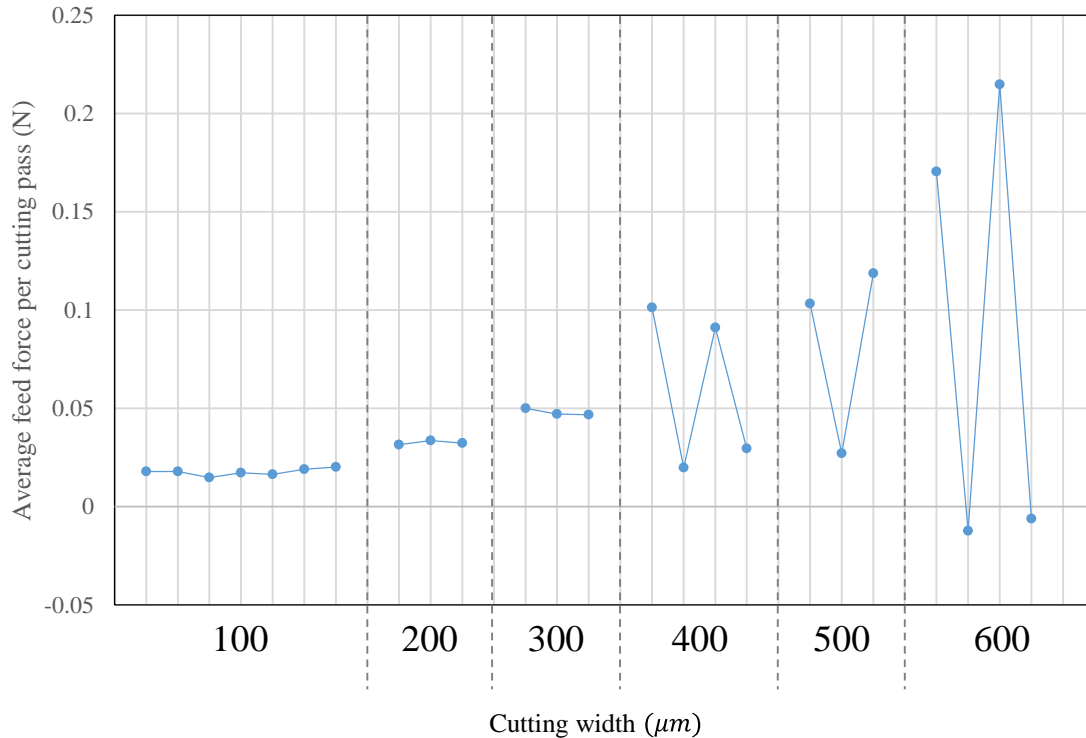


Figure 6.3: Measured average feed force per cutting pass, at different cutting widths. Each data point is presented in the sequence the cut was performed. At  $400\ \mu\text{m}$  the cutting behavior changes, but is still consistent with stable behavior (the average feed force appears to be settling to a final steady-state value). At  $500\ \mu\text{m}$ , the cut appears to have become unstable (the average feed force does not look like it's converging to a final steady-state value), and by  $600\ \mu\text{m}$  the cut is certainly series-unstable – the average force drops below zero, indicating skip sectioning as discussed in 6.2.2.

The final instability signaling behavior is related to the feed force variation (corresponding to a change in the feed position) observed each pass, and its trend.

### 6.2.3 Feed position variance increase per pass

This instability signaling behavior is described by the variance propagation model developed in Section 3.3, and the predicted instability behavior is described in Section 5.3.3 – when the system is no longer series-stable, each cutting pass the variance of the offset will increase without stabilizing to a steady-state variance, as would be the case for a steady system.

Figure 6.4 shows the feed force standard deviation per pass for the compliant knife cutting Delrin. When the system has become unstable, the feed force standard deviation per pass

will increase each pass instead of settling to a steady-state value for that cutting width. The transition between stable and unstable behavior happens here suddenly enough that the quasi-static behavior leading up to instability can't be observed – the variation in the feed force remains small and below the sensor's noise floor, until the system becomes unstable and the variation jumps out. Future experiments with a finer cutting width increment and a more sensitive could better characterize the quasi-stable behavior, but that would be an academic exercise; in this work, the interest lies in understanding when the system has gone unstable, and this binary stable/unstable signaling behavior is sufficient.

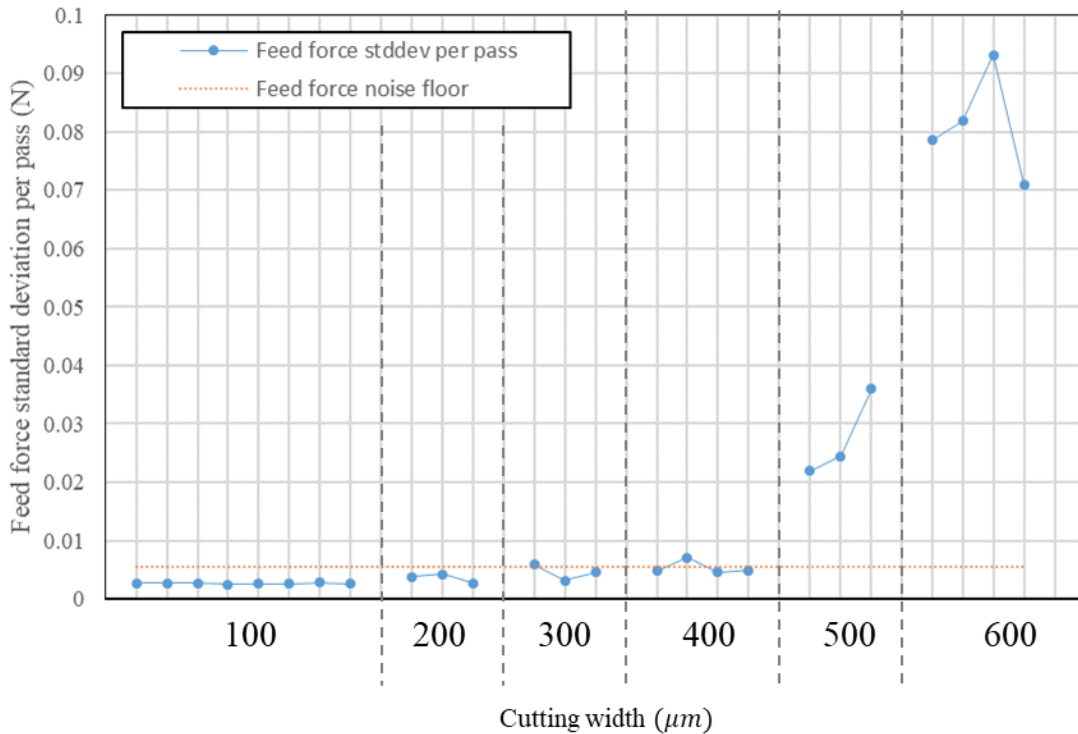


Figure 6.4: Plot of measured feed force standard deviation, vs cutting width. Each data point represents a measured standard deviation for a cutting pass. Cuts at widths smaller than 500  $\mu\text{m}$  had feed force standard deviations below the force sensor's noise floor (95% confidence interval). At 500  $\mu\text{m}$  width, the feed force variance increases every cutting pass.

From this signal, it is concluded that the system has become unstable at 500  $\mu\text{m}$  cutting width. A difficulty with this signal however is that it would be difficult near the cutting width

threshold of stability to differentiate between a stable system which is taking many passes to reach a steady-state equilibrium, versus a system that has just gone unstable.

#### 6.2.4 Measured vs predicted maximum series-stable cutting widths

The three instability-signaling behaviors are compared to reach a conclusion about when the system became series unstable.

According to the model developed in Section 3.2.1, using Equation (3.32), the maximum stable cutting width for this system was  $1370 \mu m$ , therefore the nearest stable tested cutting width was  $1300 \mu m$ . However, this system appears to have crossed the stability threshold at a cutting width of  $500 \mu m$ , therefore the maximum stable tested cutting width was  $400 \mu m$ . This observed maximum stable cutting width of  $400 \mu m$  has an error of  $-71\%$  with respect to the modeled maximum stable cutting width of  $1370 \mu m$ . The parameters for the calculation are given in Table 6-7.

Table 6-7: Calculated vs measured maximum stable cutting width

Parameter	Value	Unit	Description
<i>Inputs</i>			
$K_f$	-1.79E+07	$N/m^2$	Specific feed pressure
$k_f$	4.90E+04	$N/m$	Cutting system feed stiffness
<i>Outputs</i>			
$a_{series}$	1.37E-03	$m$	Predicted series cutting stability limit
$a_{series.exp}$	4.0E-04	$m$	Observed max stable cutting width
$e_{model}$	-71	%	Percent error w.r.t. model prediction

This discrepancy is addressed in Section 6.4.

### 6.3 Feed force and position variance propagation with cutting width

The model developed in Section 3.3 made predictions of how the standard deviation of the feed cutting force  $k$  is expected to grow with continued cutting passes and increases in cutting width. In this section, the progression predicted by the model is compared to the experimentally



measured feed force standard deviation,  $\sigma_{Ff}$ , per cut for the system cutting the acetal resin with the compliant knife. The system experiences a growth in  $\sigma_{Ff}$  earlier than predicted by the model due to a lower stiffness than initially modeled; this discrepancy is addressed in Section 6.4.

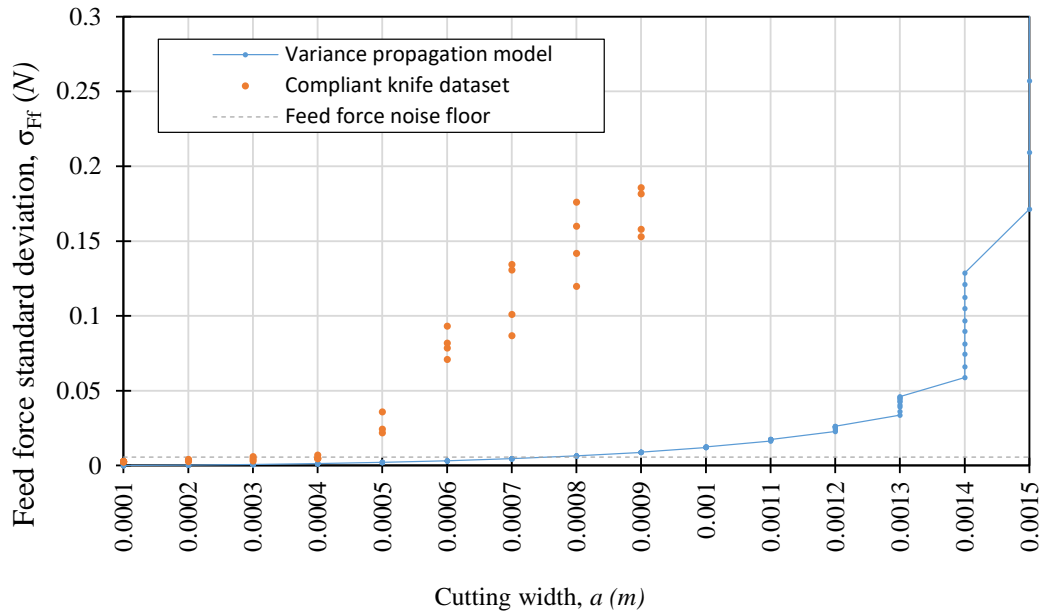
Experimentally,  $\sigma_{Ff}$  is measured, as opposed to the feed position standard deviation  $\sigma_x$ . The feed position standard deviation  $\sigma_x$  is calculated from the measured feed force by transforming the measured feed force variance via:

$$\sigma_x = \left( \left| \frac{1}{K_f a} \right| \right) \sigma_{Ff} \quad (6.11)$$

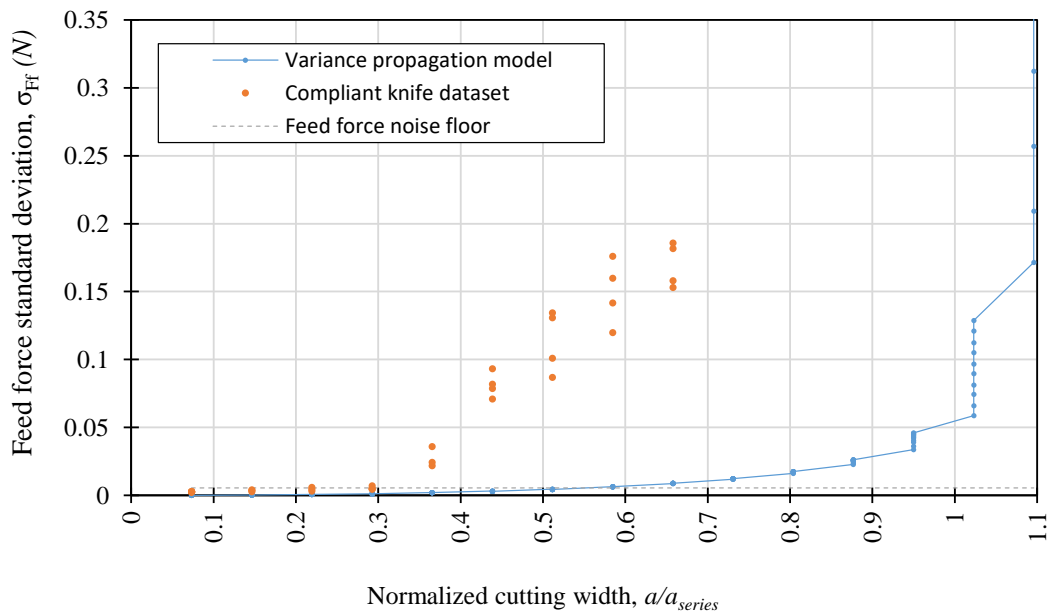
Transforming the measured feed force standard deviation into feed position deviation allows for normalizing the feed position standard deviation against the nominal depth of cut; the model is expected to no longer be applicable as this ratio approaches 1 – at this point, the tool would be frequently disengaging from the material. This model applicability limit is not obvious from the feed force data, so it is useful to transform the feed position variance. In the following sections, the variance propagations of both the feed force and the derived feed position are plotted against cutting width and compared to the models developed in Chapter 3.

### 6.3.1 Feed force standard deviation vs cutting width

The resulting cutting data from the stepped specimen and compliant knife cutting experiment is plotted alongside the numerical implementation of the variance propagation model in Figure 6.5a and Figure 6.5b. These are the same plots, except that in plot (b), the cutting width (the horizontal axis) is normalized against the predicted series stability limit  $1.37 \text{ mm}$ .



(a)



(b)

Figure 6.5: Measured feed force standard deviation vs cutting width (a) plotted with cutting width on the horizontal axis (b) plotted with normalized cutting width, normalized against the nominal series stability limit

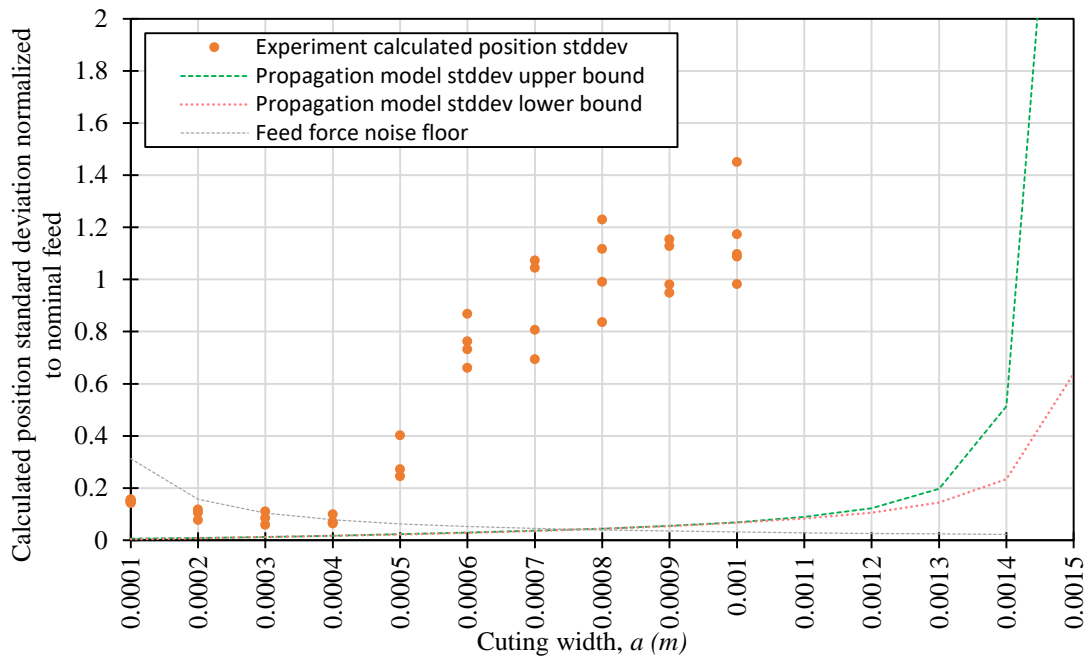
Table 6-8: Parameters used for feed force and position propagation model used in Sections 6.3.1 and 6.3.2

Parameter	Value	unit	Description
$Kf$	-1.79E+07	$N/m^2$	Specific feed pressure
$kf$	4.90E+04	$N/m$	Feed stiffness
$a_{min}$	1.00E-04	$m$	Cutting width, min
$a_{max}$	1.5E-03	$m$	Cutting width, max
$a_{inc}$	0.1E-04	$m$	Cutting width increment
$N_{pass}$	10		Cutting passes per cutting width
$t_o$	1.00E-05	$m$	Nominal feed
$\sigma_a$	1.40E-06	$m$	Cutting width standard deviation
$\sigma_{Kf}$	1.50E+06	$N/m^2$	Specific feed pressure standard deviation
$\sigma_{kf}$	0	$N/m$	Feed stiffness standard deviation
$\sigma_{xr}$	1.00E-06	$m$	Initial regenerative surface ('seed')
$\sigma_{to}$	5.00E-07	$m$	Nominal feed standard deviation

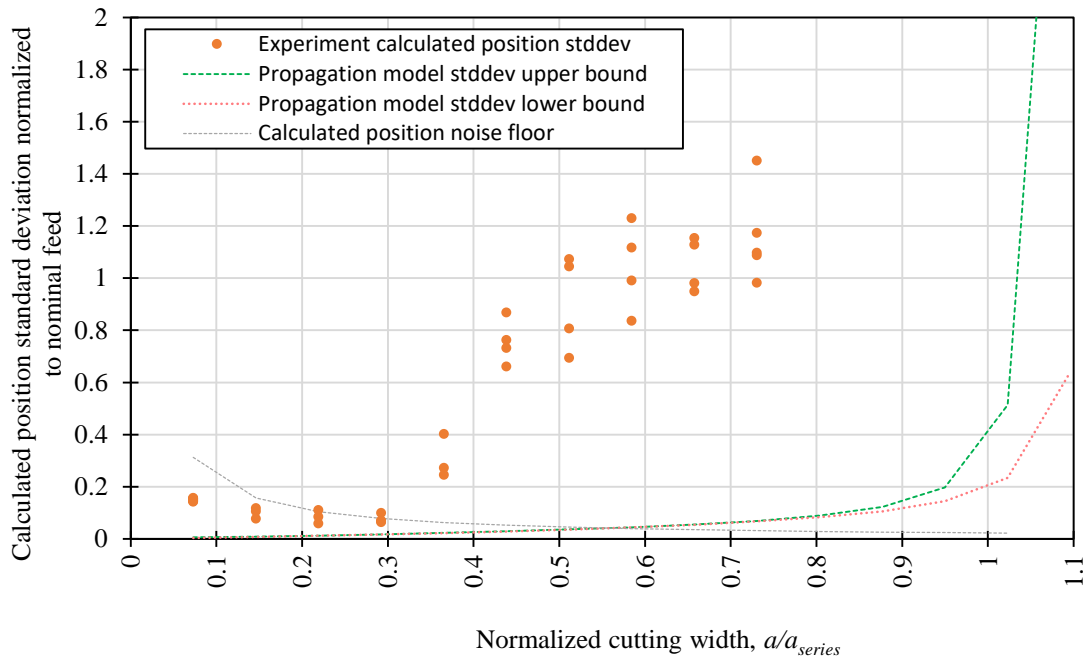
As can be seen in Figure 6.5a and Figure 6.5b, the cutting system  $\sigma_{Ff}$  starts to “lift off” from the horizontal axis sooner than predicted, at a normalized cutting width  $a/a_{series}$  of about 0.4 versus the model-predicted value of 0.9. This discrepancy is attributable to the system having a lower stiffness than modeled, similarly to the series dig-in stability limit discrepancy noted in Section 6.2; the source of the reduced stiffness is discussed and resolved in Section 6.4.

### 6.3.2 Position standard deviation vs cutting width

As described in the introduction to Section 6.3 introduction, the feed force variance can be transformed into feed position variance to assess when the model is expected to no longer apply by normalizing against the nominal depth of cut. Figure 6.6a plots the normalized position standard deviation against the width of cut (in  $m$ ) and Figure 6.6b plots the same data, but normalizes the width of cut against the model-predicted maximum stable width of cut for series cutting  $a_{series}$ . The parameters used for the numerical model are the same as were used in Section 6.3.1.



(a)



(b)

Figure 6.6: Feed position variance progression plotted in terms of the derived feed position. (a) Normalized position standard deviation vs cutting width (b) Normalized position standard deviation vs normalized cutting width, normalized to series stability limit

In this dataset it is evident that the feed position variance begins to grow much earlier than expected with the model and parameters used. This discrepancy is resolved in the next section.

## **6.4 Resolving the discrepancy between modeled and observed dig-in instability behavior**

The stepped specimen and compliant knife cutting system reached instability at a narrower cutting width than expected from the stability models derived in Chapter 3. This section describes the efforts taken to resolve the discrepancy between the dig-in stability model, and the experimental data. It was ultimately concluded that localized knife-tip deflections feasibly explain the additional compliance, and earlier instability.

### **6.4.1 Troubleshooting stiffness via microscope video**

Cutting videos that were recorded at cutting widths with large enough deflections to be measured (400  $\mu\text{m}$ , 500  $\mu\text{m}$ ) were inspected to reveal compliance problems. Specifically, if the compliance observed based on the displacements and the recorded forces were consistent with the design compliance of the compliant knife. The knife tip stiffness was optically measured to be 18.2  $N/mm$ , compared to the compliant knife body's nominal stiffness of 49  $N/mm$ , a value 62% lower than nominal.

#### *6.4.1.1 Stiffness measurements via microscope tool tip deflection measurements*

Knife tip deflections in response to cutting loads were measured by inspecting frames from cutting videos with tool deflections large enough to be visible on the microscope, at 500  $\mu\text{m}$  cutting width. For a pair of frames, the feed was measured using pixel measurements. One frame was taken as a reference, the change in feed position change in feed force was calculated,

then calculate the instantaneous local feed stiffness  $\Delta F/\Delta x$ . The measured stiffness was then compared to the nominal system stiffness.

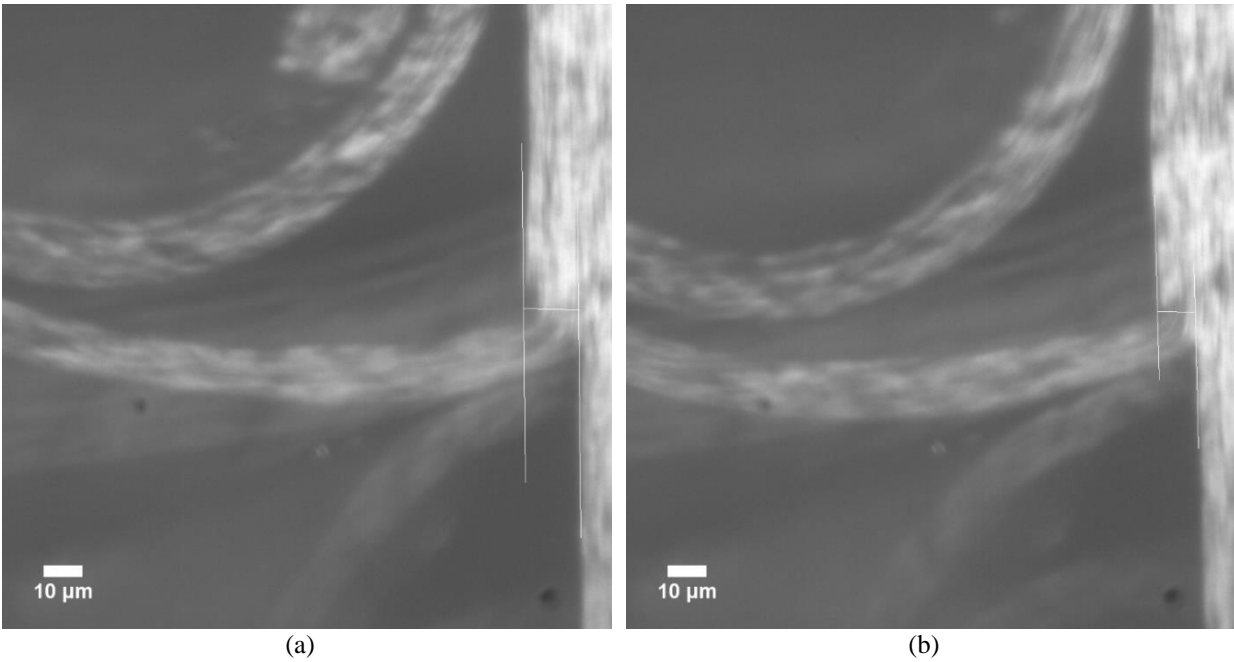


Figure 6.7: Cutting system stiffness measurement using video frames (a) frame 1, t1487 f226 (b) frame 2, t1487 f213, reference frame

A summary of the optical measurements and the calculated stiffnesses are shown in Table 6-9.

Table 6-9: Optical stiffness measurements

Video ID	Cutting width ( $\mu m$ )	Frame 1	Frame 2 (reference)	$F_1 - F_2$ (N)	$x_1 - x_2$ ( $\mu m$ )	Stiffness (N/mm)
t1487	500	226	213	0.082	4.50	18.2

The calculated cutting system stiffness from the microscope deflection measurements was significantly lower than the nominal value of  $49 N/mm$ . The cutting instrument was ruled out as the additional source of compliance based on the measurements performed in Section 4.9.5, and the knife tip was *initially* ruled out as a source of additional compliance based on the

analysis from Section 3.5. However, the knife tip deflection analysis from Section 3.5 was performed as two-dimensional analysis assuming that the entire knife edge was engaged in resisting the cutting forces, and it was suspected that the additional compliance could be a localized phenomenon – in practice not all of the 6.35 mm of knife edge would resist the cutting forces beyond a certain distance from the area of knife-material engagement.

#### 6.4.2 Knife tip 3D FEA reveals additional compliance

A finite element analysis in Solidworks Simulation 2018 was set up to investigate the possibility of localized tip compliance. A 3D CAD model of the knife tip was made based on measurements from two sets of microscope images with different fields of view. An image from the survey microscope (Figure 6.8) was used to measure the larger dimensions, whereas higher resolution images from cutting video stills were used to model the geometry at the very tip (Figure 6.9).

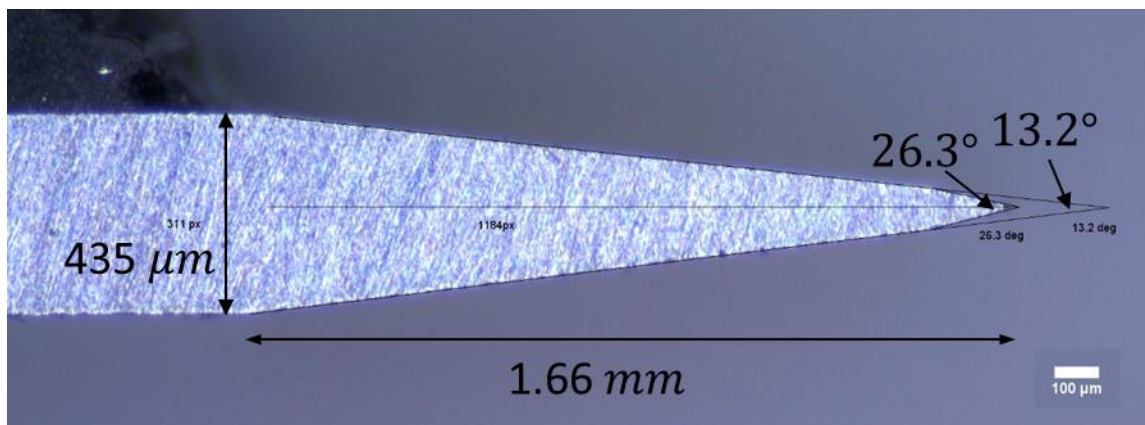


Figure 6.8: Survey microscope image of knife geometry; the knife appears to have a second bevel, although the very tip cannot be resolved.

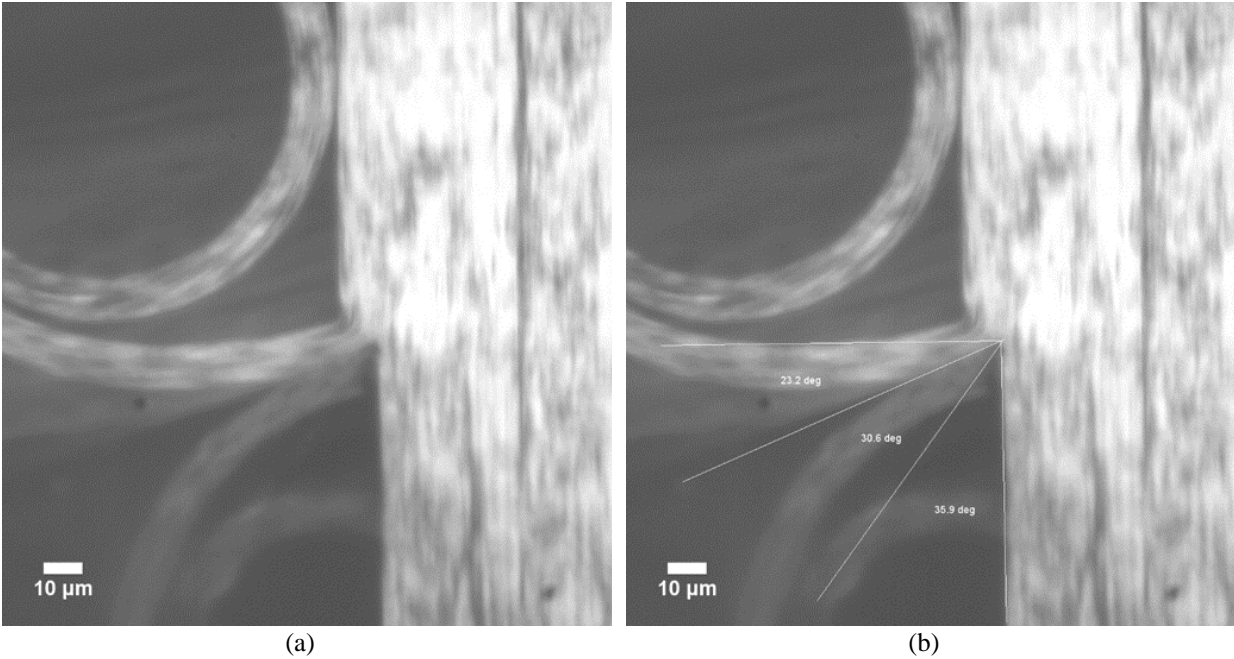


Figure 6.9: Close-up of knife tip and workpiece interaction zone used to obtain knife tip geometry for FEA simulation. (a) (b) with measurements overlaid

The CAD model is split into multiple zones to allow for defining a contact zone, and defining a high-density mesh in the loaded zone (Figure 6.10). Simulations were set up for three different cutting widths, 100  $\mu\text{m}$ , 400  $\mu\text{m}$ , and 500  $\mu\text{m}$ . The width of Zone 1 changes depending on the modeled cutting width. The load was assumed to be acting uniformly over a 10  $\mu\text{m}$  zone radially away from the virtual tip of the knife wedge (Figure 6.10 inset); this contact zone length was estimated based on reviewing cutting videos and observing that the chip would pull away from the knife rake face at around this distance (about one nominal feed's worth of distance along the rake face).



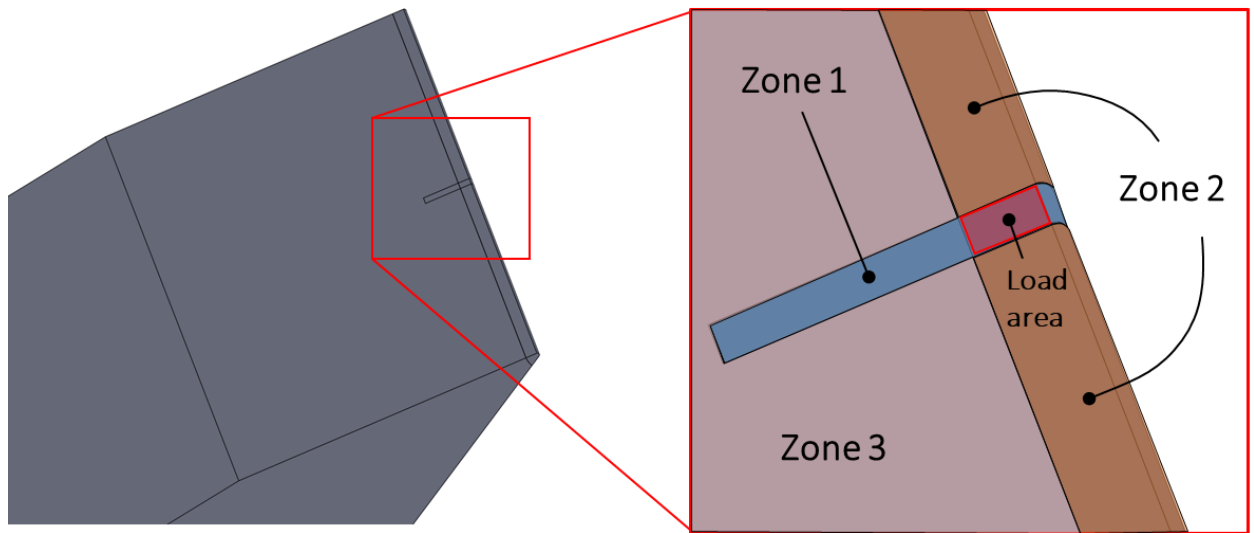


Figure 6.10: Knife tip mesh zones detail. Control meshes are applied in two zones: Zone 1 for high-density meshing at the load application area, Zone 2 for an edge general mesh, and Zone 3 is the knife body general mesh. The load acts uniformly over the load area within Zone 1 (inset, highlighted). Mesh parameters are given in Table 6-10.

The resulting mesh is shown in Figure 6.11, and the mesh parameters are given in Table 6-10.

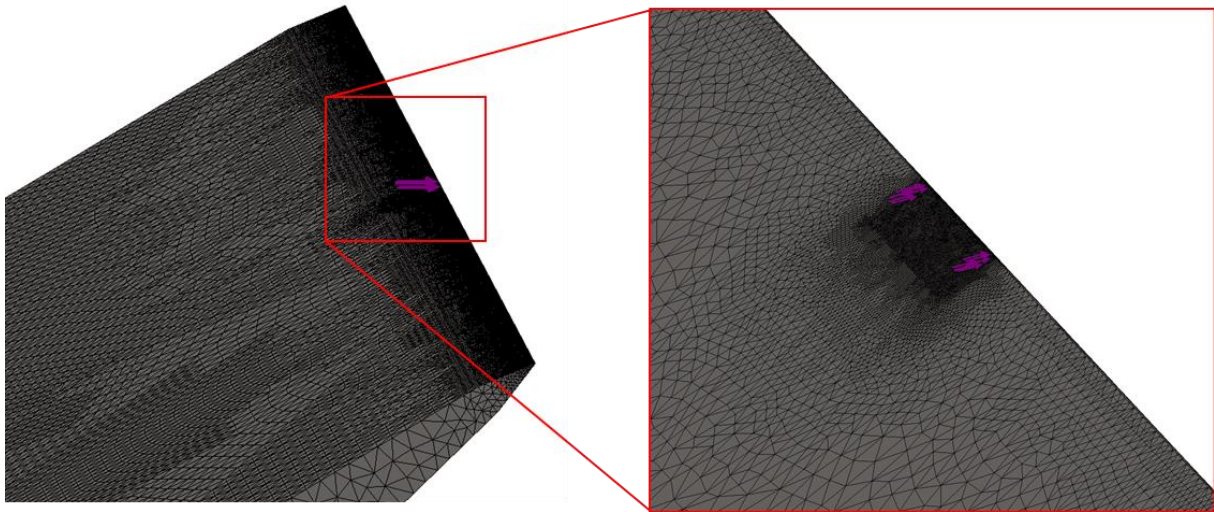


Figure 6.11: Mesh and close-up of contact zone (Zone 1).

Table 6-10: FEA meshing parameters for knife tip localized deflection simulations, at  $100\ \mu\text{m}$  cut width. The wider cut widths used the same parameters for the control mesh, with a resulting larger number of mesh elements.

Parameter	Value	unit	Description
<b>Zone 1</b>			<b>Chip contact zone mesh</b>
Size	0.001	mm	
Ratio	1.5		
<b>Zone 2</b>			<b>Edge general mesh</b>
Size	0.005	mm	
Ratio	1.2		
<b>Zone 3</b>			<b>Knife body general mesh</b>
Size max	0.06	mm	Max element size
Size min	0.012	mm	Min element size
<b>Mesh general</b>			
Total elements	695,877		Number of meshing elements

The input loads and resulting displacements are shown in Table 6-11. For reference, with the nominal compliant knife body feed stiffness of  $49\ \text{N/mm}$ , the deflections would be  $-0.39\ \mu\text{m}$ ,  $-2.04\ \mu\text{m}$ , and  $-2.43\ \mu\text{m}$  at the  $100\ \mu\text{m}$ ,  $400\ \mu\text{m}$ , and  $500\ \mu\text{m}$  cutting widths, respectively; the feed deflections induced by the  $F_y$  force due to cross-compliance are of the same order of magnitude as the nominal deflections.

Table 6-11: FEA input loads and calculated displacements, at different cutting widths. Input loads were based on measured values in the compliant knife and acetal resin cutting dataset. Loads were applied one at a time, and the resulting  $\delta x, \delta y$  displacements were measured as the average value of the elements in the Load Area shown in Figure 6.10.

100 $\mu\text{m}$ width			400 $\mu\text{m}$ width			500 $\mu\text{m}$ width		
Input loads			Input loads			Input loads		
$F_x$	-0.019	N	$F_x$	-0.1	N	$F_x$	-0.119	N
$F_y$	0.16	N	$F_y$	0.775	N	$F_y$	0.96	N
$F_y/F_x$	-8.42		$F_y/F_x$	-7.75		$F_y/F_x$	-8.07	
FEA Displacements ( $\mu\text{m}$ )			FEA Displacements ( $\mu\text{m}$ )			FEA Displacements ( $\mu\text{m}$ )		
	$\delta x$	$\delta y$		$\delta x$	$\delta y$		$\delta x$	$\delta y$
$F_x$	-0.071	0.074	$F_x$	-0.186	0.211	$F_x$	-0.197	0.226
$F_y$	-0.625	0.777	$F_y$	-1.632	2.069	$F_y$	-1.814	2.307

Figure 6.12a shows a section view of feed deflection at the midplane, and Figure 6.12b shows a 3D view of the deflection.

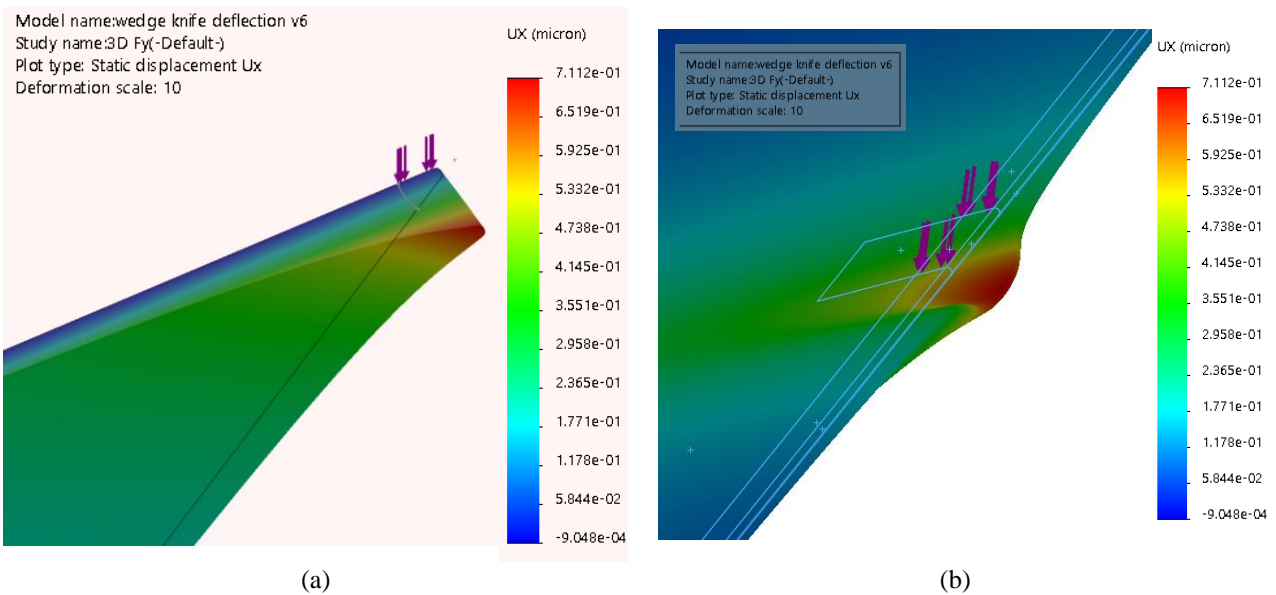


Figure 6.12: 3D Knife tip deflection FEA results screenshots at 100  $\mu\text{m}$  width (a) section view showing deflection in the loaded area with little deflection away from the loaded zone (b) 3D view of deflections; the loads on the edge cause local deformations

The compliance matrices computed from the finite element analysis displacements and loads are given in Figure 6.13. The compliance of the knife tip decreases as the width of cut increases, however it should be kept in mind that these compliance matrices are based off of

averaged deflection values in the loading zone, and that the center part of the loading zone deflects more than the edges.

$$C_{tip.100} = \begin{bmatrix} 3.71 & -3.91 \\ -3.92 & 4.86 \end{bmatrix} \frac{\mu m}{N}$$

$$C_{tip.400} = \begin{bmatrix} 1.86 & -2.11 \\ -2.11 & 2.67 \end{bmatrix} \frac{\mu m}{N}$$

$$C_{tip.500} = \begin{bmatrix} 1.65 & -1.89 \\ -1.90 & 2.40 \end{bmatrix} \frac{\mu m}{N}$$

Figure 6.13: FEA-derived compliance matrices for localized tip bending, averaged over estimated chip contact area

The presence of cross-compliance (off-diagonal) terms of the same order of magnitude as the compliance entries on the main diagonal mean that the feed deflections will depend not only on the feed force, but also on the slice force applied. In orthogonal cutting, the slice force is typically ~5 to 10 times higher than the feed force, so feed deflections will be higher than what is predicted by the feed compliance alone. This phenomenon and its implications are discussed further in the next section.

#### 6.4.2.1 *Effect of cross-compliance terms and the apparent feed stiffness*

The cutting system contains non-negligible cross-compliance terms, meaning that loads applied in the cutting direction will result in a displacement in the feed direction, which is critical for dig-in stability. A feed-direction force is always accompanied by a slice-direction force, although the reverse isn't true – for the right combination of cutting parameters, the feed force can be zero. The analysis done in Chapter 3 assumed a feed stiffness that depended only on the feed force, but in the physical system, slice forces can also cause feed displacements due to the cross-compliance terms. This means that for a given feed force, there would be a larger

deflection than would be expected without the cross-compliance terms, and thus the *real* stiffness is lower than expected.

To model this effect, the model is updated to include the effect of cross-compliance terms in the 2D compliance matrix of the cutting system,

$$\mathbf{C} = \begin{bmatrix} C_{xx} & C_{xy} \\ C_{xy} & C_{yy} \end{bmatrix} \quad (6.12)$$

Using the full two-dimensional compliance matrix, an expression can be derived for the apparent feed stiffness  $F_x/\delta_x$  for a given cut due to non-negligible cross-compliance terms.

$$\vec{\delta} = \mathbf{C}\vec{F}, \quad \vec{\delta} = \begin{bmatrix} \delta_x \\ \delta_y \end{bmatrix}, \quad \vec{F} = \begin{bmatrix} F_x \\ F_y \end{bmatrix} \quad (6.13)$$

$$\delta_x = C_{xx}F_x + C_{xy}F_y \quad (6.14)$$

An expression for the cutting force in terms of the feed force can be written with the assumption that the cutting force is a constant multiple of the feed force,

$$F_y = nF_x \quad (6.15)$$

Note that the multiple  $n$  can also be negative, in the case of dig-in feed forces pulling the tool into the cut. The feed deflection can then be written in terms of the x cutting force

$$\delta_x = C_{xx}F_x + C_{xy}(nF_x) \quad (6.16)$$

and the apparent feed stiffness can be written as

$$\frac{F_x}{\delta_x} = k_{f.app} = \frac{1}{C_{xx} + nC_{xy}} \quad (6.17)$$

For the three simulated cutting widths,

$$k_{f.app.100} = 17.5 \text{ N/mm} \quad (6.18)$$

$$k_{f.app.400} = 25.9 \text{ N/mm} \quad (6.19)$$

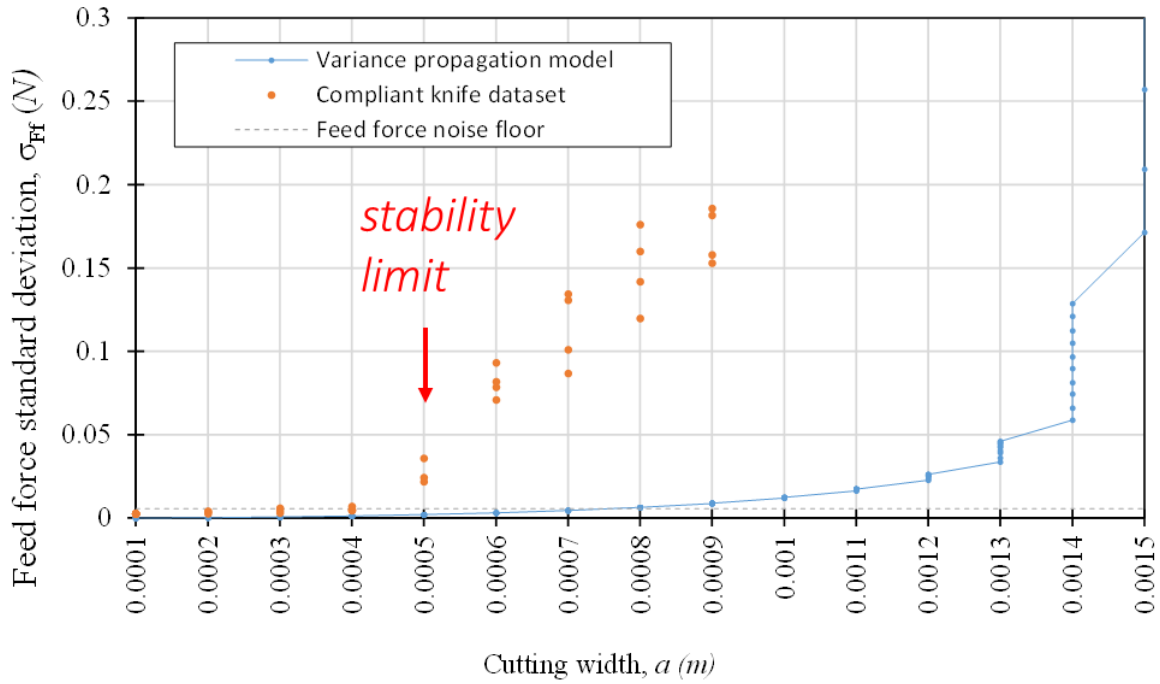
$$k_{f.app.500} = 26.8 \text{ N/mm} \quad (6.20)$$

These apparent stiffnesses are smaller than the nominal cutting stiffness of  $49 \text{ N/mm}$  by a factor of between  $0.36 - 0.55$ , and would lower the overall stiffness of the cutting system; this would cause earlier onset of instability and erratic cutting behavior, as was observed in the cutting data.

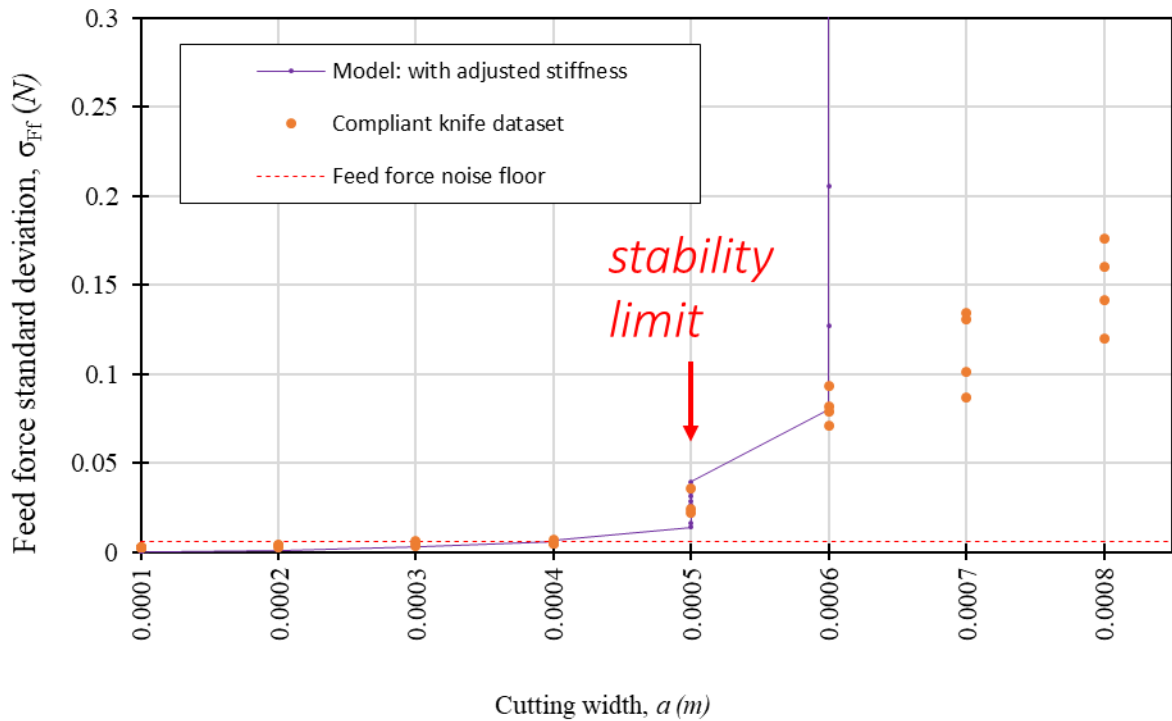
### 6.4.3 Stability limits with additional compliance

Using the knife tip compliance matrix derived from the FEA analysis at the  $100 \mu\text{m}$  cutting width (which is also consistent with the measurements taken from inspecting microscope video), the stability limits and variance propagations are calculated with the cross-compliance adjusted feed stiffness. The knife tip compliance is put in series with the compliant knife carrier via addition of the two compliance matrices (it is assumed for the compliant knife carrier that only the  $C_{xx}$  term is nonzero).

The variance propagation model is plotted against the experimentally measured feed force standard deviation using the nominal stiffness value (Figure 6.14a) and using the adjusted stiffness value  $k_{f.app.100}$  (Figure 6.14b). These plots show how the variation within a single cut evolves as the cutting progresses with the number of cutting passes and the width of cut. The variation is expected to grow only when the system is approaching instability. Without the stiffness adjustment, the model overpredicts system stability; with the adjusted stiffness value, the model correctly predicts when the system begins to go unstable.



(a)



(b)

Figure 6.14: Measured feed force standard deviation at each cutting width, with lower bound of apparent tip stiffness,  $k_{f.app.100}$ , (a) plotted against cutting width (b) with cut width normalized against the stability limit at this apparent stiffness. The observed stability limit is indicated on the plots; experimental data points are not expected to correspond with the variance propagation model.

The additional feed-direction compliance introduced by the localized deflections of the knife tip and the interaction between the slice and feed compliance due to the cross-compliances cannot be ignored, and once these are considered the variance propagation model syncs with the experimental observations.

## 6.5 Comparison of cutting behavior for positive and negative $K_f$

In the positive- $K_f$  cutting dataset, the mean feed force steadily increases with the width of cut. In contrast, the negative- $K_f$  dataset, the mean initially increases with cut width, then begins to oscillate, until the oscillations are large enough to reach zero magnitude, or flip sign entirely (i.e., switch from digging-in to pushing-out).

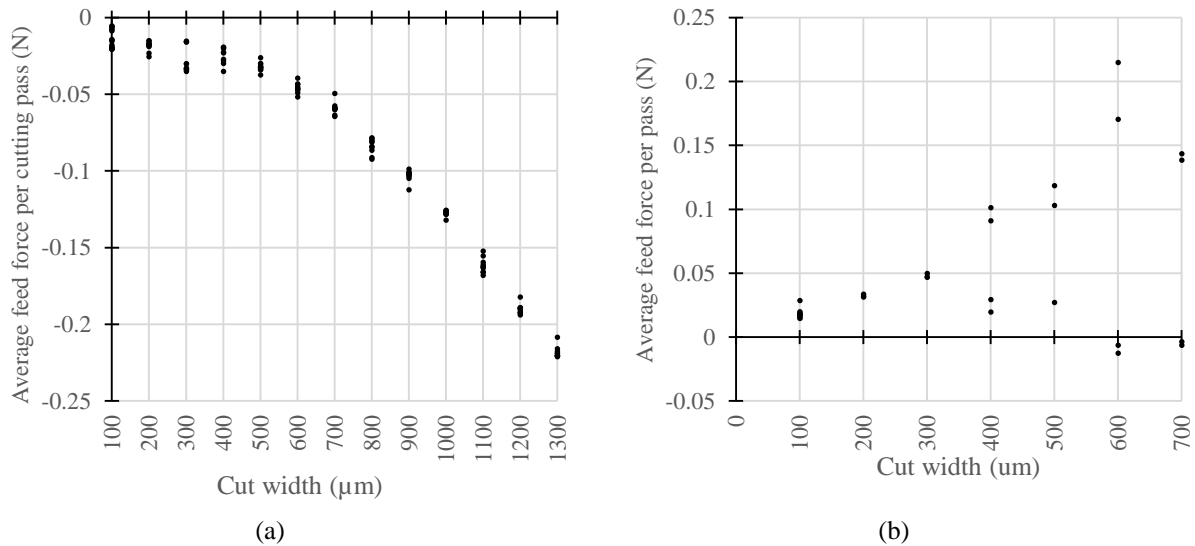


Figure 6.15: Comparison between positive and negative  $K_f$  dataset – Feed force mean increase with cut width (a) positive  $K_f$  dataset (b) negative  $K_f$  dataset

In both datasets, the spread in the feed force increases with cutting width, and generally increases with each cut. The magnitude of the increase is larger in the negative- $K_f$  dataset, and



the rapid increase in the feed force variation is hampered by the tool jumping out of the cut; the positive- $K_f$  cutting dataset does not experience this effect.

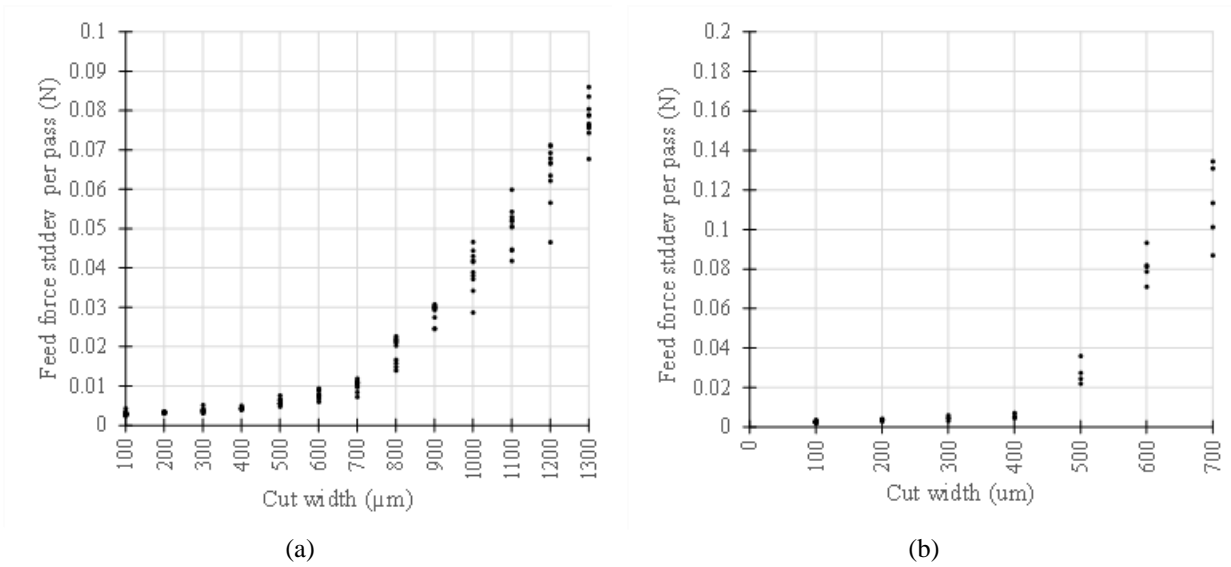


Figure 6.16: Comparison between positive and negative  $K_f$  dataset –  $F_f$  stddev increase with cut width

*(this page intentionally left blank)*

## CONCLUSIONS AND FUTURE WORK

---

In this final chapter, conclusions from the experimental results are discussed, contributions are summarized, and future work is proposed.

### 7.1 Conclusions

Care must be taken when discussing section thickness variations in microtome cutting. Calling these variations chatter doesn't give physical insight into its origins, as chatter can originate from several different phenomena, for example a forced vibration versus a regenerative vibration.

The dig-in instability must be considered in designing a sectioning machine or process – it should be part of a design checklist. Furthermore, the dig-in stability is not a binary phenomenon – there is a transition zone where cutting performance degrades. The variance propagation model describes the magnitude of the effect within the transition zone, and gives design engineers guidance in reducing the size of the transition zone if so desired. Engineers can now model how much extra system stiffness is required to maintain high fidelity cutting at larger widths of cut approaching the stability limit.

With the dig-in instability models, several new things are enabled. Once the specific feed pressure of the cutting system is known (either by looking up a tabulated value or via measurement) a machine can be designed to cut at a desired width of cut successfully. The

maximum width of a cut for an existing cutting machine can be determined by characterizing its stiffness characteristics and measuring the workpiece/tool  $K_f$  value. Lastly, if the sectioning equipment is equipped with a force sensor, this can be used as a process alarm to alert the operator that the process is going unstable, if for example the force variation grows begins to grow in accordance with the variance propagation model.

## 7.2 Contributions

This work is a step towards realizing robust large-width serial sectioning cutting systems.

The central contributions of this thesis are as follows:

1. An instrument to characterize cutting and stability
2. Identifying the dig-in instability as a major cause of serial sectioning failure
  - a. Core knowledge for understanding and mitigating dig-in
  - b. Maximum cutting width before series cutting dig-in instability onset
  - c. Understanding of the system sensitivity leading up to dig-in instability
3. Defined key process characteristics and how to measure them
4. Linking instrument and cutting parameters to cutting stability, Set requirements on machine and cutting parameters for large-area sectioning via stiffness requirements for a given specific feed pressure
5. A description of additional effects influenced by the same parameters that also influence dig-in stability
  - a. Thick-thin sectioning and skip-sectioning
  - b. Section accuracy (via the steady-state offset)

## 7.3 Future work

In the course of this work, several potential avenues of further research were identified, but due to time and resource constraints were not explored in-depth in this work. However,

further work in these areas would greatly augment the understanding between instrument characteristics, cutting parameters, and sectioning stability.

### **7.3.1 An improved understanding of the specific feed pressure**

The models developed in this work all rely on the specific feed pressure  $K_f$  as a critical parameter for the dig-in stability of a cutting system, but an in-depth understanding of  $K_f$  and its relation to cutting and material parameters is currently lacking, especially in materials of interest (such as embedded organic tissues) and at cutting parameters relevant to microtome cutting. The machining literature (such as in [44]) provides charts tabulating  $K_f$  for selected polymers at several cutting speeds, feeds, and rake angles relevant to machining, but without information on how much  $K_f$  variation to expect within a given cut. Such  $K_f$  variation could be due to spatial variation in material properties. Specifically, it would be useful to know

- $K_f$  and  $K_c$  for a given tool/material combination, and cutting parameters such as feed and speed
- How these values change with cutting parameters such as feed, speed, rake angle, and lubrication
- How these values change with additional parameters such as the temperature of the work zone, or humidity
- How much variation there is in  $K_f$  and  $K_c$  within a given cut
- How stable  $K_f$  and  $K_c$  are over time, and if they will change through a series of cutting, due to for example edge wear, or material buildup on the rake face during cutting

To design a machine capable of reliably sectioning large samples of embedded tissue, there needs to be more information on  $K_f$  and its variation both during a single cut as well as its stability over a series of cuts, for a particular embedded tissue.

### **7.3.2 An improved model for localized knife tip compliance**

Understanding dig-in stability limits requires understanding the net compliance of the entire cutting system's structural loop, and this includes the knife edge. In this work, a two-dimensional plane-strain model based on a tapered cantilevered beam was used to estimate the compliance contribution from the knife tip, but it became apparent that this model was insufficient, and that localized effects are important given the parameters used in this work, in particular the wedge angle of the knife tip. Before generating this model, a literature search with special emphasis on the machining cutting literature for studies done on cutting tool tip compliance had turned up empty. In machining, there simply hasn't been enough interest in studying the tool tip compliance, especially since in machining the tools tend to be much stockier and cube-like rather than the slender wedges found in microtome cutting – it is very likely that the limiting compliance in a machining operation is something else in the system (typically the workpiece geometry itself, or deflections in the machine tool).

It is important to know when the knife tip will become the dominating compliance in the cutting system. A study which establishes knife tip compliance matrices based on the wedge angle of the tool (considering any additional microbevels), the knife tip length, and the tool material, ideally with experimental validation, would establish when the cutting system's net compliance (and thus the cutting system stability) is knife-dominated. It would also be very useful to establish safe operating regimes for the stresses in the knife tip based on the knife and cutting parameters – experience has shown that too slender and keen of a knife cannot be used for microtome cutting (or machining, for that matter) because it will have both insufficient strength and rigidity, but this has not been analytically modeled and studied.

### 7.3.3 Expanding dig-in stability criteria to cross-coupled MDOF stiffness

In the course of this work it became apparent that the cross-coupled nature of the system stiffness could not be ignored; in cutting, a feed force is always accompanied by a cutting force, usually with the cutting force being of larger magnitude. If the system has any stiffness interactions between its degrees of freedom (i.e., the system compliance or stiffness matrix has entries not on the main diagonal), these result in earlier system instability than expected based on the nominal values for one degree of freedom stability modeling.

Initial modeling work in this area was done to troubleshoot and explain why the system was going unstable earlier than expected compared to the stability limit predicted based on the nominal system stiffness values.

A simple model for a two degree-of-freedom (DOF) system with cross-coupling between the two degrees of freedom can be written out starting from the two degree-of-freedom equation of motion

$$\vec{F} = \mathbf{K}\vec{\delta} \quad (7.21)$$

$$\begin{bmatrix} F_x \\ F_y \end{bmatrix} = \begin{bmatrix} k_{xx} & k_{xy} \\ k_{yx} & k_{yy} \end{bmatrix} \begin{bmatrix} \delta_x \\ \delta_y \end{bmatrix} \quad (7.22)$$

Note that the cross-stiffness terms should be equal, e.g.,  $K_{xy} = K_{yx}$ . If the stiffness matrix is not singular, these stiffness matrix entries can be written in terms of the compliance matrix entries (Eqs (7.25)-(7.27)); in many cases it is simpler to characterize a system via its compliances by applying loads and measuring resulting deflections;

$$\vec{\delta} = \mathbf{C}\vec{F} \quad (7.23)$$

$$\begin{bmatrix} \delta_x \\ \delta_y \end{bmatrix} = \begin{bmatrix} C_{xx} & C_{xy} \\ C_{yx} & C_{yy} \end{bmatrix} \begin{bmatrix} F_x \\ F_y \end{bmatrix} \quad (7.24)$$

$$k_{xx} = \left( \frac{1}{C_{xx}C_{yy} - C_{xy}^2} \right) C_{yy} \quad (7.25)$$

$$k_{yy} = \left( \frac{1}{C_{xx}C_{yy} - C_{xy}^2} \right) C_{xx} \quad (7.26)$$

$$k_{xy} = - \left( \frac{1}{C_{xx}C_{yy} - C_{xy}^2} \right) C_{xy} \quad (7.27)$$

A two-DOF equation of motion can be written as was done before when modeling single-DOF dig-in stability and regenerative chatter, using the mechanistic model for cutting forces, and taking  $x$  and  $y$  as the displacement values from the system's rest positions in the  $X$  (feed) and  $Y$  (slice) directions, respectively

$$m_x \ddot{x} + b_x \dot{x} + k_{xx}x + k_{xy}y = K_f a(t_o - x) \quad (7.28)$$

$$m_y \ddot{y} + b_y \dot{y} + k_{yy}y + k_{xy}x = K_c a(t_o - x) \quad (7.29)$$

It is assumed that  $a, t_o, n, k_{xx}, k_{yy}$  and the mass variables are all positive. In general, the analysis of this already-simplified system is made more challenging because the ultimate behavior depends on the magnitude of  $n$ , and the sign of the cross stiffness  $k_{xy}$  as well as its relative magnitude to  $k_{xx}, k_{yy}$ . The poles of this system of equations can be used to derive an expression for the single-pass dig-in stability limit by writing an expression for the value of  $a$  which causes a system pole to have a positive real part instead of a negative real part (keeping in mind that now the system can go unstable in the  $X$  and the  $Y$  directions).



$$a_{dig} = -\frac{k_{xx}k_{yy} - k_{xy}^2}{K_f(k_{yy} - nk_{xy})}, \quad K_f > 0 \quad (7.30)$$

$$a_{dig} = -\frac{k_{xx}k_{yy} - k_{xy}^2}{K_f(k_{yy} + nk_{xy})}, \quad K_f < 0 \quad (7.31)$$

Of high interest is the fact that a single-pass dig-in stability limit exists at all in the positive- $K_f$  case; in the single-DOF case, positive- $K_f$  cutting was always dig-in stable. This implies that cutting in the positive- $K_f$  regime is no guarantee that the system will not be vulnerable to dig-in instability, and that special attention must be made to the mechanical design of cutting instruments to avoid introducing cross-stiffnesses that could cause dig-in instability.

Formula for the series dig-in stability (as opposed to the single-pass dig-in stability) can be derived in the same manner as for the single-DOF system. First, an expression for the steady-state equilibrium position offset from nominal feed can be derived,

$$x_{eq} = \frac{K_f a t_o (k_{yy} - k_{xy}n)}{K_f a k_{yy} + k_{xx}k_{yy} - K_f a n k_{xy} - k_{xy}^2} \quad (7.32)$$

$$y_{eq} = \frac{K_f a t_o (k_{xy} - k_{xx}n)}{K_f a k_{yy} + k_{xx}k_{yy} - K_f a n k_{xy} - k_{xy}^2} \quad (7.33)$$

These steady-state offset expressions can be used to derive an expression for the series dig-in stability using the same analysis as for the single-DOF series dig-in stability derivation in Section 3.2.1. For the negative and positive  $K_f$  case respectively, the series is unstable if

$$a > \frac{1}{2} \frac{k_{xy}^2 - k_{xx}k_{yy}}{K_f a (k_{yy} + nk_{xy})}, \quad K_f < 0 \quad (7.34)$$

$$a > \frac{1}{2} \frac{k_{xy}^2 - k_{xx}k_{yy}}{K_f a (k_{yy} - nk_{xy})}, \quad K_f > 0 \quad (7.35)$$

If the cross-stiffness  $k_{xy}$  is zero, this expression reverts to the single-DOF dig-in stability expression. There is much to be explored in the stability behavior for the coupled 2-DOF system, and could be a stepping stone to even more complex systems.

### **7.3.4 Understanding excitation source for chatter regeneration**

In Section B.3, it was discussed that one of the major deviations between the proposed regenerative chatter model and the observed experimental behavior, was a lack of understanding of the spectral content of the cutting forces generated during cutting. The model had predicted that the only system spectral content would be its own transient response during the initial transient response of the cutting system. It is clear from reviewing the cutting data that cutting does not generate a static cutting force value; there is some “noise” in the cutting not attributable to electrical noise in the force sensors, that there is some spectral component to the process force generated during cutting. Some of it could be tribological in nature, due to the nature of the contact between the section sliding across the rake face. There could be an interaction between the system’s stiffnesses and material properties, such as the “sawtoothing” behavior observed when cutting Acrylic. Understanding the spectral content of the cutting forces and how the spectrum is related to cutting parameters could ultimately lead to a viable regenerative chatter model for microtome cutting.

### **7.3.5 Roll/twist dig-in**

There are two possibilities to consider with respect to rolling motions of the tools (Figure 7.1). The first is a roll-type dig-in caused by one end of the knife digging into the material with the other end lifting out of the material; this could set up an instability where one end of the knife continues to dig-in, which increases the forces on that part of the knife, with the opposite occurring on the end that is lifting out of the cut.

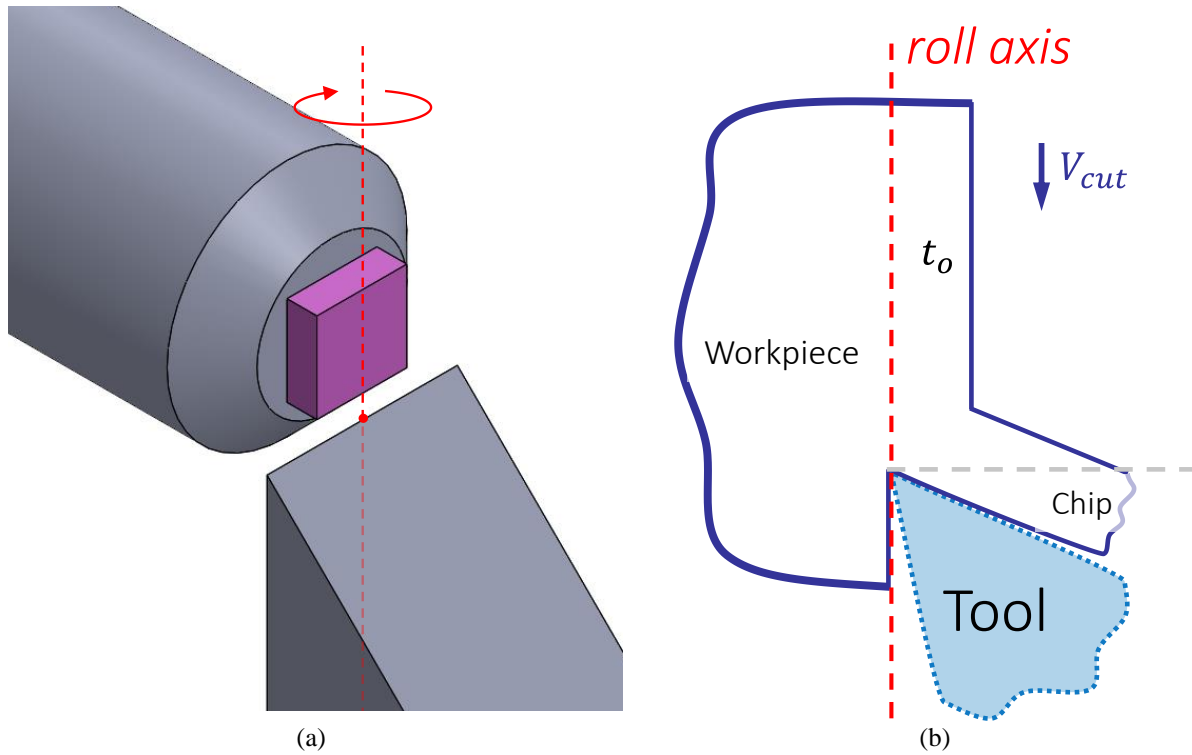


Figure 7.1: Roll/twist dig-in. (a) 3D view – the knife tip rotates about the dashed line (b) 2D side view. Rotations about this line would cause one end to dig deeper into the workpiece, and the other end to lift out of the material.

The second aspect to consider with regards to rolling motions between the knife and workpiece, is that feed force variation across the knife edge could in the worst case induce a rolling torque. At increased width of cut, this rolling torque and subsequent rotation due to the finite rolling stiffness of the cutting system will cause displacements in the feed direction that vary along the knife edge Figure 7.2.

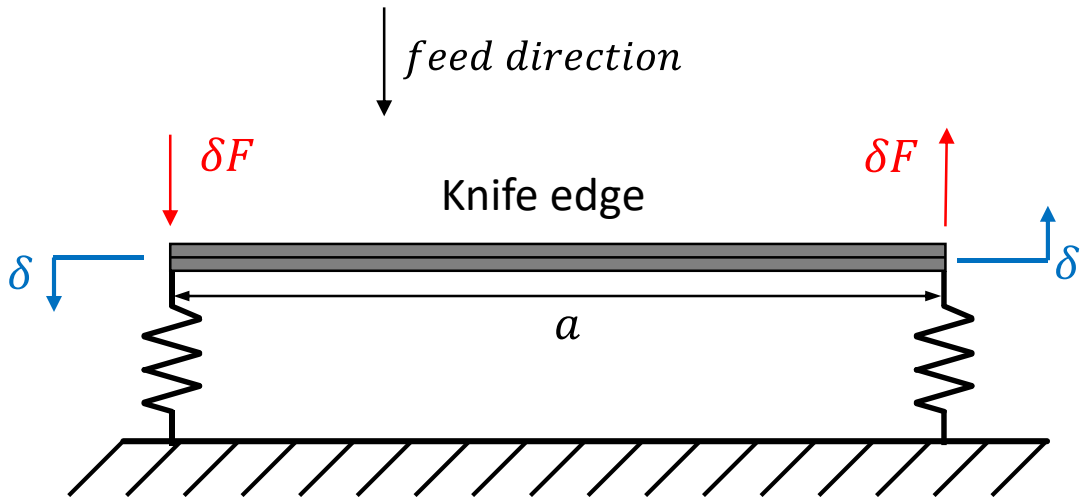


Figure 7.2: Knife rolling motions caused by force variations across the width of the knife edge; the knife as drawn here is seen looking down towards the knife edge, as if the knife was moving towards the viewer. In the worst case, the max variation  $\delta F$  acts on each side of the knife edge, in opposite directions, which causes displacements at each edge in opposite rotations.

For a back of the envelope calculation, the knife edge's rotational stiffness is lumped as a rigid bar supported by a spring on each end, and it is assumed that the stiffness at each end is  $1 \text{ N}/\mu\text{m}$ , and that  $\delta F$  is approximately  $10 \text{ mN}$ ; these stiffnesses and force values are based on values from this work. This would cause each end to deflect by  $10 \text{ nm}$ , for a total feed variation of  $20 \text{ nm}$  across the entire edge. If the sectioning process ultimately takes place at nanometer-scale feeds (around  $30 - 50 \text{ nm}$ ), this represents an error of between 60-40% of the nominal feed.

In this work, it was assumed that the stiffness and deflections were linear, but it is here posited that rotational stiffnesses could also cause errors in section thickness and potentially a source of additional instability.

# REFERENCES

---

- [1] H. Horstmann, C. Körber, K. Sätzler, D. Aydin, and T. Kuner, "Serial Section Scanning Electron Microscopy (S3EM) on Silicon Wafers for Ultra-Structural Volume Imaging of Cells and Tissues," *PloS one*, vol. 7, p. e35172, 2012.
- [2] S. Mikula, "Progress Towards Mammalian Whole-Brain Cellular Connectomics," *Frontiers in Neuroanatomy*, vol. 10, 2016-June-30 2016.
- [3] J. M. Perkel, "MAPPING NEURAL CONNECTIONS," *Biotechniques*, vol. 57, pp. 230-236, 2013.
- [4] A. WANNER, M. KIRSCHMANN, and C. GENOUD, "Challenges of microtome-based serial block-face scanning electron microscopy in neuroscience," *Journal of Microscopy*, 2015.
- [5] G. Knott and C. Genoud, "Is EM dead?," *Journal of cell science*, vol. 126, pp. 4545-4552, 2013.
- [6] S. Mikula and W. Denk, "High-resolution whole-brain staining for electron microscopic circuit reconstruction," *Nature methods*, 2015.
- [7] V. Marx, "Neurobiology: brain mapping in high resolution," *Nature*, vol. 503, pp. 147-152, 2013.
- [8] K. L. Briggman and D. D. Bock, "Volume electron microscopy for neuronal circuit reconstruction," *Current Opinion in Neurobiology*, vol. 22, pp. 154-161, 2// 2012.
- [9] J. Kornfeld and W. Denk, "Progress and remaining challenges in high-throughput volume electron microscopy," *Current opinion in neurobiology*, vol. 50, pp. 261-267, 2018.
- [10] J. G. White, E. Southgate, J. N. Thomson, and S. Brenner, "The structure of the nervous system of the nematode *Caenorhabditis elegans*," *Philosophical Transactions of the Royal Society of London. B, Biological Sciences*, vol. 314, pp. 1-340, 1986.
- [11] S. W. Emmons, "The beginning of connectomics: a commentary on White et al.(1986)'The structure of the nervous system of the nematode *Caenorhabditis elegans*'," *Philosophical Transactions of the Royal Society B: Biological Sciences*, vol. 370, p. 20140309, 2015.
- [12] N. Kasthuri, K. J. Hayworth, D. R. Berger, R. L. Schalek, J. A. Conchello, S. Knowles-Barley, *et al.*, "Saturated reconstruction of a volume of neocortex," *Cell*, vol. 162, pp. 648-661, 2015.
- [13] P. Webster, D. Bentley, and J. Kearney, "The ATUMtome for automated serial sectioning and 3-D imaging," *Microsc AnalMarch*, pp. 19-23, 2015.
- [14] W. Denk and H. Horstmann, "Serial block-face scanning electron microscopy to reconstruct three-dimensional tissue nanostructure," *PLoS biology*, vol. 2, p. e329, 2004.

- [15] A. Eberle, S. Mikula, R. Schalek, J. Lichtman, M. K. TATE, and D. Zeidler, "High-resolution, high-throughput imaging with a multibeam scanning electron microscope," *Journal of microscopy*, 2015.
- [16] I. Gatan, "3View2: Serial Block Face Imaging," ed, 2011.
- [17] G. Knott, H. Marchman, D. Wall, and B. Lich, "Serial section scanning electron microscopy of adult brain tissue using focused ion beam milling," *The Journal of Neuroscience*, vol. 28, pp. 2959-2964, 2008.
- [18] C. S. Xu, K. J. Hayworth, Z. Lu, P. Grob, A. M. Hassan, J. G. Garcia-Cerdan, *et al.*, "Enhanced FIB-SEM systems for large-volume 3D imaging," *Elife*, vol. 6, p. e25916, 2017.
- [19] A. J. Bushby, K. M. Y. P'ng, R. D. Young, C. Pinali, C. Knupp, and A. J. Quantock, "Imaging three-dimensional tissue architectures by focused ion beam scanning electron microscopy," *Nat. Protocols*, vol. 6, pp. 845-858, 05//print 2011.
- [20] K. Amunts, C. Lepage, L. Borgeat, H. Mohlberg, T. Dickscheid, M.-É. Rousseau, *et al.*, "BigBrain: An Ultrahigh-Resolution 3D Human Brain Model," *Science*, vol. 340, pp. 1472-1475, 2013.
- [21] D. Mayerich, L. Abbott, and B. McCormick, "Knife-edge scanning microscopy for imaging and reconstruction of three-dimensional anatomical structures of the mouse brain," *Journal of Microscopy*, vol. 231, pp. 134-143, 2008.
- [22] T. Ragan, L. R. Kadiri, K. U. Venkataraju, K. Bahlmann, J. Sutin, J. Taranda, *et al.*, "Serial two-photon tomography for automated ex vivo mouse brain imaging," *Nature Methods*, vol. 9, pp. 255-258, 2012.
- [23] K. J. Hayworth, "Electron Imaging Technology for Whole Brain Neural Circuit Mapping," *International Journal of Machine Consciousness*, vol. 4, pp. 87-108, 2012.
- [24] K. J. Hayworth, C. S. Xu, Z. Lu, G. W. Knott, R. D. Fetter, J. C. Tapia, *et al.*, "Ultrastructurally smooth thick partitioning and volume stitching for large-scale connectomics," *Nature methods*, vol. 12, pp. 319-322, 2015.
- [25] S. McGee-Russell, W. De Bruijn, and G. Gosztanyi, "Hot knife microtomy for large area sectioning and combined light and electron microscopy in neuroanatomy and neuropathology," *Journal of neurocytology*, vol. 19, pp. 655-661, 1990.
- [26] N. Reid, "Ultramicrotomy," *Practical methods in electron microscopy. North-Holland Publ. Co.: Amsterdam, Oxford. American Elsevier Publ. Co.: New York*, pp. 213-353, 1975.
- [27] M. J. Dykstra, *A manual of applied techniques for biological electron microscopy*: Springer Science & Business Media, 1993.
- [28] L. D. Peachey, "Thin Sections. I. A Study of Section Thickness and Physical Distortion Produced during Microtomy," *The Journal of Biophysical and Biochemical Cytology*, vol. 4, pp. 233-242, 1958.
- [29] J. S. Guntupalli, "Physical sectioning in 3D biological microscopy," Texas A&M University, 2007.

- [30] H. F. Steedman, *Section Cutting: in microscopy*: Blackwell Scientific Publicati, 1960.
- [31] R. Phillips, "Diamond knife ultra microtomy of metals and the structure of microtomed sections," *British Journal of Applied Physics*, vol. 12, p. 554, 1961.
- [32] H. Aldrich and H. Mollenhauer, "Secrets of successful embedding, sectioning, and imaging," in *Ultrastructure techniques for microorganisms*, ed: Springer, 1986, pp. 101-132.
- [33] D. G. C. Hildebrand, M. Cicconet, R. M. Torres, W. Choi, T. M. Quan, J. Moon, *et al.*, "Whole-brain serial-section electron microscopy in larval zebrafish," *Nature*, vol. 545, p. 345, 2017.
- [34] H. F. Helander, "Some observations on knife properties and sectioning mechanics during ultramicrotomy of plastic embedding media," *J Microscopy*, vol. 101, pp. 81-93, May 1974.
- [35] A. J. Saubermann, W. D. Riley, and R. Beeuwkes, "Cutting work in thick section cryomicrotomy," *Journal of Microscopy*, vol. 111, pp. 39-49, 1977.
- [36] A. Willis, "Design and development of and instrumented microtome," University of Reading, 1988.
- [37] A. Willis and J. Vincent, "Monitoring cutting forces with an instrumented histological microtome," *Journal of Microscopy*, vol. 178, pp. 56-65, 1995.
- [38] R. T. Allison and J. F. V. Vincent, "Measuring the forces acting during microtomy by the use of load cells," *Journal of microscopy*, vol. 159, pp. 203-210, 1990.
- [39] M. L. Ericson and H. Lindberg, "Design and potential of instrumented ultramicrotomy," *Polymer*, vol. 38, pp. 4485-4489, 1997.
- [40] M. L. Ericson and H. Lindberg, "Method of measuring energy dissipation during crack propagation in polymers with an instrumented ultramicrotome," *Journal of Materials Science*, vol. 31, pp. 655-662, 1996.
- [41] M. Reck, "Case Study for an Automated Lathe Ultramicrotome," in *2010 Spring Topical Meeting, ASPE Proceedings, Control of Precision Systems*, Massachusetts Institute of Technology, 2010.
- [42] A. Atkins, *The science and engineering of cutting: the mechanics and processes of separating, scratching and puncturing biomaterials, metals and non-metals*: Butterworth-Heinemann, 2009.
- [43] E. Oberg, F. D. Jones, H. L. Horton, and H. H. Ryffel, *Machinery's Handbook*, 30 ed. South Norwalk: Industrial Press, Inc, 2016.
- [44] A. Kobayashi, *Machining of plastics*: R.E. Krieger Pub. Co., 1981.
- [45] M. C. Shaw, *Metal cutting principles* vol. 2: Oxford University Press New York, 2005.
- [46] Y. Altintas, *Manufacturing automation: metal cutting mechanics, machine tool vibrations, and CNC design*: Cambridge university press, 2012.
- [47] C. Van Luttervelt, T. Childs, I. Jawahir, F. Klocke, P. Venuvinod, Y. Altintas, *et al.*, "Present situation and future trends in modelling of machining operations progress report

- of the CIRP Working Group ‘Modelling of Machining Operations’,” *CIRP Annals-Manufacturing Technology*, vol. 47, pp. 587-626, 1998.
- [48] G. Quintana and J. Ciurana, "Chatter in machining processes: A review," *International Journal of Machine Tools and Manufacture*, vol. 51, pp. 363-376, 2011.
- [49] Y. Altintas and M. Weck, "Chatter stability of metal cutting and grinding," *CIRP Annals-Manufacturing Technology*, vol. 53, pp. 619-642, 2004.
- [50] F. F. Kollmann, E. W. Kuenzi, and A. J. Stamm, *Principles of wood science and technology: II Wood Based Materials*: Springer Science & Business Media, 2012.
- [51] U. M. Rao, J. D. Cumming, and E. G. Thomsen, "Some Observations on the Mechanics of Orthogonal Cutting of Delrin and Zytel Plastics," *Journal of Engineering for Industry*, vol. 86, pp. 117-121, 1964.
- [52] W. C. Young and R. G. Budynas, *Roark's formulas for stress and strain* vol. 7: McGraw-Hill New York, 2002.
- [53] K. L. Johnson, *Contact mechanics*: Cambridge university press, 1987.
- [54] A. H. Slocum, *Precision machine design*: Society of Manufacturing Engineers, 1992.
- [55] Engineering ToolBox. (2003). *Young's Modulus - Tensile and Yield Strength for common Materials*. Available: [https://www.engineeringtoolbox.com/young-modulus-d\\_417.html](https://www.engineeringtoolbox.com/young-modulus-d_417.html)
- [56] Engineering ToolBox. (2008). *Engineering Materials*. Available: [https://www.engineeringtoolbox.com/engineering-materials-properties-d\\_1225.html](https://www.engineeringtoolbox.com/engineering-materials-properties-d_1225.html)
- [57] Engineering ToolBox. (2003). *Specific Heat of some common Substances*. Available: [https://www.engineeringtoolbox.com/specific-heat-capacity-d\\_391.html](https://www.engineeringtoolbox.com/specific-heat-capacity-d_391.html)
- [58] D. A. Stephenson and J. S. Agapiou, *Metal cutting theory and practice*: CRC press, 2016.
- [59] Engineering ToolBox. (2005). *Thermal Conductivity of Metals, Metallic Elements and Alloys*. Available: [https://www.engineeringtoolbox.com/thermal-conductivity-metals-d\\_858.html](https://www.engineeringtoolbox.com/thermal-conductivity-metals-d_858.html)
- [60] W. Gao, R. J. Hocken, J. A. Patten, and J. Lovingood, "Experiments using a nano-machining instrument for nano-cutting brittle materials," *CIRP Annals-Manufacturing Technology*, vol. 49, pp. 439-442, 2000.
- [61] M. Ericson and H. Lindberg, "Instrumented ultramicrotomy- A method to study nano-scale crack growth," in *International Conference on Deformation, Yield and Fracture of Polymers, 10 th, Churchill College, Cambridge, United Kingdom*, 1997, pp. 306-309.
- [62] I. D. Marinescu, E. Uhlmann, and T. Doi, *Handbook of lapping and polishing*: CrC Press, 2006.
- [63] R. M. Voyles, J. D. Morrow, and P. K. Khosla, "The Shape From Motion Approach to Rapid and Precise Force/Torque Sensor Calibration," *Journal of Dynamic Systems, Measurement, and Control*, vol. 119, pp. 229-235, 1997.
- [64] S. Timoshenko and J. Goodier, *Theory of Elasticity*, 3rd ed.: McGraw-Hill book Company, 1970.



- [65] L. C. Hale, "Principles and techniques for designing precision machines," Massachusetts Institute of Technology, Dept. of Mechanical Engineering, 1999.
- [66] J. B. Hopkins, "Design of flexure-based motion stages for mechatronic systems via freedom, actuation and constraint topologies (FACT)," Massachusetts Institute of Technology, 2010.

*(this page intentionally left blank)*

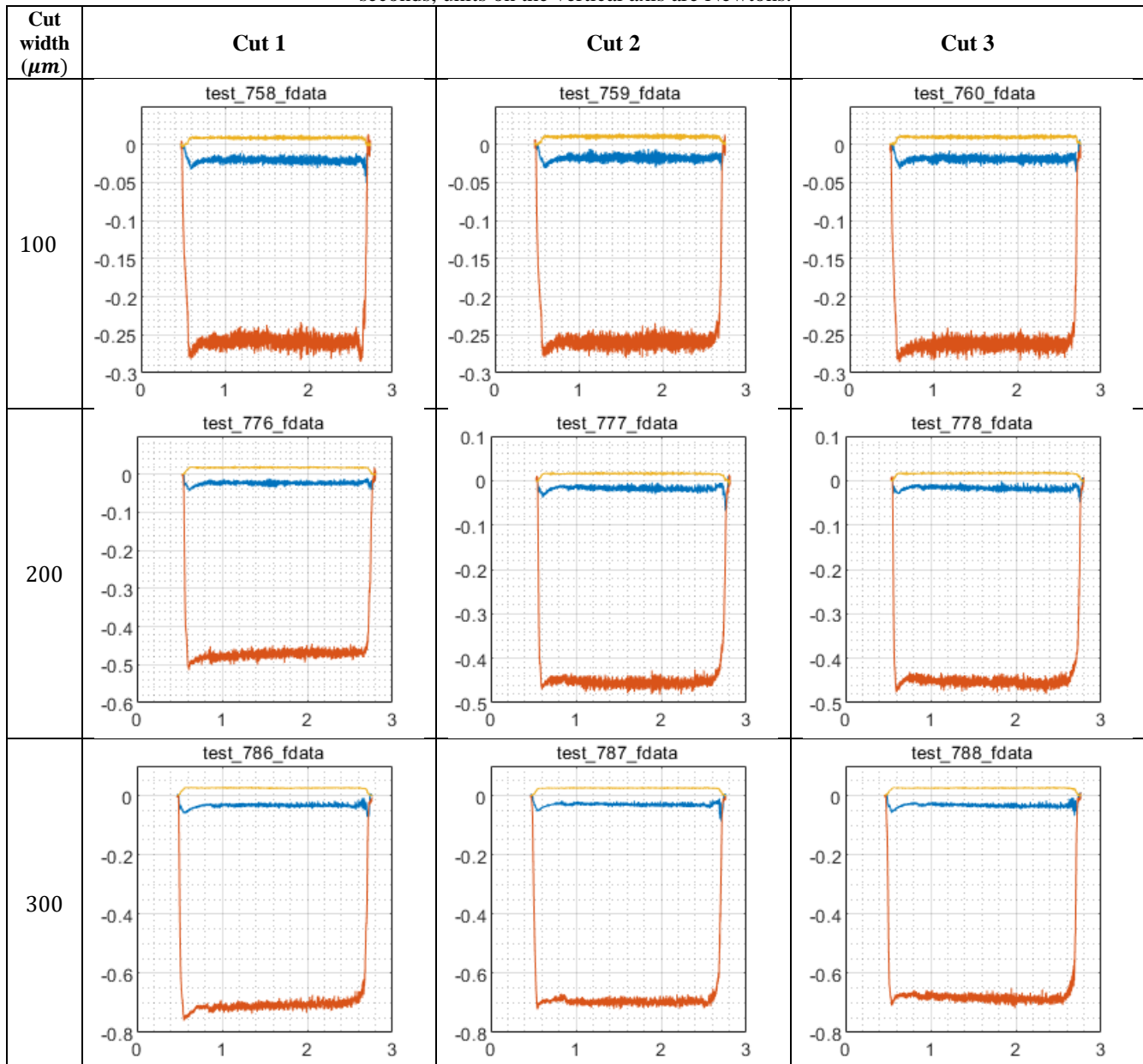
# A

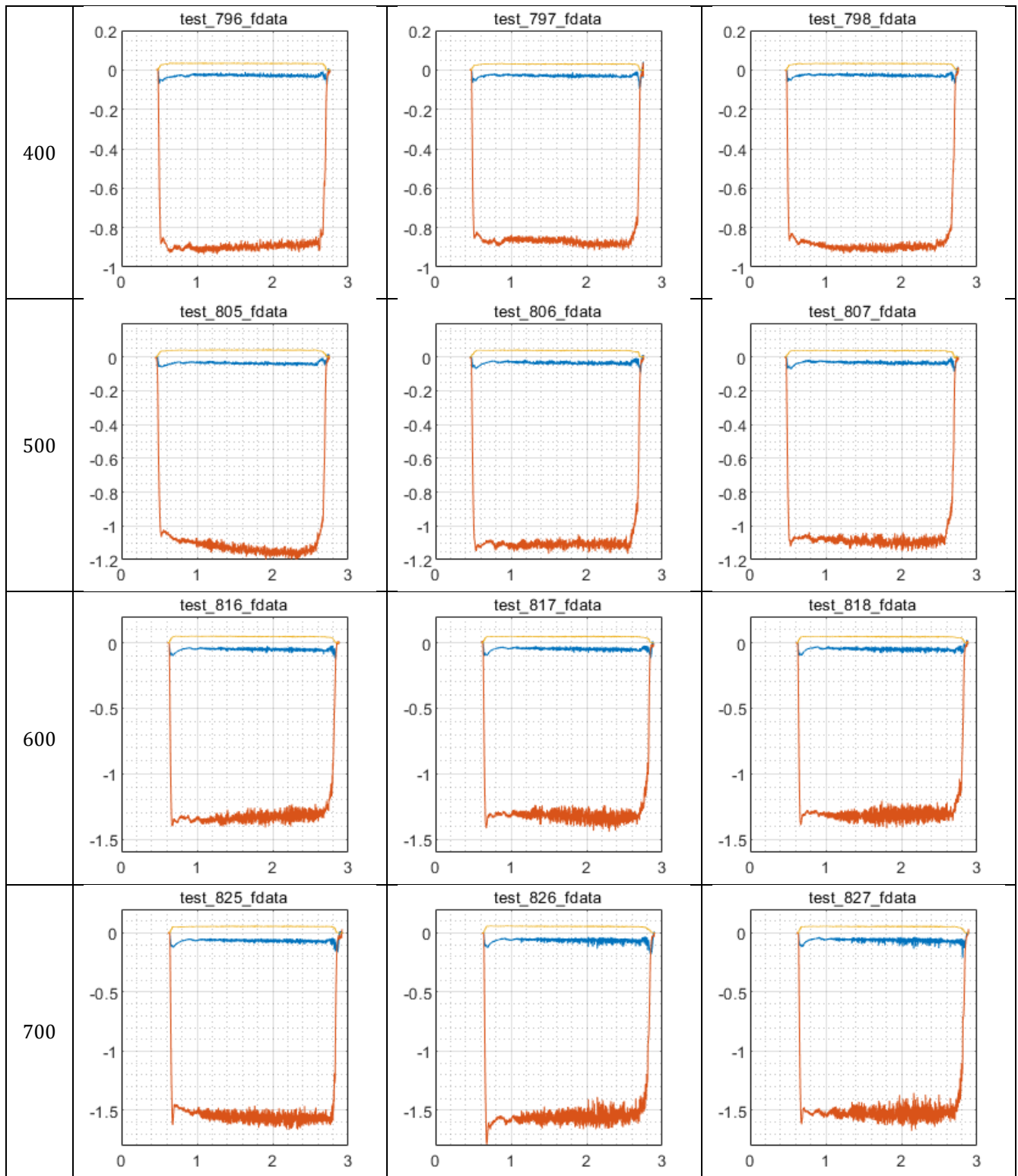
## CUTTING WITH POSITIVE $K_f$

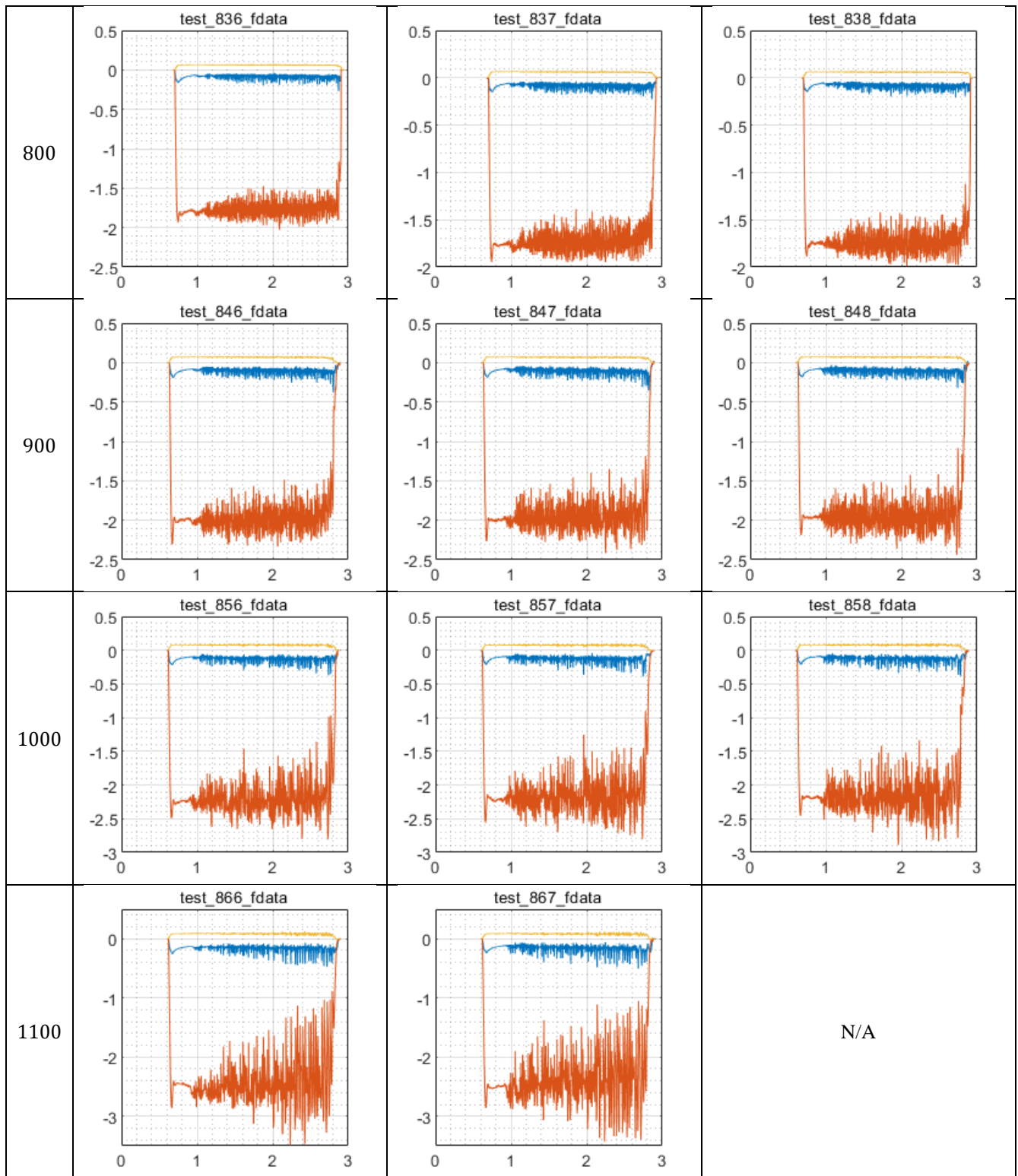
---

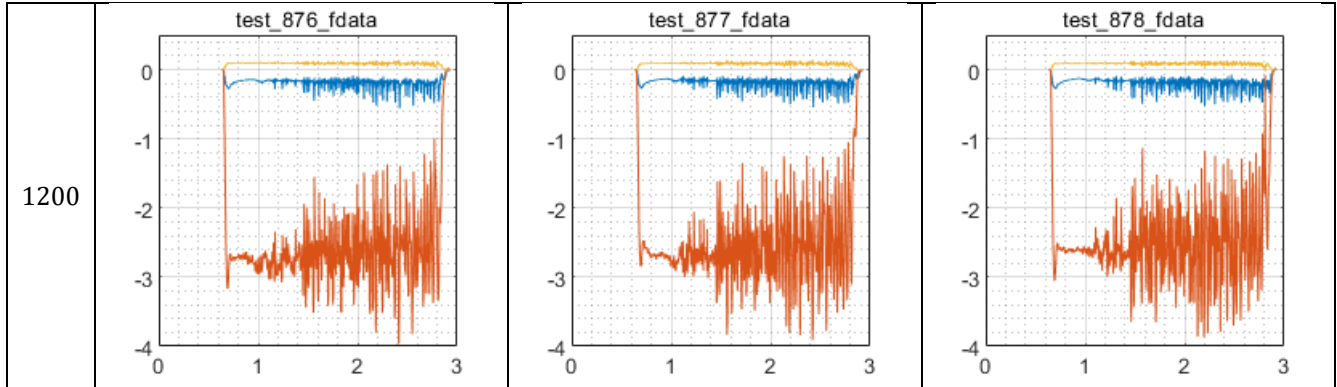
In this experiment, an Acrylic specimen was used instead of Delrin, which resulted in a positive  $K_f$ . Cutting force data for the positive- $K_f$  stepped-width and compliant knife dataset is presented in Table A-1; three cutting forces vs time plots are shown at each cut width to show how the cutting forces evolve as the cutting progresses.

Table A-1: Force plots from stepped-width Acrylic specimen and compliant knife cutting (a positive  $K_f$  combination). Cutting forces are plotted at each cutting width.  $F_x$  blue,  $F_y$  red,  $F_z$  yellow. The feed force is nominally negative, according to the coordinate system in Figure 6.1. This indicates a push-out force. Units on the horizontal axis are seconds, units on the vertical axis are Newtons.









Cutting statistics for the positive  $K_f$  dataset at each cut width are presented below in

Table A-2.

Table A-2: Cutting force mean and standard deviation in each force direction for the positive- $K_f$  stepped-width cutting dataset. Units for statistics are Newtons.

Cutting width ( $\mu\text{m}$ )	$n$	$\mu_x$	$\sigma_{Fx}$	$\mu_y$	$\sigma_{Fy}$	$\mu_z$	$\sigma_{Fz}$
100	18	-0.0145	0.0030	-0.2592	0.0062	0.0093	0.0012
200	9	-0.0176	0.0033	-0.4596	0.0068	0.0168	0.0011
300	9	-0.0267	0.0038	-0.6839	0.0089	0.0249	0.0011
400	9	-0.0239	0.0046	-0.8808	0.0124	0.0313	0.0011
500	9	-0.0321	0.0060	-1.0933	0.0197	0.0387	0.0015
600	9	-0.0455	0.0082	-1.3212	0.0326	0.0470	0.0019
700	9	-0.0596	0.0108	-1.5420	0.0393	0.0538	0.0022
800	9	-0.0841	0.0195	-1.7507	0.0764	0.0612	0.0030
900	9	-0.1034	0.0292	-1.9847	0.1329	0.0689	0.0046
1000	9	-0.1274	0.0407	-2.2146	0.2102	0.0770	0.0069
1100	9	-0.1626	0.0513	-2.4100	0.2988	0.0822	0.0095
1200	9	-0.1909	0.0661	-2.6760	0.4294	0.0905	0.0141

## A.1 Specific feed pressure calculation

The specific feed pressure for the compliant knife when cutting Acrylic was not constant throughout cutting. The mean forces during the initial cuts are used to calibrate the material – however, in this dataset, the mean forces change between the beginning and end of the cut, with no detectable (via microscope videos) change in the depth of cut or in the cutting behavior (all of the videos in this series are exemplary of ideal orthogonal cutting).

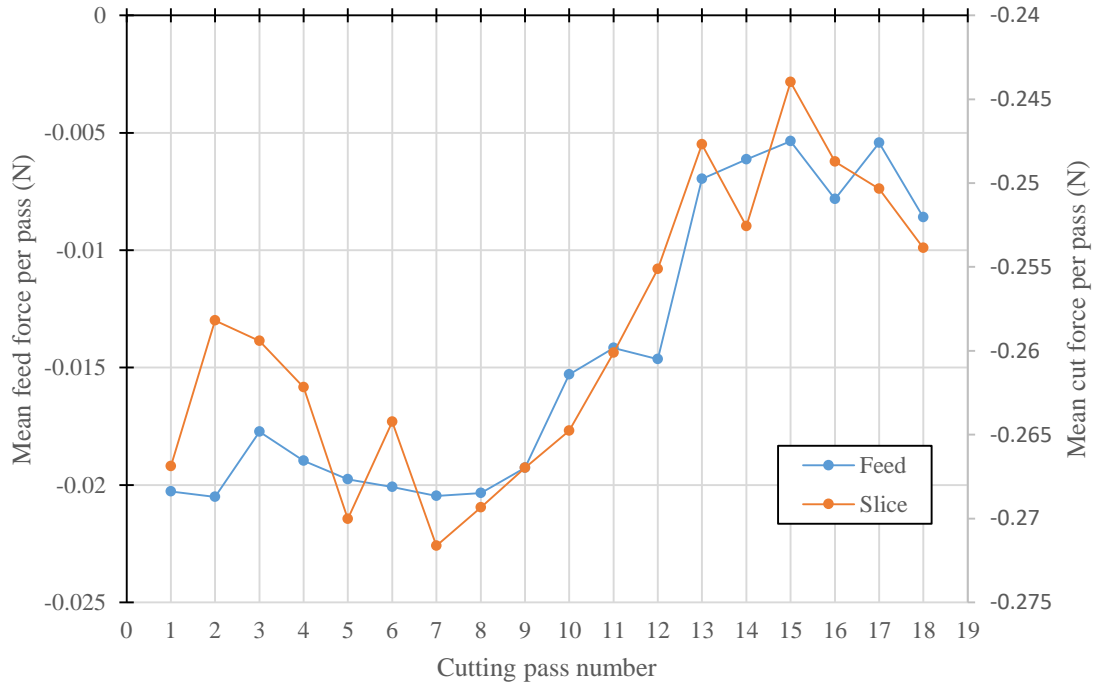


Figure A.3: Mean forces vs cutting pass for the 100  $\mu\text{m}$  width  $K_f$  calibration cuts in the positive- $K_f$  dataset with stepped width specimen and compliant knife.

It is possible that this shift is caused by cutting through a vitrified layer of Acrylic left behind from machining (the specimens were machined from extruded Acrylic rod stock), or a change in the tribological conditions between the material and the tool rake face after several cuts. The first nine cuts and the final six cuts in this series both appear to have an average; these can be used to bound the specific feed pressure. The high value of  $K_f$  is 19.7  $\text{N}/\text{mm}^2$  based on the initial cuts, the low  $K_f$  is 6.7  $\text{N}/\text{mm}^2$  based on the final cut in the 100  $\mu\text{m}$  series.

## A.2 Mean feed force vs cutting pass – positive $K_f$

Since the specific feed pressure is not constant throughout the calibration cuts and doesn't settle to a steady value, a transformation cannot be reliably made between the mean feed force and the tool position; the specific feed pressure cannot be assumed constant throughout the



cutting. Instead, the mean feed force is plotted against the cutting width (Figure A.4). The observed behavior is that the average feed force monotonically increases with cutting width.

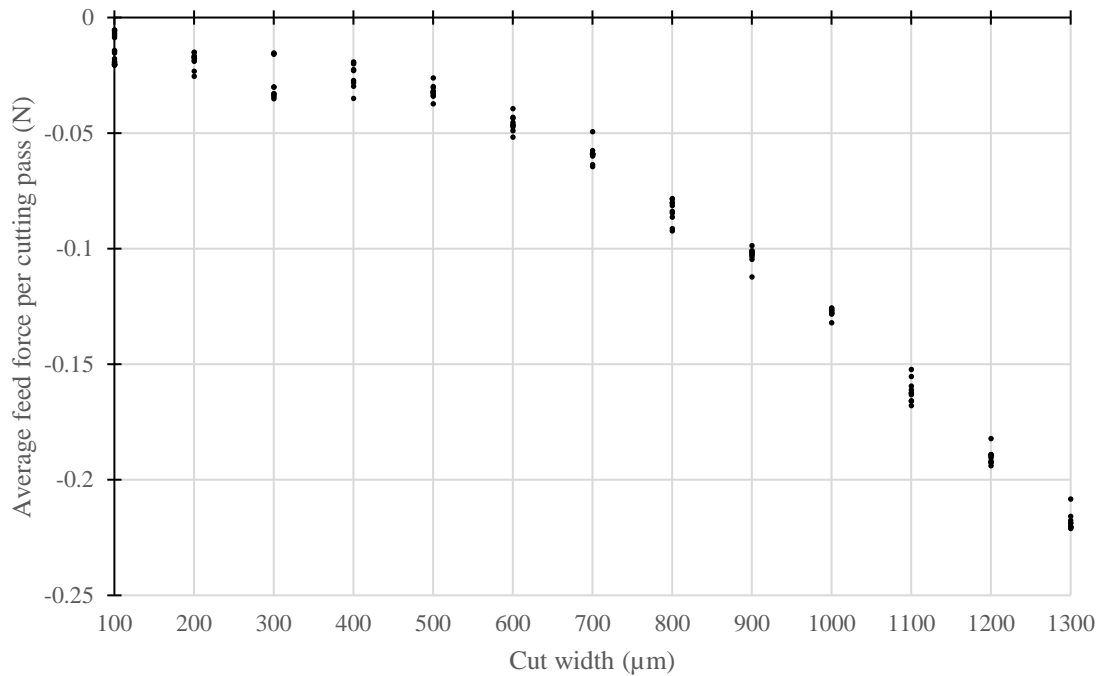


Figure A.4: Mean feed force per cutting pass, positive  $K_f$  dataset, Acrylic specimen and compliant knife

### A.3 Feed force standard deviation vs cutting pass - positive $K_f$

The feed force standard deviation vs cutting width is shown compared to the variance propagation model in Figure A.5.

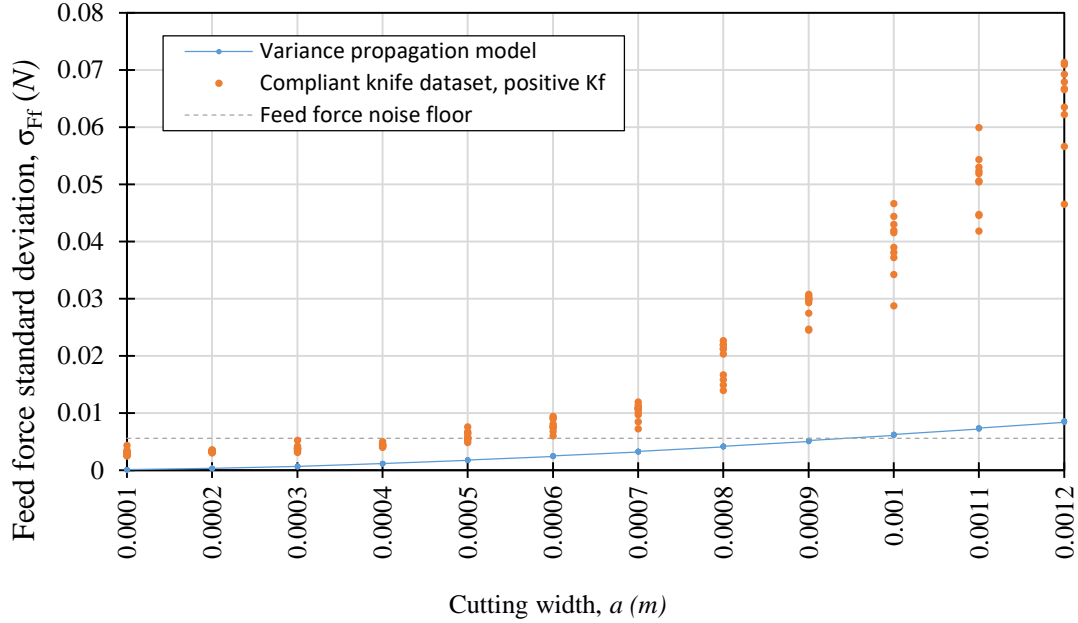


Figure A.5: Feed force standard deviation vs cutting width, positive- $K_f$  dataset (Acrylic and compliant knife)

The parameters used for the variance propagation model are given below in Table A-3.

Table A-3: Parameters used for feed force and position propagation model used in Figures

Parameter	Value	unit	Description
$K_f$	2.06E+07	$N/m^2$	Specific feed pressure
$k_f$	4.90E+04	$N/m$	Feed stiffness
$a_{min}$	1.00E-04	$m$	Cutting width, min
$a_{max}$	1.5E-03	$m$	Cutting width, max
$a_{inc}$	0.1E-04	$m$	Cutting width increment
$N_{pass}$	10		Cutting passes per cutting width
$t_o$	1.00E-05	$m$	Nominal feed
$\sigma_a$	1.40E-06	$m$	Cutting width standard deviation
$\sigma_{K_f}$	1.50E+06	$N/m^2$	Specific feed pressure standard deviation
$\sigma_{k_f}$	0	$N/m$	Feed stiffness standard deviation
$\sigma_{xr}$	1.00E-06	$m$	Initial regenerative surface ('seed')
$\sigma_{to}$	5.00E-07	$m$	Nominal feed standard deviation

## A.4 Positive- $K_f$ cutting dataset discussion

The variance of the feed force (Figure A.5), and by proxy the feed position of the tool edge, increases faster than is predicted by the variance propagation model; both the variation within a cut width, and the progression with the cutting width, are larger than predicted. This is most likely due to a material tear-out effect which was observed to cause increased surface roughness, which is an unmodeled effect in the variance propagation model. This tearing out led to increasingly erratic cutting traces and saw-tooth like force profiles evident in **Table A-1**.

## A.5 Material tear-out and “sawtooth” forces

In the Acrylic cutting dataset, with positive  $K_f$ , a phenomenon was noted that was not present in the Delrin dataset (with negative  $K_f$ ) and is hypothesized to be due to a combination of Acrylic’s brittleness, the tool rake angle, and the combined slice and feed stiffness characteristics of the cutting system. It was observed in the cutting videos that material would be pulled up and torn from the base material, leaving a ragged “sawtooth” surface reminiscent of a bandsaw blade and contributing to surface and cutting force variation (Figure A.6). A cyclical behavior was observed whereby the tool suddenly reduces its depth of cut by about half, then cuts into the material back to its starting depth of cut, leaving a small jagged tear on the surface. A possible explanation for this behavior is that the cutting forces (in particular forces causing tension in the brittle material) are causing the material to tear out, and when the material tears, the knife tip springs up before re-engaging the material, leaving behind the jagged surface.

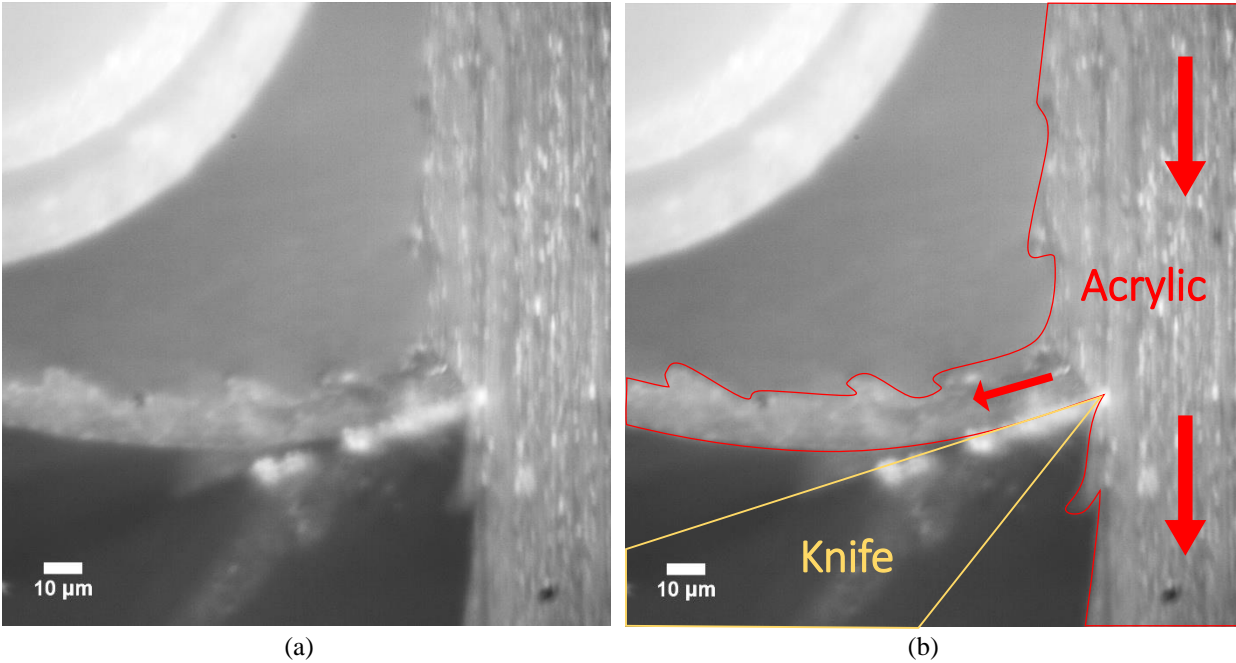


Figure A.6: Tear-out cutting observed in an Acrylic stepped-width specimen cutting experiment, test ID #868, frame 732, 1.1 mm width of cut (a) original video still (b) annotated video still highlighting the jagged tear-outs on the incoming material left over from the previous cutting pass and on the newly-created surface. The direction of material flow is shown with filled red arrows.

Figure A.7 below shows the associated forces. The force plots are roughly cyclical, and the feed force appears to reach a maximum magnitude when the cutting force reaches a minimum magnitude.

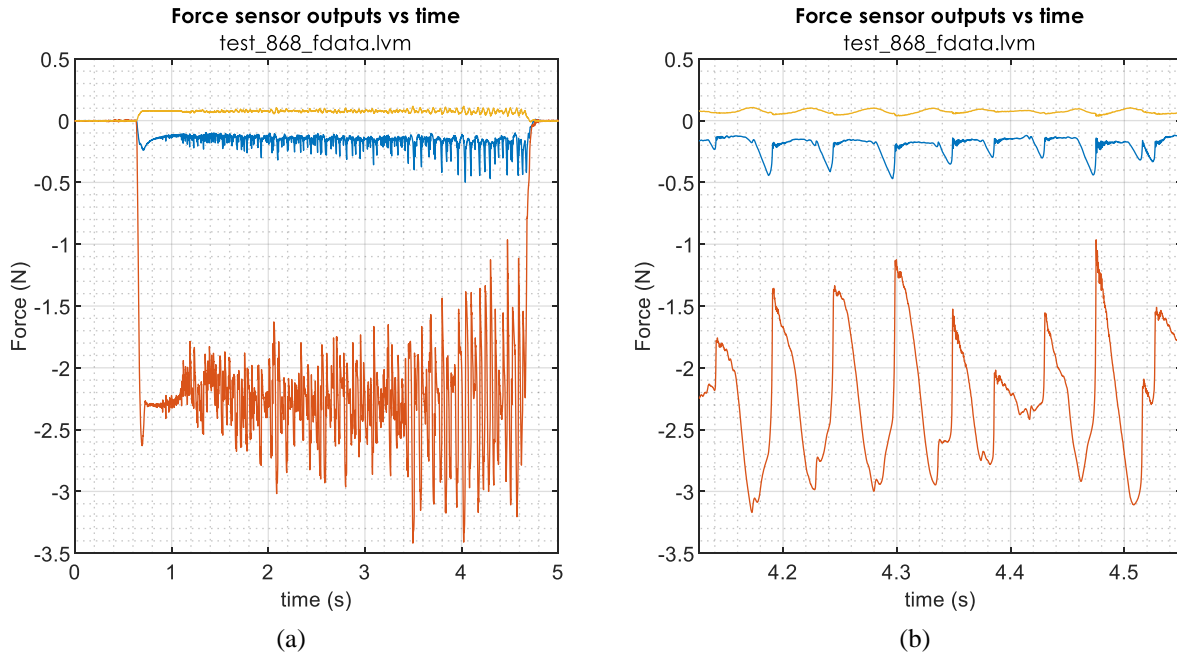


Figure A.7: Force plots for test #868, frame 732, Acrylic stepped-width specimen at 1.1 mm width of cut (a) entire force trace (b) zoomed in on time around 4.306 s, corresponding to frame 732. In each plot, the top trace corresponds to the out-of-plane force, the intermediate trace corresponds to the feed force, and the bottom trace corresponds to the cutting force. This cut was slowed down to 0.75 mm/s compared to 1.5 mm/s for the rest of the dataset to capture higher-quality images less affected by motion blur.

The beginning of the cut appears to be much less affected by this phenomenon, and the amplitude of the sawtoothing appears to increase in magnitude towards the end of the cut. The behavior evident here is not captured in any of the models generated in this work, but would be interesting for further study – specifically, what material property controls whether this tearing out will happen, and at what rake angles can the tearing out be expected.

*(this page intentionally left blank)*

# B

## REGENERATIVE CHATTER

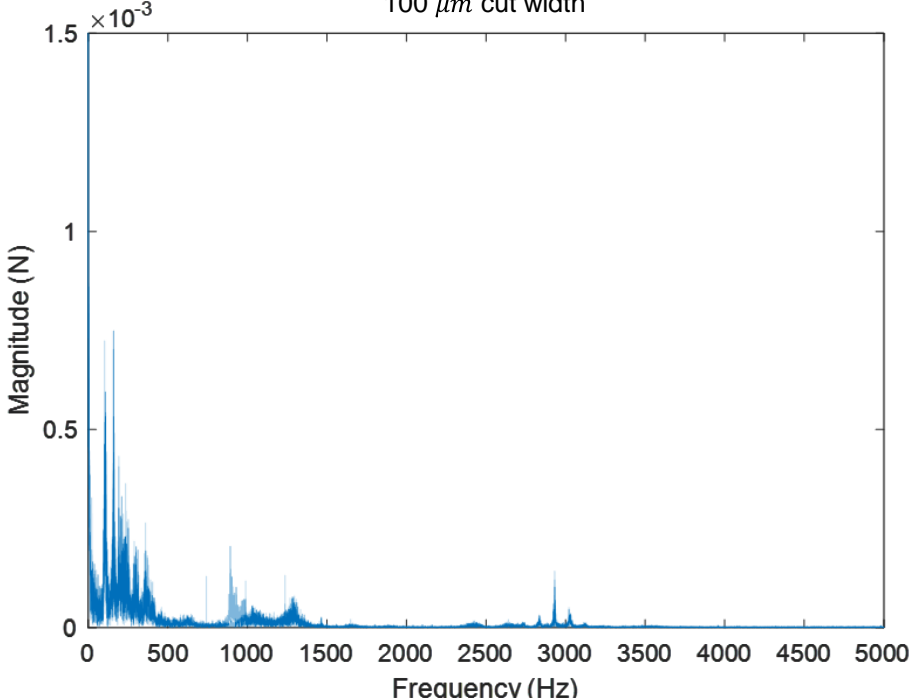
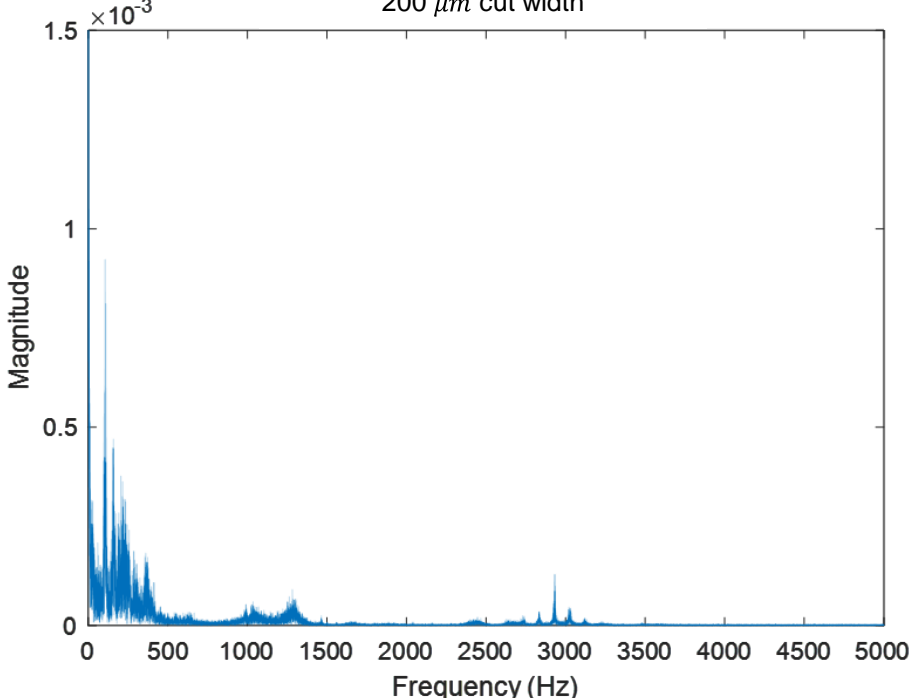
---

To assess the presence of regenerative chatter, the FFT of the force data was examined. A cutting system undergoing regenerative instability should exhibit frequency content which increases in magnitude every cutting pass.

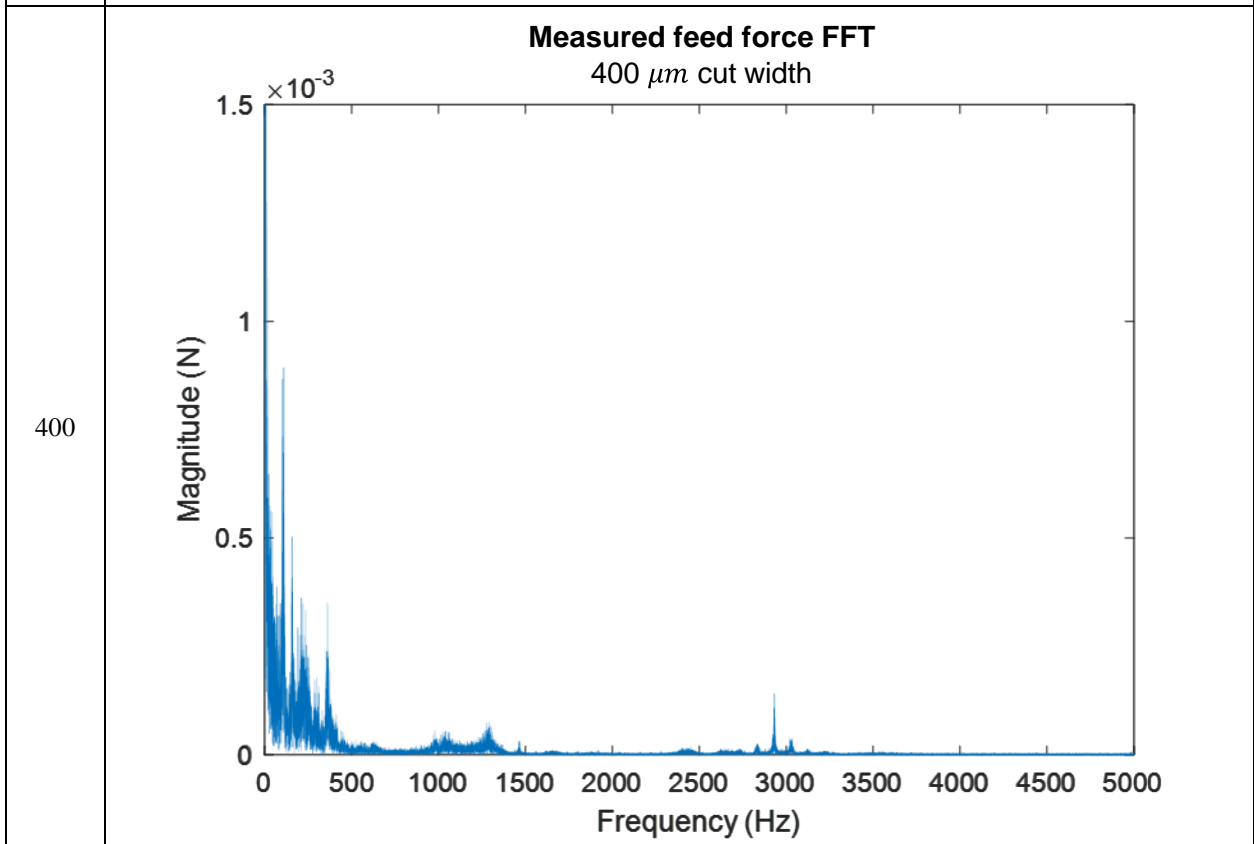
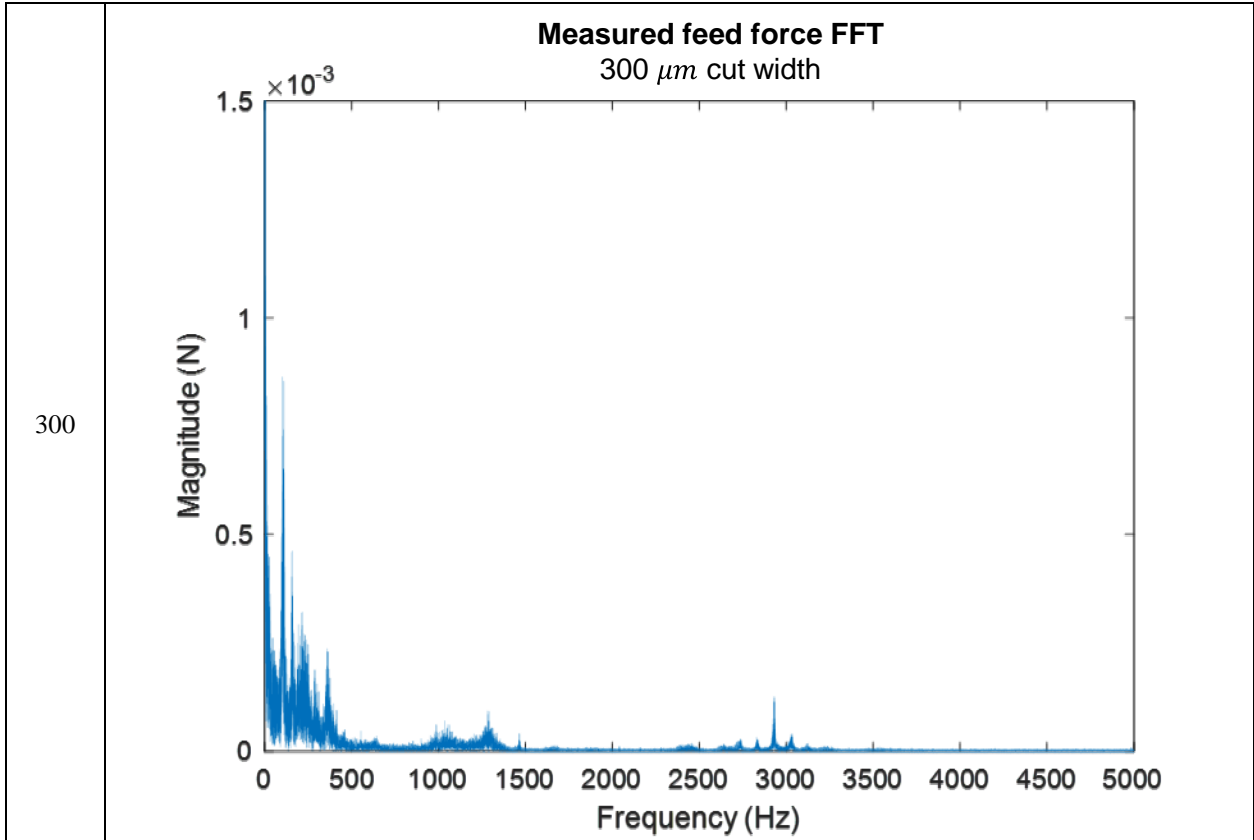
### **B.1 Compliant knife and Delrin, negative $K_f$**

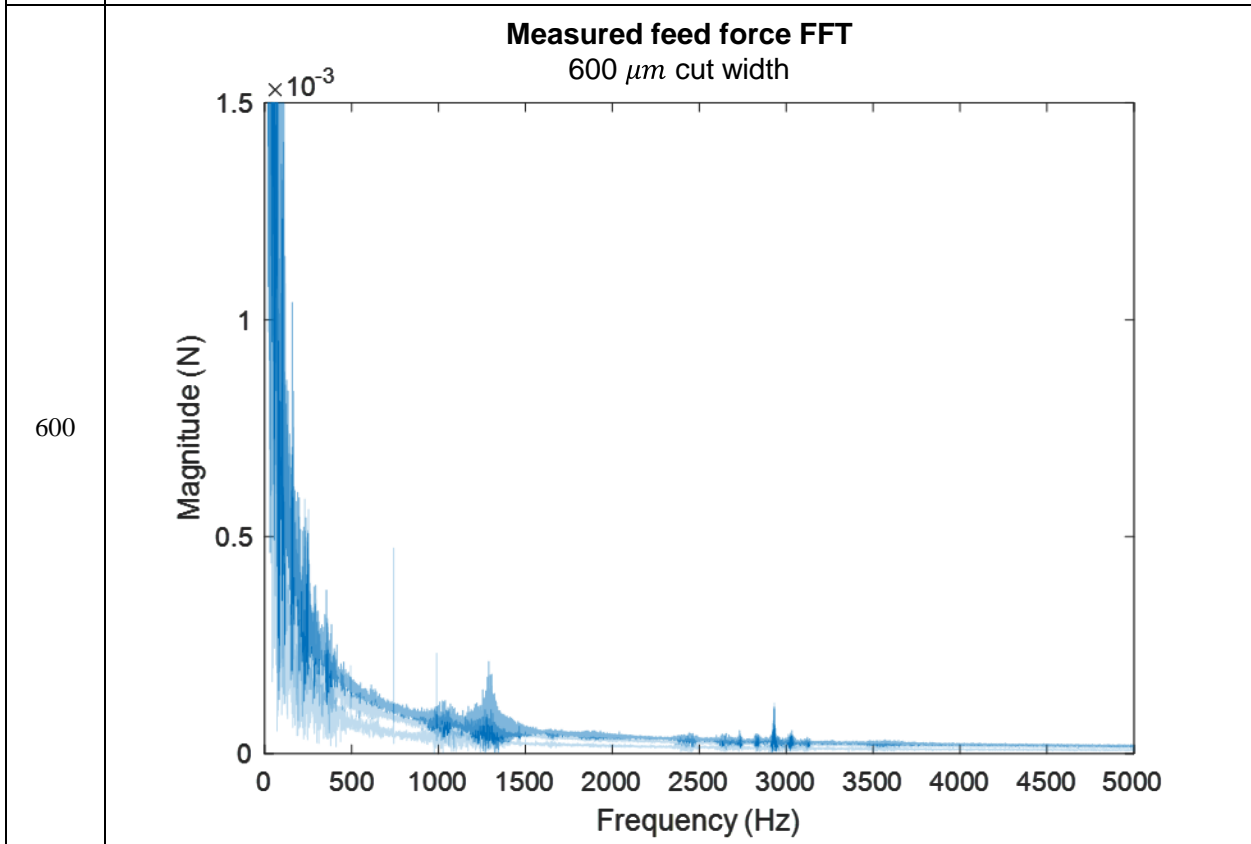
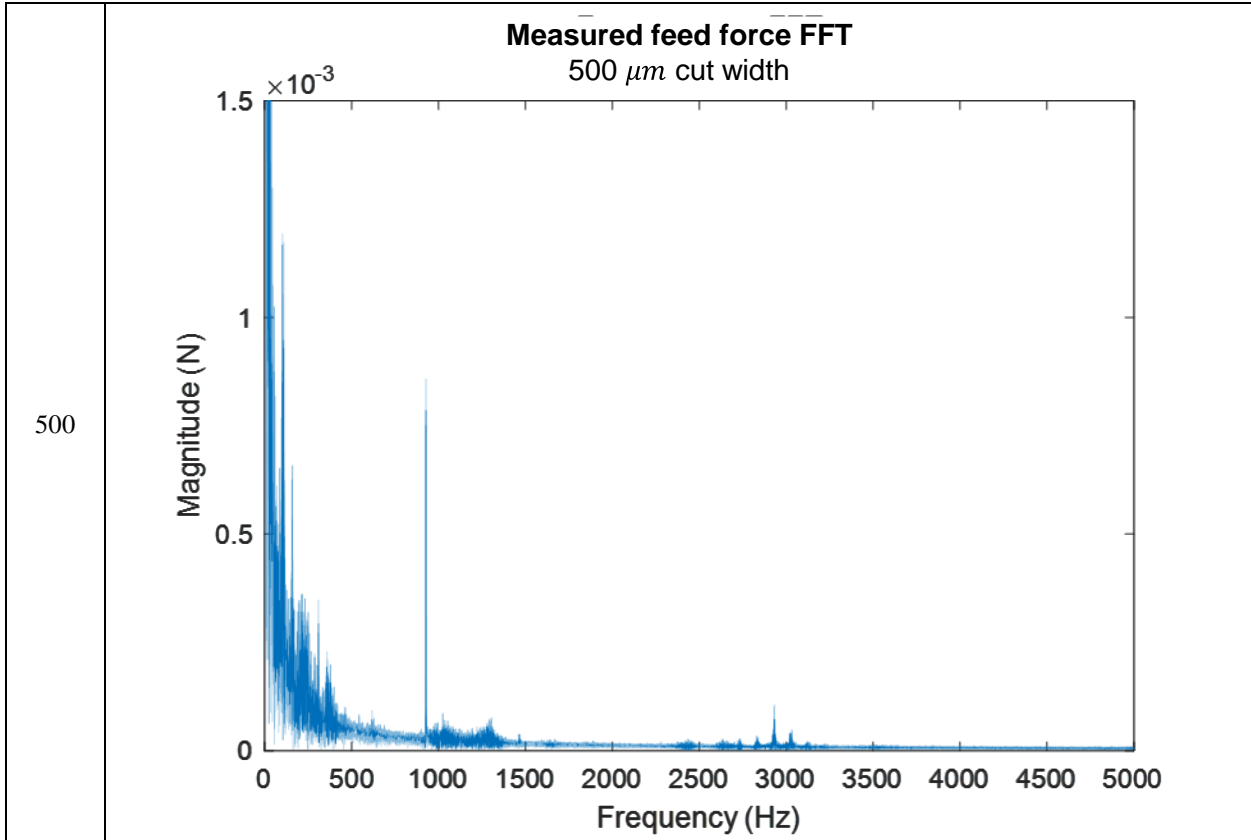
Plots of the FFT magnitude for the compliant knife and Delrin cutting test are shown in Table B-1; 3-4 cut FFTs are overlaid on one another, with the first cut in the series at the bottom of the stack, and each subsequent FFT overlaid with 50% transparency. Regenerative growth will be apparent as regions with spectral spikes which grow in height with each cutting pass.

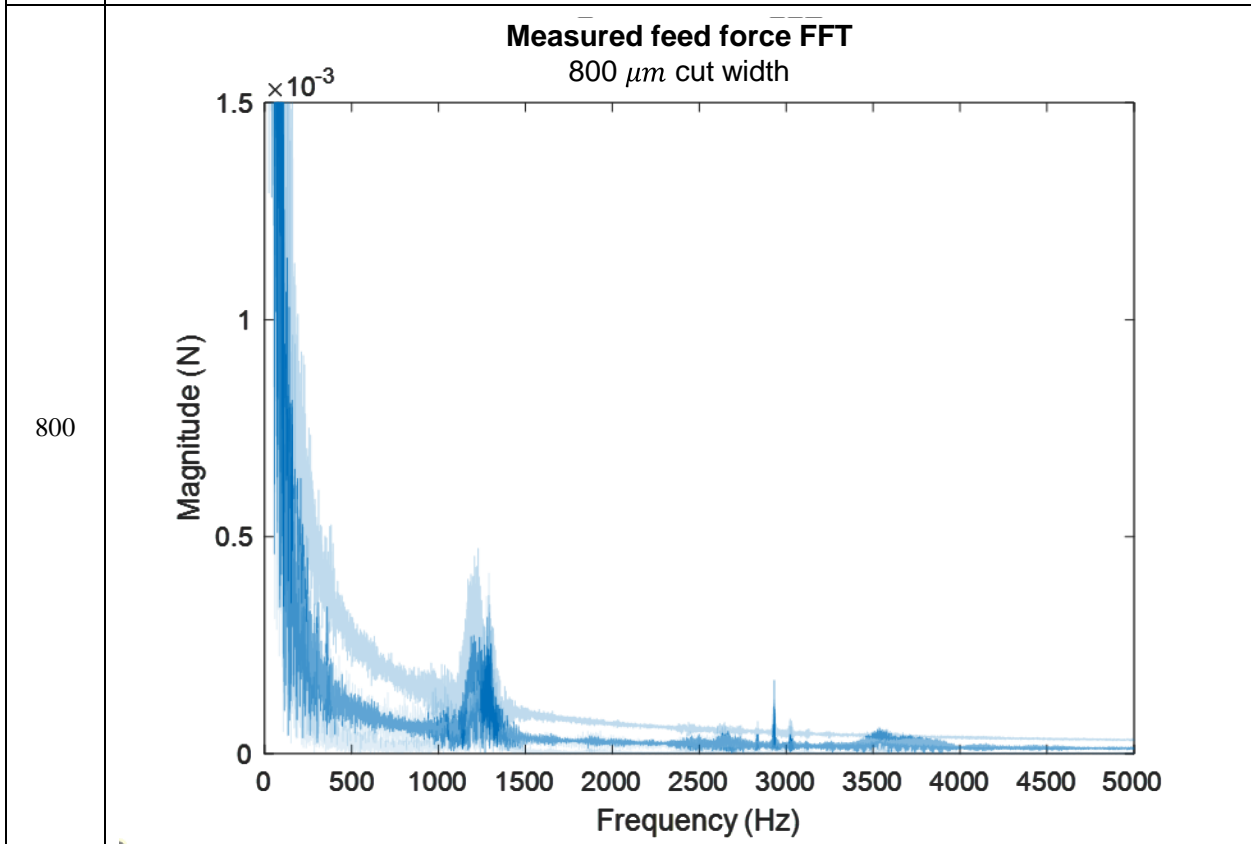
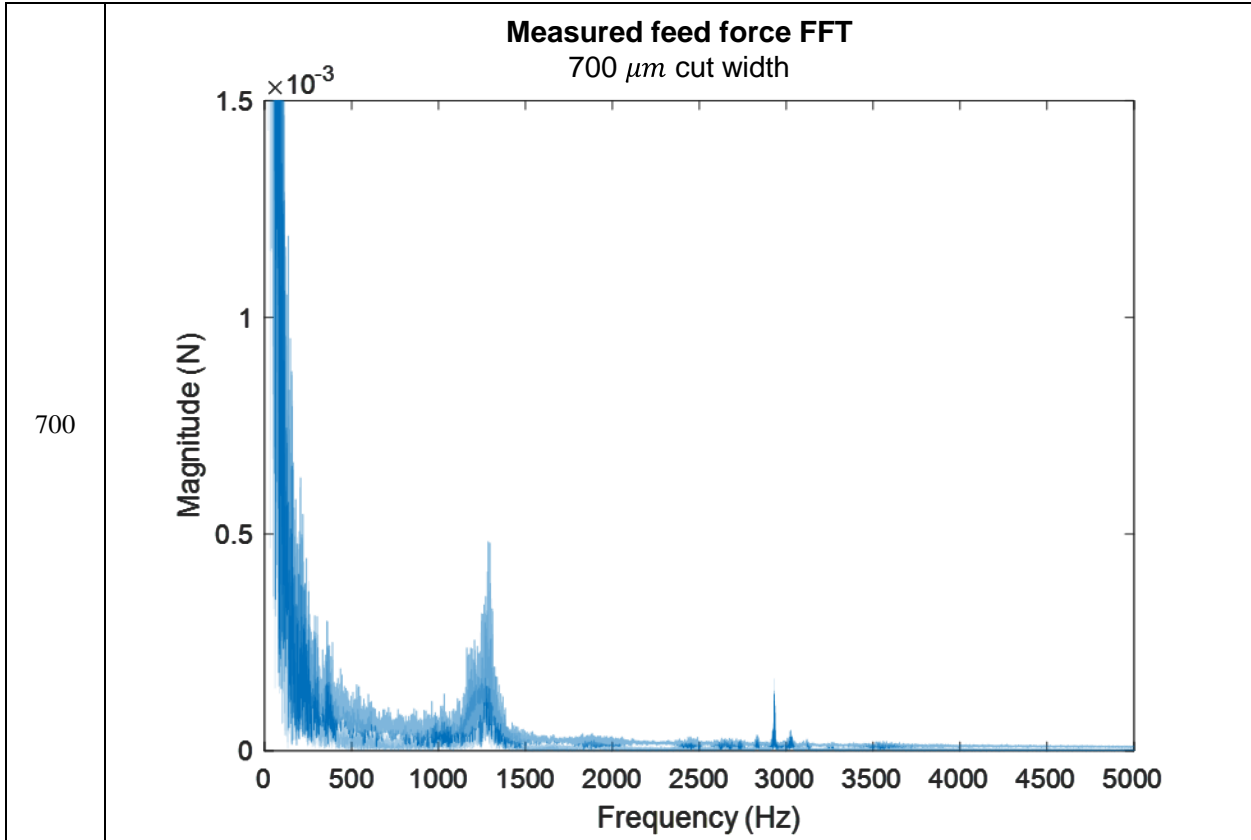
Table B-1: FFT X data, compliant knife and Delrin (negative  $K_f$  dataset)

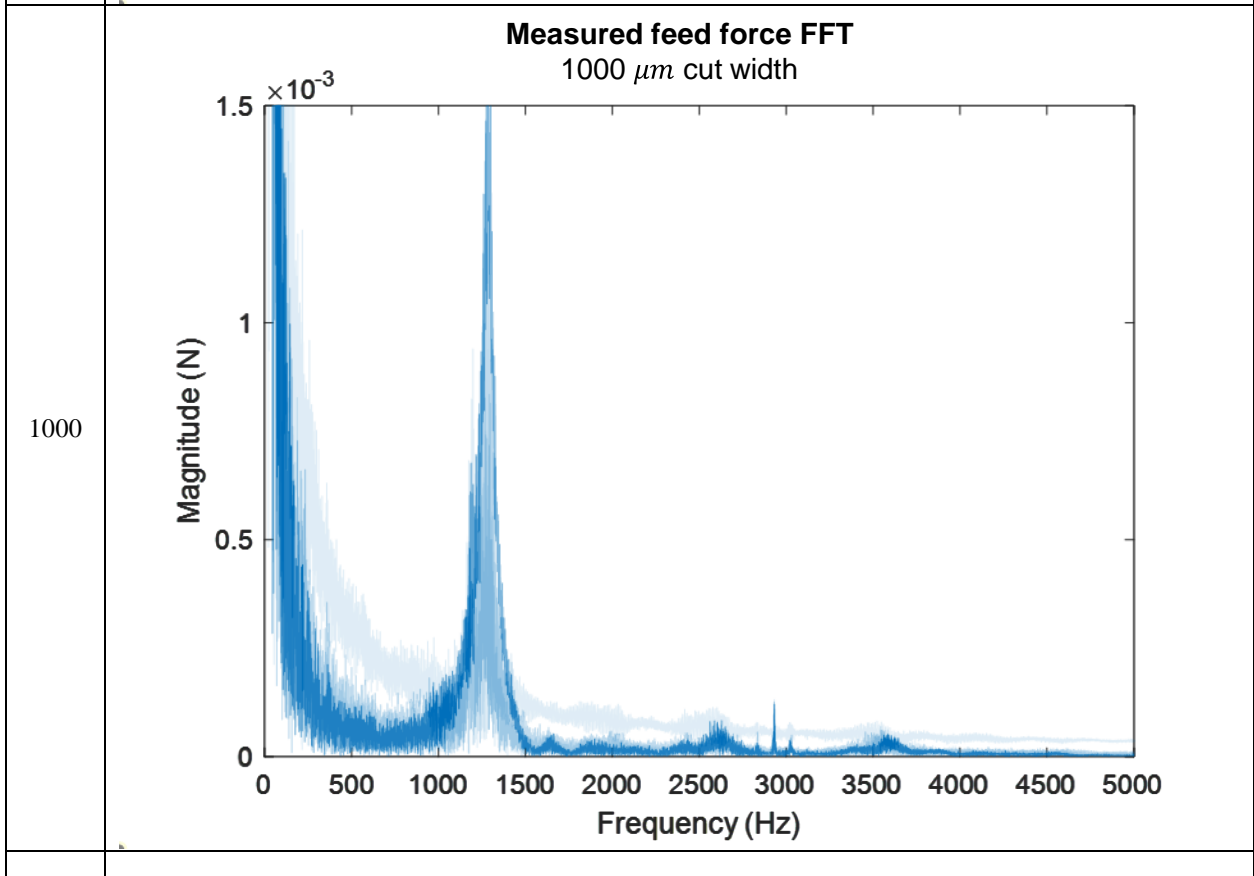
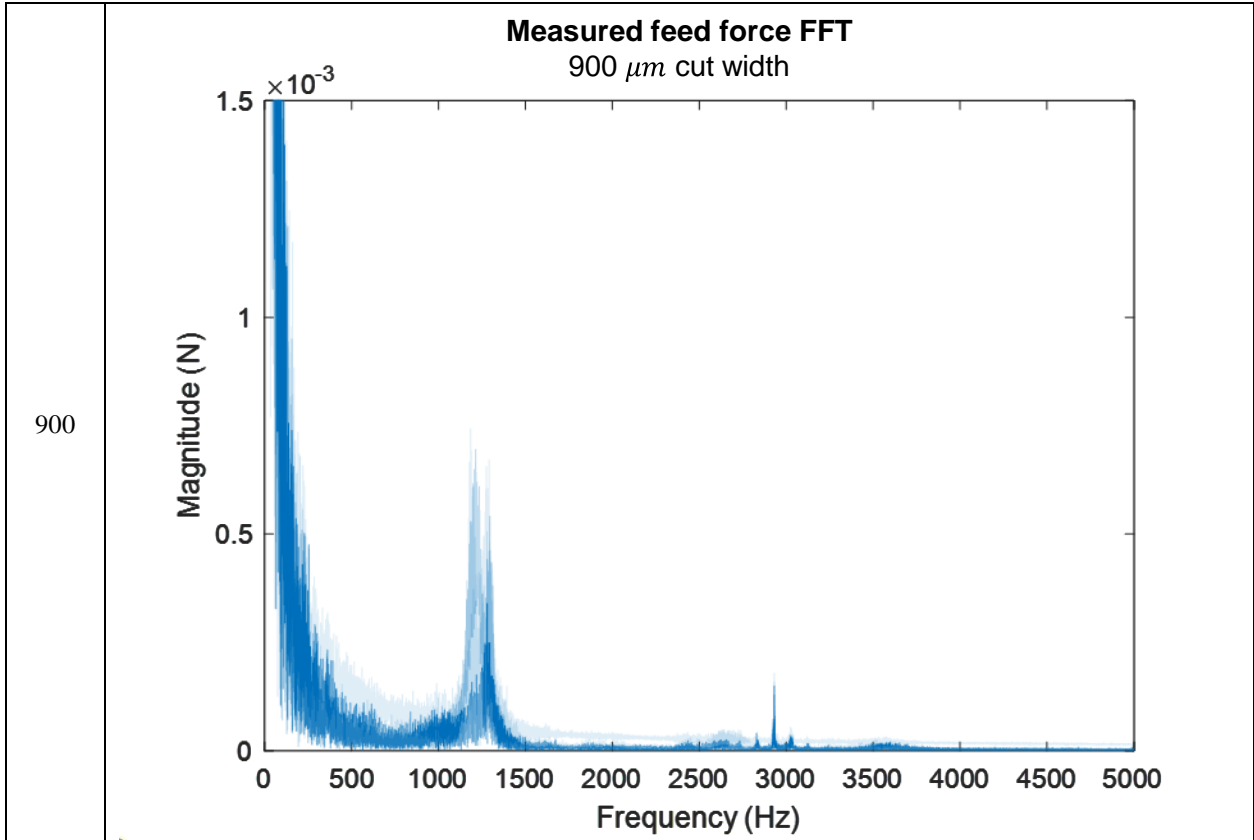
Cut width	X FFT progression
100	<p style="text-align: center;"><b>Measured feed force FFT</b> 100 <math>\mu m</math> cut width</p> 
200	<p style="text-align: center;"><b>Measured feed force FFT</b> 200 <math>\mu m</math> cut width</p> 







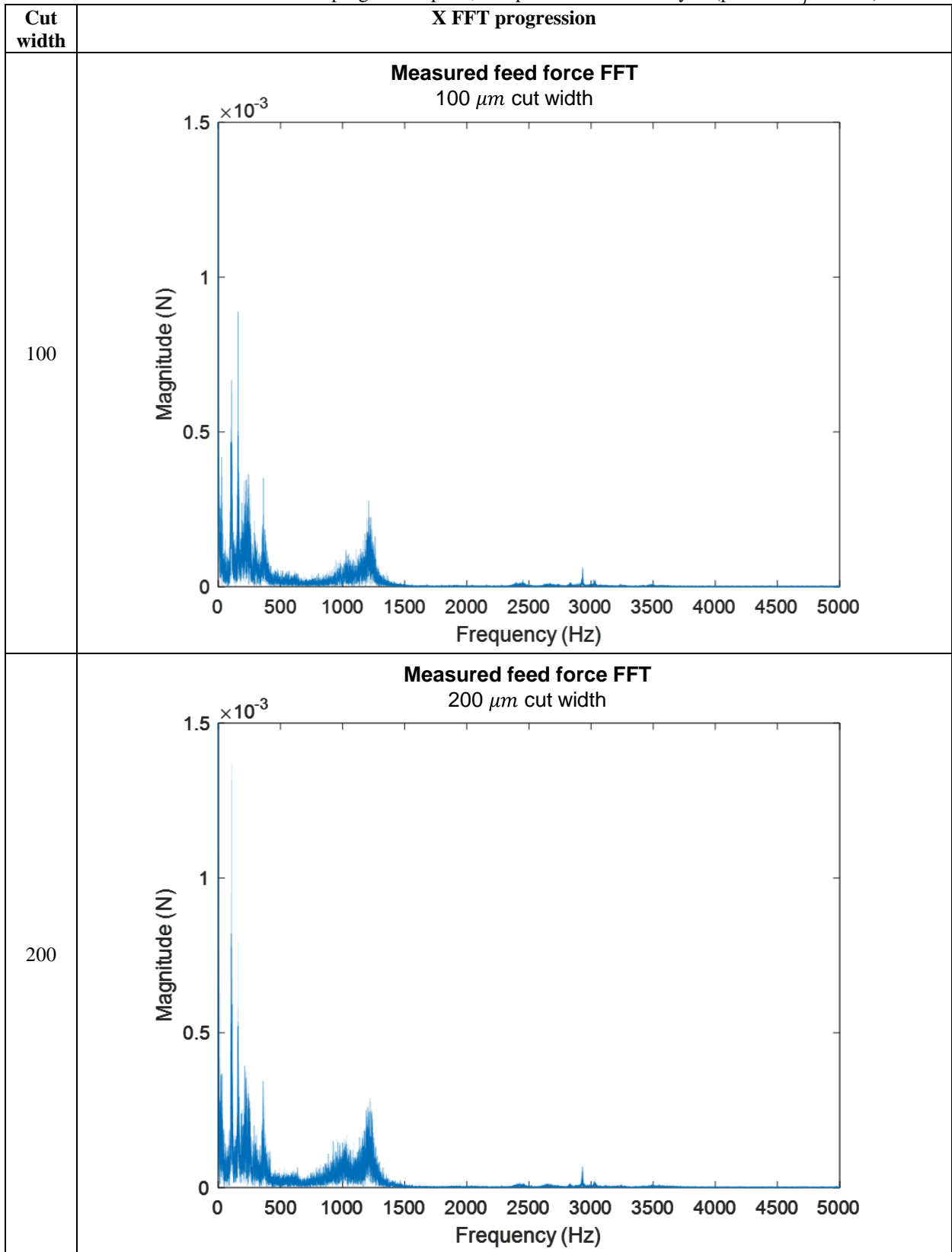


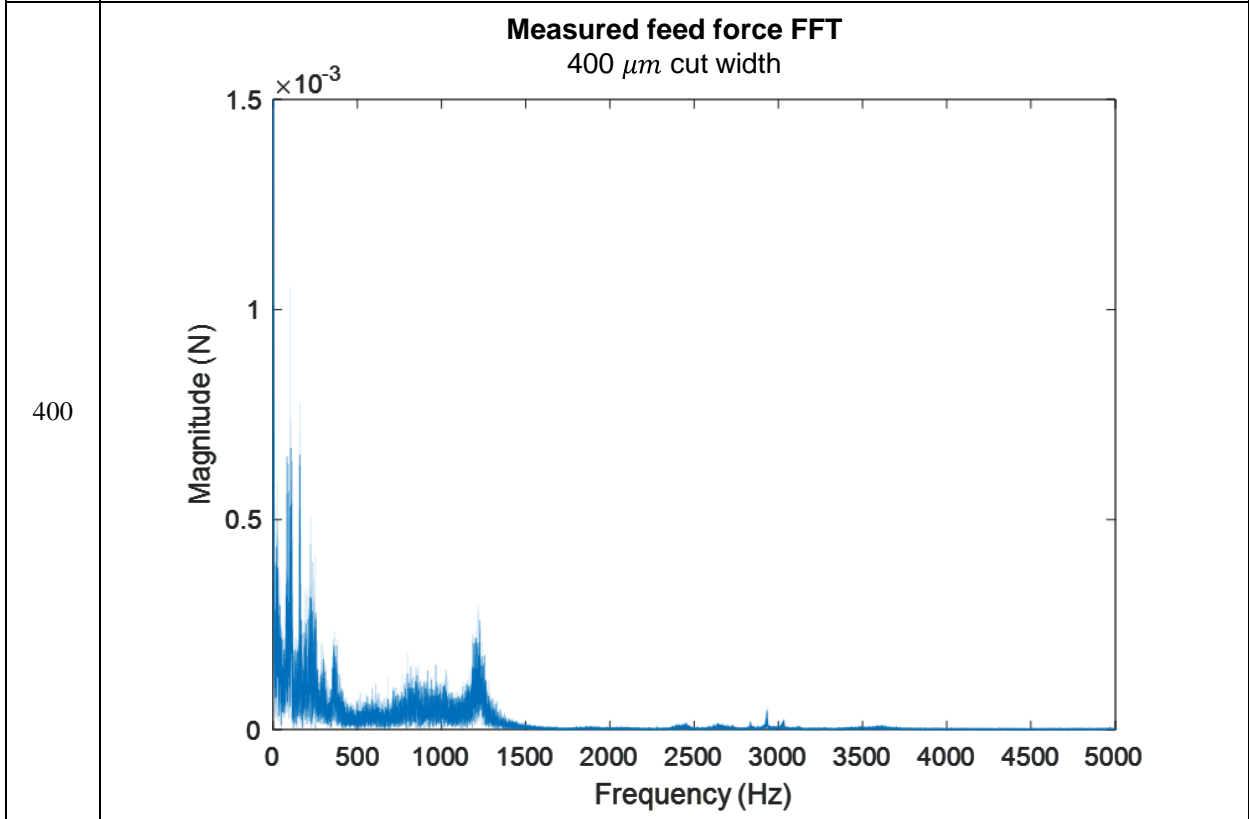
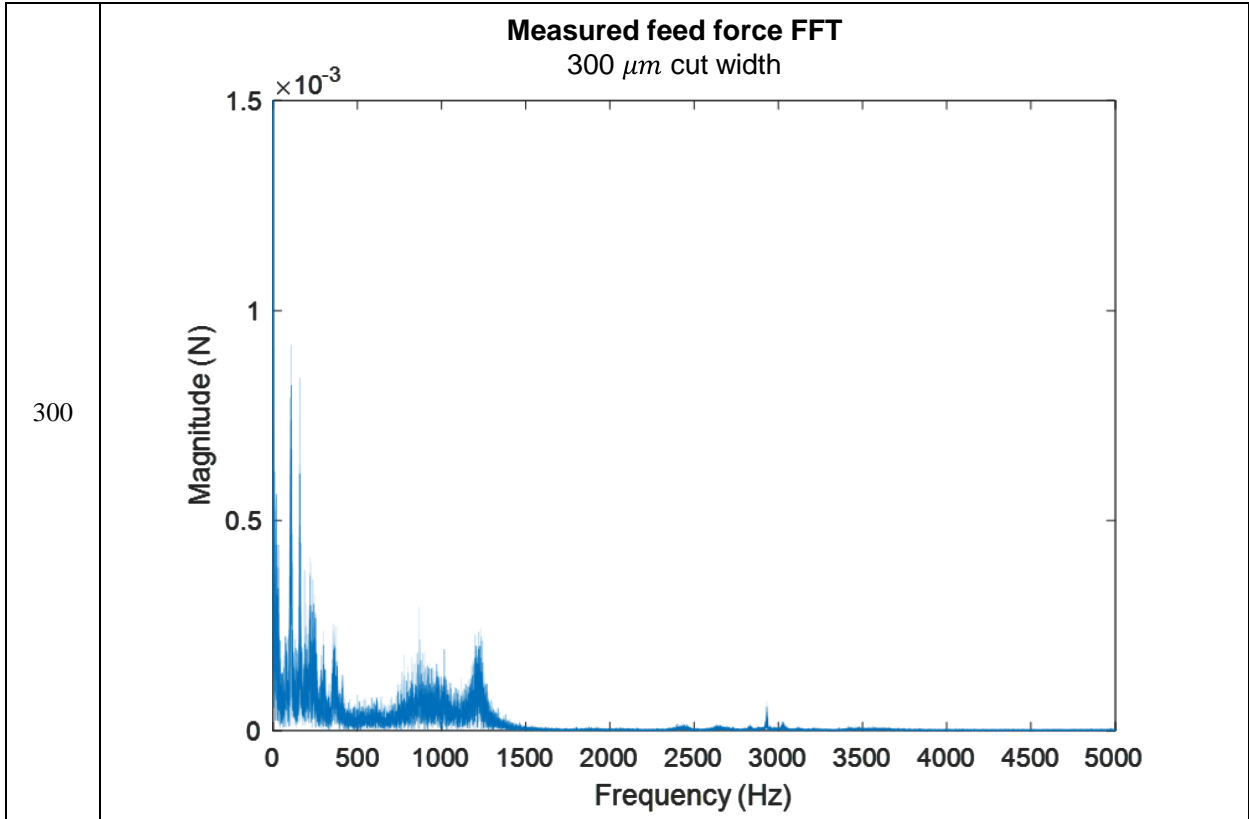


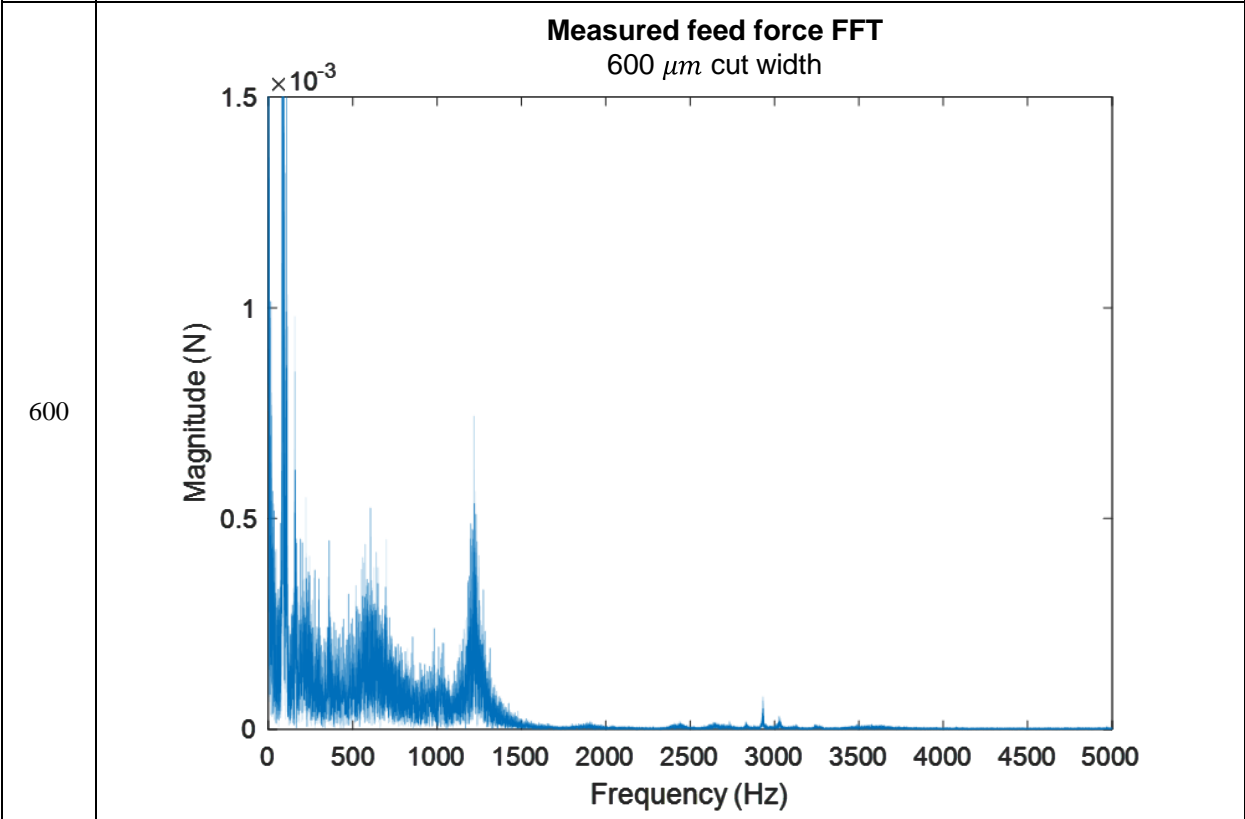
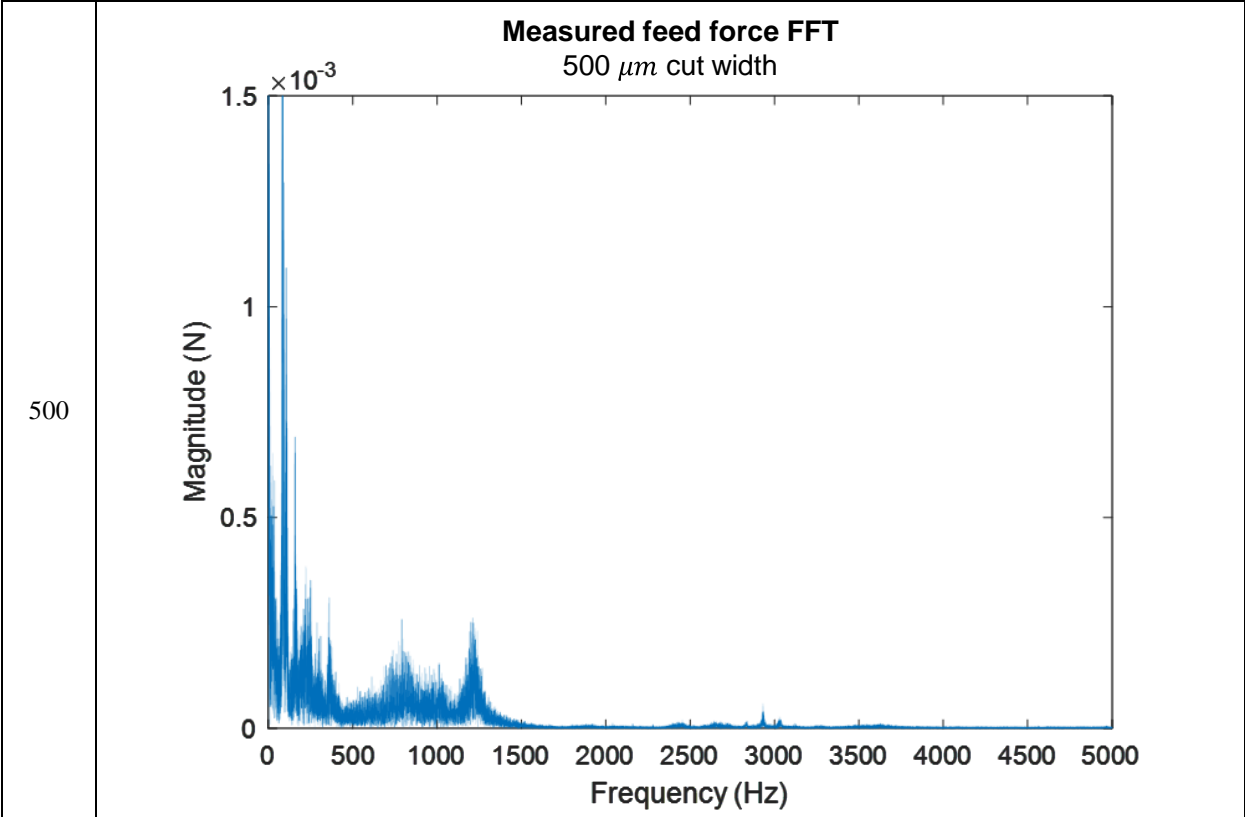
## **B.2 Compliant knife and Acrylic, positive $K_f$**

Similarly, overlaid X FFT progression plots are made for the positive  $K_f$  dataset with the compliant knife and Acrylic.

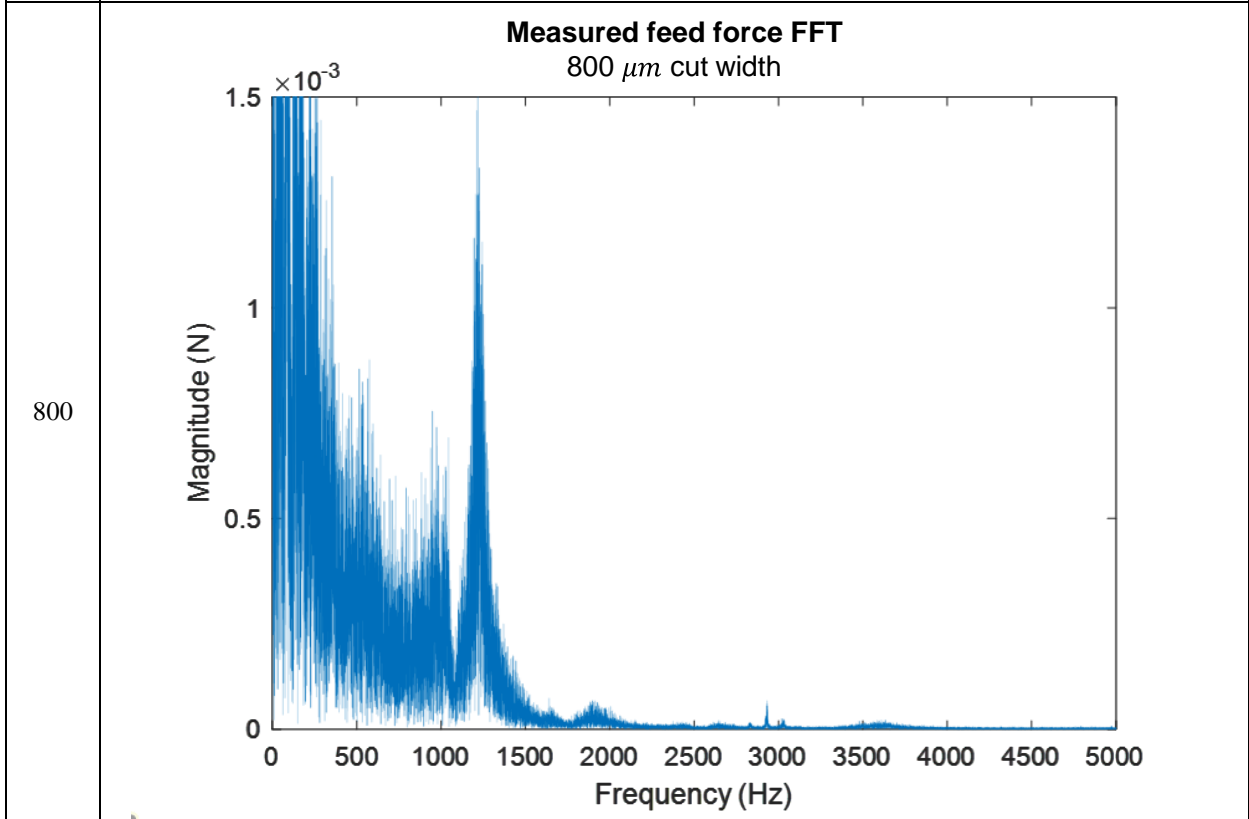
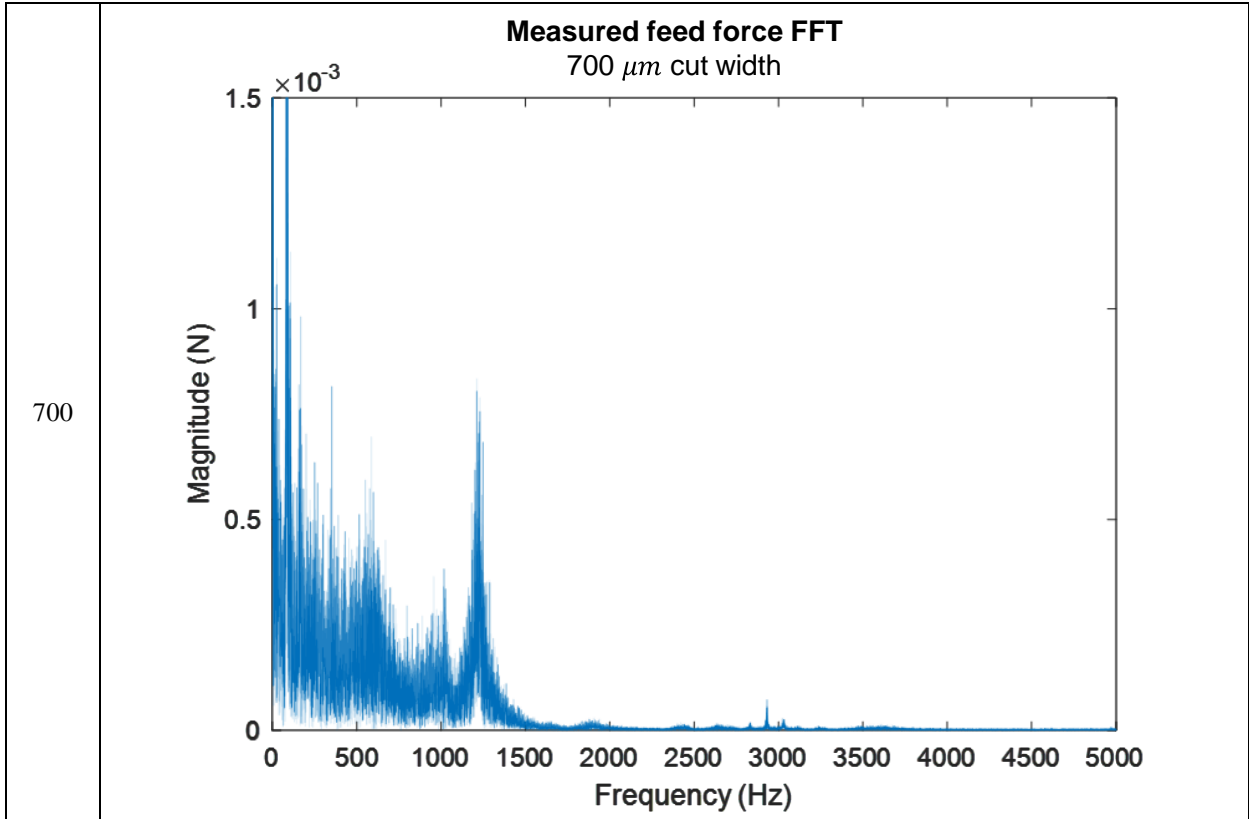
Table B-2: Feed direction FFT progression plots, compliant knife and Acrylic (positive  $K_f$  dataset)

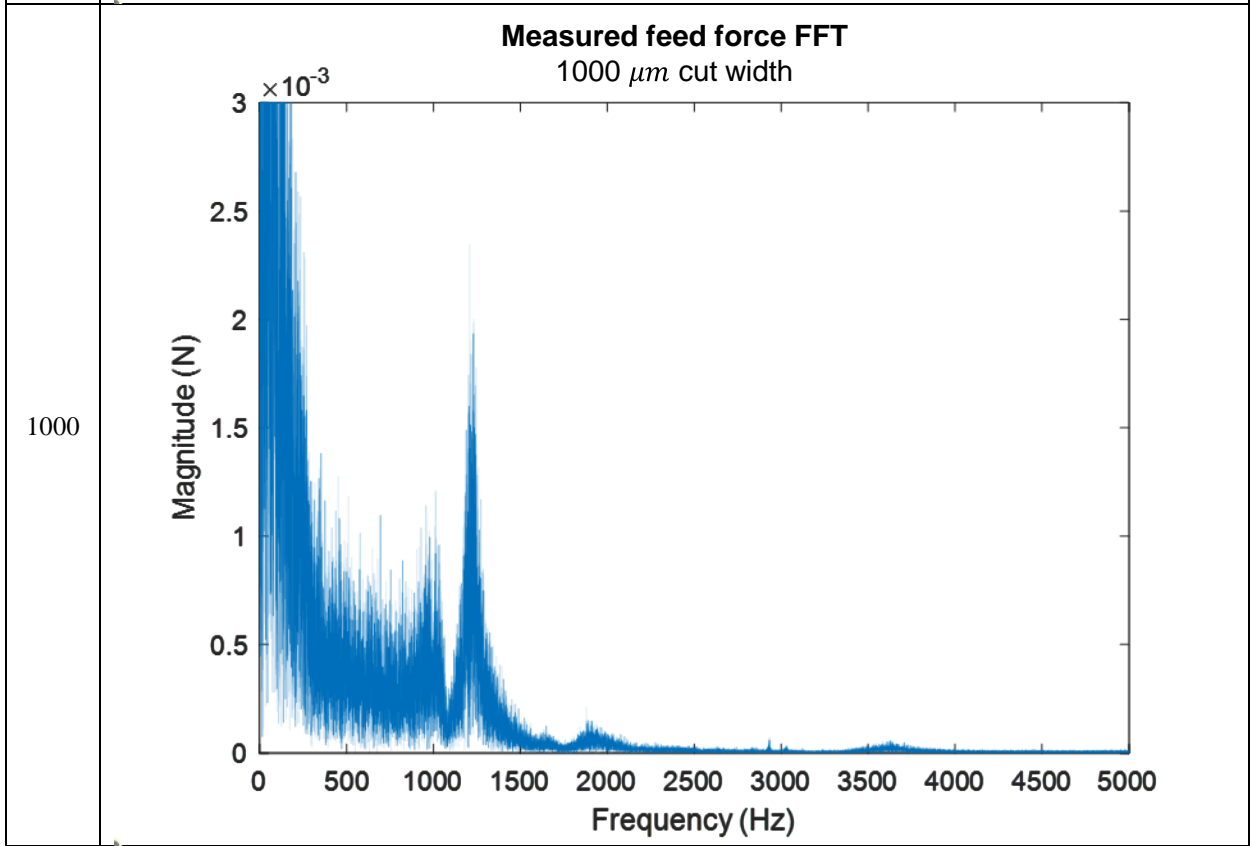
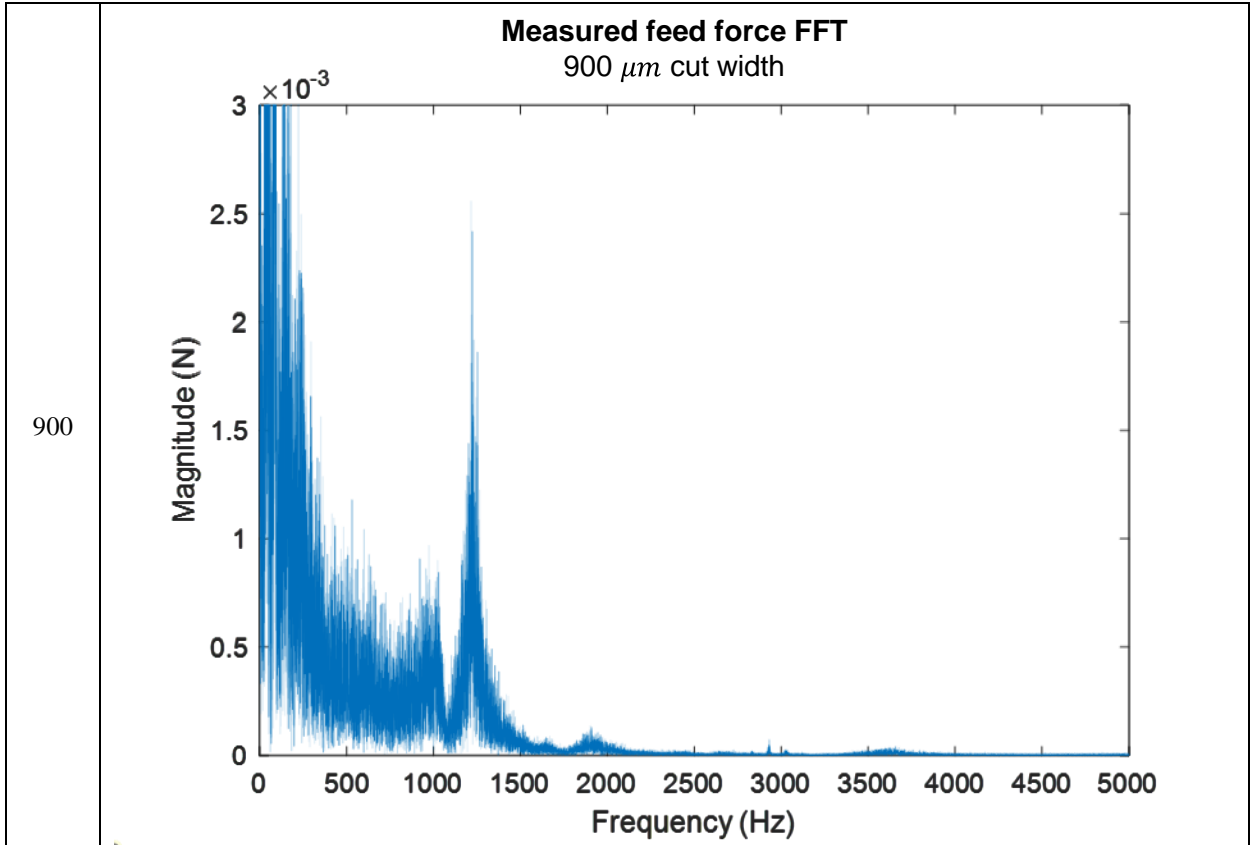












### B.3 Regenerative chatter discussion

The central prediction made by the regenerative chatter model introduced in Section 3.4.2 was that after increasing the width of cut past the maximum stable value, any vibration content near the system's natural frequency would be amplified each cutting pass while other vibrations would be attenuated; eventually, the system would be dominated by the unstable frequency. However, what was observed was a general  $1/f$  – like excitation, with very strong spectral content at lower frequencies that seemed to generally increase with cutting width, but not within a single cutting width over consecutive passes.

The simulations assumed that the only input frequency content present during cutting and regeneration would be vibrations due to the cutting system's own dynamics – the initial ringing at the start of the cut in the transient phase of cutting. In practice, this entry ringing was not always apparent – the start of the cut would often be messier as the tool entered the material and initiated the cut and would typically not result in an ideal ringing transient response. In addition, there are other disturbance forces with frequency content that influence the cutting system response – for example, in the positive- $K_f$  cutting with Acrylic, the appearance of the 'sawtooth' cutting, which has a distinct dynamic character.

The regenerative chatter predicted by the regenerative chatter model developed here was not observed in these experiments. The regenerative chatter model introduced in this work as it currently stands is insufficient to predict the occurrence of regenerative chatter, but could perhaps in the future be augmented to capture more relevant physics – an important augmentation would be in understanding the input spectral content during cutting. The orthogonal cutting model assumes that cutting is steady state and continuous, thus that the force

during cutting should be constant; however, cutting is a complex process that has dynamic aspects to it, for example, material shearing at the shear zone not being a perfectly continuous process, or the frictional contact at the tool rake face causing a broadband excitation force.

# C

## COMPLIANCE ERROR MODELING AND GEOMETRY DEFINITIONS

---

The analytical models generated and used to predict the relative error between the tool and specimen in response to cutting loads are described in this appendix. Details of each analytical model are provided in this section, coordinate system (CS) by coordinate system, from one end of the structural loop to the other (Figure C.1).

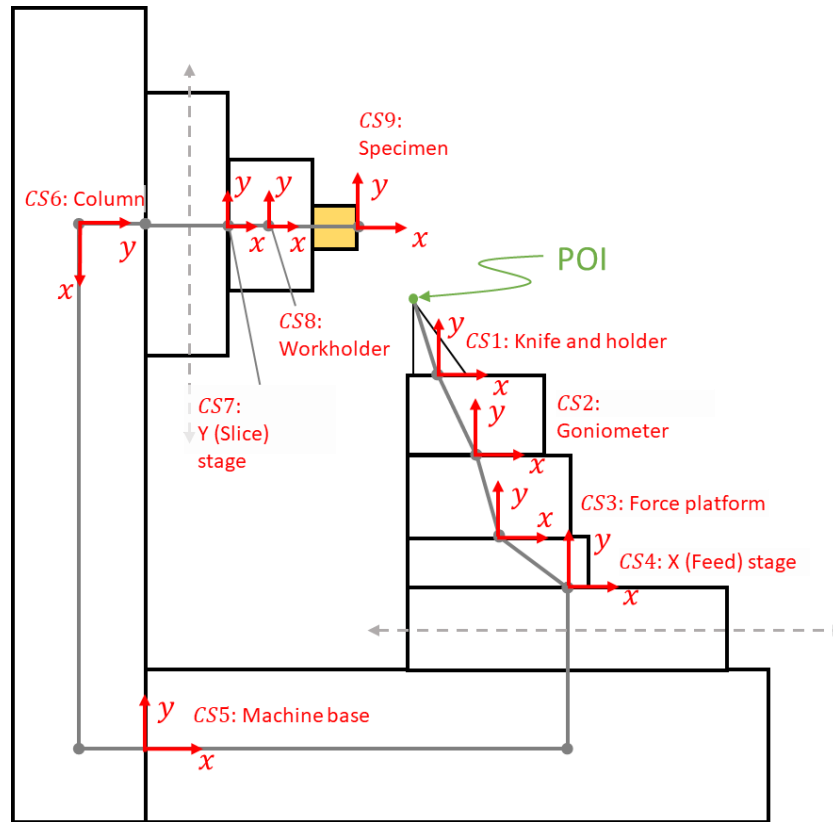


Figure C.1: Stick figure model of the cutting instrument, with coordinate systems labeled. Each coordinate system was used to capture a specific source of compliance. CS9 is fixed and used as a reference frame, and the cutting loads are applied at the labeled POI. The gap between CS9 and the POI is exaggerated for clarity.

## C.1 Knife and knifeholder – CS1

The geometry between the POI and the CS1 origin is shown in Figure C.2, and the distance between the POI and the CS1 origin is given in Table C-1.

Table C-1: POI location with respect to CS1

Direction	Value	Unit
X	-13.4	mm
Y	31.7	mm
Z	0	mm

The goal of the CS1 stiffness analysis was to parametrically model how loads applied at the POI result in deflections at the POI, with respect to the CS1 origin. The knifeholder compliance model is built by considering the parallel sum of stiffnesses of each contact stiffness, transformed to the point of interest (POI). Each point contact (Contacts 1, 2 and 3 in Figure C.2a)

is modeled as a single stiffness along the contact normal (i.e., the stiffness matrix for each element contains one entry only). The modeling strategy was to first transform the ring contact, Contact 4 in Figure C.2a, to an equivalent stiffness matrix about its centroid, and then transform this stiffness matrix to the POI and combine it in parallel with the transformed stiffnesses from contacts 1,2, and 3. The stiffness matrix is then inverted to obtain the compliance matrix.

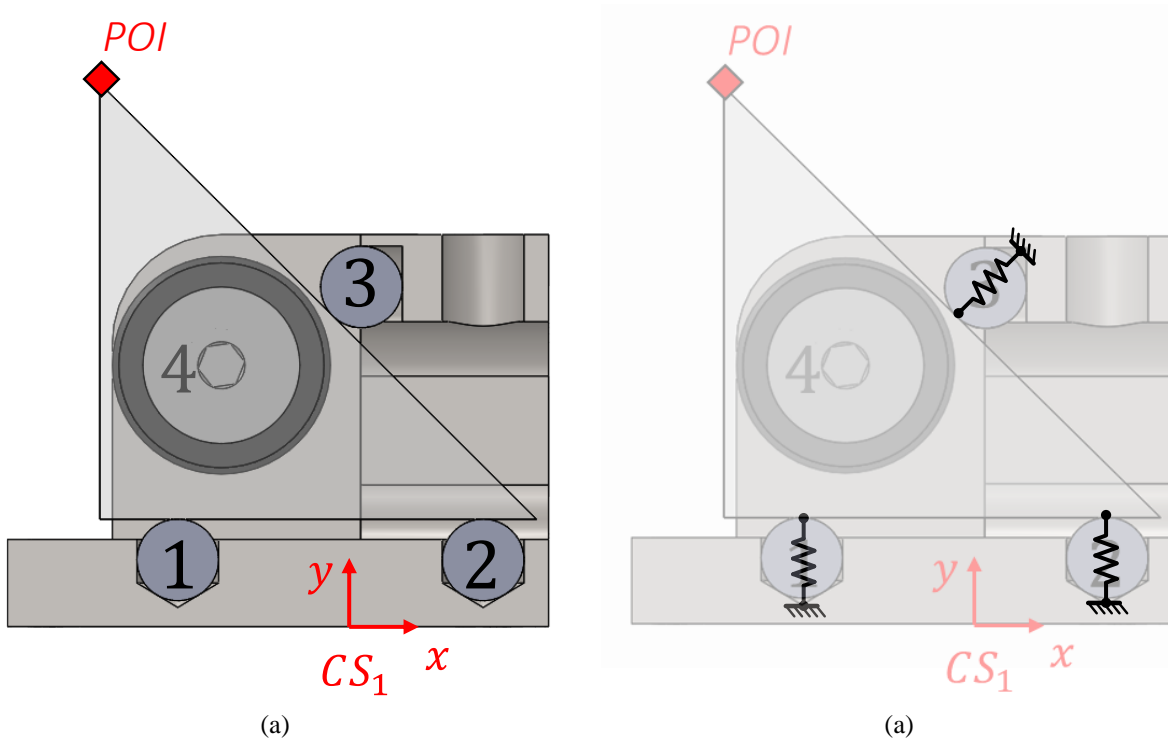


Figure C.2: Knifeholder CAD model (a) cross section (b) with contacts replaced by springs to be modeled with Hertzian contacts

Modeling the ring contact requires an extra modeling step, as the ring will also provide moment resistances about the  $X$  and  $Y$  axes in Figure C.3a, and this needs to be captured in the stiffness transformation or else the stiffness matrix will be underconstrained and result in a singular matrix. The ring contact's moment stiffness is modeled by modeling each quadrant of the ring as a uniaxial tension/compression stiffness acting in the  $Z$  direction (Figure C.3b and c); each of these sub-stiffnesses is transformed to the equivalent stiffness matrix at the centroid, and

the four equivalent stiffness matrices are added in parallel to obtain the single effective stiffness matrix representing the stiffness of the ring about its centroid.

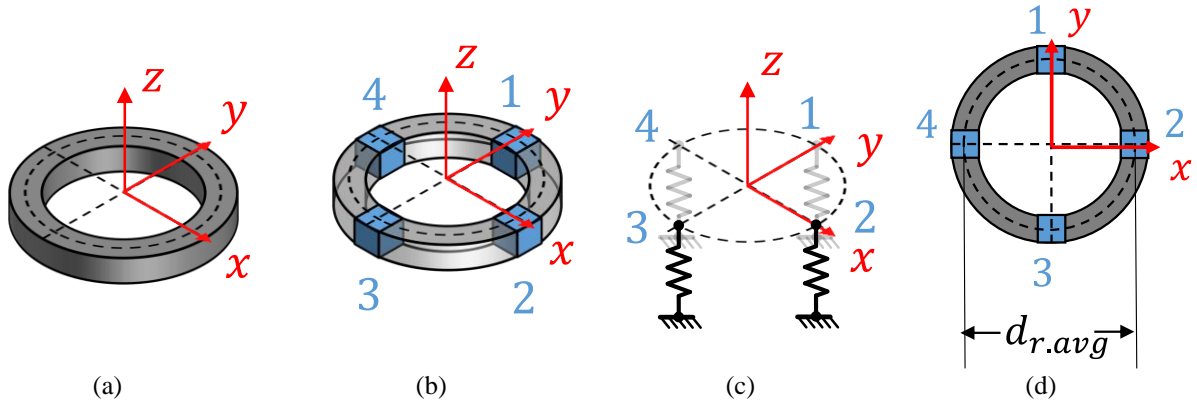


Figure C.3: Ring contact stiffness modeling (a) the ring clamping pad is (b) subdivided into four quadrants. (c) Each quadrant is modeled as a uniaxial tension/compression stiffness (d) planar model

The stiffness matrix of ring about its centroid with the coordinate system shown in Figure C.3 is written out as

$$\begin{bmatrix}
 0 & 0 & 0 & 0 & 0 & 0 \\
 0 & 0 & 0 & 0 & 0 & 0 \\
 0 & 0 & 4k_{rnode} & 0 & 0 & 0 \\
 0 & 0 & 0 & \frac{1}{2}k_{rnode}d_{ravg}^2 & 0 & 0 \\
 0 & 0 & 0 & 0 & \frac{1}{2}k_{rnode}d_{ravg}^2 & 0 \\
 0 & 0 & 0 & 0 & 0 & 0
 \end{bmatrix} \quad (C.1)$$

The individual stiffnesses are all transformed to an effective stiffness matrix at the POI, which is then inverted to obtain a compliance matrix (Table C-2)



Table C-2: Knifeholder compliance matrix modeling the deflections at the POI w.r.t. CS1 origin, capturing deflections due to the knifeholder contacts (units are  $mm/N$  for translations,  $rad/N\text{-}mm$  for rotations)

	$F_x$	$F_y$	$F_z$	$M_x$	$M_y$	$M_z$
$\delta x$	1.03E-04	4.45E-05	-5.94E-07	-1.66E-07	3.00E-07	-6.02E-06
$\delta y$	4.45E-05	2.28E-05	-4.33E-06	-2.89E-07	6.16E-08	-2.67E-06
$\delta z$	-5.94E-07	-4.33E-06	6.87E-05	3.60E-06	1.14E-06	1.04E-07
$\delta\theta_x$	-1.66E-07	-2.89E-07	3.60E-06	2.27E-07	-1.94E-08	8.84E-09
$\delta\theta_y$	3.00E-07	6.16E-08	1.14E-06	-1.94E-08	2.04E-07	-5.82E-09
$\delta\theta_z$	-6.02E-06	-2.67E-06	1.04E-07	8.84E-09	-5.82E-09	3.62E-07

## C.2 Goniometer and knife edge adjustment – CS2

The geometry between the CS1 origin with respect to the CS2 origin is given in Table C-3.

Table C-3: Geometry definitions: location of CS1 origin w.r.t CS2

Direction	Value	Unit
X	-8.75	mm
Y	21.3	mm
Z	0	mm
$\theta_x$	0	deg
$\theta_y$	0	deg
$\theta_z$	0	deg

Stiffness modeling was done in two stages – first, the stiffness at each contact was parametrically modeled using Hertzian contact analysis [53]. Then, the location and orientation of each contact was added in parallel to obtain a net stiffness with respect to a reference point. The compliance matrix obtained was then used in the error model to assess the impact of the module’s compliance to the overall error.

The general layout of the contact points is shown below in Figure C.4, and the final values of the parameters are shown in Table C-4.

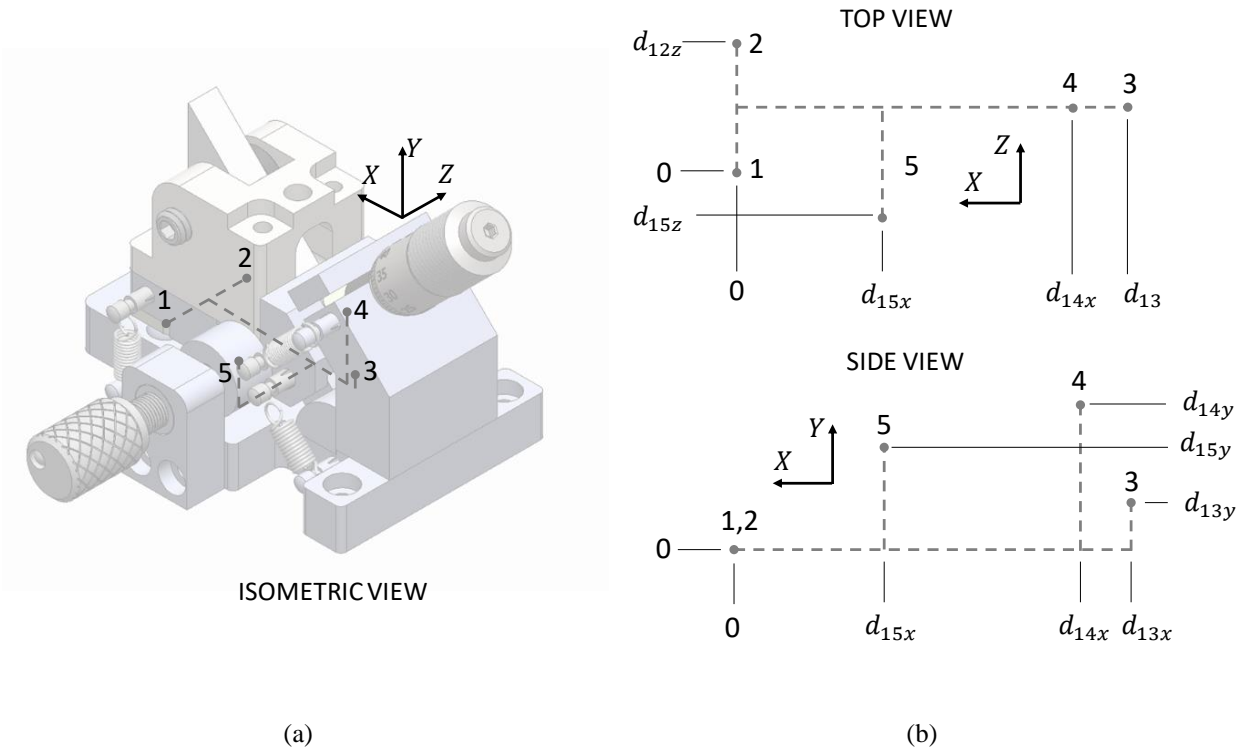


Figure C.4: Geometry of contact layout for kinematic goniometer (a) isometric (b) top view and side view

Table C-4: Parameters used to define kinematic goniometer geometry

Parameter	Value (mm)
$d_{12}$	17
$d_{13}$	37.7
$d_{13y}$	3
$d_{14x}$	34.8
$d_{14y}$	15
$d_{15x}$	18
$d_{15y}$	9
$d_{15z}$	5

Each contact was modeled as having a stiffness only in the direction of the constraint, thus the stiffness estimate will be somewhat conservative since the contacts will also have some tangential stiffness.

Table C-5: Summary of modeled contact stiffnesses

Contact #	Type	Stiffness (N/um)
1	Point	13.3
2	Point	13.3
3	Line	258
4	Point	5.7
5	Point	10.3

The resulting compliance matrix is given in Table C-6.

Table C-6: Kinematic goniometer module compliance matrix used for load-induced error modeling (units are  $mm/N$  for translations,  $rad/N\cdot mm$  for rotations)

	$F_x$	$F_y$	$F_z$	$M_x$	$M_y$	$M_z$
$\delta x$	9.71E-05	3.89E-05	-1.84E-07	2.75E-08	-3.47E-08	2.99E-06
$\delta y$	3.89E-05	2.93E-05	-1.19E-07	2.75E-08	-2.75E-08	6.23E-07
$\delta z$	-1.84E-07	-1.19E-07	1.19E-04	-2.38E-06	3.68E-06	0
$\delta\theta_x$	2.75E-08	2.75E-08	-2.38E-06	5.51E-07	-5.51E-07	0
$\delta\theta_y$	-3.47E-08	-2.75E-08	3.68E-06	-5.51E-07	6.95E-07	0
$\delta\theta_z$	2.99E-06	6.23E-07	0	0	0	1.37E-07

### C.3 Force sensor – CS3

This force sensor analysis supplement covers details on the geometry of the coordinate system used for error propagation modeling, details on the stiffness modeling and the effective compliance between CS2 and CS3, and details on the shear force shunting membrane used to isolate the force sensors from non-sensed loads. CS3 encapsulates the compliance error contributions due to the force sensor assembly.

#### C.3.1 Force sensor coordinate system geometry definitions

The CS2 and CS3 layout is shown in Figure C.5 with corresponding parameters in Table C-7.

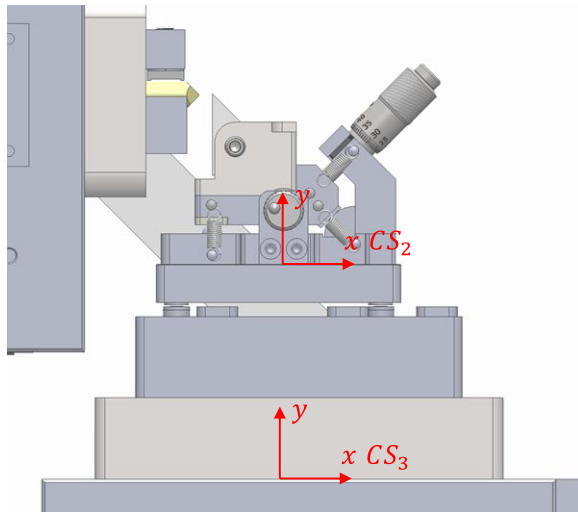


Figure C.5: CS2 and CS3 geometric definitions

Table C-7: Geometry definitions: location of CS2 origin w.r.t CS3

Direction	Value	Unit
X	1.6	mm
Y	41.6	mm
Z	0	mm
$\theta_x$	0	deg
$\theta_y$	0	deg
$\theta_z$	0	deg

### C.3.2 Force sensor stiffness model and compliance matrix

The stiffness transformation method was used to derive a compliance matrix encapsulating the compliance contribution of the force sensing platform, modeling the compliance between CS2 and CS3 with compliance contributions from the force sensors and the shear membrane (Figure C.6); the stiffnesses were transformed into a net compliance as seen at the point of interest (the CS2 origin). The resulting compliance matrix was then used in the error model to assess the impact of the sensor layout on the load-induced error in the system and was used to iteratively design the force sensor assembly. Geometry and stiffness parameters are summarized in Table C-8 below.

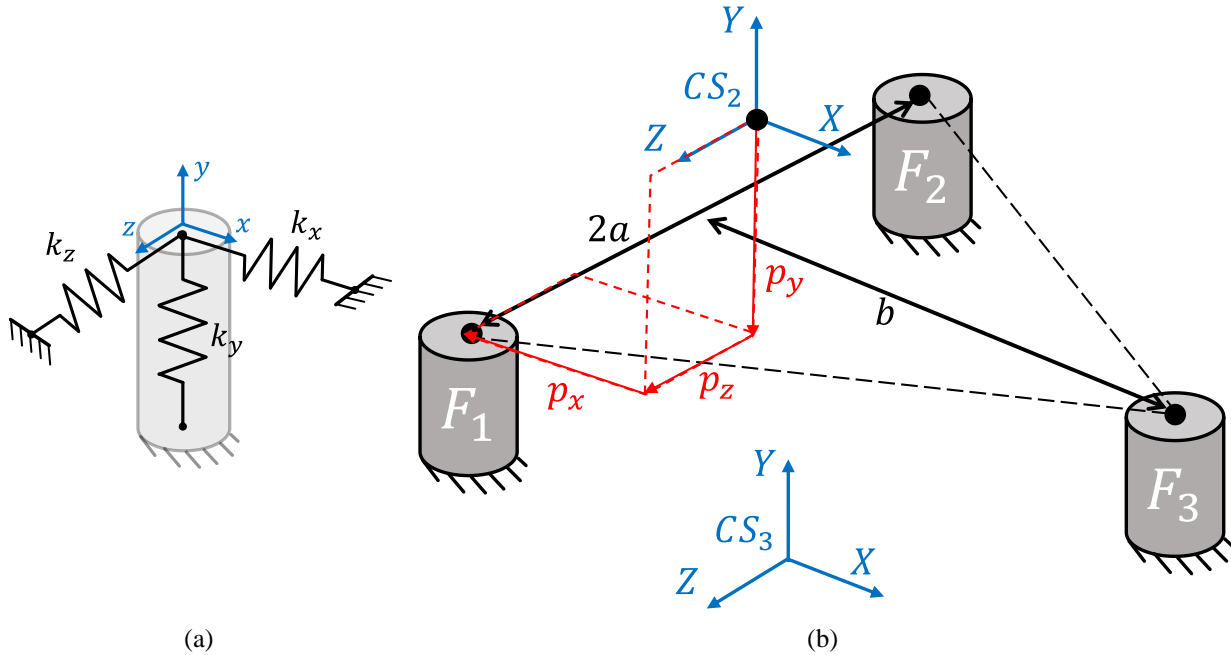


Figure C.6: (a) Individual force sensor local coordinate system used to define the stiffness matrix at each node. The y direction is the sense direction. (b) Geometry used to derive the compliance matrix between  $CS_2$  and  $CS_3$ . The goal is to compute the equivalent compliance of this system for loads applied at the  $CS_2$  origin, with respect to  $CS_3$ .

Table C-8: Force sensor stiffness model parameters

Parameter	Value	Unit	Description
$a$	19.05	mm	Sensor triangle half-width
$b$	63.5	mm	Sensor triangle altitude
$p_x$	33.34	mm	Node 1 x distance from $CS_2$ origin
$p_y$	12.7	mm	Node 1 y distance from $CS_2$ origin
$p_z$	19.05	mm	Node 1 z distance from $CS_2$ origin
$k_x$	83,000	N/mm	stiffness along x axis
$k_y$	15,000	N/mm	Sensor stiffness along sense axis
$k_z$	83,000	N/mm	stiffness along Z axis

The resulting compliance matrix after the stiffness transformation is given in Table C-9.

Table C-9: Force sensor compliance matrix used for load-induced error modeling for deflections seen at CS2 origin, due to loads at CS2 origin, with respect to CS3 orientation (units are  $mm/N$  for translations,  $rad/N\text{-}mm$  for rotations)

	$F_x$	$F_y$	$F_z$	$M_x$	$M_y$	$M_z$
$\delta x$	8.016e-6	-3.834e-6	0	0	0	-3.15e-7
$\delta y$	-3.834e-6	2.59e-5	0	0	0	3.019e-7
$\delta z$	0	0	1.935e-5	1.167e-6	-4.296e-8	0
$\delta\theta_x$	0	0	1.167e-6	9.185e-8	0	0
$\delta\theta_y$	0	0	-4.296e-8	0	3.529e-9	0
$\delta\theta_z$	-3.15e-7	3.019e-7	0	0	0	2.48e-8

### C.3.3 Bend and shear force shunting membrane design

The bend/shear shunting membrane flexure is designed to allow Y-direction forces to be sensed by the force sensors while shunting any X or Z forces, which the sensors cannot sense, will contribute to cross-talk noise, and potentially damage the sensors, to mechanical ground. The force sensors and the XZ-force shunt membrane are arranged in parallel; for the design to be effective, the XZ stiffness of the membrane should be high enough such that it bears most of the XZ loads Figure C.7(a). Simultaneously, the membrane must be compliant enough in the Y direction that it won't also shunt Y forces to ground and leave nothing for the force sensors to detect.

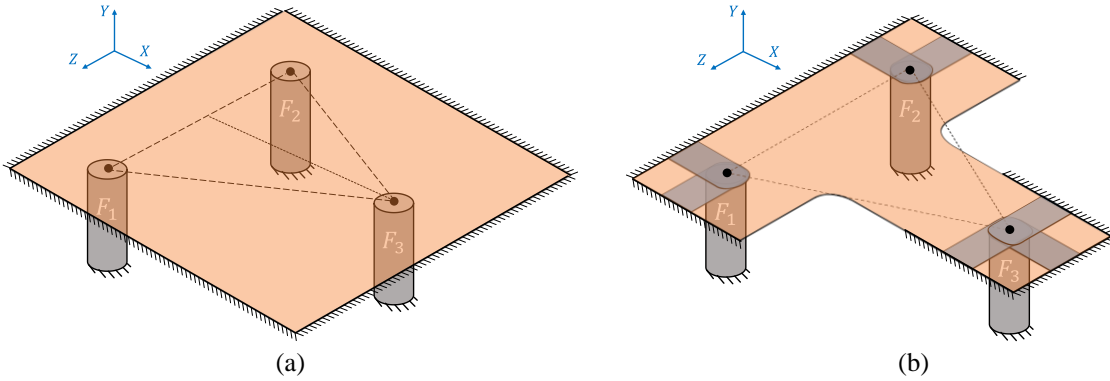


Figure C.7: Force sensor triad with shear shunting membrane (a) basic implementation and (b) slightly more refined version used for a basic stiffness model, with the supports closer to  $F_3$ . The shaded areas are the “strips” of material which will take the brunt of the  $XZ$  loads and are used to model the  $XZ$  stiffnesses.

To design this assembly, the force sensors’ bending stiffness is compared to the membrane  $XZ$  stiffness, and the force sensors’ axial stiffness is compared to the membrane  $Y$  (bending stiffness). At each node, the membrane and force sensor stiffnesses act in parallel (they share the same displacement); whichever element is stiffer will have most of the force flowing through it.

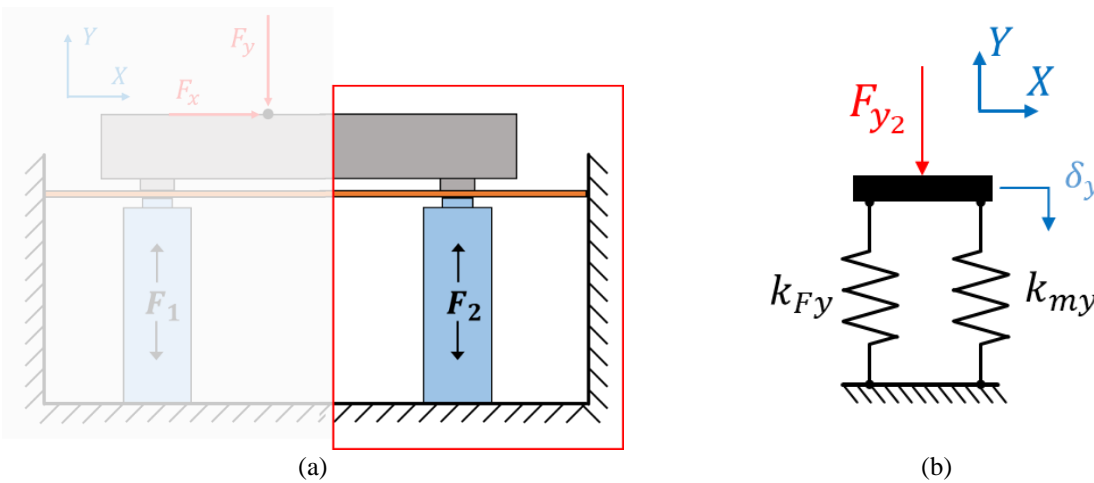


Figure C.8: (a) Schematic of force sensor and membrane assembly and spring model, focusing on a single force sensor/membrane attachment node. (b) Each attachment node will have a stiffness contribution from the force sensor and the membrane; if the membrane is too stiff, no force will be sensed by the sensor.

Utilizing the fact that the two springs share the same displacement, the force in the force sensor (the left spring in the figure above) can be expressed as

$$F_{sensor} = \frac{k_{Fy}}{k_{Fy} + k_{my}} F_{y2} \quad (C.2)$$

If the relative stiffness is parametrized as  $k_{Fy} = Nk_{my}$ , this relationship can be written as

$$F_{sensor} = \frac{N}{N + 1} F_{y2} \quad (C.3)$$

The fraction of the input load sensed by the sensor is presented in Table C-10 for various  $N$  values:

Table C-10: Relative stiffness vs percentage of input load sensed

Relative stiffness $N = \frac{k_{Fy}}{k_{my}}$	Fraction of input Y force sensed
0.1	0.09
1	0.5
10	0.91
100	0.99

A similar analysis can be made for the XZ loading – in this case, the membrane needs to be the stiffer element, so that it takes more of the load.

The force sensors are assumed to be composed of steel (in reality, they are composed of piezo crystals in a steel tube) and are modeled as cantilever to obtain their XZ stiffness. This yields a conservative estimate, since the sensor is fairly stubby and the Euler-Bernoulli beam bending equations will underestimate the amount of deflection, predicting a stiffer beam.

Next, the bending stiffness of the membrane is modeled, again using Euler-Bernoulli beam theory, and the in-plane (XZ) stiffness of the membrane is modeled using uniaxial tension/compression. For modeling the XZ membrane stiffness, it was assumed that only a strip of material from the attachment node to the support bears the tension/compression load (shaded



strips in Figure C.7(b)), which would also be conservative since more material would be engaged in the deflection.

Table C-11: Parameters used to compare membrane stiffness to force sensors bending stiffness

Parameter description	Value	Unit	Comments
<i>Inputs</i>			
Membrane material	200	GPa	
Sensor bending material	200	GPa	Assume sheath dominates (further from N.A.)
Membrane width	10	mm	Assume a strip of material from node to ground bears the load
Membrane thickness	0.5	mm	
Membrane length	12	mm	Portion of membrane in between support and sensor node
<i>Calculated output values</i>			
Sensor bend stiffness	27.2	N/ $\mu$ m	Overestimate; stubby beam using Euler-Bernoulli
Sheet in-plane stiffness	83	N/ $\mu$ m	Underestimate; more material is engaged
Membrane/sensor XZ stiffness ratio	3.1	-	Will shunt 75% of shear/bend loads
Sensor Y/membrane Y stiffness ratio	415	-	Will shunt away less than 1% of the sensing force

## C.4 Feed stage – CS4

CS3 and CS4 are shown overlaid on the machine CAD model in Figure C.9, and the distance between the two with respect to CS4 given in Table C-12.

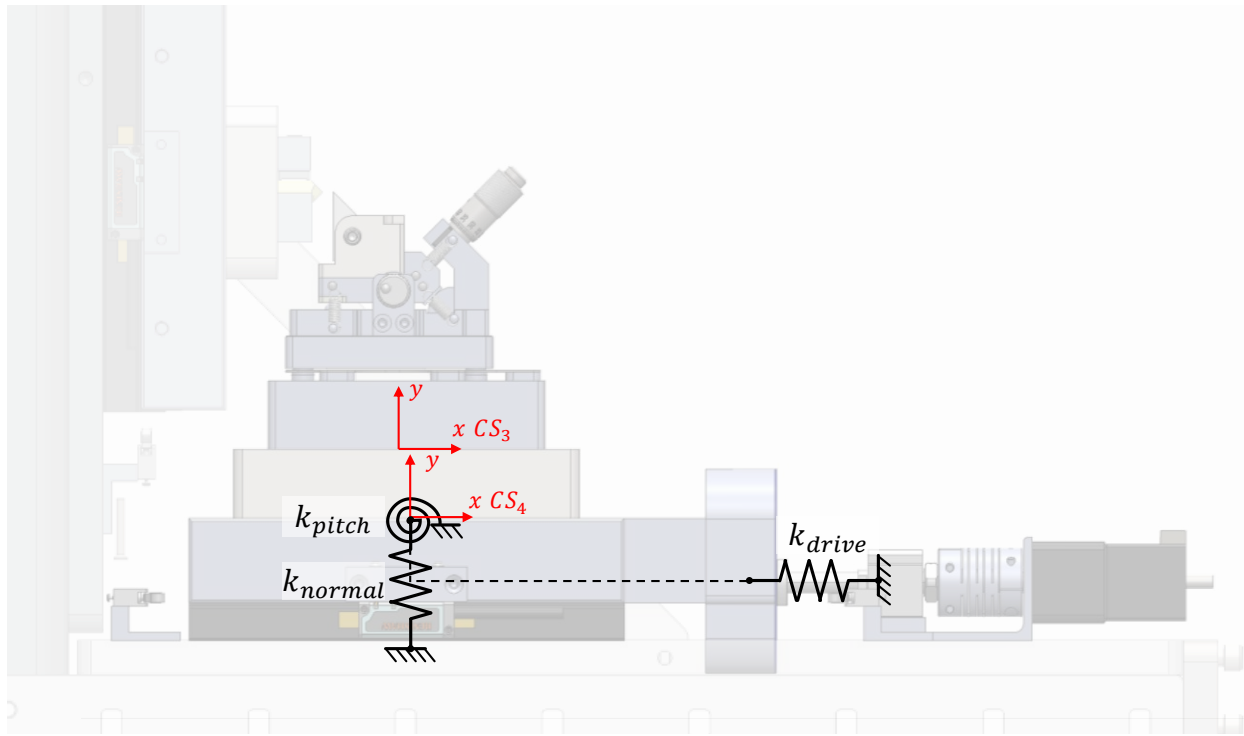


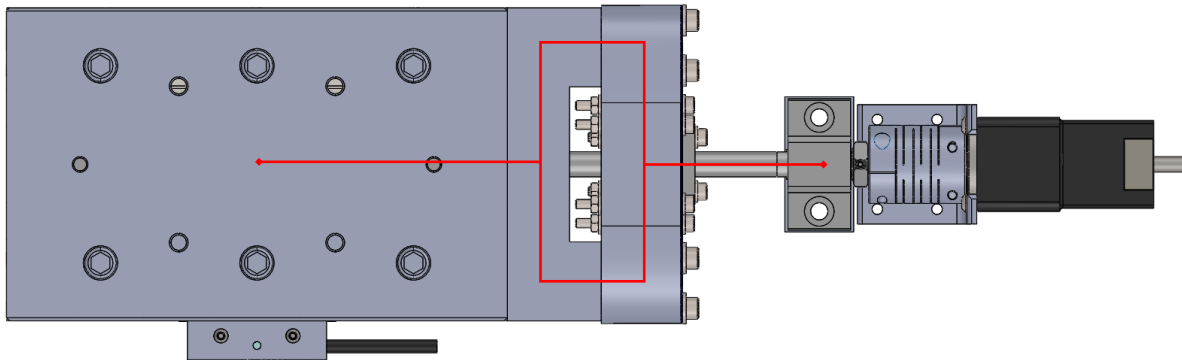
Figure C.9: Feed stage stiffness model schematic

Table C-12: Geometry definitions: location of CS3 origin w.r.t CS4

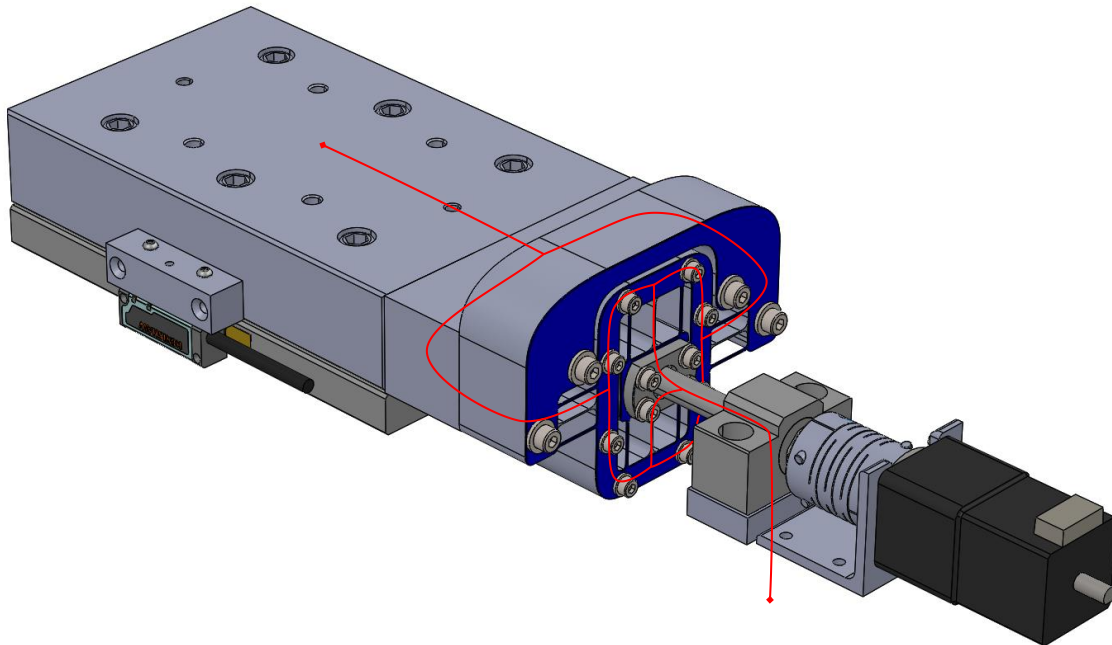
Direction	Value	Unit
X	-6.5	mm
Y	25	mm
Z	0	mm
$\theta_x$	0	deg
$\theta_y$	0	deg
$\theta_z$	0	deg

The primary contributors to the compliance of the feed stage (CS4) are the compliances of the crossed-roller bearing stage, and the drive stiffness of the ballscrew-decoupler-bearing drivetrain assembly. To model the feed stage's load-induced error contributions, the CS4 origin was set to be coincident with the top-center of the linear motion table. This is the location for which the table's stiffness specifications are provided. Stiffness in the X direction is modeled by the drivetrain components, the bearing table by itself would provide no X stiffness as it is free to move in this direction. The drivetrain stiffness is itself composed of multiple stiffness elements in series – the ballscrew nut decoupler ( $45 \text{ N}/\mu\text{m}$ ), the ballscrew nut ( $80 \text{ N}/\mu\text{m}$ ), and the

ballscrew support unit ( $35 \text{ N}/\mu\text{m}$ ), for a total series drive stiffness of  $16 \text{ N}/\mu\text{m}$ . In the Y and Z directions ( $k_{normal}$ ) the VRU6160 stage is rated at  $287 \text{ N}/\mu\text{m}$ , and the pitching stiffness  $k_{pitch}$  is rated at  $1.86\text{E}8 \text{ N}\cdot\text{mm}/\text{rad}$ . These stiffnesses are applied to the CS4 origin and used to compute CS4 load-induced deflections.



(a)



(b)

Figure C.10: Feed stage load path for determining X stiffness. (a) top view (b) oblique view

## C.5 Machine basebeam – CS5

The CS5-CS4 pair definition captures the deflections of the basebeam subsystem.

Figure C.11 shows the CS5/CS4 geometry definitions overlaid on the machine CAD model, and Table C-13 gives the exact geometric relationship between CS5 and the CS4 origin, with respect to the CS5 orientation.

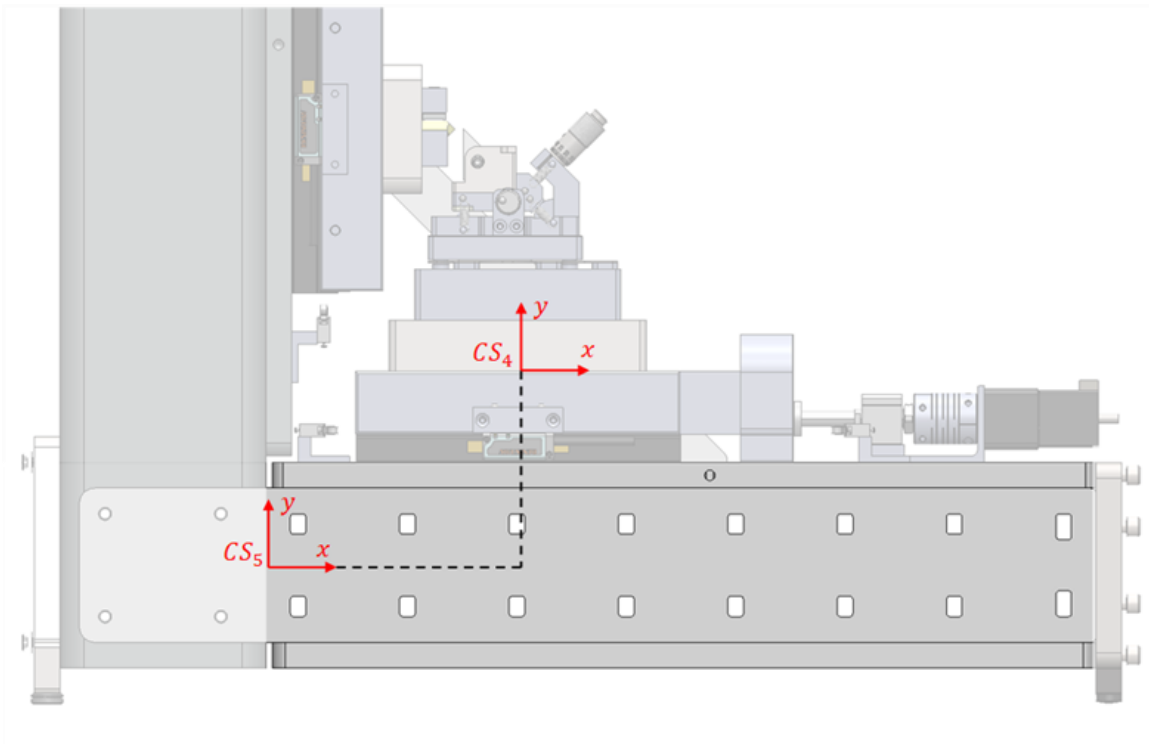


Figure C.11: CS5 geometry definitions capturing compliance of the basebeam with respect to the top of the X feed bearing table

Table C-13: Geometry definitions: location of CS4 origin w.r.t CS5

Direction	Value	Unit
X	124.5	mm
Y	97.1	mm
Z	0	mm
$\theta_x$	0	deg
$\theta_y$	0	deg
$\theta_z$	0	deg

To model the deflections of the CS4 origin w.r.t. CS5, the basebeam was modeled as an Euler-Bernoulli (E-B) cantilevered beam. The compliance model uses the compliance matrix from Appendix D.4.2, a cantilever beam loaded away from its neutral axis. The cross section used was that of a hollow box beam built up from two sets of plates, whose dimensions are given in Figure C.12.

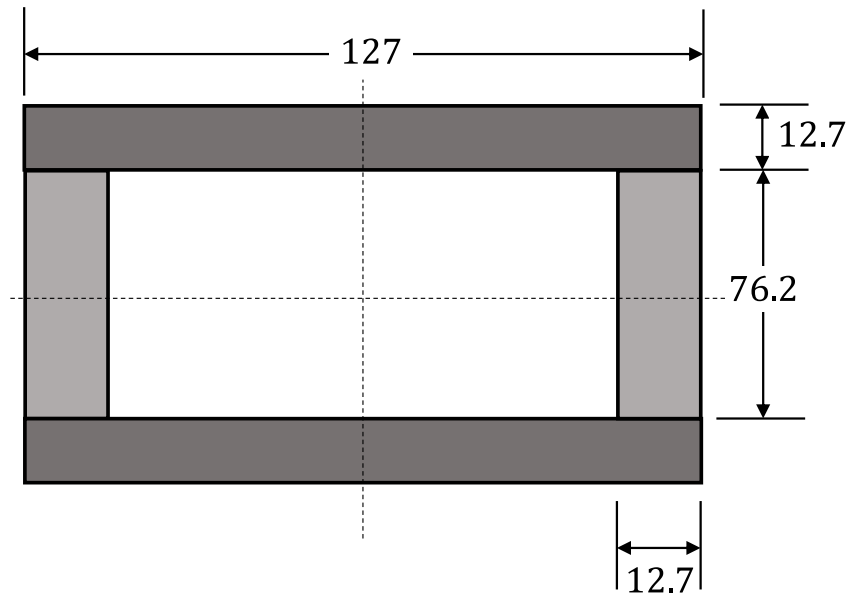


Figure C.12: Basebeam box beam member dimensions. Units are in *mm*

The resulting compliance matrix is given in Table C-14.

Table C-14: Compliance matrix of box beam, with box beam fixed at CS5 origin and loaded at CS4 origin (units are  $mm/N$  for translations,  $rad/N-mm$  for rotations)

	$F_x$	$F_y$	$F_z$	$M_x$	$M_y$	$M_z$
$\delta x$	1.27E-06	-6.81E-07	0	0	0	-1.13E-08
$\delta y$	-6.81E-07	5.62E-07	0	0	0	7.02E-09
$\delta z$	0	0	3.88E-07	8.78E-12	-4.83E-09	0
$\delta\theta_x$	0	0	8.78E-12	9.04E-14	0	0
$\delta\theta_y$	0	0	-4.83E-09	0	8.04E-11	0
$\delta\theta_z$	-1.13E-08	7.02E-09	0	0	0	1.17E-10

### C.6 Machine column – CS6

The coordinate system definitions used to model column deflections are given in

Figure C.13.

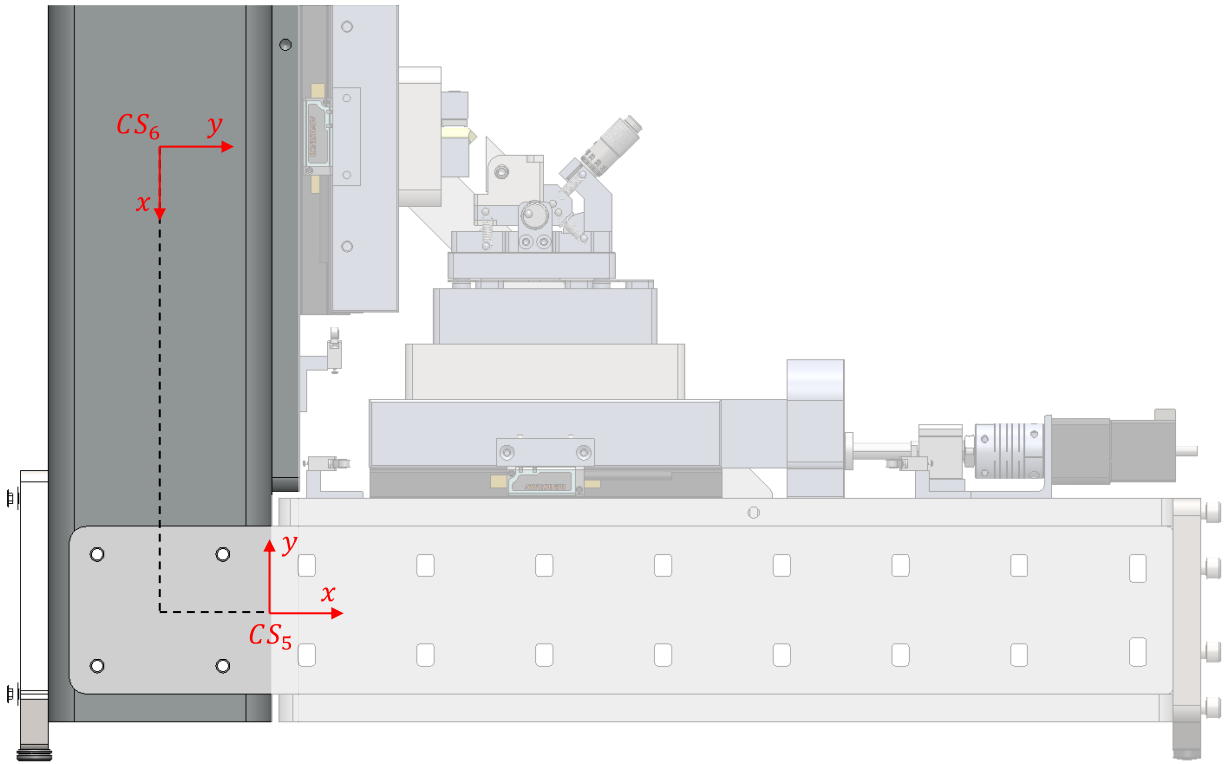


Figure C.13: CS5 and CS6 locations, used to model column deflections

Table C-15: Geometry definitions: location of CS5 origin with respect to CS6

Direction	Value	Unit
X	215.9	mm
Y	50.8	mm
Z	0	mm
$\theta_x$	0	deg
$\theta_y$	0	deg
$\theta_z$	90	deg

Column cross section used for modeling bending section modulus properties is shown in Figure C.14.

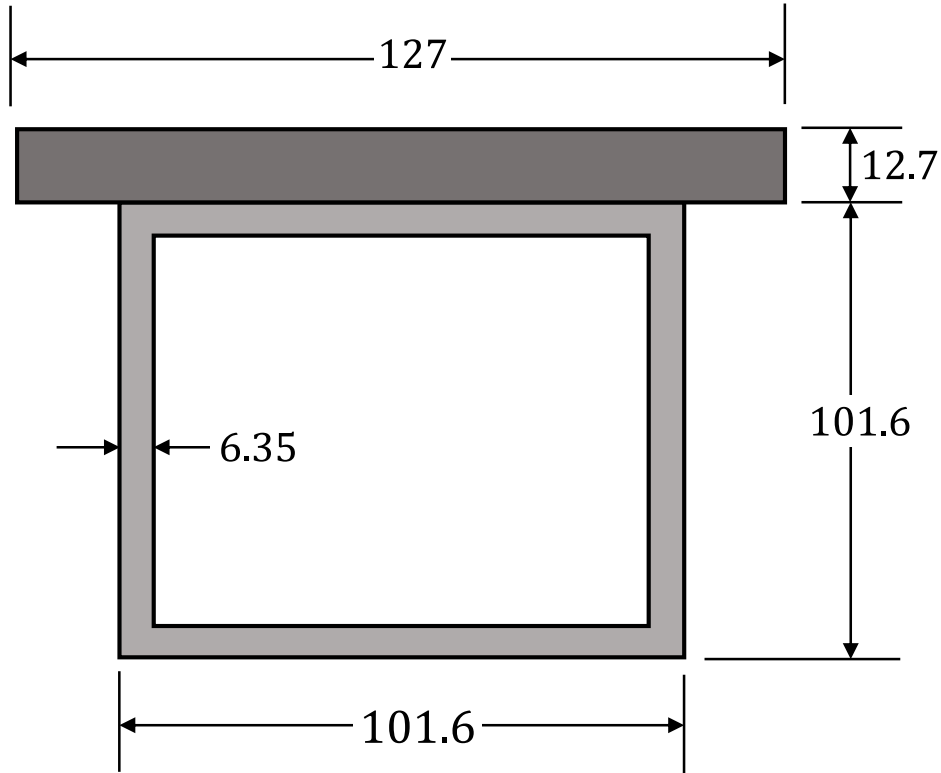


Figure C.14: Column with attached faceplate dimensioned cross section (units in *mm*)

The deflection is modeled by using the compliance matrix of a cantilevered beam with loading offset from the neutral axis, given in Appendix D.4.

Table C-16: Compliance matrix of displacements at CS5 origin w.r.t. CS6, modeling deflections of the column tube with faceplate subassembly (units are *mm/N* for translations, *rad/N-mm* for rotations)

	$F_x$	$F_y$	$F_z$	$M_x$	$M_y$	$M_z$
$\delta x$	6.74E-07	-8.63E-07	0	0	0	-8.00E-09
$\delta y$	-8.63E-07	2.45E-06	0	0	0	1.70E-08
$\delta z$	0	0	4.23E-06	2.67E-08	-1.99E-08	0
$\delta\theta_x$	0	0	2.67E-08	5.25E-10	0	0
$\delta\theta_y$	0	0	-1.99E-08	0	1.85E-10	0
$\delta\theta_z$	-8.00E-09	1.70E-08	0	0	0	1.57E-10



## **C.7 Slice stage – CS7**

The slice stage uses identical components as the feed stage for all of the stiffness-critical components; the same bearing stage, ballscrew, ballscrew nut, and ballscrew support unit are used. The stiffness model is identical, except that it is rotated by  $90^\circ$  so that the drive is now aligned with the vertical direction against gravity.

The slice stage compliance is captured in CS7; the manufacturer stiffness specifications are applied to the CS7 origin, as was done for the feed stage. The drivetrain is modeled identically to the feed stage drivetrain. Load induced errors are computed similarly to CS4, by lumping the drivetrain and bearing stage stiffnesses at the CS7 origin and computing the deflections based on the stiffnesses.

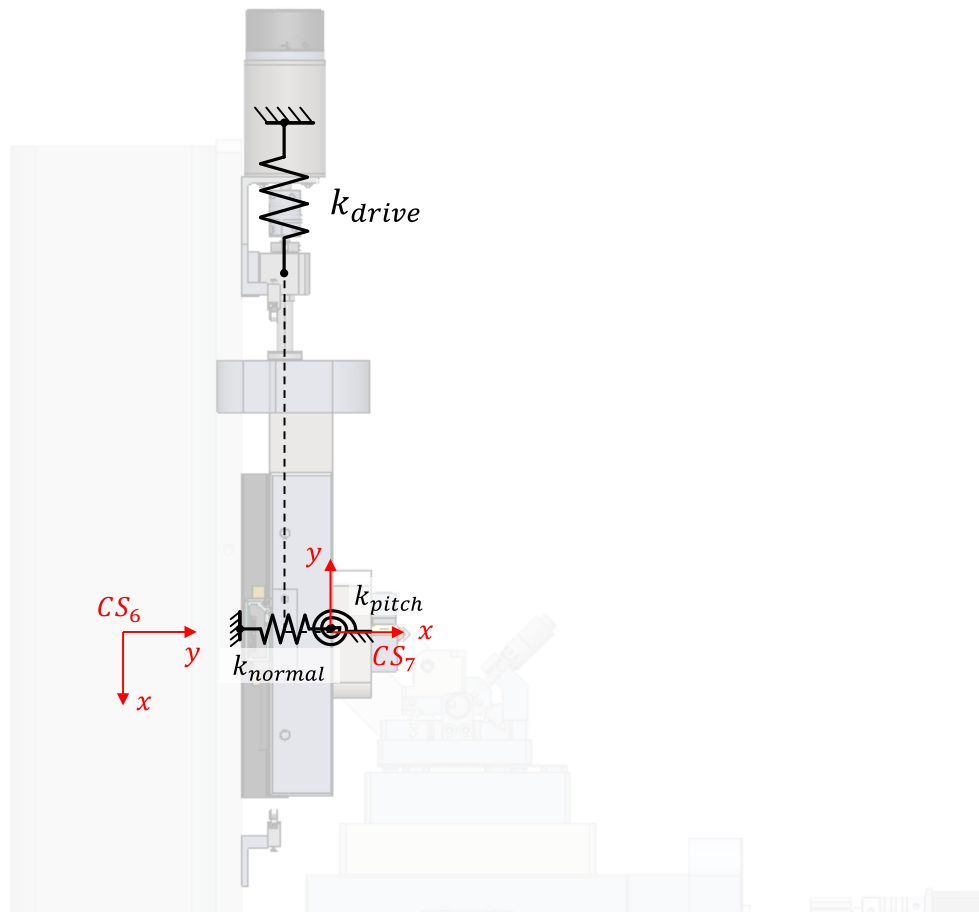


Figure C.15: Slice stage stiffness model. Loads are applied at the CS6 origin and deflections are calculated with respect to CS7.

The geometry definitions required to make the transformation between CS7 and CS6 is given in Table C-17.

Table C-17: Geometry definitions, locating CS6 origin in CS7

Direction	Value	Unit
X	-108.5	mm
Y	0	mm
Z	0	mm
$\theta_x$	0	deg
$\theta_y$	0	deg
$\theta_z$	-90	deg

## C.8 Workholder contact stiffness – CS8

CS8 (Figure C.16) models the compliance contributions due to workholder contact stiffnesses; the compliances modeled are the contact stiffnesses at the vise-workpiece interfaces, with loads applied at the CS7 origin (the top face centroid of the slice carriage). The modeling strategy and geometry definitions are discussed here.

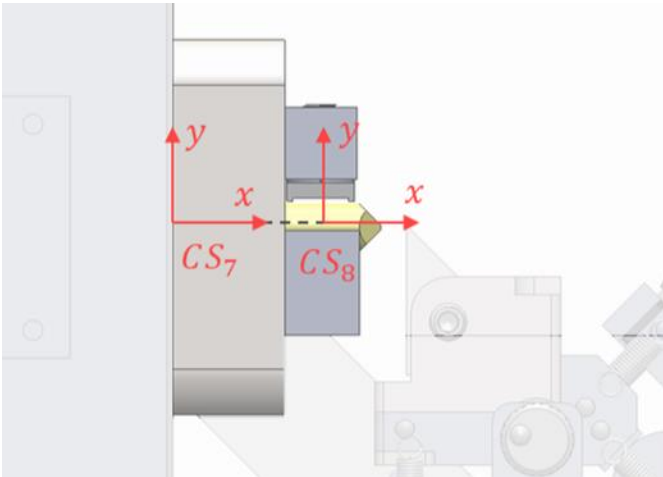


Figure C.16: CS8 geometry definitions – modeling compliance contributions due to the workholder contact stiffnesses, with the CS7 origin as the load input

Table C-18: Geometry definitions, locating CS7 origin in CS8

Direction	Value	Unit
X	-35.4	mm
Y	0	mm
Z	0	mm
$\theta_x$	0	deg
$\theta_y$	0	deg
$\theta_z$	0	deg

The spring locations are defined with respect to the CS8 origin; the springs are then transformed into a single effective stiffness at the CS7 origin using the stiffness transformation technique.

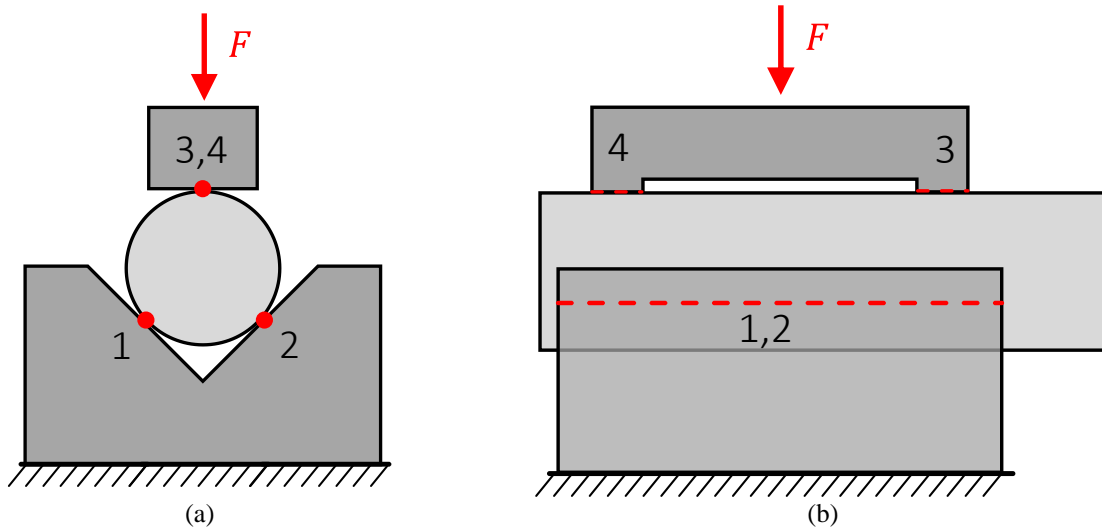


Figure C.17: Contact definitions for workholder stiffness modeling; four line contact regions are modeled.

A local coordinate system orientation and local stiffness matrix for each line contact must be defined (Figure C.18) prior to transformation; each local stiffness is then reflected to the reference coordinate frame CS7, and the reflected stiffness matrices are added together as they are in parallel. This net stiffness matrix is then inverted to obtain the effective compliance matrix for loads applied at the CS7 origin due to the ‘nest of springs’ in CS8. Figure C.18 shows the line contact coordinate system and axis labeling convention used for these calculations. The  $X$  direction is aligned with the surface normal direction; the  $Y$  direction represents the direction parallel to the rectangular’s line contact axis, and the  $Z$  direction represents the direction perpendicular to the rectangular contact axis.

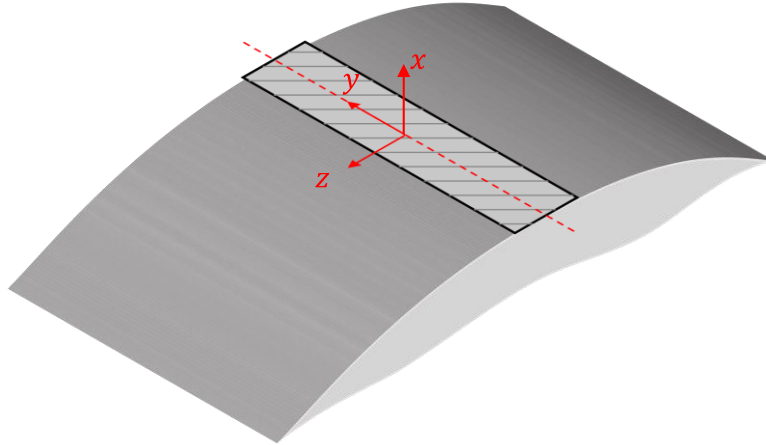


Figure C.18: Local contact stiffness coordinate system for contacts modeled in the workholder stiffness model.

Each contact is modeled with stiffnesses in the X, Y, and Z directions, as well as a moment stiffness about the Z direction. The resulting compliance matrix after the stiffness transformation is given in Table C-19.

Table C-19: Compliance matrix modeling deflections at CS7 origin with respect to CS8, capturing the compliance of the workpiece vise contact stiffnesses (units are  $mm/N$  for translations,  $rad/N\text{-}mm$  for rotations)

	$F_x$	$F_y$	$F_z$	$M_x$	$M_y$	$M_z$
$\delta x$	1.07E-04	1.85E-04	0	0	0	-7.26E-06
$\delta y$	1.85E-04	3.49E-03	-8.91E-07	5.62E-07	0	-1.33E-04
$\delta z$	0	-8.91E-07	3.29E-03	3.05E-06	1.26E-04	0
$\delta\theta_x$	0	5.62E-07	3.05E-06	9.61E-06	0	0
$\delta\theta_y$	0	0	1.26E-04	0	4.94E-06	0
$\delta\theta_z$	-7.26E-06	-1.33E-04	0	0	0	5.24E-06

## C.9 Specimen stub cantilever deflections – CS9

Specimen deflections are potentially a source of compliance considering that the specimen is made of polymer material, therefore the compliance contributions in both the feed (X) and slice (Y) directions of the polymer specimen protruding from the vise were modeled.

Two different models for modeling deflections in beams with very short span-to-depth ratios are

used and compared against FEA simulation. The results of the Euler-Bernoulli cantilever bending calculation are also presented. Using these deflection formulas for the stub specimen, a compliance matrix is built to model specimen deflections and used for error modeling. The coordinate system layout and geometry parameters used to model load-induced errors caused by specimen deflections are shown in Figure C.19.

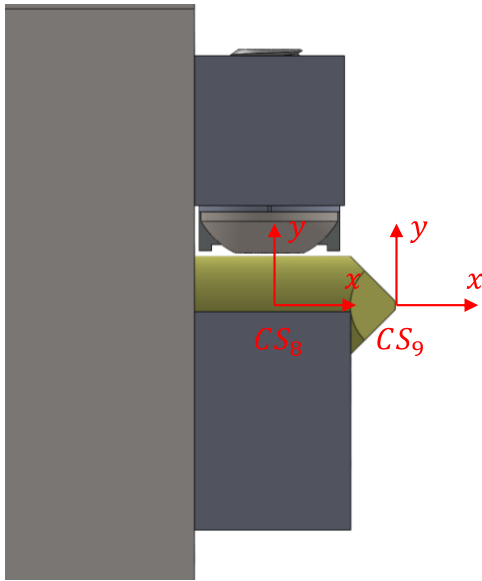


Figure C.19: CS9 error modeling geometry definitions, layout of coordinate system geometry between CS8 and CS9

Table C-20: Geometric relationship for CS8 w.r.t CS9 origin and orientation

Direction	Value	Unit
X	-35.4	mm
Y	0.8	mm
Z	0	mm
$\theta_x$	0	deg
$\theta_y$	0	deg
$\theta_z$	0	deg

The representative geometry used for modeling deflections was a machined rectangle  $w = 1 \text{ mm}$  wide,  $h = 3 \text{ mm}$  height, and overhanging the support by  $L = 1 \text{ mm}$  (Figure C.20).

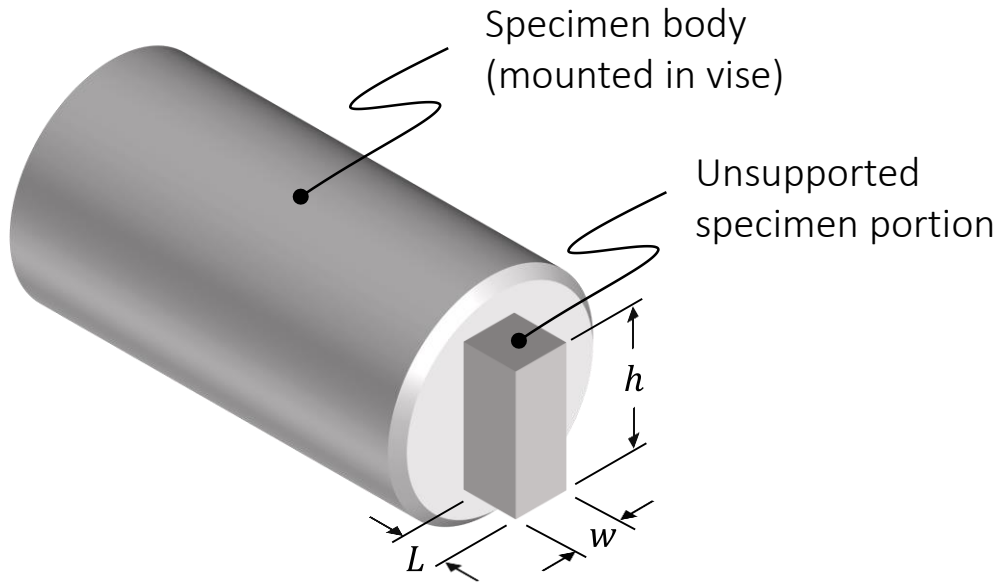


Figure C.20: Modeled geometry for specimen deflection analysis – it is modeled that the cylindrical shank of the specimen is firmly held in the vise, and a portion of the specimen is machined to a controlled geometry to be cut during testing. The machine portion of the specimen protrudes from the vise and is unsupported, and will deflect in response to cutting loads.

The X direction compliance was calculated by modeling the stub cantilever as a tension/compression element. Y direction deflections were calculated 3 different ways:

1. Using a model which considers only the vertical shear in the beam to calculate the deflection at the beam face [52].
2. Using a model which considers bending moment and shear in the beam [64].
3. Using the Euler-Bernoulli beam bending formula, for reference only [52]. This model is only accurate for beams with larger span to depth ratios; it greatly overestimates stiffness for specimens which do not meet the length-to-depth criteria, and the calculation is provided here only for reference.

The calculations are implemented in a MathCAD worksheet, and compared against FEA results in Table C-21.

A SolidWorks CAD model was created for the specimen geometry and imported into SolidWorks Simulation. A mesh was generated with a global element size of  $80 \mu m$  (Figure

C.21a). The rear face of the specimen was modeled as a fixed boundary condition. A 1 *N* load in either the X direction (normal to the face) or in the Y direction (parallel to the face along its longer direction) was applied. The measured effective displacement of the specimen was measured as the average displacements of the nodes on the front face of the specimen– it can be seen that there is some variation, by about a factor of two, in the deflection between the middle of the specimen, and the corners (Figure C.21b).



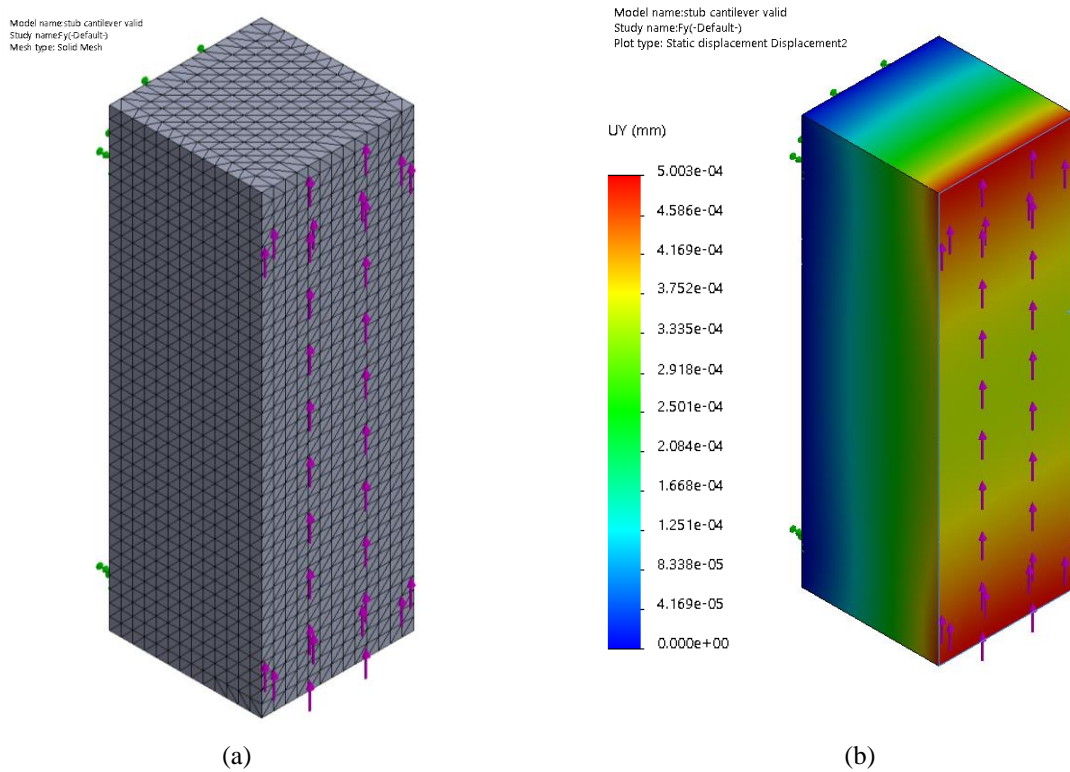


Figure C.21: Stub cantilever FEA validation modeled in SolidWorks Simulation. (a) Mesh setup and (b) Y-direction deflections

Table C-21: Comparison of results of different stub-beam deflection models

<b>Stiffness source</b>	<b>Stiffness</b>	<b>Unit</b>
<i>Deflection models</i>		
Tension/compression stiffness	8.4	$N/\mu m$
Castigliano shear force integration	2.625	$N/\mu m$
Timoshenko + Goodier	2.442	$N/\mu m$
Euler-Bernoulli beam	18.9	$N/\mu m$
<i>FEA results</i>		
FEA, X stiffness	9.20	$N/\mu m$
FEA, Y stiffness	2.49	$N/\mu m$

In the specimen compliance matrix, only the XX compliance and YY compliance entries are entered, the other entries are set to zero (rigid).

Table C-22: CS9 specimen deflections compliance matrix used for modeling load-induced errors (units are  $mm/N$  for translations,  $rad/N\cdot mm$  for rotations)

	$F_x$	$F_y$	$F_z$	$M_x$	$M_y$	$M_z$
$\delta x$	1.19e-4	0	0	0	0	0
$\delta y$	0	4.096e-4	0	0	0	0
$\delta z$	0	0	0	0	0	0
$\delta\theta_x$	0	0	0	0	0	0
$\delta\theta_y$	0	0	0	0	0	0
$\delta\theta_z$	0	0	0	0	0	0

# D

## COMPLIANCE MODELING FORMULAE

---

This chapter contains supplemental details or descriptions of the compliance/stiffness modeling and design work done in support of the analytical error modeling for the cutting instrument used in this work.

### **D.1 Description of compliance matrix transformation technique**

A useful method of representing the net stiffness or compliance of a collection of springs with respect to some point of interest is via the stiffness transformation technique which is described in depth with examples in [65], and is used extensively in this work. The technique requires a local stiffness or compliance matrix defined for each compliant element and the geometric transformation required to align each local compliance element's coordinate system to the point of interest's reference coordinate system. This technique is extremely useful for load-induced error modeling, as it allows an analyst to lump a complex system of compliances into a single effective compliance matrix; however, the decision of how to lump the system is still at the analyst's discretion and extreme care must be taken that all geometry has been input properly and that stiffness matrices have been defined consistent with the coordinate systems being used.

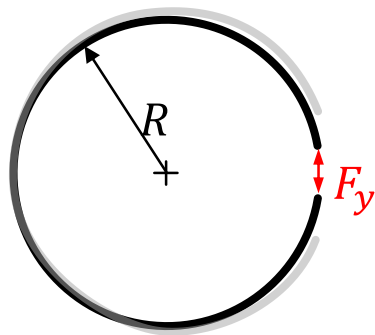
### **D.2 Miscellaneous stiffness and compliance formulas**

Several miscellaneous formulae used in this work are catalogued in this section.

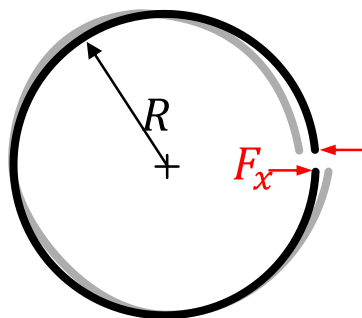
### D.2.1.1 Planar C-frame deflection formulae

The following deflection formulas derived using the Castigliano method are useful for modeling the deflections of a planar C-frame. In this work they were used for first-order modeling of the overall stiffness of the machine structural loop.

Table D-1: Formulae for calculating the effective stiffness of the stiffnesses of a planar ring, subject to prying and shearing forces



$$k_y = \frac{1}{3\pi} \frac{EI}{R^3}$$



$$k_x = \frac{1}{\pi} \frac{EI}{R^3}$$

## D.3 Ballscrew decoupler design

The ideal ballscrew/leadscrew decoupler flexure would allow motion in all directions except torsional (e.g., the “wind-up” direction) and along the axis of the leadscrew. This would allow for misalignment between the leadscrew axis and the axis of motion, which is always present to some extent due to the practicalities of fabrication and assembly. The design process here follows the theory and design process used to design a leadscrew decoupler using Freedom, Actuation, and Constraint Topologies (FACT) from [66]. The decoupler required here has the

same constraint requirements, but has different physical mounting requirements. To design the decoupler, one must first analyze the desired motions, identify the number of intermediate stages required, and generate and select a concept. Once a concept is selected, design detailing consists of assessing the maximum stresses in the beams, ensuring the overall stiffnesses of the decoupler are appropriate, and that the design will fit in the required volume as well as be manufacturable.

### D.3.1 Concept description

The desired constraints are achievable only via a 2-stage design. The chosen concept is shown in isometric and front view in Figure D.1

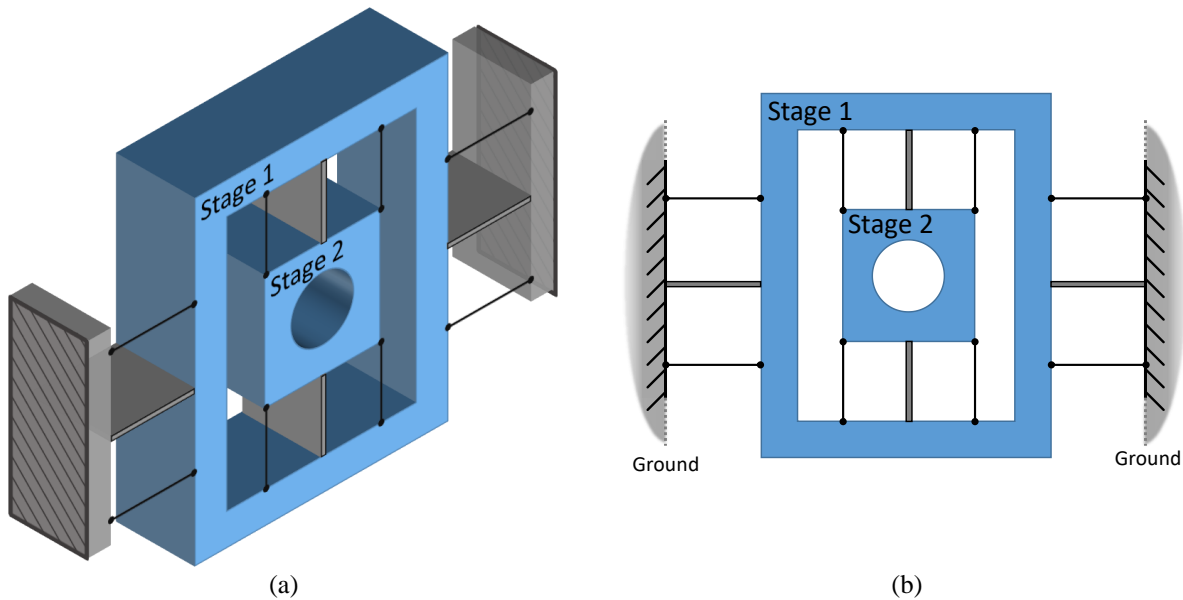


Figure D.1: Two-stage ballscrew decoupler concept (a) isometric view (b) front view. The thin lines represent wire constraints, and the thicker gray bodies are ideal blade constraints. Achieving the desired constraint will require two stages in series.

In the chosen concept, more constraints are provided than are necessary (some are redundant); exact constraint can be achieved with fewer constraints, however, the designer must consider that real constraints are not infinitely stiff, and that design's center of stiffness should be placed as close as possible to the loading point to avoid large pitching moments; it is generally a good idea to maintain symmetry.

### D.3.2 Decoupler analysis and modeling

A MathCAD parametric worksheet was set up for the analysis. The spacing between each set of blades and wires were parametrized as shown in Figure D.2. The blade and wire flexures will have finite stiffness, which can be modeled using information about the flexures' geometry and material. The individual blade and wire flexures, combined with their locations, are combined to compute the overall stiffness of the decoupler.

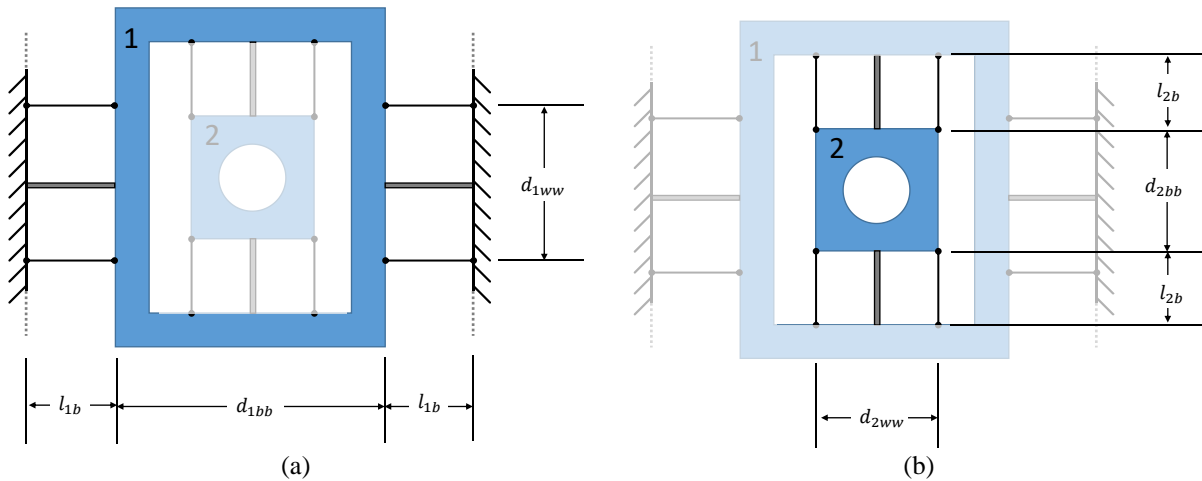


Figure D.2: Decoupler design parametrization

It is desirable to maintain the lowest stiffness possible in the decoupled degrees of freedom, and maximizing stiffness in the constrained directions, while avoiding making the flexures so thin that they would buckle or be difficult to fabricate accurately.

### D.3.3 Decoupler design process

The decoupler consists of two components: the decoupler body, and the wire flexure plate. The decoupler body contains the blade flexures, the intermediate stage, and the mounting points; the wire flexure plate contains the wire flexure constraints and bolts on to the body.

Key considerations in detailing the decoupler are 1) ensuring that the decoupler will not break, 2) the decoupler will fit within the required envelope, and 3) the decoupler effectively decouples while providing high stiffness in the constrained direction.

The first point was addressed by modeling each wire or blade as a beam element and calculating the maximum stresses as a function of maximum expected misalignments. The second criteria was met by updating the CAD model concurrently with the design work and checking for volume limitations. The last criteria was fulfilled by concurrent use of the decoupler parametric model, and the overall system error model. A general axial (along the axis of the leadscrew, i.e., the overall drive axis) stiffness target was set by considering the other elements in series with the decoupler: the ballscrew nut and the ballscrew bearing support unit. Because these elements are in series, and the stiffness of the overall assembly is dominated by the most compliant element, it would be wasteful to set a design target far exceeding the stiffness of the aforementioned elements.

#### **D.3.4 Ballscrew decoupler design concept**

The ballscrew design concept CAD model is shown in Figure D.3. The wire plates are fabricated from 1095 spring steel, and the body with the flexure blades are cut from A514 steel plate.

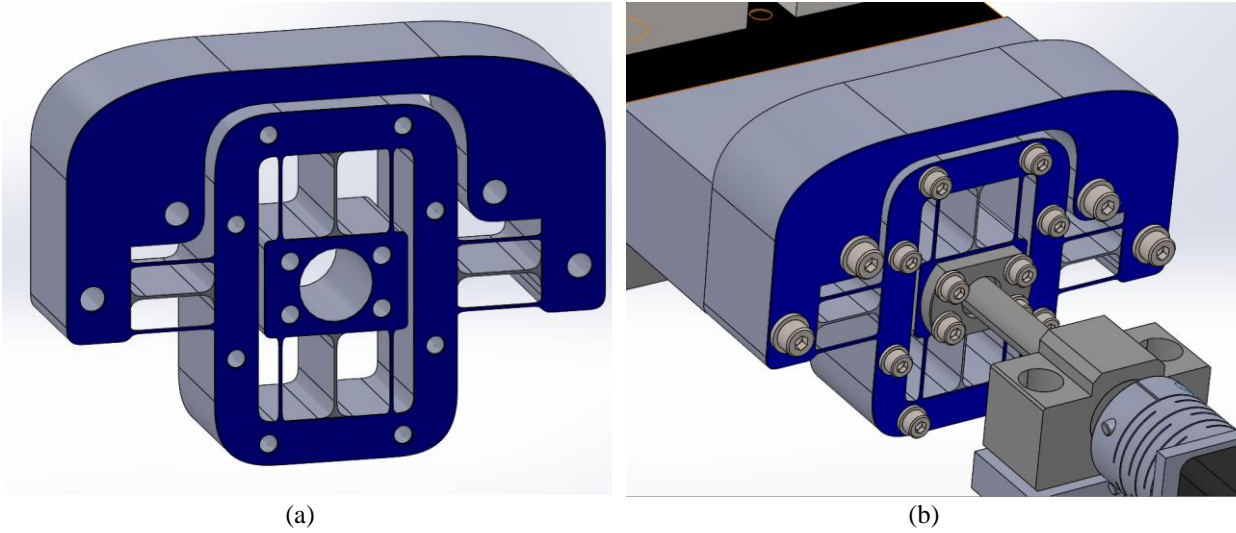


Figure D.3: CAD model of finalized decoupler design (a) the decoupler body and faceplate (b) assembled and mounted in the drivetrain

## D.4 Cantilever beam compliance matrices

The cantilever beam compliance matrix is useful for modeling slender machine elements under bending loads. A basic compliance matrix is presented in Section D.4.1, and a more general compliance matrix with the beam loaded away from the neutral axis (thus introducing additional moments and torques) is presented in D.4.2.

### D.4.1 Cantilever beam loaded at its tip, at its neutral axis

The compliance matrix presented in Eq. (D.1) represents the deflections

$\vec{\delta} = [\delta_x \quad \delta_y \quad \delta_z \quad \delta\theta_x \quad \delta\theta_y \quad \delta\theta_z]^T$  induced at the loading point with respect to a static ground frame, in response to the loading vector  $\vec{F} = [F_x \quad F_y \quad F_z \quad M_x \quad M_y \quad M_z]^T$ , via  $\vec{\delta} = \mathbf{C}\vec{F}$ . The coordinate system orientation is shown in Figure D.4, and the length  $L$  is measured from the support to the loading point.



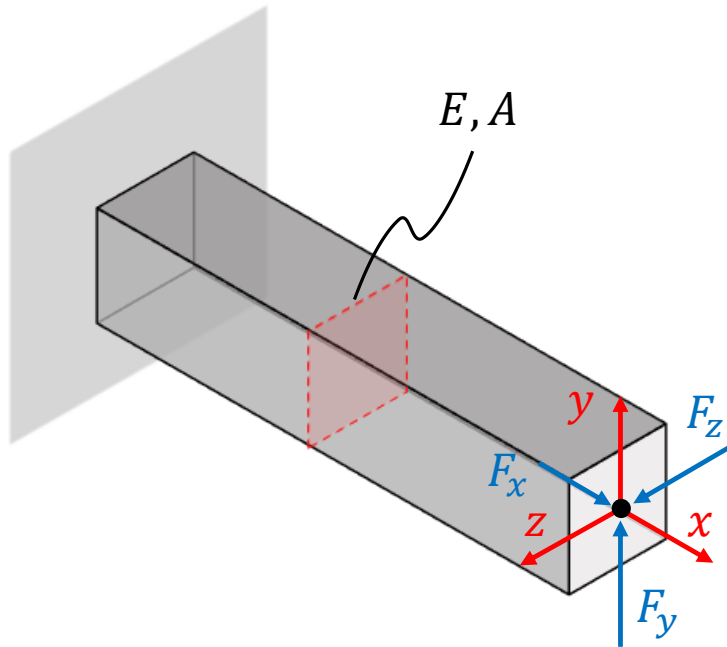


Figure D.4: Loads and coordinate system for cantilever beam compliance matrix

$$\begin{bmatrix}
 \frac{L}{EA} & 0 & 0 & 0 & 0 & 0 \\
 0 & \frac{L^3}{3EI_{zz}} & 0 & 0 & 0 & \frac{L^2}{2EI_{zz}} \\
 0 & 0 & \frac{L^3}{3EI_{yy}} & 0 & -\frac{L^2}{2EI_{yy}} & 0 \\
 0 & 0 & 0 & \frac{L}{GJ} & 0 & 0 \\
 0 & 0 & -\frac{L^2}{2EI_{yy}} & 0 & \frac{L}{EI_{yy}} & 0 \\
 0 & \frac{L^2}{2EI_{zz}} & 0 & 0 & 0 & \frac{L}{EI_{zz}}
 \end{bmatrix} \quad (D.1)$$

### D.4.2 Cantilever beam loaded at its tip, offset from its neutral axis

Similarly to the previous section, a compliance matrix is defined here for a cantilevered beam except that now the loading point is offset from the neutral axis as shown in Figure D.5.

Additional terms are introduced as a result.

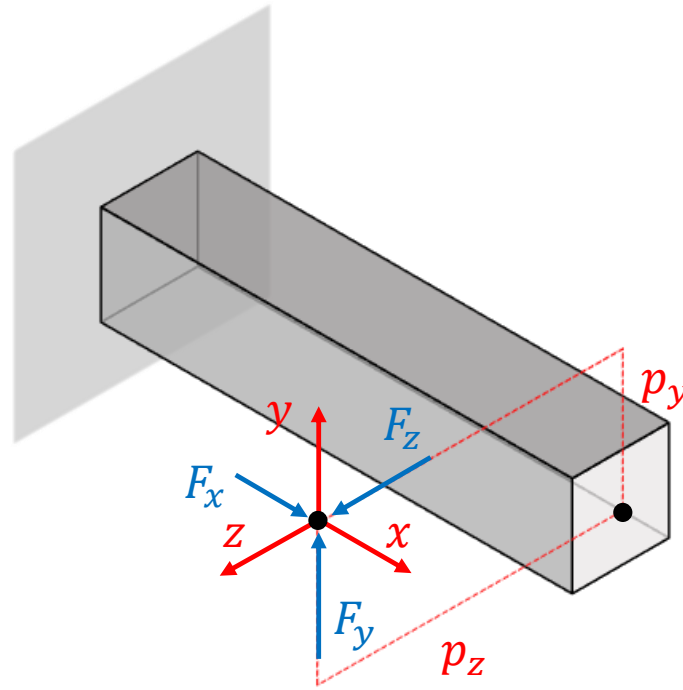


Figure D.5: Loads and coordinate system for off-axis cantilever beam compliance matrix

$$\begin{bmatrix}
 \frac{L}{EA} + \frac{Lp_z^2}{EI_{yy}} + \frac{Lp_y^2}{EI_{zz}} & -\frac{L^2 p_y}{2EI_{zz}} & -\frac{L^2 p_z}{2EI_{yy}} & 0 & \frac{Lp_z}{EI_{yy}} & -\frac{Lp_y}{EI_{zz}} \\
 -\frac{L^2 p_y}{2EI_{zz}} & \frac{L^3}{3EI_{zz}} + \frac{Lp_z^2}{GJ} & -\frac{Lp_y p_z}{GJ} & -\frac{Lp_z}{GJ} & 0 & \frac{L^2}{2EI_{zz}} \\
 -\frac{L^2 p_z}{2EI_{yy}} & -\frac{Lp_y p_z}{GJ} & \frac{L^3}{3EI_{yy}} + \frac{Lp_y^2}{GJ} & \frac{Lp_y}{GJ} & -\frac{L^2}{2EI_{yy}} & 0 \\
 0 & -\frac{Lp_z}{GJ} & \frac{Lp_y}{GJ} & \frac{L}{GJ} & 0 & 0 \\
 \frac{Lp_z}{EI_{yy}} & 0 & -\frac{L^2}{2EI_{yy}} & 0 & \frac{L}{EI_{yy}} & 0 \\
 -\frac{Lp_y}{EI_{zz}} & \frac{L^2}{2EI_{zz}} & 0 & 0 & 0 & \frac{L}{EI_{zz}}
 \end{bmatrix} \quad (D.2)$$